Conception d'algorithmes temps réel pour transpondeurs optiques élastiques à très haut débit

Marwa Kazdoghli Lagha

DOCTORAT BRETAGNE LOIRE / MATHSTIC

UNIVERSITÉ DE RENNES 1

THÈSE DE DOCTORAT DE

L'UNIVERSITÉ DE RENNES 1

ÉCOLE DOCTORALE N° 601
Mathématiques et Sciences et Technologies de l'Information et de la Communication
Spécialité : « *Télécommunications* »

Par

« Marwa KAZDOGHLI LAGHA »

« Conception d'algorithmes temps réel pour transpondeurs optiques élastiques à très haut débit »

Thèse présentée et soutenue à « Lannion », le 21 juin 2021
Unité de recherche : « IRISA »

Rapporteurs avant soutenance :

Laurent CLAVIER	Professeur, IMT Lille Douai, France
Laurent ROS	Professeur des Universités, Université de Grenoble, France

Composition du Jury :

Président :	Laurent ROS	Professeur des Universités, Université de Grenoble, France
Examinateurs :	Christophe LAOT	Professeur des Universités, IMT Atlantique, France
	Stéphanie SAHUGUÈDE	Maître de Conférences, Université de Limoges, France
	Erwan PINCEMIN	Ingénieur Recherche et Développement, Orange Labs, France
Dir. de thèse :	Pascal SCALART	Professeur des Universités, Université de Rennes 1, France
Co-encadrant de thèse :	Robin GERZAGUET	Maître de Conférences, Université de Rennes 1, France

Contents

LIST OF FIGURES

List of Tables

List of acronyms

ADC analog-to-digital converter.

AI artificial intelligence.

AIR achievable information rate.

ASE amplified spontaneous emission.

AWG arbitrary waveform generator.

AWGN additive white Gaussian noise.

B2B back-to-back.

BASS blind and adaptive source separation.

BER bit error rate.

BPS blind phase search.

BPSK binary phase-shift keying.

BSS blind source separation.

CD chromatic dispersion.

CFO carrier frequency offset.

CMA constant modulus algorithm.

CPD conventional phase detector.

CPR carrier phase recovery.

CRB Cramer-Rao bound.

CW continuous wave.

DAC digital-to-analog converter.

DCF dispersion compensating fiber.

DD-LMS decision-directed least mean square.

DFB distributed feedback.

DFT discrete Fourier transformation.

DGD differential group delay.

DSP digital signal processing.

EASI equivariant adaptive separation via independence.

EC ellipse correction.

ECL external cavity laser.

EDC electronic dispersion compensation.

EDFA erbium-doped fiber amplifier.

EVM error vector magnitude.

FBG fiber Bragg gratings.

FEC forward error correction.

FFT fast Fourier transformation.

FIR finite impluse response.

FPGA field programmable gate array.

FWM four wave mixing.

GSOP Gram-Schmidt orthogonalization procedure.

IDFT inverse discrete Fourier transformation.

IFFT inverse fast Fourier transformation.

IIR infinite impulse response.

IQ imbalance in-phase and quadrature imbalance.

ISI inter-symbol interference.

LASER light amplification by stimulated emission of radiation.

LDPC low density parity check.

LED light-emitting diode.

LMS least mean square.

LO local oscillator.

LPN laser phase noise.

MIMO multiple-input multiple-output.

MMA multi-modulus algorithm.

MMF multi-mode fiber.

MPD modified phase detector.

MSE mean squared error.

MZM Mach-Zehnder modulator.

OBPF optical band pass filter.

OSNR optical signal-to-noise ratio.

PBC polarization-beam combiner.

PBS polarization-beam splitter.

PDL polarization-dependent loss.

PM polarization-division multiplexing.

PMD polarization-mode dispersion.

PSK phase-shift keying.

QAM quadrature amplitude modulation.

QPSK quadrature phase shift keying.

R-BPS recursive blind phase search.

RDE radius directed equalization.

RMS root mean square.

RW-BPS recursive probability weighted blind phase search.

SFO sampling frequency offset.

SMF single-mode fiber.

SNR signal-to-noise ratio.

SOP state of polarization.

SPM self-phase modulation.

SR symbol rate.

SRRC square root raised cosine.

SSMF standard single-mode fiber.

TED timing error detector.

VOA variable optical attenuator.

VODL variable optical delay line.

WDM wavelength-division multiplexing.

XPM cross phase modulation.

RÉSUMÉ

Les systèmes de transmission optique élastique à base de réception cohérente sont aujourd'hui d'une importance considérable puisqu'ils permettent d'augmenter à la fois l'efficacité spectrale et le débit. La technologie cohérente nécessite la mise au point d'algorithmes de traitement numérique du signal (*Digital Signal Processing*) capables de compenser les diverses distorsions linéaires et non linéaires liées à la transmission optique. Ces algorithmes doivent également assurer un compromis convenable entre les performances d'adaptation au canal de propagation optique, la rapidité de convergence liée à la flexibilité de la couche physique et la complexité d'implémentation temps réel à très haut débit.

Cette thèse vise à la sélection et/ou l'optimisation d'une chaîne de réception cohérente dans le cadre d'une communication optique tout en prenant en considération les problèmes de complexité des traitements dans le choix des solutions algorithmiques. Les principaux axes de cette thèse sont les techniques utilisées pour augmenter l'efficacité spectrale, notamment le multiplexage en polarisation, et les méthodes permettant d'assurer des communications optiques fiables, notamment les techniques permettant de compenser le bruit de phase des lasers dans un contexte de communication flexible en terme de largeur de bande ou formats de modulation permettant ainsi d'augmenter ou de baisser le débit selon le besoin. Ainsi, les contributions de la recherche sont les suivantes

1. Proposition d'une approche conjointe pour le démultiplexage de polarisation et de compensation du déséquilibre IQ dit l'algorithme "joint".
2. Proposition d'un algorithme à structure bouclée de compensations de bruit de phase de laser nommé l'algorithme à "détecteur de phase de type décisions dirigées (DD) modifié".
3. Proposition d'un algorithme à structure directe et implémenté en parallèle pour la compensation de bruit de phase de laser intitulé l'algorithme "R-BPS".

Les performances des algorithmes proposés sont évaluées par divers critères appliqués sur les signaux compensés tels que la moyenne de la valeur absolue de l'error (error vector magnitude (EVM)), l'erreur quadratique moyenne (EQM), le taux d'erreur binaire (TEB),

le rapport signal sur bruit (RSB) requis pour un taux d'erreur requis pour atteindre une qualité de service donnée ou taux d'erreur cible, etc. Aussi, les approches introduites ont été validées sur des bancs d'expérimentations.

Description de l'algorithme "joint"

La majorité des approches de démultiplexage de polarisation proposées dans la littérature se reposent sur une structure de filtre dit en "papillons". D'autre part, plusieurs techniques de compensation du déséquilibre IQ existent notamment la procédure d-'orthogonalisation de Gram-Schmidt (GSOP) [1], la méthode de correction d'ellipse (EC) [2] et des modèles paramétriques de compensation d'IQ pour lesquels les paramètres sont obtenus par filtrage adaptatif en optimisant un critère d'ajustement donné [3, 4]. La méthode GSOP est utilisée pour blanchir le signal reçu et et construire à l'aide de la procédure de Gram-Schmidt en sortie de traitement deux composantes mutuellement orthogonales et de même énergie. Mais la méthode GSOP n'est applicable qu'à la compensation des déséquilibres IQ au niveau du récepteur et est inefficace pour compenser les déséquilibres au niveau de l'émetteur. L'algorithme EC est utilisé pour ajuster la courbe d'ellipse selon la méthode des moindres carrés. Cependant, EC est utilisé pour compenser les déséquilibres IQ de l'émetteur et ne convient pas aux signaux d'ordre de modulation élevé (supérieur à 4). L'approche d'estimation des paramètres d'un modèle paramétrique de compensation du déséquilibre IQ peut être utilisé pour compenser à la fois le déséquilibres IQ de l'émetteur et du récepteur.

Cependant, peu de travaux ont été consacrés à la compensation du déséquilibre IQ et le démultiplexage de polarisation de manière conjointe. Dans cette thèse, nous proposons une approche conjointe exploitant plus particulièrement les algorithmes "blind and adaptive source separation (BASS)" [5] et "equivariant adaptive separation via independence (EASI)" [6] qui ont été initialement proposés pour les problématiques de compensation du déséquilibre IQ et de séparation aveugle de sources et ce de manière non conjointe. A partir de la proposition d'une modélisation sous forme matricielle des effets liés conjointement au multiplexage de polarisation et au déséquilibre IQ, l'algorithme proposé tire profit des capacités de séparation de sources de l'algorithme BASS et de celles d'orthogonalisation de l'algorithme EASI.

Contributions de l'algorithme "joint"

Les contributions de l'approche conjointe sont les suivantes

— Évaluation de l'efficacité de l'algorithme en présence du déséquilibre IQ que celui-ci ait été introduit à l'émetteur, ou au récepteur (ou qu'il soit présent à la fois en émission et en réception) et en présence de rotations de polarisation;

— Évaluation des performances de l'algorithme en présence d'autres distorsions telles que la perte de puissance liée à la polarisation, la dispersion modale de polarisation et la dispersion chromatique;

— Comparaison des résultats avec une approche 2×2 multi-entrées multi-sorties basée sur le critère du forçage à module constant (CMA) [7] mise en cascade avec deux structures de compensation du déséquilibre IQ (l'une sur chaque polarisation), nommée algorithme "CMA+BASS";

— Comparaison des résultats avec la solution optimale définie dans la thèse comme l'application du critère de forçage à zéro, c'est à dire l'inverse de la matrice de distorsion (dont les coefficients s'expriment en fonction des paramètres du déséquilibre IQ et de rotation de polarisation).

— Investigation sur la capacité de l'algorithme conjoint à suivre dynamiquement les variations des canaux. Deux types de variations ont été étudiés: le mélange de polarisation et le changement de formats de modulation;

— Validation expérimentale de l'approche proposée.

Analyse des résultats de l'algorithme "joint"

Les analyses des résultats de simulations ont permis de conclure les points suivants.

La comparaison de la robustesse de notre approche et celle du "CMA+BASS" face à la présence du déséquilibre IQ au niveau de l'émetteur et du récepteur a été étudiée sur des systèmes 4-, 16-, et 64-QAM utilisant le multiplexage en polarisation.

Dans un premier temps, les performances des deux algorithmes ont été évaluées en RSB requis pour atteindre un taux d'erreurs binaires de 10^{-3} en fonction du déséquilibre en gain (le déséquilibre en phase étant nul), ce déséquilibre étant considéré comme identique sur les deux polarisations. Dans ces conditions, les signaux sont mélangés par une matrice de rotation de polarisation. On constate que notre algorithme présente grossièrement les mêmes performances que l'approche optimale alors que le "CMA+BASS" présente

moins de tolérances pour des valeurs importantes de déséquilibre en gain surtout pour les modulations 16- et 64-QAM.

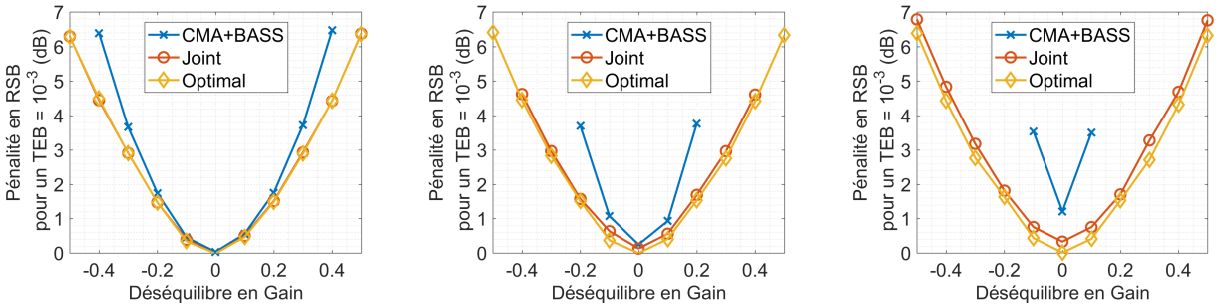

(a) (b) (c)

Figure 1 – RSB requis pour un TEB $= 10^{-3}$ en fonction du déséquilibre en gain et en absence du déséquilibre en phase ($\alpha = 30°, \theta = 50°$) (a) 4-QAM, (b) 16-QAM, (c) 64-QAM.

En outre, le RSB requis pour un taux d'erreurs binaires cible de 10^{-3} en fonction du déséquilibre en phase appliqué de manière égale sur les signaux mélangés (avec les mêmes paramètres de rotation et le déséquilibre en gain étant nul) a été évalué. L'algorithme proposé présente de meilleurs résultats en le comparant avec le "CMA+BASS" car il offre une plus large tolérance vis-à-vis du déséquilibre en phase en phase et ce pour les 3 modulations utilisées.

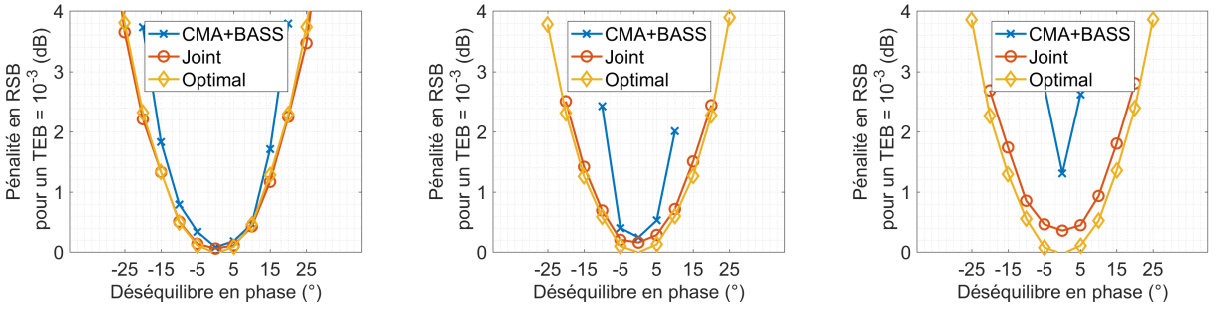

(a) (b) (c)

Figure 2 – RSB requis pour un TEB $= 10^{-3}$ en fonction du déséquilibre en phase et en absence du déséquilibre en gain ($\alpha = 30°, \theta = 50°$) (a) 4-QAM, (b) 16-QAM, (c) 64-QAM.

Dans des conditions de forts déséquilibre en gain et avec une polarisation contrôlée, la solution proposée permet de gagner 2 dB sur le RSB requis pour atteindre un TEB de 10^{-3}(voir Fig. 1(b)). Dans des conditions où le déséquilibre en gain est moins pénalisant, la solution proposée présente sensiblement les mêmes performances que la structure

concurrente “CMA + BASS” mais avec une complexité algorithmique moindre. Aussi, pour des forts déséquilibres en phase, l’approche “joint” offre un gain de l’odre de 1.5 dB en RSB pour un TEB de 10^{-3} (voir Fig. 2(b)) et en 4-QAM les 2 algorithmes présentent globalement les mêmes performances.

D’autre part, le RSB requis pour un taux d’erreurs binaires cible de 10^{-3} en fonction de la perte dépendante de la polarisation a été évalué sur des modulations 4-, 16- et 64-QAM utilisant le multiplexage en polarisation. Les simulations ont été effectués sur des signaux déformés avec un déséquilibre IQ au niveau de l’émetteur et mélangé avec la matrice de rotation. On constate que les approches “joint” et “CMA + BASS” présentent grossièrement les mêmes résultats sur les systèmes 4- et 16-QAM. Néanmoins, la tolérance de notre configuration à la perte dépendante de la polarisation est plus élevée que le “CMA + BASS” en 64-QAM.

Les expérimentations menées montrent que l’algorithme “joint” opère convenablement pour des fortes valeurs de PDL contrairement à l’algorithme “CMA+BASS” qui ne tolère que des valeurs plus faibles.

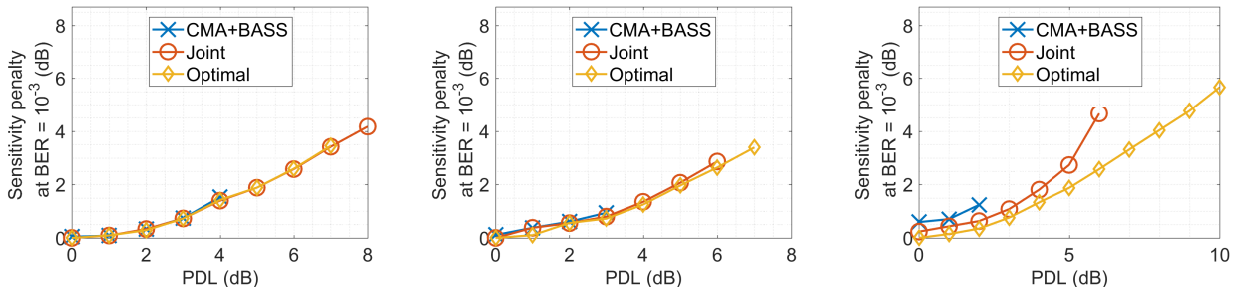

Figure 3 – RSB requis pour un TEB $= 10^{-3}$ en fonction de la PDL (a) 4-QAM, (b) $16-$ QAM, (c) 64-QAM.

Dans un second temps, nous avons étudié l’impact de la présence d’un temps de groupe différentiel (DGD) entre les deux voies de polarisation. En effet, la mise à jour de la matrice de compensation de l’algorithme « joint » étant effectuée à chaque instant, il est important que les deux voies de polarisation soient synchronisées c’est-à-dire que ce retard de groupe puisse être compensé en amont de l’application de l’algorithme « joint ». Des simulations numériques ont été réalisées sur un système 4-QAM avec un RSB fixée à 30 dB, mélangé par des paramètres de rotation de polarisation de ($\alpha = 30°$ et $\theta = 50°$), et distordu avec déséquilibre IQ à l’émetteur de ($\epsilon = 0.1$ et $\varphi = 6°$) de manière égale sur les

deux polarisations. Des temps de groupe différentiel, normalisés par rapport à la durée symbole et variant de -0.5 à 0.5 sont appliqués sur les 2 voies de polarisation. L'effet du temps de groupe différentiel non compensé sur les performances de l'algorithme "joint" est qualifié à travers le calcul du RSB sur les signaux de sortie. Plus le temps de groupe différentiel augmente plus le RSB diminue. Ainsi, l'algorithme "joint" n'est pas fonctionnel en présence du DGD. Une solution a été proposée pour estimer et compenser le temps de groupe différentiel.

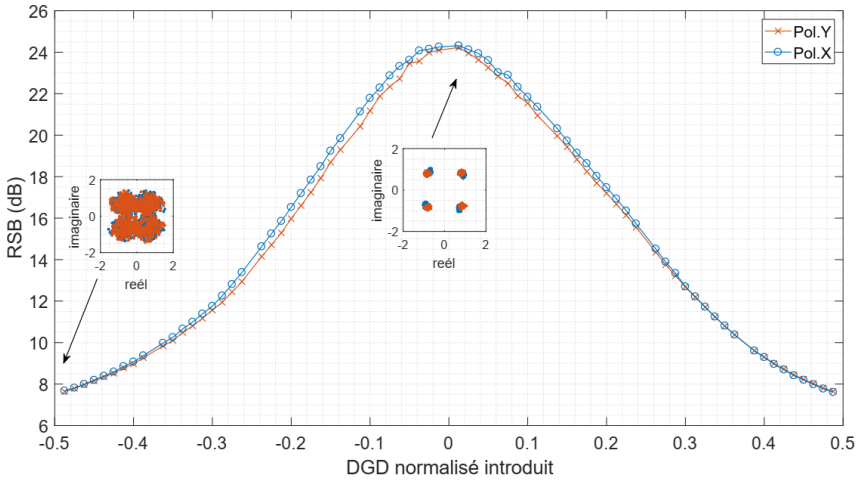

Figure 4 – Effet du DGD sur le RSB des signaux ($E_s/N_0 = 30$ dB, $\alpha = 30°$, $\theta = 50°$).

Enfin, les performances de l'algorithme proposé de compensation ont été étudiées en présence de dispersion chromatique (DC). Lorsque l'égalisation statique de la dispersion chromatique est opérée, l'algorithme "joint" démontre son efficacité à récupérer les données. En fait, comme la quantité la plus importante de DC a déjà été compensée par l'égaliseur statique, l'algorithme traitant la séparation de polarisation et la compensation du déséquilibre IQ peut opérer avec un seul coefficient. Les performances de notre algorithme en évaluant le RSB des signaux récupérés sont à peu près égales à celle de l'approche optimale.

Enfin, l'approche "joint" a été également testée dans un contexte de multiplexage dynamique de polarisation et dans le cas d'un contexte de communication flexible.

Concernant le premier point, les signaux sont mélangés avec des rotations de polarisation qui varient aléatoirement au cours du temps conduisant à des interférences inter-polarisations. Grâce à des simulations numériques, nous démontrons que l'algorithme proposé est robuste à suivre ces variations de rotation de polarisation et que les signaux à sa sortie sont parfaitement séparés. Tandis que,Dans les mêmes conditions expérimentales, l'approche « CMA + BASS » ne parvient pas à séparer les signaux pour les mêmes

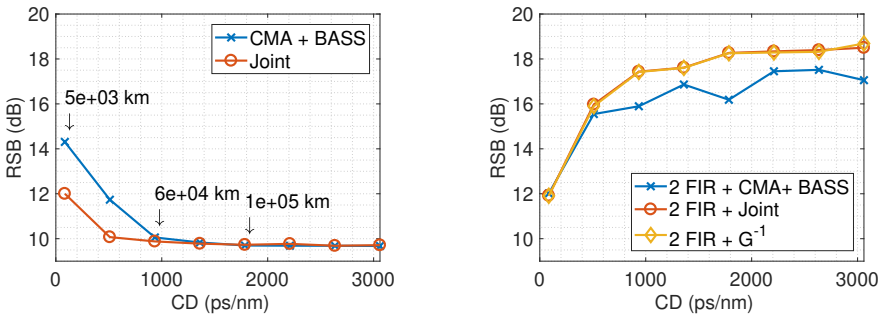

(a) (b)

Figure 5 – RSB versus la DC résiduelle(a) sans égalisation statique du DC (b) avec égalisation statique de la DC.

paramètres de simulation.

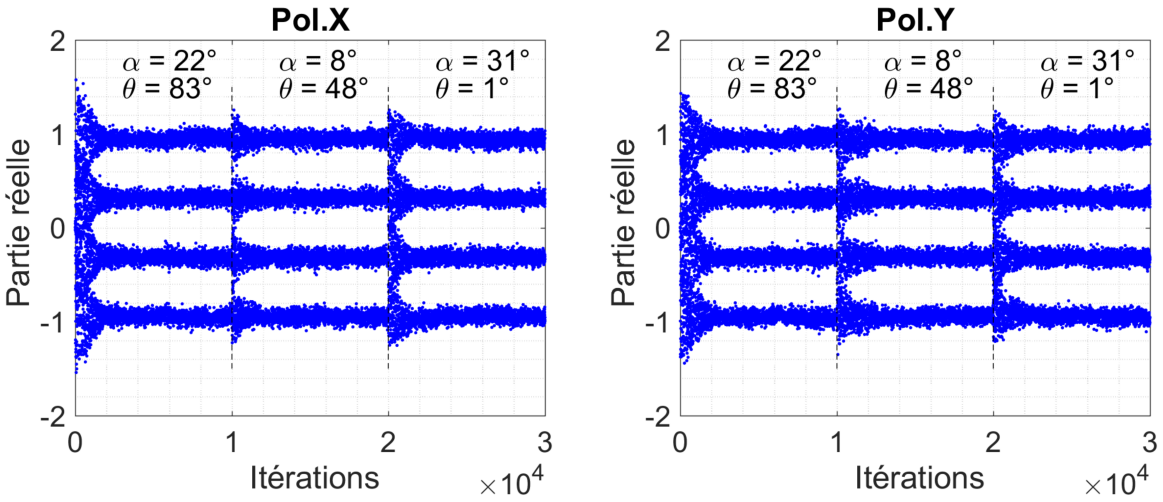

(a) (b)

Figure 6 – Partie rélle des signaux 16-QAM après démultiplexage dynamique avec l'algorithme "Joint" en présence du déséquilibre Tx-IQ ($E_s/N_0 = 30$ dB, $\epsilon_{p,Tx} = 0.1$, $\phi_{p,Tx} = 6°$).

Ainsi, la solution proposée "joint" parvient à séparer la rotation de polarisation dynamique d'une manière active et flexible, ce qui fait de notre algorithme un outil robuste répondant aux critères d'adaptation évolutif du canal de propagation contrairement à la solution du "CMA + BASS" qui ne peut compenser le changement aléatoire de la rotation de polarisation ce qui le rend inadapté au contexte de transmissions flexibles.

En ce qui concerne les changements dynamiques de formats de modulations, nous avons comparé l'évolution de l'EQM (par rapport à la compensation optimale et dans

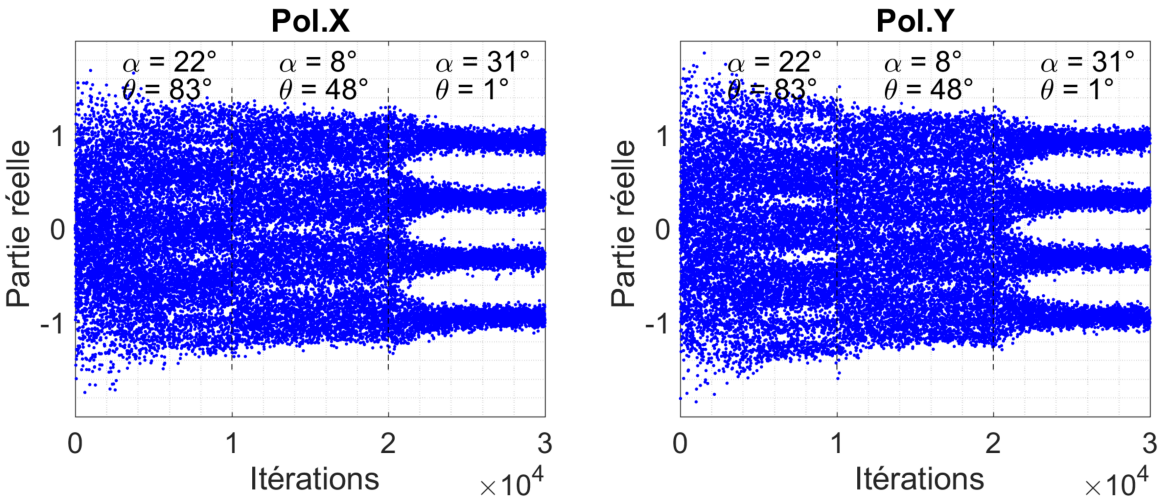

(a) (b)

Figure 7 – Partie rélle des signaux 16-QAM après démultiplexage dynamique avec l'algorithme "CMA+BASS" en présence du déséquilibre Tx-IQ ($E_s/N_0 = 30$ dB, $\epsilon_{p,Tx} = 0.1$, $\phi_{p,Tx} = 6°$).

les mêmes conditions de simulation) obtenue à l'aide de l'approche "CMA + BASS" et à l'aide de l'algorithme proposé. Pour ce faire, des symboles 4-, 16- et 64-QAM répartis séquentiellement et équitablement sur trois intervalles de temps ont été générés. Ces signaux ont le même RSB. Lorsque le rayon du CMA est maintenu à la valeur calculée pour la modulation 4-QAM, le CMA n'a aucune information sur le changement de format de modulation qui se produit par la suite. Ainsi, lors d'un changement de format de modulation de 4- à 16-QAM, l'algorithme "CMA + BASS" démontre une évolution temporelle très lente de son EQM par rapport à l'algorithme "joint" qui s'adapte activement à ce changement. De plus, l'algorithme "CMA + BASS" maintient une EQM plus élevée que celui de l'algorithme "joint" en régime permanent. D'autre part, l'EQM est évalué lorsque l'algorithme CMA change de rayon en fonction du format de modulation introduit. Cela correspond à la situation idéale lorsque le récepteur possède la capacité à estimer en aveugle le format de modulation utilisé par le transmetteur. Dans ce cas, le "CMA + BASS" converge rapidement mais présente toujours une EQM en régime permanent plus élevée que l'algorithme "joint". En conclusion, l'ensemble des expérimentations menées a permis de montrer que l'algorithme proposé maintient un meilleur compromis en termes de vitesse de convergence et de valeurs en régime permanent que "CMA + BASS" dans la situation où l'efficacité spectrale de la liaison optique varie dynamiquement au cours du

temps.

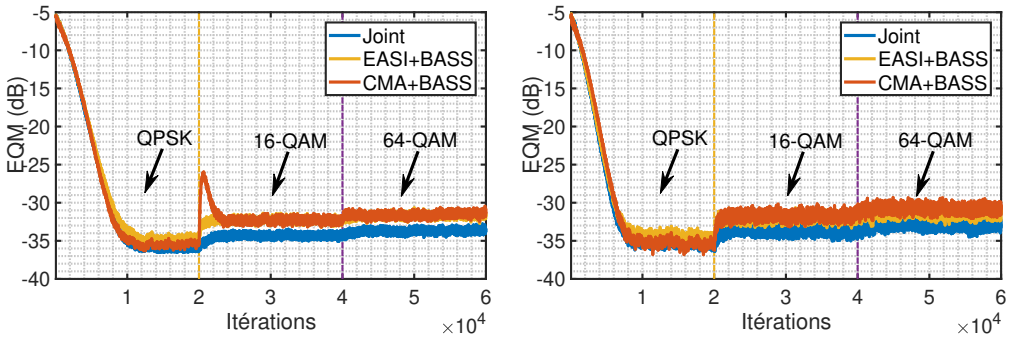

Figure 8 – Coubes d'EQM en présence du déséquilibre Tx-IQ et de multiplexage de polarization pour différents ordre de modulation ($E_s/N_0 = 23$ dB, $\epsilon_{p,Tx} = 0.1, \phi_{p,Tx} = 6°$, $\alpha = 30°, \theta = 50°$)(a) Le changement du format de modulation est à l'insu du CMA, (b) Le changement du format de modulation est au su du CMA.

Deux expérimentations matérielles ont été réalisées pour vérifier le bon fonctionnement de l' algorithme "joint". Nous avons considéré deux contextes expérimentaux différents. Le premier consiste à optimiser manuellement de des états de polarisation du signal optique présent aux récepteur et le second consiste à ne pas appliquer de compensation manuelle de polarisation et donc à travailler dans un contexte de multiplexage de polarisation. Les expérimentations menées à 44 Gbits/s (4-QAM) et 88 Gbits/s (16-QAM) ont montré que les diagrammes de constellation observés à l'entrée du circuit de décision ne présentent pas de distorsions et correspondent parfaitement à ce qui était attendu compte-tenu du OSNR mesuré. En conséquence, nous pouvons conclure que l'algorithme proposé compense effectivement les distorsions présentes dans la chaîne de transmission (IQ au Tx, IQ au RX, et multiplexage de polarisations). Aussi, à travers les courbes de TEB obtenues (Fig. 5.14(b)) des deux expérimentations, on déduit l'efficacité de l'approche à accomplir ses objectifs.

Description du détecteur de phase de type DD modifié

De manière générale, les techniques de récupération de phase des structures bouclées classiques dérivent du critère du maximum de vraisemblance et peuvent être pilotées soit par les données de transmission (Data Aided), soit par les décisions dirigées (Decision Directed), soit avec un mode de synchronisation aveugle (Non-Data Aided). Dans cette partie, on

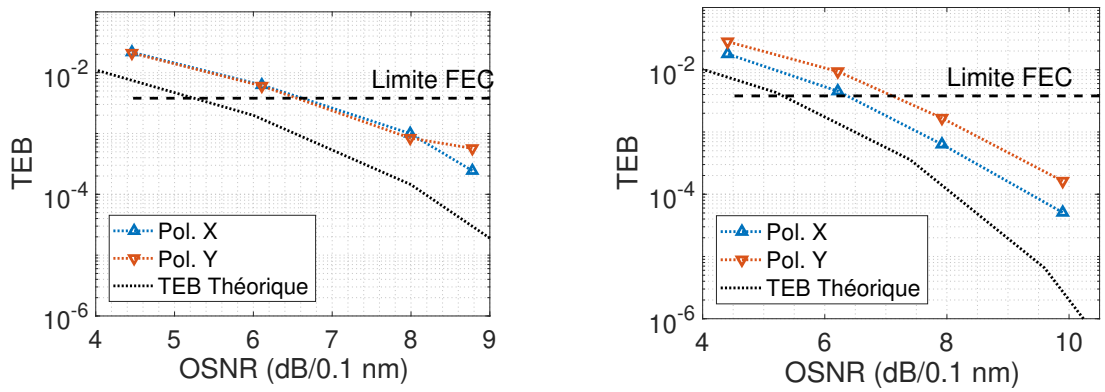

(a) (b)

Figure 9 – TEB en fonction de l'OSNR après compensation du déséquilibre IQ et démultiplexage de polarisation sur des signaux 4-QAM (a) "fixed polar" (b) "any polar".

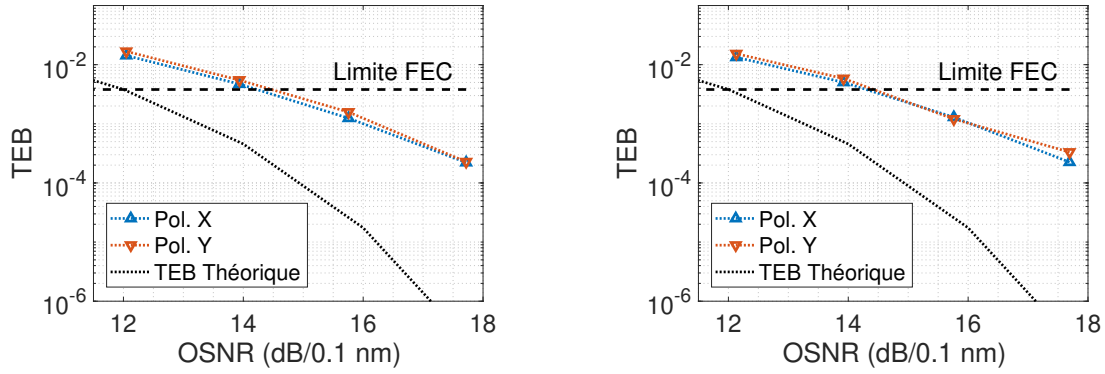

(a) (b)

Figure 10 – TEB en fonction de l'OSNR après compensation du déséquilibre IQ et démultiplexage de polarisation sur des signaux 16-QAM (a) "fixed polar" (b) "any polar".

s'intéresse aux architectures des structures bouclées de type DD pour la récupération du bruit de phase [8]. Un système bouclé construit la phase estimée à partir de la sortie du détecteur de phase de façon récursive. Le détecteur de phase conventionnel de type DD est le gradient stochastique de l'erreur quadratique moyenne par rapport à l'erreur de phase. Le nouveau détecteur de phase qui a été proposé au cours de cette thèse s'applique que sur des signaux 16-QAM et repose sur la mise à puissance 4 des signaux reçus et sur la modification du schéma de décision classique.

Contributions du détecteur de phase de type DD modifié

Les contributions du détecteur de phase de type DD modifié sont les suivantes

— Comparaison des caractéristiques de la courbe en S du détecteur de phase conventionnel avec celles de l'approche proposée : domaine de linéarité de la réponse, gain de la réponse;

— Évaluation de l'approche conventionnelle et celle proposée en présence de fréquences porteuses résiduelles non compensées;

— Analyse de l'influence de la présence de bruit blanc additif gaussien sur les performances de l'approche conventionnelle et celle proposée;

— Étude de l'effet du retard en boucle fermée des deux algorithmes sur le RSB requis pour un taux d'erreur binaire de 10^{-3} et comparaison des performances;

— Validation expérimentale des performances de l'algorithme introduit.

Analyse des résultats du détecteur de phase de type DD modifié

La courbe en S d'un détecteur de phase (ou la caractéristique en boucle ouverte) permet de prévoir l'évolution en moyenne de l'erreur de la phase instantanée. Cette information est importante pour l'évaluation des performances de la boucle. L'analyse des propriétés des courbes en S à savoir la réponse linéaire, le gain est nécessaire afin de pouvoir comparer les deux algorithmes en termes de capacité d'accrochage[9]. En effet, la réponse linéaire de la courbe en S est la région permettant d'amener le système de synchronisation en état de verrouillage. Cette zone, marquée par une pente positive, est caractérisée par une sortie du détecteur de phase proportionnelle à l'erreur de phase autour du point d'équilibre stable. Ainsi, un détecteur de phase correctement conçu doit fournir une réponse linéaire la plus large possible. D'autre part, le gain est défini comme la pente de la courbe en S à l'origine. Le gain d'un détecteur de phase est un bon indicateur des performances de la boucle en terme de temps d'accrochage.

En traçant la courbe S pour le modèle proposé, on constate que cette courbe maintient approximativement le même gain quelle que soit la valeur du RSB, ce qui assure une vitesse d'accrochage importante. En revanche, le détecteur classique possède un gain qui varie en fonction du RSB. Dans une telle situation, des résultats insatisfaisants sont obtenus opérant avec un gain fixe, en particulier lors d'un fonctionnement à bas RSB. De plus, le détecteur de phase modifié présente une région de réponse linéaire plus large que celle du détecteur classique et présente une amplitude maximale de la courbe en S qui est importante et fixe. Ceci conduit à un système de récupération de phase à large zone de capture, donc plus robuste aux résidus de la fréquence porteuse. Tous les avantages

mentionnés font du détecteur de phase modifié un algorithme approprié à la fois pour la capacité de verrouillage de boucle (grâce à la plage de réponse linéaire) et un temps d'accrochage court (grâce au gain important).

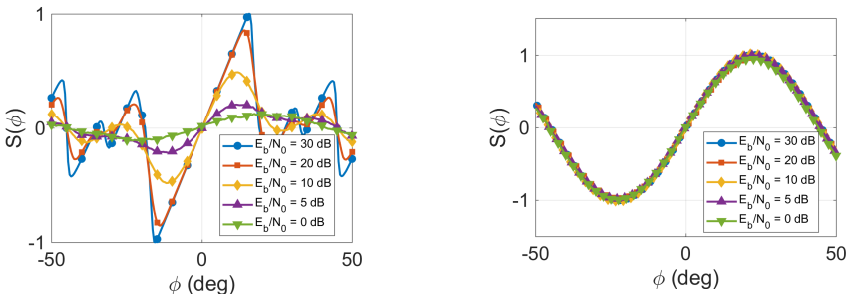

(a) (b)

Figure 11 – Courbes en S en fonction de différentes valeurs de RSB: (a) Détecteur de phase classique, (b) Détecteur de phase modifié.

Afin d'illustrer les performances de notre détecteur de phase modifié face à des résidus de la fréquence porteuse, on évalue la pénalité en RSB pour un taux d'erreur binaire de 10^{-2} (par rapport à un système non altéré par le bruit de phase de laser) en présence de bruit de phase (pour des valeurs du produit entre la largeur de raie du bruit de phase et le temps symbole (Δf T) inférieures à 10^{-5}) et du résidu de fréquence porteuse normalisé (inférieur à 6×10^{-3}). Le RSB requis augmente considérablement à l'augmentation de bruit de phase qui, à forte valeur, peut projeter brusquement l'erreur de phase instantanée en dehors de sa région de capture du zéro stable, ce qui provoque le décrochage de la boucle de contrôle. Le détecteur de phase proposé répond de manière robuste au bruit de phase puisque la pénalité en RSB ne dépasse pas 0.08 dB sur les plages du bruit de phase et des écarts résiduels de fréquences étudiés. Au contraire, l'approche classique atteint une pénalité en RSB plus importante (0.15 dB) sur la même plage de paramètres étudiés.

Dans un second temps, les performances des deux détecteurs de phase classique et modifié ont été évaluées sur des signaux 16-QAM altérés par du bruit de phase (caractérisé par Δf T$= 9 \times 10^{-5}$), l'écart de fréquence normalisé de 10^{-3} et de bruit blanc additif Gaussien faisant varier leurs RSB de 14 à 22 dB. Des courbes de simulation évaluant l'EQM du bruit de phase estimé montrent que notre approche a une meilleure précision d'estimation que le détecteur de phase conventionnel indépendamment du RSB introduit sur les signaux.

Pour mettre en évidence l'efficacité des deux détecteurs de phase par rapport à

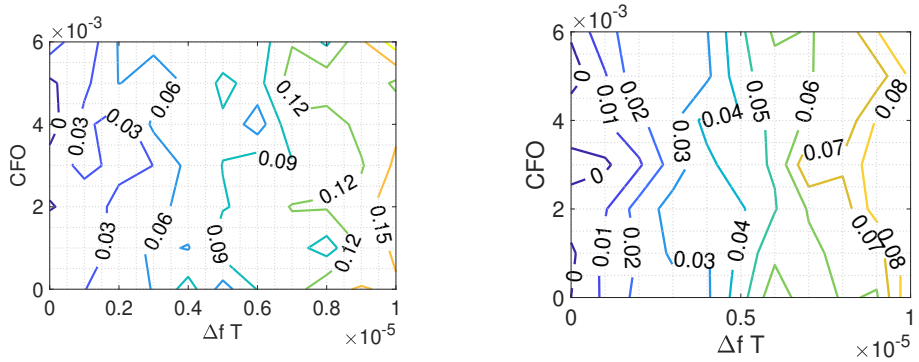

Figure 12 – Pénalité en RSB pour un TEB = 10^{-2}, in dB, pour différents CFO et Δf T caractérisant le bruit de phase (a) Détecteur de phase classique, (b) Détecteur de phase modifié.

différentes latences, correspondant à un retard entre l'estimation de la phase et sa compensation, (de valeurs de 1, 5, 10, 15 symboles) introduites dans la boucle de rétroaction en raison de considérations imposées par l'implémentation matérielle, le RSB requis pour un taux d'erreur binaire de 10^{-3} en fonction de bruit de phase (caractérisé par Δf T inférieur à 10^{-5}) est comparée. Pour les différentes latences introduites, l'algorithme proposé maintient une large tolérance pour pour les valeurs précédemment mentionnées du bruit de phase, tandis que la version classique du détecteur de phase démontre une tolérance plus faible pour les mêmes valeurs de bruit de phase et de latence introduites.

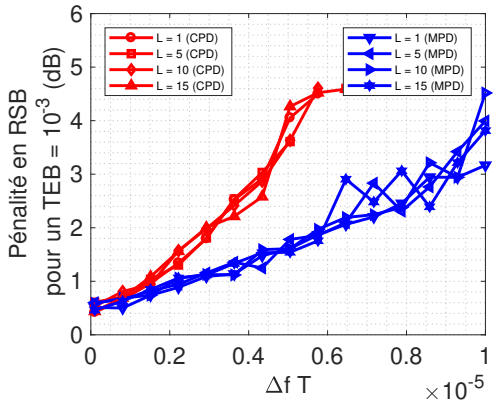

Figure 13 – Effet du délai sur la performance de la boucle récursive utilisant le détecteur de phase conventionnel et le détecteur de phase modifié.

Enfin, l'empreinte calculatoire en termes de multiplications et d'additions des deux approches a été comparé. Le détecteur de phase modifié requiert davantage d'opérations

matérielles par échantillon traité (ajout de 6 multiplications réelles et 2 additions réelles) par rapport à l'approche classique.

L'efficacité de l'algorithme proposé a été vérifié en traitant des données expérimentales. Des signaux 16-QAM avec une rapidité de modulation de 44 Gbit/s et altérés par un bruit de phase de largeur de raie totale de 200 kHz ont été récupérés pour le traitement. Les résultats numériques montrent que les deux algorithmes arrivent à compenser le bruit de phase et le RSB des signaux après compensation est de 24.6 dB pour le détecteur de phase modifié contre 24.3 dB avec le détecteur de phase classique, assurant un gain RSB de $0,3$ dB.

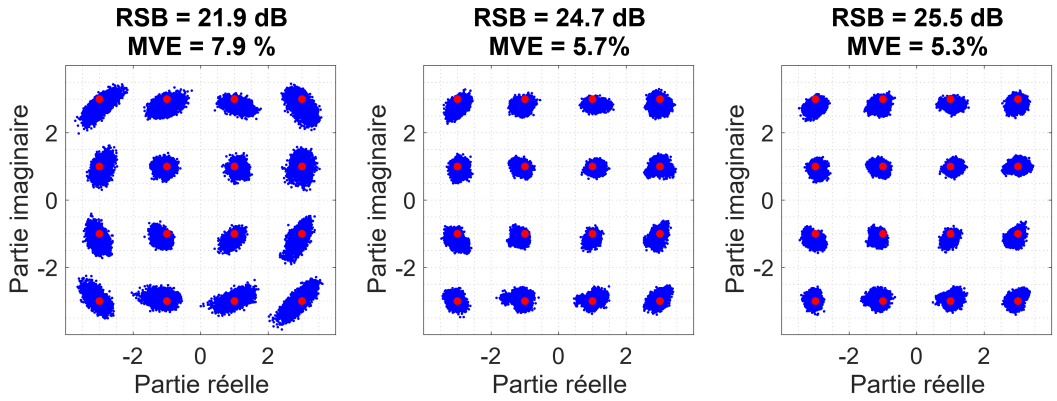

(a) (b) (c)

Figure 14 – Diagrammes de constellation : (a) sans CPR, (b) avec le détecteur de phase classique, (c) avec le détecteur de phase modifié.

Description de l'algorithme R-BPS

Il existe également des structures directes pour la compensation de la phase porteuse. Parmi ces structures, celle proposée par Pfau, nommée blind phase search (BPS) [10] s'est imposée dans les applications de communications optiques. Cette technique est basée sur un ensemble de rotations de test et une décision effectuée à chaque test pour estimer la phase assurant le minimum de l'erreur quadratique moyenne aux bornes de l'organe de décisions. Aussi, l'algorithme recursive probability weighted blind phase search (RW-BPS) proposé par Rozental réalise un compromis entre les approches à implémentation directe (feedforward) et celles à implémentation récursive (backward). L'avantage de cette technique réside en sa capacité de corriger l'effet du bruit de phase de laser avec un

nombre minimal de phase de tests réduisant ainsi la complexité globale de l'algorithme. Un algorithme de compensation de bruit de phase a été inspiré du RW-BPS. La nouveauté du recursive blind phase search (R-BPS) proposé par rapport au RW-BPS réside dans la suppression de la pondération par probabilités après le calcul des erreurs moyennées car, sur la base de nos simulations, l'utilisation de ces probabilités n'apportent aucun avantage de performance et de plus leur réglage/paramétrage est délicat car elles dépendent de la puissance de bruit de phase présent introduite par les lasers. Enfin, l'intérêt du traitement parallèle du R-BPS a été considéré afin de montrer l'impact du parallélisme sur les performances. Ainsi, l'encodage différentiel est opéré d'une manière parallèle et indépendante pour chaque étage de parallélisme.

Contribution de l'algorithme R-BPS

Les principales contributions de l'algorithme R-BPS sont

— Comparaison des performances de l'algorithme R-BPS proposé et BPS en fonction des paramètres principaux (puissance du bruit de phase du laser, présence de fréquence porteuse résiduelle, variation des formats de modulation);

— Étude de la complexité arithmétique de la solution proposée par rapport à celle du BPS;

— Validation expérimentale de l'algorithme proposé.

Analyse des résultats de l'algorithme R-BPS

On présente la courbe du RSB requis pour un taux d'erreur binaire de 10^{-3}, en fonction du bruit de phase (caractérisé par Δf T variant de 10^{-6} à 10^{-3}) pour les signaux 4-, 16- et 64-QAM. Les simulations ont été effectuées pour un filtre moyenneur de l'EQM pouvant comporter une nombre de coefficient inférieur à 9 et pour un nombre d'étages de parallélisme inférieur à 8. Pour le BPS, le nombre de phases de test est de 32 pour les signaux 4- et 16-QAM et 64 phases pour les signaux 64-QAM. En ce qui concerne le R-BPS proposé, le nombre de phases de test aboutissant à une mise en œuvre à coût très réduit est fixé à 6 pour les modulations 4-, 16- et 64-QAM. Les résultats montrent que pour tous les formats de modulation utilisés, l'algorithme R-BPS offre une tolérance en Δf T plus large que l'algorithme BPS, en particulier avec les signaux 64-QAM (R-BPS offre un gain en sensibilité de 1 dB par rapport au BPS pour les valeurs Δf T $\leq 10^{-5}$) et les signaux 16-QAM (gain de sensibilité d'environ 0.5 dB pour Δf T $\leq 10^{-5}$).

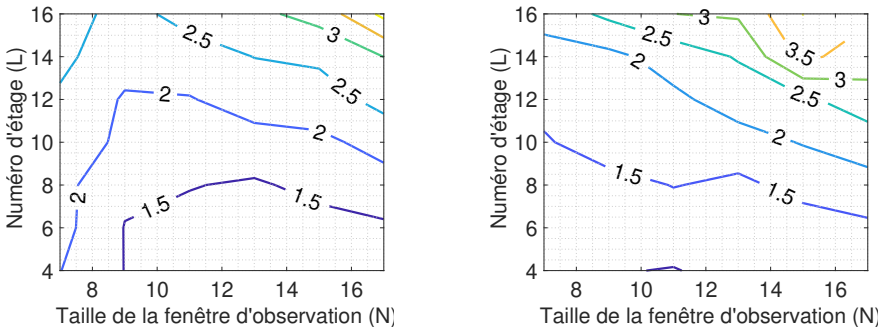

(a) (b)

Figure 15 – Pénalité en RSB pour un TEB = 10^{-3} en fonction des paramètres N, L pour des signaux 16-QAM et $\Delta fT = 10^{-5}$ for (a) algorithme BPS parallèle, (b) algorithme R-BPS parallèle.

Le décalage résiduel de fréquence de porteuse peut être inclus dans la modélisation du bruit de phase et peut être géré avec des algorithmes de compensation de bruit de phase. Le décalage résiduel de fréquence de porteuse peut être déterminant car, plus la fenêtre d'observation utilisée est grande, plus la dérive de ce décalage en fréquence est grande. Pour étudier la pertinence de notre méthode proposée par rapport à la présence de décalage en fréquence, une implémention parallèle du R-BPS avec 8 étages avec une fenêtre d'observation de 9 symboles est proposée. Cette configuration est testée avec différentes valeurs de bruit de phase (caractérisé par Δf T variant de 0 à 10^{-5}) et différents décalages résiduels de fréquence porteuse normalisée (variant de 0 à 3×10^{-4}) sur un système 16-QAM. Le RSB requis pour un taux d'erreur binaire de TEB = 10^{-3} a été évalué. Les résultats de simulation montrent que pour une valeur Δf T fixe, plus le décalage résiduel de fréquence introduit est élevé, plus le RSB requis est important. De même, pour une valeur de décalage résiduel de fréquence fixe, plus la valeur Δf T est grande, plus le RSB requis est grand en raison de l'effet du bruit de phase dans la production d'erreurs de décision de symbole. Cependant, le R-BPS parallèle présente des valeurs plus faibles en termes de RSB requis pour un TEB de 10^{-3} que l'implémentation du BPS parallèle. Cela signifie que l'approche proposée répond de manière robuste au bruit de phase puisque les valeurs du RSB requis sont inférieures à celle du BPS parallèle sur les plages de bruit de phase et de décalage résiduel en fréquence étudiées.

Pour évaluer la robustesse de l'algorithme concernant le changement dynamique de l'ordre de modulation, l'EQM du bruit de phase estimé a été évaluée sur des formats de modulation 4-, 16- et 64-QAM respectivement opérant sur des RSB de 10 à 30 dB. Le

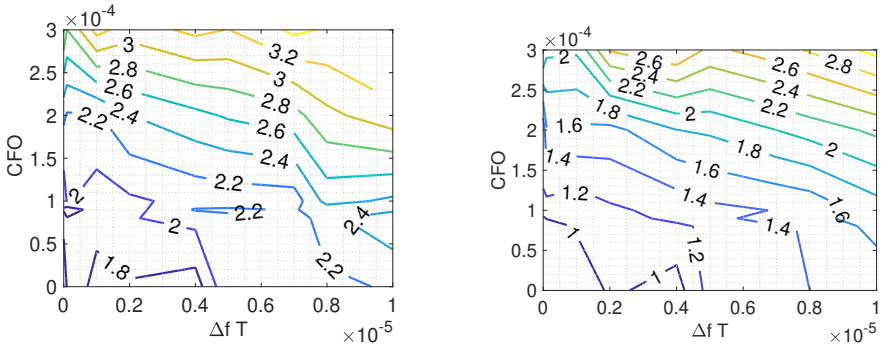

Figure 16 – Pénalité en RSB pour un TEB = 10^{-3}, in dB, pour différentes valeurs de CFO et Δf T caractérisant le bruit de phase (a) BPS parallèle, (b) R-BPS parallèle.

passage d'un format de modulation à un autre se fait sur des seuils de 16 et 22 dB pour les signaux 16-QAM et 64-QAM. Le produit de Δf T est fixé à 10^{-5} pour chaque schéma de modulation. Le nombre de phases de test est maintenu fixe pour tous les formats de modulation et il est B = 6 pour l'approche R-BPS et B = 32 pour le schéma BPS. Le paramètre de taille de fenêtre est le même pour les deux algorithmes et fixé à 9. Enfin, le traitement parallèle est effectué sur 8 étages.

Les résultats de simulation montrent que le R-BPS permet une meilleure estimée du bruit de phase quel que soit l'ordre M (2,4, ou 16) de la modulation utilisée et sa courbe d'EQM ne présente pas de forme fluctuante. Cependant, l'algorithme BPS présente une évolution temporelle de la courbe d'EQM moins "lissse" notamment lors des instants de changements de l'ordre de la modulation QAM utilisée. Cela démontre que le R-BPS propose des performances de suivi et d'estimation de bruit de phase supérieures à celle proposé par le BPS.

Pour ce qui concerne les comparaisons de complexité algorithmique, nous avons montré que l'algorithme R-BPS est clairement moins complexe que le BPS. En effet, le nombre de phases de test requis pour l'algorithme R-BPS est nettement inférieur à celui requis pour l'algorithme BPS.

Pour la validation de ces algorithme, nous avons fait l'acquisition en temps réel de signaux modulés 4- et 16-QAM en entrée du récepteur sur une plateforme expérimentale puis le traitement au récepteur a été effectué hors-ligne. Les signaux sont altérés par un bruit de phase de laser à largeur de raie totale 200 kHz. Les résultats de traitement montrent que l'implémentation parallèle du R-BPS (à un seul étage / à 4 étages) présente moins de saut de cycle que le BPS et réussit à compenser le bruit de phase de laser tout

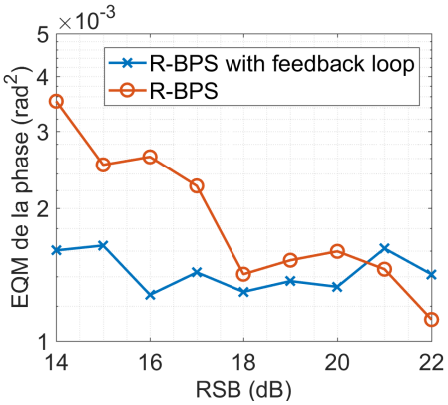

Figure 17 – Évolution de l'EQM de la phase estimée *vs.* E_s/N_0.

en offrant des gains en RSB (par rapport au BPS) à la sortie des signaux.

ACKNOWLEDGEMENT

I would like to take this opportunity to acknowledge all those people whose support was key to this very moment. I start with my supervisors: Pascal SCALART, my main supervisor, for his frequent encouragement and numerous fruitful discussions. He has helped me to comprehend the field of laser and fiber optical communication and untangle its complexities. Robin GERZAGUET, whose technical expertise, eye for details and unwavering support made it an enjoyable and learning experience. Our discussions were always stimulating and greatly contributed to progress in my PhD thesis.

Honorable mention to Christophe PEUCHERET who kindly agreed to be the advanced reviewer of my scientific papers and of my thesis report.

Laurent BRAMERIE, Mathilde GAY and Marie-Laure CHARES-SCALART and the FOTON High Speed Transmission Laboratory team members for providing me the opportunity to work with them and benefit from their experience.

I express my gratitude to LTC and its management for funding my doctoral studies and providing me the opportunity to work closely with leading universities and companies.

I continue with my GRANIT and CAIRN colleagues at the laboratory of IRISA that made my day-to-day life simply better.

Finally yet importantly, I would like to thank my family for their countless blessings and unwavering support all the time. Without their unconditional love and support, nothing could have been possible.

Chapter 1

Introduction

1.1 Context

Today's Internet communities' demands are growing exponentially in tremendous space. Connectivity has become a defining feature of the modern society from communicating via e-mail or watching the streaming videos to cloud-based computing and its diverse services. Also, two-thirds of the global population will have Internet access by 2023, as the total number of Internet users is expected to rise from 3.9 billion in 2018 to 5.3 billion by 2023 with a compound annual growth rate of 6% [11] (see Fig 1.1).

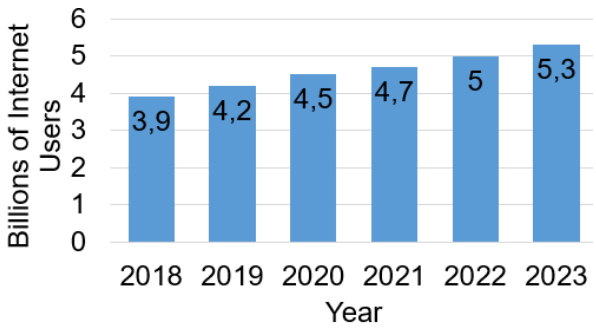

Figure 1.1 – Global Internet user growth expected form 2018 to 2023 [11].

To respond to these demands, data transmission is nowadays essentially provided via fiber-optics cable. Thus, the usage of optical fiber links also ranges from submarine cables covering thousands of kilometers to high capacity networks in data centers. Also, optical systems are in their way to access smaller transmission distance. Nowadays, optical chip-to-chip or intra-chip connections are highly studied [12, 13]. For instance, in central processing unit chips, an important surface considered for data transmission is filled with electric lines. In this case, optical transmission will be a good replacement in terms of space and energy consumption added to high-speed transmission.

Regarding optical network configurations, fibers are used in various fields of applications including the access (for distance < 100 km), metropolitan (100 up to 300 km), regional (300 up to 1000 km) and (ultra) long-haul (> 1000 km) terrestrial or submarine transmission. Fibers are used for carrying information from one point to another in the form of light. More precisely, optical fiber transmission uses wavelengths that are in the near-infrared portion of the spectrum, just above the visible. Light is emitted either from light amplification by stimulated emission of radiations (LASERs) or light-emitting diodes (LEDs) to be transmitted over optical fiber.Typical fiber optic system requires electric to optical device at the transmitter, which converts an electrical signal into a light signal, a channel where the light is carried, and a receiver that accepts the light signal and converts it back into an electrical signal. Fiber optic system complexity depends on the bit rate and the transmission distance (see Fig. 1.2). Therefore, several fiber components have been considered for improvements.

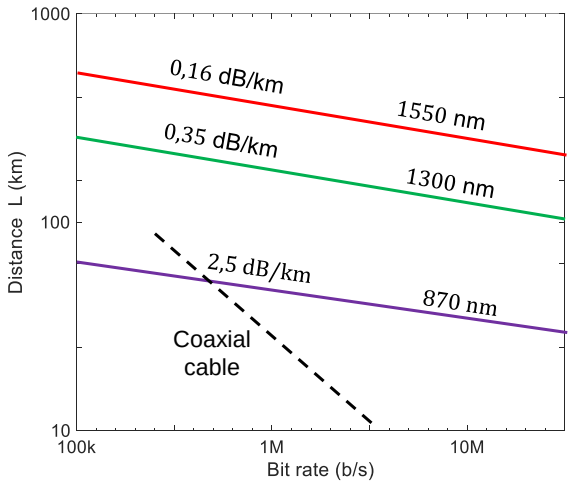

Figure 1.2 – Maximum fiber length L as a function of bit rate under attenuation-limited conditions for fused silica-glass fiber operating at wavelengths 870, 1300 and 1550 nm assuming fiber attenuation coefficients of 2.5, 0.35, and 0.16 dB/km, respectively. For comparison, the L versus bit rate relation for a typical coaxial cable is also shown. [14]

In a nutshell, fiber optical communication assets are now the indispensable backbone of today's data transmission and this comes with consecutive revolutions that have enabled fiber optical communication and the increase of data throughput (see Fig. 1.3).

It starts, in the 1960s, by the laser invention [16] followed by another second progress of the low loss optical fiber [17] a decade after. Technological developments and inventions are afterward realized including the optical amplifier in the 1980s, notably the erbium-

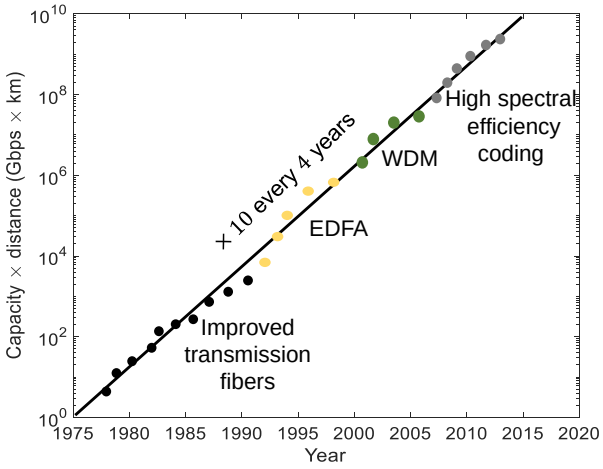

Figure 1.3 – Evolution of optical transmission systems, inspired from [15]

doped fiber amplifier (EDFA) [18], and at a similar time, wavelength-division multiplexing (WDM) [19] which increased significantly the throughput since more than 100 wavelengths can be transmitted simultaneously over a single mode optical fiber.

The demand for further increase in transmission capacity triggered the renewed interest in coherent optical communication technologies after 2000. At that time, the systems deployed could transport a hundred wavelengths, each modulated at a speed of 10 Gb/s over thousands of kilometers. Since then, worldwide research efforts were conducted to establish powerful DSP techniques to compensate transmission and system impairments, or to propose solutions for data rate improvements through the use of more complex constellations.

Indeed, by exploring the two orthogonal polarization of light, polarization-division multiplexing (PM) systems double the throughput compared to a single polarization transmission. As a matter of fact, in 2008, PM-quadrature phase shift keying (QPSK) were commercialized for 40 Gb/s per channel transmission [20].

At present, field trials for metropolitan distances achieved 600 Gb/s single-wavelength transmission, employing modulation formats up to 64-QAM and symbol rates up to 69 Gbaud [21].

In addition to spectral efficiency improvements and higher data rate targets, researches have tackled the resource allocation perspective. In fact, due to the diversity and heterogeneous aspect of the traffic demands, it could be beneficial to allocate resources adaptively according to communication demands. This promising solution called flexible optical communication responds to this issue by switching various routes, modulations, bandwidths

and power spectral densities in the channel. Consequently, fiber throughput is improved by allowing the needed transmitter powers and modulation formats and optimizing these variables jointly.

These awaiting data rates and throughput are not met without effective DSP algorithms controlled and validated. Thanks to practical field-trial experiments or numerical simulations, algorithms could be tested and verified. Simulations are easier to conduct and generally used to explore and reduce costs compared to some experimental investigations. Moreover, simulations are based on mathematical models and are optimised in conjunction with experimental validation.

As a matter of fact, Fig. 1.4 depicts some Lab results overall trend in throughput × distance product since 2009 for hero-experiments [22–26] for transmissions around hundred of kilometers and for long-haul transmission over more than 6000 km [27–36]. Currently, the hero experiments throughput product has reached 115 Tb/s transmission over 100 km [26] whereas the long-haul throughput has attained 74.38 Tb/s over 6300 km [36]. To respond to the Internet-traffic increase growth, more technological advances, new fibers and system components in addition to collaborative worldwide research efforts are united to help boost the capacity of optical networks.

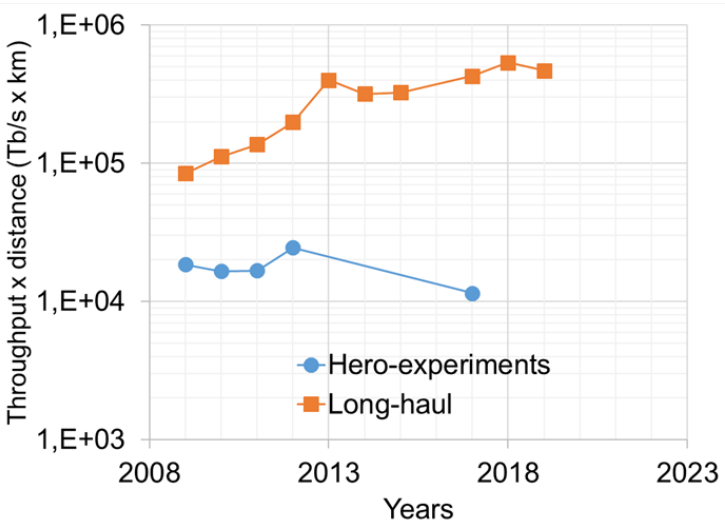

Figure 1.4 – Throughput evolution during the past decade for hero-experiments and long-haul transmission using a SMF.

Optical communications will also continue to be subject to continuous development and challenges. In this respect, multi-level modulations, polarization multiplexing, coherent detection and digital processing are essential as they upgrade and complement each other.

On the other hand the introduction of a flexible network brought about a novel concepts to improve the use of resources available in the optical network and participate in the enhancement in the field of the management of telecommunications traffic. In this context, the aim of this thesis is to move along the field of coherent optical communications, to explore, propose and demonstrate new state-of-the-art algorithms for flexible coherent optical transceivers.

1.2 Contributions

This Ph.D. work aims at the investigation, development, and optimization of various digital signal processing algorithms for compensation of different types of optical transmission and system impairments while handling the flexible optical communication aspects as well as the complexity of the algorithms.

The main contributions of this Ph.D. work are listed as follows:

— First, a blind algorithm for both polarization demultiplexing and in-phase and quadrature imbalance (IQ imbalance) compensation is proposed. This algorithm meets the modern requirements of the dynamic switching concept in terms of modulation formats, thus paving the way towards agile communication for fiber. The robustness of the algorithm against other polarization imperfections (namely the polarization-dependent loss (PDL) and the differential group delay (DGD)) and its low computational complexity are also reported.

— Second, this work investigates and designs a feedback carrier phase recovery (CPR) algorithm. This approach is dedicated to 16-QAM modulation formats and robust against different signal-to-noise ratio (SNR) values.

— Third, carrier phase recovery is reconsidered. In this part, a feed-forward approach in a parallel interleaving implementation is investigated. In this respect, a high data rate transmission and low complexity are required.

The work presented in this manuscript has led to the following publications:

Journal paper

— M. K. Lagha, R. Gerzaguet, L. Bramerie, M. Gay, M. -L. Chares, C. Peucheret and P. Scalar: Blind Joint Polarization Demultiplexing and IQ Imbalance Compensation for M-QAM Coherent Optical Communications, IEEE Journal of Lightwave Technology, August 2020.

Conference papers

— M. K. Lagha, P. Scalart, R. Gerzaguet, L. Bramerie and A. Carer: Modified Decision-Directed Carrier Recovery Loop for 16-QAM Signals, Asia Communications and Photonics Conference (ACP), October 2018.

— M. K. Lagha, P. Scalart, C. Peucheret, R. Gerzaguet, and L. Bramerie: Modulation Format Independent joint Polarization Demultiplexing and IQ Imbalance Compensation, OSA Advanced Photonics Congress (AP), July 2019.

1.3 Thesis Organization

This thesis is structured as follows

Chapter 2 presents briefly some fundamentals of digital communications and coherent optical communication systems that will be necessary in the description of the original work reported in the thesis. Transmitter and receiver blocks are presented and the main required quality criteria for optical transmission evaluation are presented.

Chapter 3 introduces the fiber-optic impairments and reviews off-line state of the art algorithms for mitigating the linear impairments created by the fiber, as well as components distortions. The chapter highlights the fact that work has to be done for mitigating the linear impairments in the context of QAM modulation.

Chapter 4 introduces the proposed DSP algorithms notably the three principal contributions cited earlier. The performance and feasibility of a joint algorithm dealing with polarization demultiplexing and IQ imbalance is investigated. The algorithm presents better results compared to cascaded conventional approaches. Furthermore, the proposed method shows good adaptation to dynamic channel variations and robustness against polarization related effects.

Moreover, two methods for carrier phase recovery were investigated. One is a feedback framework working on 16-QAM modulation. The method is a modified version of the classical decision-directed CPR and it can operate well at low SNR values. The other method proposes a low complexity, feedforward carrier phase recovery suitable for parallel implementation. The proposed method outperforms the well known and widely used blind phase search algorithm at low SNR and shows lower cycle slip rate.

Chapter 5 details the experimental investigations for algorithms validations. Experimental setups as well as the subsequent results are demonstrated.

Finally, the last chapter draws the major conclusions of the present work and exposes some perspectives.

Chapter 2

Fundamentals of Coherent Optical Communication Systems

A typical block diagram of a digital communication system is as shown in Fig. 2.1(a). The system is composed of a transmitter part where the digital data (sequence of bits) are encoded and modulated, the communication medium or the channel to convey data to the destination, and finally, the receiver, which purpose is to recover the sent data.

In optical communication or light-wave systems, the means of communication is light and it implies guided or unguided systems. The unguided, or free-space optical communication systems [37] suppose that the information carried in the light beam is transferred in free space. Subsequently, thanks to this technology, IP traffic is carried out through the line of sight and fiber space optics communication is achieved with 10 Gb/s of data rate by full duplex (bidirectional) connectivity.

Free space optics communication is now more evolved. It is used as a tool to communicate between point-to-point links (e.g., two buildings) and point-to-multi-point links (e.g. from aircraft to ground or satellite to ground, for short and long reach communication). For example, this communication link is currently in use for many services at many places such as in indoor LiFi technology as an alternative technology or an upgrade of traditional wireless networks.

Meanwhile, the guided or fiber-optic communication systems, as the name suggests, involve the use of fiber technology as a waveguide (see Fig. 2.1(b)). In this thesis, only the case where the optical fiber is the medium is considered. Therefore, "optical communications" and "fiber-optic communications" are two terms that will be understood as synonyms. Depending on the conveyed distance, fiber-optic technology differs. In general, communication systems operate by means of long and short-haul links.

For instance, the short-haul links are used in data-centers and access (passive) optical networks. These kinds of links do not exceed 100 km and are expected to have significant costs in terms of installation and equipment. Nevertheless, multi-mode fibers (MMFs)

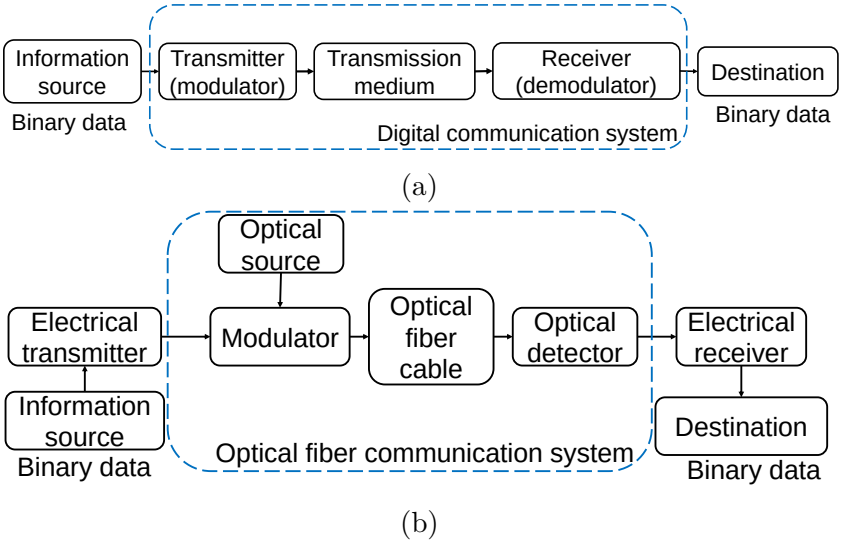

Figure 2.1 – (a) A general communication system, (b) an optical fiber communication system.

offer efficient coupling from light sources and low cost splices and connectors between fibers. These advantages remain true even today and MMF is still the fiber of choice for short distance links.

On the contrary, long haul links are supposed to transmit data over thousands of kilometers requiring SMF systems.

The difference between single-mode and multi-mode resides in fiber design technology. Basically, a fiber is composed of a silica core in the very center of the cable, enveloped by a cladding with a lower refractive index ensuring waveguiding of light. Other protective layers of acrylate polymer or polyimide surround the cladding to prevent harmful external impacts such as mechanical vibrations.

The single-mode fiber is characterized by a small core diameter (5 µm to 10 µm) (see Fig. 2.2(a)) whereas multi-mode fiber (see Fig. 2.2(b)) has a larger core diameter (50 µm to 100 µm). The core of the MMF is large, hence it can support a higher number of modes. Injected light can then couple to several modes (depending on the overlap integral between the launched field and the mode profiles). As a result, the channel capacity of a multi-mode fiber is larger than that of a single-mode fiber as a MMF fiber can carry M guided modes [38]. Assuming no power coupling among modes, the channel capacity can consequently be enhanced by the factor M. Nevertheless, in reality, due to refractive index fluctuations along the fiber, there is an exchange of power among modes, leading to

cross-talk which can be compensated by using digital signal processing techniques. Also, due to intermodal dispersion, MMF fibers are not suitable for long-haul and/or high bit rate applications.

Typically, the transmission reach of a MMF fiber-optic link at a bit rate of 1 Gb/s is limited to a few kilometers. In terms of the performance in MMF fibers, the difference lies in the fiber's bandwidth, or the signal-carrying capacity. Bandwidth is actually specified as a bandwidth $\times$ distance product with units of MHz-km that depends on the data rate. As the data rate goes up (MHz), the distance that rate can be transmitted (km) goes down. Thus, a higher fiber bandwidth can enable you to transmit at higher data rates or for longer distances. For example, 50 µm multi-mode fiber offers nearly three times more bandwidth (500 MHz-km) than 62.5 µm fiber(160 MHz-km) at 850 nm. Intermodal dispersion would be absent if there was only one mode. Therefore, single-mode fibers are used for long-haul (1000 km-30000 km) and high-bit-rate (10 Gb/s-100 Gb/s) applications.

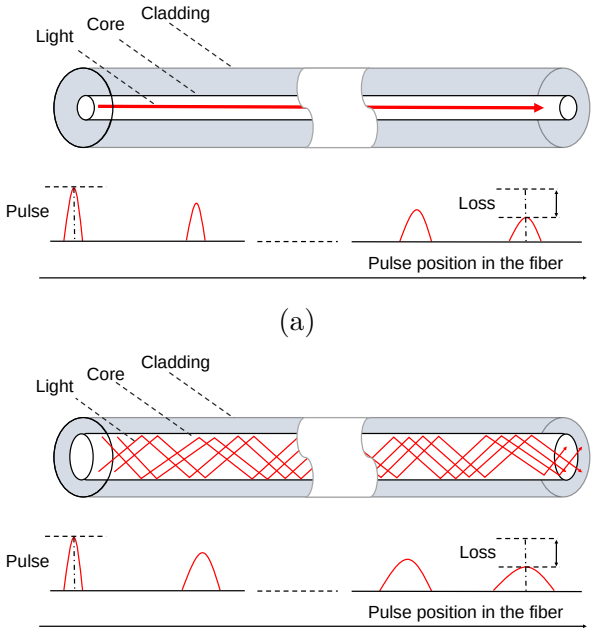

Figure 2.2 – Fiber-optic cables (a) Single-mode fiber, (b) multi-mode Fiber.

Despite advanced fiber design, digital communication would not be possible without effective optical transmitter (see section 2.1.1) and receiver (see section 2.1.2) elements. To keep responding to the evolving society's information needs, more efficient optical components are investigated for better bandwidth use (spectral efficiency) and for the

improvement of the energy efficiency. In this thesis, we focus on long-haul transmission (up to 4200 km) using single-mode fibers. This implies the investigation of the overall architecture of the coherent fiber-optic communication (in section 2.1), and the required criteria for optical transmission evaluation (in section 2.2).

2.1 Coherent Optical Communication Systems

In this section, the different building blocks of coherent fiber-optic communication are discussed. A generic fiber-optic communication system as depicted in Fig. 2.3, includes the transmitter, the propagation channel and the receiver. The transmitter maps binary data to optical waveforms which propagate through the channel to the receiver. The channel is made of consecutive amplified fiber spans to reach the target length of a link. The receiver estimates the transmitted data and makes decisions according to the received optical waveforms. In what follows, the building blocks of transmitter and receiver modules are detailed.

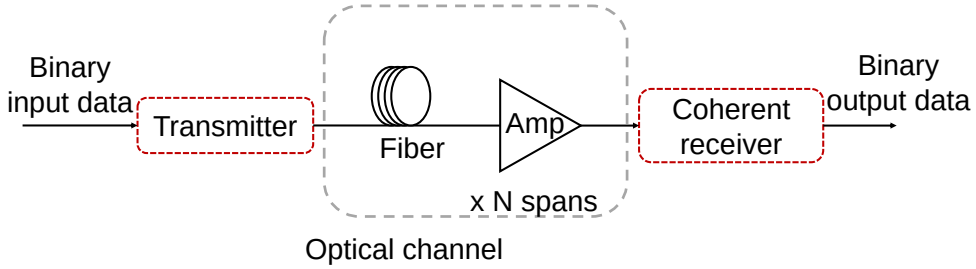

Figure 2.3 – Basic schematic of fiber-optic transmission system.

2.1.1 Transmitter

The main objective of a digital optical communication transmitter is to impose binary information onto an optical carrier wave. This requires basically three different operating blocks implemented in the digital, electrical and optical domain, as illustrated in Fig. 2.4. The digital domain blocks deal with discrete-time representation of bits or complex symbols at a fixed oversampling rate (with respect to the Nyquist sampling). Thanks to the use of digital to analog converters, discrete digital signals are transformed to continuous analog electrical baseband signals. Finally, the electrical signal is modulated onto optical carrier

wave with the use of a dual-polarization optical in-phase and quadrature modulator, resulting in an effective up-conversion of the signal spectrum from being DC-centered to being centered around the optical carrier wave frequency. In the following, digital, analog and optical operating blocks are discussed.

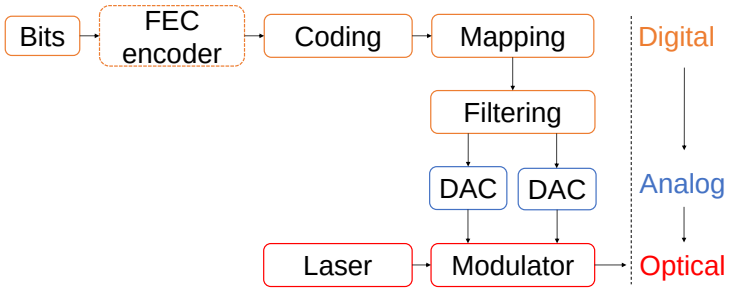

Figure 2.4 – Building blocks of a coherent transmitter. Steps are performed in the digital, analog electrical and optical domains.

2.1.1.1 Digital Domain Blocks

2.1.1.1.1 From bits to symbols

Generally, the forward error correction (FEC) encoder is the first digital building block. It adds redundant bits to the source information bit sequence so that after transmission over a noisy channel, the decoder at the receiver exploits this redundancy to try to detect, and possibly correct errors induced by the channel. Currently, the increased use of low density parity check (LDPC) codes [39], turbo codes [40] and polar codes [41] allow systems to operate at higher effective data rates and transmission distances. As a matter of fact, the use of LDPC with overhead around 20% is nowadays used in commercial products [42]. Nevertheless, here we only consider source information bit sequence transmission over the optical system, ignoring detailed discussions on FEC techniques.

Binary information data are mapped into symbol sequences, which can carry one or several bits. The number of bits N_b representing each symbol is directly given by $N_b = \log_2(M)$, with M being the order of the modulation format. To decide on which complex constellation symbol to address, the bit stream is divided into blocks of N_b bits and a look-up-table with a mapping is used. In Table 2.1, an example of such a mapping for 16-QAM is illustrated.

In the complex plane, the full set of symbols constitute a constellation. A signal

Table 2.1 – Bit to symbol mapping for 16-QAM, $N_b = 4$. The selected mapping is of Gray-type.

Bit Sequence	Output Symbol	Bit Sequence	Output Symbol
{0,0,1,0}	$(-3+3j)$	{0,0,1,1}	$(-3+1j)$
{0,0,0,1}	$(-3-1j)$	{0,0,0,0}	$(-3-3j)$
{0,1,1,0}	$(-1+3j)$	{0,1,1,1}	$(-1+1j)$
{0,1,0,1}	$(-1-1j)$	{0,1,0,0}	$(-1-3j)$
{1,1,1,0}	$(1+3j)$	{1,1,1,1}	$(1+1j)$
{1,1,0,1}	$(1-1j)$	{1,1,0,0}	$(1-3j)$
{1,0,1,0}	$(3+3j)$	{1,0,1,1}	$(3+1j)$
{1,0,0,1}	$(3-1j)$	{1,0,0,0}	$(3-3j)$

modulated with quadrature amplitude modulation can be represented by a 2-dimensional vectors (or a complex symbol). The real part of the set of symbols represents the in-phase component or I path, whereas its imaginary part represents the quadrature component or Q path. Although polarization multiplexed signals can be represented by 4-dimensional vectors representing the in-phase and quadrature of each of the orthogonal polarization, they are typically represented by two separated 2-dimensional vectors due to the difficulty to graphically represent 4-dimensional space.

Fig. 2.5 illustrates different examples of square quadrature amplitude constellations. More modulation formats can be found in [43]. Typically, the constellation points are zero mean and have an average symbol energy of

$$E_s = \frac{1}{M}\sum_{k=1}^{M}\|\mathbf{s}_k\|^2, \tag{2.1}$$

where $\mathbf{s}_k$ represents the vector of symbol alphabets, $\|\mathbf{s}_k\|^2$ is the energy of k^{th} symbol.

Coherent transmission enables more efficient use of the available spectrum of the coherent light as higher order quadrature amplitude modulation combined with dual-polarization multiplexing techniques improve the spectral efficiency.

This can be seen in Fig. 2.6 where the achievable information rates (AIRs) for the additive white Gaussian noise (AWGN) channel for conventional M-QAM constellations are plotted. AIRs are information-theoretic quantities that are, by definition, linked to the amount of reliable information that can be transmitted through a given channel.

As seen, when compared at the same SNR, a larger QAM constellation can operate at a higher information rate. Also, we observe that each curve saturates at $\log_2(M)$ and for

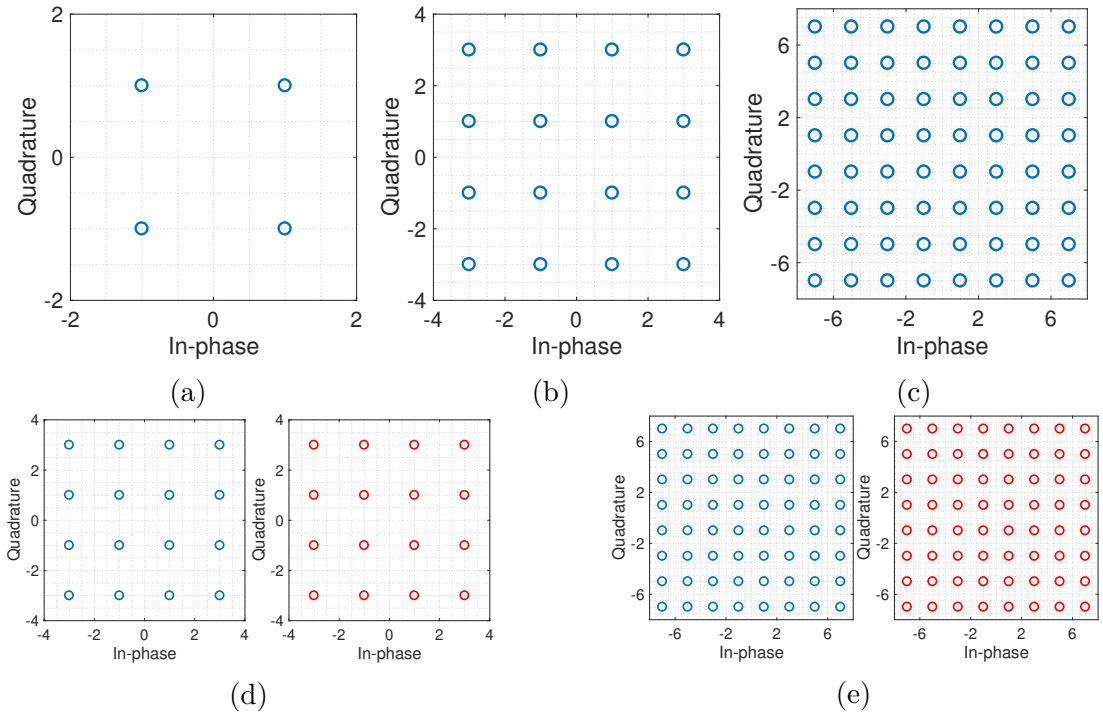

Figure 2.5 – Examples of modulation formats commonly used in coherent optical communications. (a) quadrature phase shift keying (QPSK), or alternatively, 4-ary QAM (4-QAM), 2 bit/symbol, (b) 16-QAM, 4 bit/symbol, (c) 64-QAM, 6 bit/symbol, (d) PM-16QAM, 8 bit/symbol, (e) PM-64QAM, 12 bit/symbol.

low SNR, these curves are quite close to the Shannon limit coming from the usage of finite equipropable alphabet.

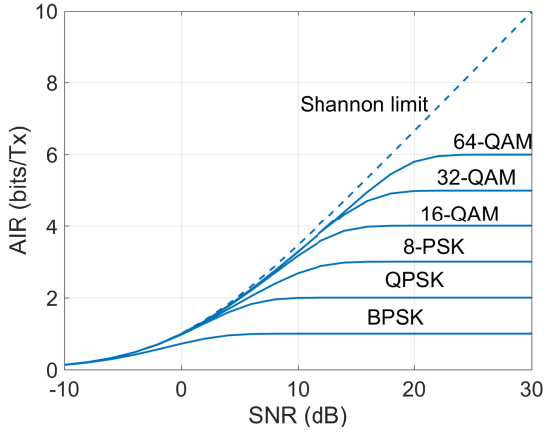

Figure 2.6 – Achievable information rates for M-QAM constellations.

On the other hand, multilevel modulation formats affect the power consumption as

they came with a higher sensitivity to transmission impairments [44]. As well, higher order modulation formats expand power consumption of analog-to-digital converters (ADCs) and all DSP since higher bit-resolution will be required. Moreover, they intensify the sensitivity to phase noise and thus requires more complex phase-tracking signal reconstruction algorithms.

Mapping with encoding process can overcome these fiber distortions and help error prone data transmission. The suitable coding in presence of AWGN is Gray code in which adjacent symbols differ only in one bit. Thus, in Gray coded designs one symbol error (between adjacent symbols) is translated to one bit error [45]. Nevertheless, a fiber-optic link is not a simple AWGN channel. It includes phase noise impairments.

As a matter of fact, a differential encoding scheme protects against phase fluctuation due to instabilities of both transmitter and receiver local oscillator lasers. Differential encoding is used for square QAM constellations to remove their phase ambiguity [46]. While not proven to be optimum, this technique has low performance penalties in terms of optical signal-to-noise ratio (OSNR) relative to the uncoded performance. This penalty for square M-QAM format is expressed by

$$F = 1 + \frac{\log_2(M)}{2(\sqrt{M} - 1)}. \tag{2.2}$$

2.1.1.1.2 Filtering

Before applying a pulse shaping filter, oversampling is needed and the complex symbols are therefore up-sampled at this point [47].

Generally, sender side pulse-shaping is combined with a matched filter in the receiver to achieve optimum tolerance for noise in the system, and must meet Nyquist inter-symbol interference criterion. Pulse shaping aims to better control the inter-symbol interference caused by the channel by determining the effective bandwidth confining the useful signal or, in other words, by shaping the signal spectrum to meet the channel requirements [48, 49]. Mathematically, this is written as

$$s(n) = \sum_{k=0}^{N} a_k p\left(n - k\right), \tag{2.3}$$

where $s(n)$ is the output discrete waveform a time instance n, a_k is the k^{th} element in the symbol sequence, $p(n)$ is the impulse response of the shaping pulse and N is the

length of the impulse response sequence. Limiting the signal in bandwidth implies inter-symbol interference (ISI) as the signal is broadened. To handle this problem, family of commonly used raised-cosine and root-raised-cosine filters respond to Nyquist ISI criterion. In practice, the raised-cosine filter is often further divided and implemented both at the transmitter and receiver side using the square-root of the raised-cosine filter response. The transfer function of the raised-cosine filter can be given as

$$H(f) = \begin{cases} T, & |f| \leq \frac{1-\beta}{2T} \\ \frac{T}{2}\left[1+\cos\left(\frac{\pi T}{\beta}\left[|f|-\frac{1-\beta}{2T}\right]\right)\right], & \frac{1-\beta}{2T} < |f| < \frac{1+\beta}{2T} \\ 0, & \text{otherwise,} \end{cases} \tag{2.4}$$

with T denoting the symbol period and β the roll-off factor. By denoting the baud-rate $R_s = 1/T$, the required bilateral base-band bandwidth is $(1+\beta)R_s$, and the ideal Nyquist filter is obtained when $\beta = 0$.

The impulse response and the transfer function of the raised-cosine filter for $\beta \in \{0.01, 0.1, 0.2, 0.5\}$ can be seen in Fig. 2.7.

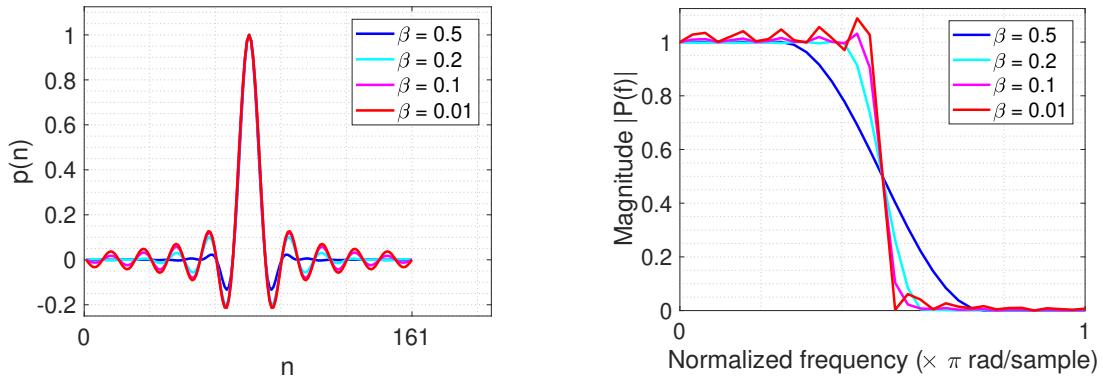

(a) (b)

Figure 2.7 – Raised cosine filtering with varying roll-off factor β, oversampling rate of 8 and a span filter of 20. (a) Impulse response, (b) Transfer function.

2.1.1.2 Digital-to-Analog Conversion

After mapping and pulse-shaping operations, the digital signal is then converted into a continuous analog signal which can be modulated on the optical carrier. Ideally, this conversion takes place without any drawbacks, but in practice, digital-to-analog converters

(DACs) present a limited resolution. Indeed, the resolution of high-speed DACs limits the performance for multi-level modulation formats [50].

The limited resolution is explained by the fact that an ADC presents a finite-precision number and that during analog-to-digital conversion, the signal voltage is represented by a binary number with a fixed number of bits.

An ideal DAC converts the digital binary number into an analog output impulse that is then processed by a reconstruction filter using some form of interpolation to fill in data between the impulses. To interpolate between consecutive samples, a conventional DAC converts the numbers into a piecewise constant function made up, for example, of a sequence of rectangular functions that are modeled with the zero-order hold. The DAC is then controlled by a sampling clock and each discrete sample is held for a sampling period T_s.

Regarding the Nyquist–Shannon sampling theorem, the sinc functions can perform ideal reconstruction of the desired analog signal signal from the sampled data provided that the bandwidth of the signal meets certain requirements (e.g., a baseband signal with bandwidth less than the Nyquist frequency). Nevertheless, implementing ideal impulse response is not feasible and most DACs use the zero-order hold functions. At the output DAC, the reconstructed signal differs from the desired one due to quantization error. Fig 2.8 illustrates the implications of quantization for a sine-wave. In this case, a low-level noise-floor is then observed for the quantized signal, compared to the floating-point representation (see Fig. 2.8(b) as an illustration of magnitude plot of 5-bit DAC outputing a raised cosine shaped signal with $\beta = 0.1$). Other effects reducing the output signal quality, added to the limited resolution, are the presence of both noise and bandwidth limitations. Finally, the output signal quality can be evaluated thanks to some metric quantities such as DAC resolution, jitter and the effective number of bits which assumes a random approximation in the quantization error [51].

2.1.1.3 Optical Domain Blocks

2.1.1.3.1 Laser source

A laser is a device that emits light through a process of optical amplification based on the stimulated emission of electromagnetic radiation. The laser holds three major properties. The most distinctive characteristics of laser emission are spatial coherence and spectral coherence. Spatial coherence is related to the beam divergence of the laser.

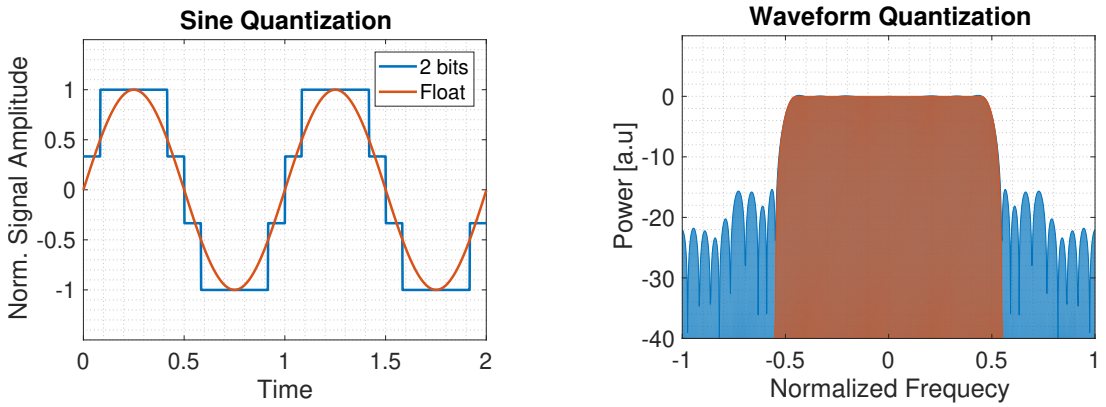

(a) (b)

Figure 2.8 – (a) No ideal signal reconstruction using the zero-order hold function to interpolate between samples for a 2-bit DAC. (b) Additional noise to a shaped waveform due to limited (5-bit) DAC resolution.

It describes the correlation between two points in the space and the ability of the two points to interfere in extent of wave in averaged time. Spectral coherence is evaluated by measuring the linewidth of laser radiation. It describes how monochromatic a light source is. Lasers have high spatial and temporal coherence meaning all the waves propagate in phase along the propagation direction (temporal coherence) and in phase across the beam diameter (spatial coherence). Lastly, lasers make it possible to deliver high intense light to small area thanks to their power property. Thus, a variety of improved and specialized laser types have been constructed and optimized for different goals such as wavelength band, linewidth, power efficiency, cost, etc. For coherent optical communication systems, a laser plays an important role. In fact, the powerful advantage of the coherent system relies on its ability to explore the full optical field, i.e. both amplitude and phase on both polarizations. Polarization multiplexing permits to double the transmission throughput, as different signals can be transmitted over orthogonal states of polarization of the same wavelength. Moreover, multi-carrier wavelength configurations could also be used to maximize the optical transmission capacity. Indeed, multiplexed frequencies are encoded on the amplitude and phase while signal orthogonality is still maintained [52]. In this thesis, we focus on single carrier systems.

2.1.1.3.2 Optical modulator

An electromagnetic wave consists of coupled oscillating electric and magnetic fields

which are always perpendicular to each other. The polarization of electromagnetic waves refers conventionally to the direction of the electric field and the orientation of its oscillation is called the state of polarization (SOP) [53].

The powerful use of IQ modulators lies in their capability to use each orthogonal E_x and E_y waves called the X and Y polarizations and modulate them independently in phase and amplitude. The typical optical coherent transmitter is depicted in Fig. 2.9.

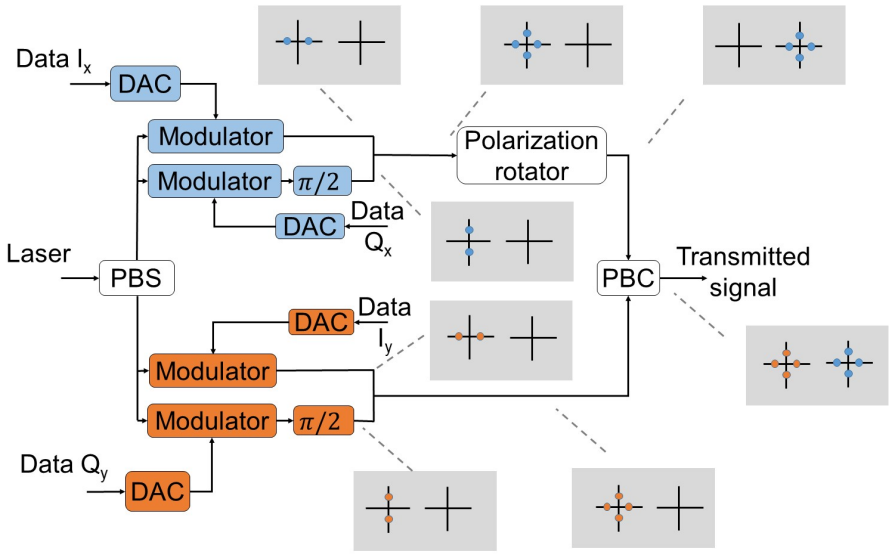

Figure 2.9 – Building blocks of optical coherent transmitter with an example of PDM-QPSK generation where the up (down) sides are used to modulated the X (Y) polarization.

In practice, the laser is split into two orthogonal beams by a polarization-beam splitter (PBS). On the other side, the electrical signals conveying data could be generated using DSP combined with arbitrary waveform generators. Thanks to two Mach-Zehnder modulators (MZMs), the in-phase and quadrature components of each beam are modulated in amplitude, separately. The quadrature component is then shifted by 90° and combined with the in-phase component. Thereafter, one of the polarization is Y-polarized as its SOP by the polarization rotator. Combination of both X and Y polarizations via a polarization-beam combiner (PBC) results in the generation of a the polarization multiplexed signal to be transmitted over optical fibers.

In addition to higher order modulation format and larger symbol-rates, the increase of the channel capacity could be achieved with flexible bit-rate optical technology [54]. With the use of adaptive transceivers, it is possible to vary the bandwidth [55]. The

purpose of this technology is to dynamically adapt the channel resources (wavelength channels, bandwidth, transmission format, data rate, etc.) in a cost-effective and elastic way according to the channel-variable conditions and demands while considering both the quality of transmission and data rate of communication requests.

In this thesis, the challenge is dealt from a flexible bit-rate systems point of view. Consequently, variable symbol rate and variable spectral efficiency are possible thanks to the introduction of flexible transponders, high resolution DACs, ADCs, coherent receivers and the advance of DSP blocks. The variable symbol rate is typically implemented by using a variable resampler. However, the variable spectral efficiency requires the operation of different QAM formats (QPSK up to 64-QAM). In this thesis, only square constellations are considered.

2.1.2 Optical Coherent Receiver

During transmission over the channel, the data information is strongly altered by the optical medium and system impairments. On the receiver side, several signal processing steps are operated for imperfection correction and signal recovery.

Receiver starts with an adequate optical front-end composed of a coherent detection block cascaded by an analog-to-digital converter. Thereafter, digital signal processing blocks and decoding steps are performed for further information retrieving. In the following, we provide a brief overview of the purpose and functionality of each subsystem.

2.1.2.1 Coherent Detection Front-End

The goal of coherent detection is to preserve the phase information of the optical received signal while converting it to the electrical domain. This is proceeded by mixing a received optical signal field $\boldsymbol{\mathcal{E}}_{\mathrm{s}}(t)$ by a local oscillator (LO) field $\boldsymbol{\mathcal{E}}_{\mathrm{LO}}(t)$ acting as a phase reference. Mathematically, the received optical field $\boldsymbol{\mathcal{E}}_{\mathrm{s}}(t)$, as well as LO optical field at the receiver input are given by

$$\begin{aligned}\boldsymbol{\mathcal{E}}_{s}(t) &= E_{\mathrm{s}}\left(t\right) e^{j(\omega_s t+\phi_s)}\mathbf{e}_s \\ &= \left(E_{s_I}\left(t\right)+jE_{s_Q}\left(t\right)\right) e^{j(\omega_s t+\phi_s)}\mathbf{e}_s.\end{aligned} \tag{2.5}$$

$$\boldsymbol{\mathcal{E}}_{\mathrm{LO}}(t) = E_{\mathrm{LO}}\left(t\right)\exp^{j(\omega_{\mathrm{LO}}t+\phi_{\mathrm{LO}})}\mathbf{e}_{\mathrm{LO}}. \tag{2.6}$$

where $E_{\mathrm{s}}(t)$ presents the useful information in its phase and amplitude components, $\mathbf{e}_s$ and $\mathbf{e}_{\mathrm{LO}}$ describe the polarization states (Jones vectors) of the optical fields. ω_s and ω_{LO} are the carriers of the signal and the LO, respectively, and ϕ_s and ϕ_{LO} are the phases of the signal and the LO, respectively. The mixing process between the received signal and light from LO is handled by the 90° hybrid also called optical hybrid. Thanks to its optical couplers and phase shifters, the optical hybrid outputs four possible states of the LO signal and mixes them with the incoming signal in the complex field space (see Fig. 2.10). Then, the four outputs are fed to two balanced detectors. Each balanced detector is composed of two photo-diodes where the in-phase and quadrature components are extracted. Consequently, the balanced detector outputs currents that are proportional to the electric in-phase and quadrature signals.

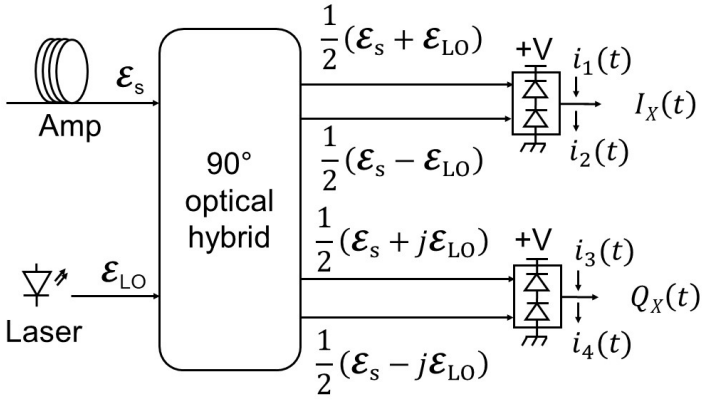

Figure 2.10 – Overview of a coherent optical receiver.

Mathematical details of photo-receiver outputs can be expressed by

$$\begin{aligned} i_1(t) &= \mathcal{S}|\boldsymbol{\mathcal{E}}_s(t) + \boldsymbol{\mathcal{E}}_{\mathrm{LO}}(t)|^2 \\ &= \mathcal{S}(|E_s(t)|^2 + E_{\mathrm{LO}}^2(t) + 2\Re\{E_{\mathrm{LO}}E_s(t)e^{j(\omega_{IF}t+\Delta\phi)}\mathbf{e}_s \cdot \mathbf{e}_{\mathrm{LO}}^*\}), \end{aligned} \tag{2.7}$$

$$\begin{aligned} i_2(t) &= \mathcal{S}|\boldsymbol{\mathcal{E}}_s(t) - \boldsymbol{\mathcal{E}}_{\mathrm{LO}}(t)|^2 \\ &= \mathcal{S}(|E_s(t)|^2 + E_{\mathrm{LO}}^2(t) - 2\Re\{E_{\mathrm{LO}}E_s(t)e^{j(\omega_{IF}t+\Delta\phi)}\mathbf{e}_s \cdot \mathbf{e}_{\mathrm{LO}}^*\}), \end{aligned} \tag{2.8}$$

$$\begin{aligned} i_3(t) &= \mathcal{S}|\boldsymbol{\mathcal{E}}_s(t) + j\boldsymbol{\mathcal{E}}_{\mathrm{LO}}(t)|^2 \\ &= \mathcal{S}(|E_s(t)|^2 + E_{\mathrm{LO}}^2(t) + 2\Im\{E_{\mathrm{LO}}E_s(t)e^{j(\omega_{IF}t+\Delta\phi)}\mathbf{e}_s \cdot \mathbf{e}_{\mathrm{LO}}^*\}), \end{aligned} \tag{2.9}$$

$$\begin{aligned} i_4(t) &= \mathcal{S}|\boldsymbol{\mathcal{E}}_s(t) - j\boldsymbol{\mathcal{E}}_{\mathrm{LO}}(t)|^2 \\ &= \mathcal{S}(|E_s(t)|^2 + E_{\mathrm{LO}}^2(t) - 2\Im\{E_{\mathrm{LO}}E_s(t)e^{j(\omega_{IF}t+\Delta\phi)}\mathbf{e}_s \cdot \mathbf{e}_{\mathrm{LO}}^*\}). \end{aligned} \tag{2.10}$$

where $\mathcal{S}$ designs the photo-diodes responsivity, $\Re$ and $\Im$ are respectively the real and imaginary part, $\omega_{IF} = \omega_s - \omega_{\mathrm{LO}}$ is the intermediate angular frequency which typical values are in the range of $[0, 5]$ GHz, $\Delta\phi = \phi_s - \phi_{\mathrm{LO}}$, and $\mathbf{e}_s \cdot \mathbf{e}_{\mathrm{LO}}^*$ is the scalar product of the two Jones vectors.

If photo-diodes have likely the same properties (same responsivity and frequency response), the balanced detector outputs could then reject the common quadratic term and conserve only the beat term. Therefore, the balanced detectors outputs are given by

$$\begin{aligned} I_X(t) &= i_1(t) - i_2(t) \\ &= 4\mathcal{S}\Re\{E_{\mathrm{LO}}E_s(t)e^{j(\omega_{IF}t+\Delta\phi)}\mathbf{e}_s \cdot \mathbf{e}_{\mathrm{LO}}^*\}, \end{aligned} \tag{2.11}$$

$$\begin{aligned} Q_X(t) &= i_3(t) - i_4(t) \\ &= 4\mathcal{S}\Im\{E_{\mathrm{LO}}E_s(t)e^{j(\omega_{IF}t+\Delta\phi)}\mathbf{e}_s \cdot \mathbf{e}_{\mathrm{LO}}^*\}. \end{aligned} \tag{2.12}$$

As expressed in Eq. 2.11 and Eq. 2.12, the beat term depends on the relative polarization states of the optical signal and LO fields. Indeed, when polarization states are orthogonal the beat terms are canceled ($\mathbf{e}_s \cdot \mathbf{e}_{\mathrm{LO}}^* = 0$). On the other hand, the beat terms are in their maximum when the polarization states are identical.

The use of the polarization diversity receiver prevents the loss of detection. As depicted in Fig. 2.11, the incoming signals, both from the fiber and from the LO laser are polarization separated with polarization-beam splitters (PBSs) and mixed in a pair of 90° optical hybrids. The arbitrary elliptical polarization of the received optical signal before the PBS

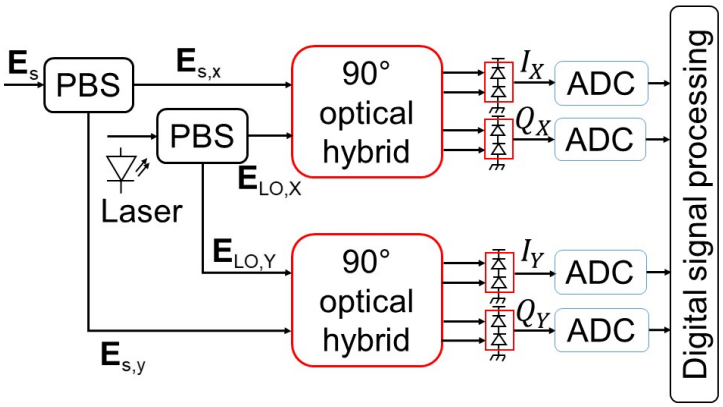

Figure 2.11 – Block diagrams for a polarization diversity coherent receiver.

$\mathbf{e}_s$ and the linear polarization of the LO $\mathbf{e}_{\mathrm{LO}}$ can be described as follows

$$\mathbf{e}_s = \begin{pmatrix} \cos(\theta) \\ e^{j\phi}\sin(\theta) \end{pmatrix}, \tag{2.13}$$

$$\mathbf{e}_{\mathrm{LO}} = \frac{1}{\sqrt{2}}\begin{pmatrix} 1 \\ 1 \end{pmatrix}. \tag{2.14}$$

where θ is the inclination angle or the azimuth, the angle between the major axis of the field polarization ellipse $\boldsymbol{\mathcal{E}}_s$ and the positive direction of the X-axis of the PBS, and defines the orientation of the ellipse in its plane [56], ϕ represents a phase lag or advance between X and Y fields of $\boldsymbol{\mathcal{E}}_s$ axis. The two projections are therefore mixed with the signal in the hybrids [57]. Under these conditions, the outputs of balanced photo-detectors used after the hybrids are described by

$$I_X(t) = 2\sqrt{2}\mathcal{S}\cos(\theta)E_{\mathrm{LO}}(E_{s_I}(t)\cos(\omega_{IF}t + \Delta\phi) - E_{s_Q}(t)\sin(\omega_{IF}t + \Delta\phi)), \tag{2.15}$$

$$Q_X(t) = 2\sqrt{2}\mathcal{S}\cos(\theta)E_{\mathrm{LO}}(E_{s_I}(t)\sin(\omega_{IF}t + \Delta\phi) + E_{s_Q}(t)\cos(\omega_{IF}t + \Delta\phi)), \tag{2.16}$$

$$I_Y(t) = 2\sqrt{2}\mathcal{S}\sin(\theta)E_{\mathrm{LO}}(E_{s_I}(t)\cos(\omega_{IF}t + \Delta\phi + \phi) - E_{s_Q}(t)\sin(\omega_{IF}t + \Delta\phi + \phi)), \tag{2.17}$$

$$Q_Y(t) = 2\sqrt{2}\mathcal{S}\sin(\theta)E_{\mathrm{LO}}(E_{s_I}(t)\sin(\omega_{IF}t + \Delta\phi + \phi) + E_{s_Q}(t)\cos(\omega_{IF}t + \Delta\phi + \phi)). \tag{2.18}$$

These four outputs are proportional to the in-phase and quadrature components of the

two polarizations and could be expressed with complex notation by

$$\begin{aligned} E_{O,X}(t) &= I_X(t) + jQ_X(t) \\ &= 2\sqrt{2}\mathcal{S}\cos(\theta)E_{\mathrm{LO}}E_s(t)e^{j(\omega_{IF}t+\Delta\phi)}, \end{aligned} \tag{2.19}$$

$$\begin{aligned} E_{O,Y}(t) &= I_Y(t) + jQ_Y(t) \\ &= 2\sqrt{2}\mathcal{S}\sin(\theta)E_{\mathrm{LO}}E_s(t)e^{j(\omega_{IF}t+\Delta\phi+\phi)}. \end{aligned} \tag{2.20}$$

Finally, the four output of the balanced photo-detector diodes are sampled in an ADC for further DSP treatment of the signal.

2.1.2.2 Analog-to-Digital Converter

The analog-to-digital converter mission is to convert the four analog photo-currents outputs to digital signals. The ADC contains two main subsystems: the sampler and the quantizer. The sampler role is to convert the continuous-time analog signal to a discrete-time signal using a fixed time-base. To ensure the preservation of all analog signal information, sampling must validate the Shannon-Nyquist criterion and the sampling frequency should be at least twice the maximum signal frequency. Regarding the bit resolution of the ADC, the quantizer discretizes the amplitude of the signal into an effective number of bit, which gives an effective amplitude resolution that will determine how many signaling levels can be used. State-of-the-art high speed CMOS analog to digital converters achieve noise floors (determined by thermal noise) in the order of 5 to 6 effective number of bits with bandwidths exceeding 20 GHz [58].

2.2 Quality Criteria For Optical Communication

In the previous sections, the building blocks of the coherent transmitter and the coherent receiver were detailed. At the receiver, the incoming signals, corrupted by system and channel distortions, need to be processed by several digital signal processing techniques. In view of all the degradation that the signal can experience during its transport through the optical fiber, it is necessary to establish criteria to judge the quality of a transmission or the optical signal. In practice, a variety of metrics are available for these purposes before and after the mitigation of the signals imperfections. Indeed, the quality of an optical signal can be estimated using the optical signal-to-noise ratio, the OSNR penalty or the error vector magnitude (EVM) suited for QAM format or the bit error rate (BER).

2.2.1 The Optical Signal to Noise Ratio

In long-haul transmission system, the transmission link is modeled as successive spans with equal lengths and separated by optical amplifiers. These optical amplifiers are responsible for the generation of amplified spontaneous emission (ASE) noise which reduces significantly the transmission performance. ASE is commonly considered as AWGN in the optical field domain.

The optical signal-to-noise ratio is defined as the average optical signal power divided by the ASE power, measured in both polarizations and within a reference bandwidth customarily fixed to 0.1 nm, i.e 12.5 GHz (at 1550 nm). The OSNR can be measured with an optical spectrum analyzer and is expressed by

$$\mathrm{OSNR} = \frac{P}{2\,N_{\mathrm{ASE}}\,B_{\mathrm{ref}}}, \tag{2.21}$$

where P is the total average signal power summed over the two states of polarization, N_{ASE} is the spectral density of the ASE in one polarization and the factor 2 expresses the fact that ASE noise is present on both polarizations, and the reference bandwidth B_{ref} is fixed to 0.1 nm (12.5 GHz at 1550 nm).

Additionally, the SNR per symbol of additive white Gaussian noise channel is given by

$$\mathrm{SNR} = \frac{E_s}{N_0}, \tag{2.22}$$

where N_0 is the noise spectral density and E_s is the energy per symbol over one polarization, $E_s = PT$ with P the power averaged over one modulated symbol and T is the symbol duration. In the case of polarization multiplexing scheme, the OSNR and SNR are related by

$$\mathrm{OSNR} = \frac{P}{2N_0 B_{\mathrm{ref}}}, \tag{2.23}$$

where P is the total average signal power summed over the two states of polarization $P = 2E_s \times R_s$, with $R_s = \frac{1}{T}$ is the symbol rate, and where N_{ASE} and N_0 are the power spectral density of ASE and are assumed to be equivalent. Hence, the OSNR over 2 polarizations is given by

$$\mathrm{OSNR} = \frac{2E_s R_s}{2N_0 B_{\mathrm{ref}}} = \frac{R_s}{B_{\mathrm{ref}}}\mathrm{SNR}. \tag{2.24}$$

Also, the SNR per bit $\mathrm{SNR}_b = E_b/N_0$ is another metric useful in digital communication,

and the relationship between the OSNR and SNR_b is expressed by

$$\mathrm{OSNR} = \frac{R_b}{B_{ref}}\mathrm{SNR}_b, \tag{2.25}$$

where R_b is the bit rate.

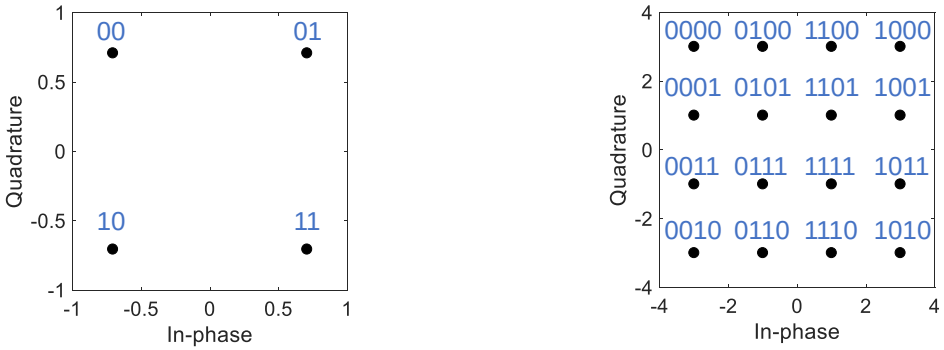

(a) (b)

Figure 2.12 – Constellation of (a) QPSK and (b) 16-QAM using Gray encoding.

2.2.2 The Bit Error Ratio

The most fundamental and conclusive metric for evaluating the performance of transmission of every digital communication system is the BER. It is expressed as the ratio of the number of incorrectly received bits to the total number of received bits.

Assuming the use of Gray coding (presented in Fig. 2.12 for 4-QAM and 16-QAM modulation formats), the theoretical error probability of square M-ary QAM constellation with coherent detection in AWGN channel assuming perfect recovery of the carrier frequency and phase is approximated as [43]

$$\mathrm{BER} = \frac{4}{\log_2(M)}\frac{\sqrt{M}-1}{\sqrt{M}}Q\left(\sqrt{\frac{3\,\log_2(M)\,\mathrm{SNR}_b}{M-1}}\right) \tag{2.26}$$

where

$$Q\left(x\right) = \frac{1}{\sqrt{2\pi}}\int_x^{+\infty} e^{-u^2/2}du = \frac{1}{2}\mathrm{erfc}\left(\frac{x}{\sqrt{2}}\right)$$

is the Gaussian tail for real-valued Gaussian variable with zero-mean and unit-variance.

Note that the performance comparison of digital modulation system does not consider only the BER curve but also other parameters such as transmission bandwidth and hardware complexity. In fact, several trade-offs exist between these specifications that must be examined carefully. For instance, to maintain a good transmission quality for coherent optical communication, a BER target in the range of 10^{-9} or 10^{-12} is considered. Suppose a BER value of 10^{-9} is kept which is a common standard target for optical system comparison goals.

While the BER is the most direct metric for quality measure, it is sometimes challenging to count it, especially for simulations and off-line processing. We further present other useful utilized metrics .

2.2.3 The OSNR Penalty

The OSNR penalty is widely used both in experiments and numerical simulations. The notion of OSNR penalty is used to justify the amount of non-noise system impairments. In fact, when the accumulated channel impairments are extremely high, the signal detection at the receiver cannot be assured with a BER lower than a certain target. Therefore, the OSNR penalty is the difference in sensitivity (in dB scale) and represents the excess OSNR required after transmission to get reference BER with respect to the requirements in the back-to-back configuration, i.e. when the transmitter and receiver are directly connected, without transmission.

2.2.4 The Error Vector Magnitude

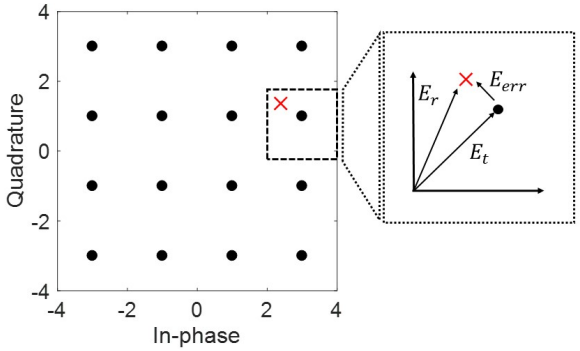

Figure 2.13 – Constellation diagram and EVM representation.

In order to compute the BER metric, it is necessary to demodulate received constellation

points. Sometimes, this task might not be possible, especially, when the receiver does not know the transmitted sequence and is not able to detect bit errors at the physical layer. Therefore it is necessary to define a different measure for which a relation with the BER could be established, which presents an approximate estimation of the received signal directly from the constellation points, without resorting to demodulation or information provided by higher layers. One of such metrics is the EVM.

The error vector magnitude describes the distance of the received complex symbol from its ideal position in the constellation diagram. Fig. 2.13 depicts a simulated noisy constellation point and its distance with respect to the 16-QAM points. As can be seen, the actually received signal vector E_r deviates by an error vector E_{err} from the ideal transmitted vector E_t. For a number of I randomly transmitted data, the EVM is given by

$$\mathrm{EVM} = \frac{\sigma_{\mathrm{err}}}{E_{\mathrm{ref}}}, \quad \sigma_{\mathrm{err}}^2 = \frac{1}{I}\sum_{i=1}^{I}\left|E_{\mathrm{err,i}}\right|^2, \quad E_{\mathrm{err,i}} = E_{r,i} - E_{t,i},$$

with $E_{\mathrm{err,i}}$ is the i^{th} symbol error vector and E_{ref} is a normalization reference.

There are two possible values for EVM normalization. The first is the constellation maximum which sets the normalization value to the maximum constellation magnitude (the level of the corner for a 16-QAM format for example).

Thus, $E_{\mathrm{ref}} = \left|E_{\mathrm{t,m}}\right| = \max_i \left|E_{\mathrm{t,i}}\right|$ denotes the power of the longest ideal constellation vector with magnitude and serves for normalization.

The second is the root mean square (RMS) reference which sets the normalization value to the RMS level of the in-phase and quadrature reference symbol points. When the modulation is impaired by the AWGN, RMS reference will make the averaged EVM approach the inverse of the SNR of the signal.

2.3 Summary

In this chapter, basic building blocks of fiber-optic communication systems were described. The transmitter modules were detailed in the digital, electrical and optical processing domains. The principle of the coherent receiver was also detailed with its subsequent required optical components. Finally, we suppose that the received signals were appropriately corrected from the fiber-optic channel and system impairments and we have presented some quantitative quality criteria to qualify the optical transmission. In what

follows, we will deal with transmission impairments that occur due to physical properties of the fiber-optic channel as well as the imperfections in various hardware components and we will detail state-of-the-art DSP blocks used for these impairments mitigation.

Chapter 3

Digital Signal Processing

In the previous chapter, we have detailed the state of the art of optical transmission systems namely the transmitter and receiver architecture in charge of generating and processing coherent PM-M-QAM signals. In this chapter, more details are provided for the physical impairments in long-haul optical fiber transmission. The physical causes as well as the impacts of linear effects on the transmitted optical signal are reviewed by taking into account transmission link accumulated dispersion, polarization dependent effects as well as system impairments. Next, the different DSP techniques needed to reliably recover transported information over the optical fiber are also introduced. Receiver operations used in the polarization multiplexing context are detailed. Additionally, in this thesis we will only focus on mitigating linear effects and we will introduce different state-of-the-art algorithms dealing with each impairment.

3.1 Fiber-Optic Impairments

The fiber-optic channel can be modeled as repeated sections called spans, where each span comprises an optical fiber and an optical amplifier. The propagation of light in an optical fiber can be modeled using the Manakov equation [59]

$$\frac{\partial \mathbf{E}(z,t)}{\partial z} = -\frac{\alpha(z)}{2}\mathbf{E}(z,t) - j\frac{\beta_2}{2}\frac{\partial^2 \mathbf{E}(z,t)}{\partial t^2} + j\gamma\frac{8}{9}\left\|\mathbf{E}(z,t)\right\|^2\mathbf{E}(z,t), \tag{3.1}$$

where $\mathbf{E} = \left[\mathbf{E_x},\ \mathbf{E_y}\right]^T$ is the complex envelope of the two polarization components of the optical field at time t and z is the propagation distance, $(\ \cdot\ )^T$ is the transposition operation, $\alpha(z)$ is the power attenuation factor, β_2 is the group velocity dispersion coefficient, γ is the nonlinear coefficient, $\left\|\mathbf{E}\right\|^2 = \mathbf{E}^H\mathbf{E}$ denotes the optical power where $(\ \cdot\ )^H$ is the Hermitian conjugate.

According to the Eq. 3.1, the first, second and third terms in the equation take into account fiber loss, chromatic dispersion and fiber nonlinearity effects, respectively.

However, a typical coherent system presents various transmission impairments. In Fig. 3.1, the typical coherent system and its related impairments are presented. The optical signal of widely used modulation formats PM-4/16-QAM are transmitted to the fiber link. When propagating over the fiber, it is altered by numerous fiber-optic channel impairments (chromatic dispersion, polarization rotation, fiber nonlinearity, polarization mode dispersion) as well as AWGN from ASE. Also, other electro-optical related distortions (sampling error, Tx or Rx IQ imbalance, carrier frequency offset and laser phase noise) may affect the optical signal. Finally, two balanced photo detectors were connected to the hybrid outputs and a real-time oscilloscope as ADC to acquire data for offline processing. In this section, we will detail these fiber-optic impairments while enlarging the scope to the propagation and system distortions.

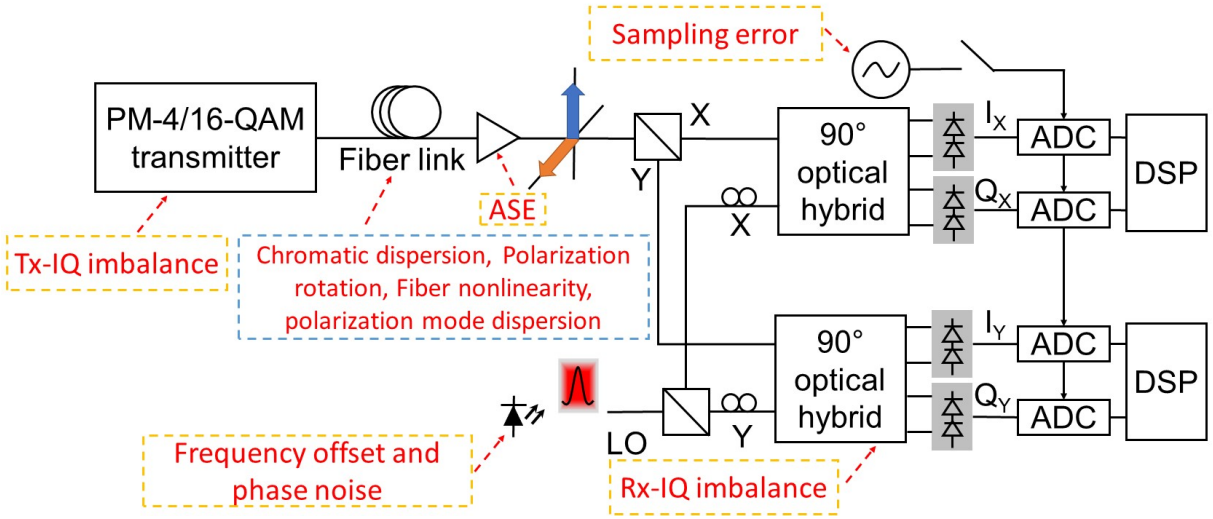

Figure 3.1 – A typical coherent system and its related impairments which are needed to be mitigated in the digital domain part.

3.1.1 System Impairments

In this part, the system imperfections disturbing the coherent receiver are presented. These sources of degradation of the signal include mainly the additive noise from optical amplifiers, the in-phase and quadrature imbalance, chromatic dispersion, polarization related distortions as well as carrier phase and frequency impairments.

3.1.1.1 Optical Amplification

Today, the most common type of optical amplifier in commercial systems as well as in research experiments is the erbium-doped fiber amplifier. In the mid of 1980's, the EDFA was invented and revolutionized fiber-optical transmission systems providing a solution capable of amplifying signals in the optical domain [60, 61] and thus allowing a significant increase in the maximum transmission distance. Fig. 3.2 details the principle of EDFA process with stimulated and spontaneous emission.

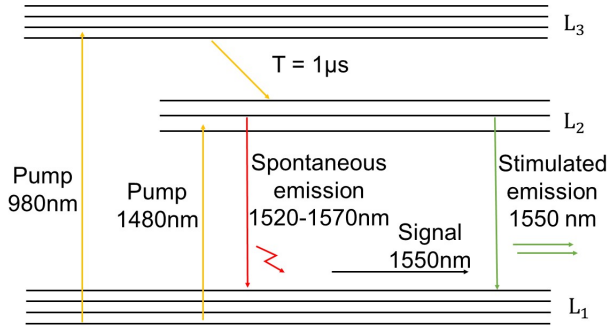

Figure 3.2 – Transitions involved in EDFA amplification.

The EDFA is constructed from a SMF fiber doped with the rare-earth element erbium pumped by semiconductor lasers emitting at 980 nm or 1480 nm. EDFA uses stimulated emission to amplify the transmitted optical signals and the principle is based on exciting Erbium ions Er^{3+} to higher energy level. At 980 nm, erbium ions from the ground level L_1 are excited into the energy state L_3. The life-time of Er^{3+} in L_3 is about 1 µs. After that, erbium ions "fall" into metastable level L_2. The pump can also work at 1480 nm to excite Er^{3+} ions directly into energy state L_2. This phenomena is called population inversion because the number of atoms in the high energy level is higher than those in the low energy level. The optical signal passing through EDFA excites Er^{3+} ions to return into energy level L_1. This return is accompanied with photons emission in the range of 1520 nm to 1570 nm wavelength. This process is known as stimulated emission. Generated photons due to stimulated emission have the same frequency, phase and polarization as the signal and are responsible for signal amplification.

Unfortunately, stimulated emission is accompanied by spontaneous emission. In fact, as the electrons have a finite excited state life-time, some of the electrons return spontaneously to the ground state L_1 and emit photons with random phases. Some of these photons propagate in the direction of the signal as noisy photons and they are also amplified. This

process is called amplified spontaneous emission (ASE) and the generated noise is thus designated ASE noise. The ASE noise reduces the transmission distance and the amount of added ASE noise can be described by the optical signal-to-noise ratio.

3.1.1.2 Sampling Frequency Offset

sampling frequency offset (SFO) refers to a mismatch between the frequencies of the sampling clocks of the digital-to-analog converter at the transmitter and the analog-to-digital converter at the receiver. In practice, the sampling clocks of the transmitter and the receiver are offset by a few parts per million [62], which can cause major deterioration in optical transmission systems if not properly compensated for.

3.1.1.3 IQ Imbalance

In-phase and quadrature imbalance (IQ imbalance) comes from either the transmitter side due to incorrect bias-points settings in the modulator and imperfect splitting ratio of couplers in the IQ modulator structure or the receiver side caused by imperfect splitting ratio on photodiodes responsivity mismatch, on miss-adjustment of the SOPs in a polarization-diversity receiver [63]. This will destroy the orthogonality between the two received channels. Indeed, as depicted in Fig. 3.3, Tx and Rx-IQ imbalances cause the constellation to change from a square to rectangles or parallelograms and contribute to performance degradation. Hence, additional digital signal processing is required to compensate for this effect.

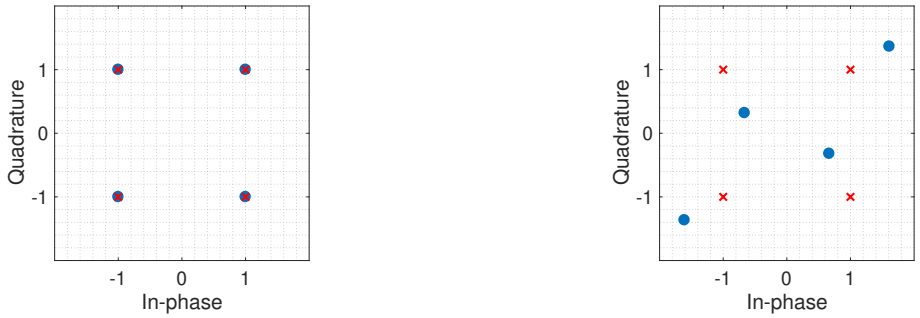

(a) Undistorted (b) Tx and Rx IQ imbalance

Figure 3.3 – Effect of amplitude and phase imbalance at Tx and Rx sides on the QPSK constellation.

3.1.1.4 Carrier Frequency Offset

Regarding coherent detection, it may be either homodyne or intradyne detections [64, 65]. In so-called intradyne detection, the LO frequency does not match the frequency of the received carrier wave. In this case, there exists a frequency mismatch between the carrier frequency and the frequency of the LO of the order of a few hundred MHz, results in carrier frequency offset impairments. Thus, the intermediate frequency is not necessarily zero and the only requirement is that the intermediate frequency needs to be less than $1/T$. Subsequently, after ADC, a linear phase rotation of the received samples appears.

3.1.1.5 Laser Phase Noise

Laser phase noise does not come only from spontaneously emitted photons that randomly change the phase of the optical field but also from the effect of carriers that change the length of the optical path, due to gain or refractive index fluctuations, and therefore the phase of the optical field changes. The amount of phase noise is characterized by the linewidth, as modeled as a Wiener process

$$\theta_i = \theta_{i-1} + \Delta_n, \tag{3.2}$$

where θ_i is the phase noise of the i^{th} symbol and Δ_i is an independent and identically distributed Gaussian random variable with zero mean and variance given as ${\sigma_\theta}^2 = 2\pi\Delta f T$, where Δf is the linewidth of the laser and T is the symbol period [66]. When using a coherent receiver, the phase noise is expressed as the mixing of the free running signal and local oscillator (LO) lasers and $\Delta f = \Delta f_{\text{sig}} + \Delta f_{\text{LO}}$ [67]. As a matter of fact, values of laser linewidth are 1 to 5 MHz for distributed feedback (DFB) lasers and 0.1 to 0.2 MHz for external cavity laser (ECL). Carrier synchronization is required at the receiver, as in coherent system, information is coded in the phase of the signal.

3.1.2 Propagation Impairments

While propagating over the optical fiber, the phase, amplitude and polarization of the signal are altered due to propagation effects. Such distortions could be divided into linear and nonlinear categories. Chromatic dispersion and polarization mode dispersion are two important limiting factors for long haul high bit rate transmission systems and are classified as linear impairments. Also, there exist nonlinear distortions mostly induced

by the Kerr effect.

3.1.2.1 Fiber Loss

The power of an optical waveform decreases while travelling through optical media due to material absorption, Rayleigh scattering, fiber splicing, dirt in the connectors, etc [68]. Fiber loss is described by the parameter of α which reflects the attenuation in power of optical signal during propagation and can be expressed by

$$P_{out} = P_{in}e^{-\alpha z}, \tag{3.3}$$

where z is the transmission distance, P_{in} and P_{out} design the powers at the input and output of the fiber span.

The attenuation, defined in units of decibels per kilometer (dB/km), depends on the carrier wavelength and it is typically around 0.2 dB/km at 1550 nm and reaches recent records (0.149 dB/km at 1550 nm [69, 70]).

Despite this development, the signal power decreases over long distances and the received signal level will be too low for appropriate detection. Hence, optical amplifiers are necessary to increase the power of optical signals periodically over the transmission length. Today's experiments and commercial systems commonly use the EDFA [71]. However, optical amplifiers result in the generation of ASE, which can be modeled as AWGN [71].

3.1.2.2 Chromatic Dispersion

When light travels through optical fibers, chromatic dispersion (CD) phenomenon occurs. Since an optical fiber is a dispersive medium, a variation in the phase and groupe velocity of light according to wavelength occurs. This causes optical signals to broaden when traveling through an optical fiber, possibly resulting in pulse overlapping.

More precisely, chromatic dispersion derives from material dispersion and waveguide dispersion. Material dispersion is due to wavelength dependency of refractive index. Waveguide dispersion is caused by the structure and the geometric properties of the optical fibers.

When considering only chromatic dispersion impairment, or in other words, neglecting nonlinearity and fiber loss (i.e. $\alpha = 0$ and $\gamma = 0$), the Eq. 3.1 could be modeled by

$$\frac{\partial \vec{\mathbf{E}}(z,t)}{\partial z} = -j\frac{\beta_2}{2}\frac{\partial^2 \vec{\mathbf{E}}(z,t)}{\partial t^2}. \tag{3.4}$$

In the spectrum domain, the solution of Eq. 3.4 is given by

$$\vec{\tilde{\mathbf{E}}}(z,\omega) = \vec{\tilde{\mathbf{E}}}(0,\omega)e^{\left(j\beta_2\omega^2 z/2\right)}. \tag{3.5}$$

Since the dispersion parameter $D = -\frac{2\pi c}{\lambda^2}\beta_2$, where c is the velocity of light and λ is the operating wavelength, equation in Eq. 3.5 can also be expressed as

$$\vec{\tilde{\mathbf{E}}}(z,\omega) = \vec{\tilde{\mathbf{E}}}(0,\omega)e^{\left(j\frac{D\lambda^2 z}{4\pi c}\omega^2\right)}, \tag{3.6}$$

where $\tilde{\mathbf{E}}(z,\omega)$ represents the Fourier transform of the time domain waveform of the envelope $\mathbf{E}(z,t)$. Based on Eq. 3.6, chromatic dispersion can be modeled as a linear all-pass filter. The amplitude of the waveform frequency is equal to one while a frequency dependent phase shift is introduced.

The impulse response of the channel can by expressed by applying the inverse Fourier transformation as

$$\mathbf{E}(z,t) = \sqrt{\frac{1}{j2\pi\beta_2 z}}e^{\frac{jt^2}{2\beta_2 z}}. \tag{3.7}$$

In Eq. 3.7, the impulse response is infinite in time and non-causal. The real and imaginary part of this response are depicted in Fig. 3.4.

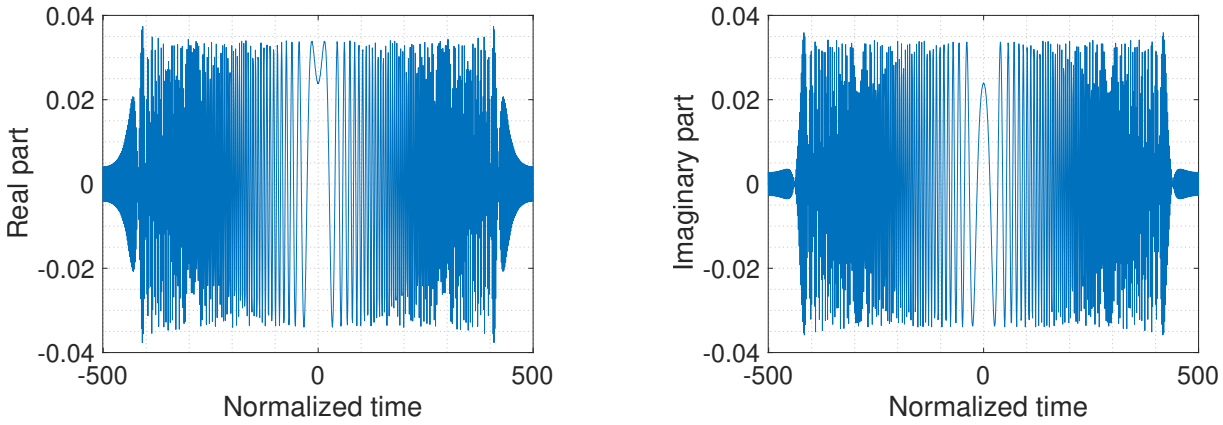

Figure 3.4 – Real and imaginary part of chromatic dispersion in time domain corresponding to 17000 ps/nm of accumulated chromatic dispersion over 10^5 km.

The effect of CD on the constellation diagram for 4-QAM and 16-QAM modulation formats and for different distances is shown in Fig. 3.5. In this simulation, 1000 symbols are generated and the dispersion parameter D is taken equal to 17 ps/km.nm. From these

figures, we show that the effect of CD scatters the points in the constellations. Additionally, the CD results in serious inter-symbol interference with long fiber length.

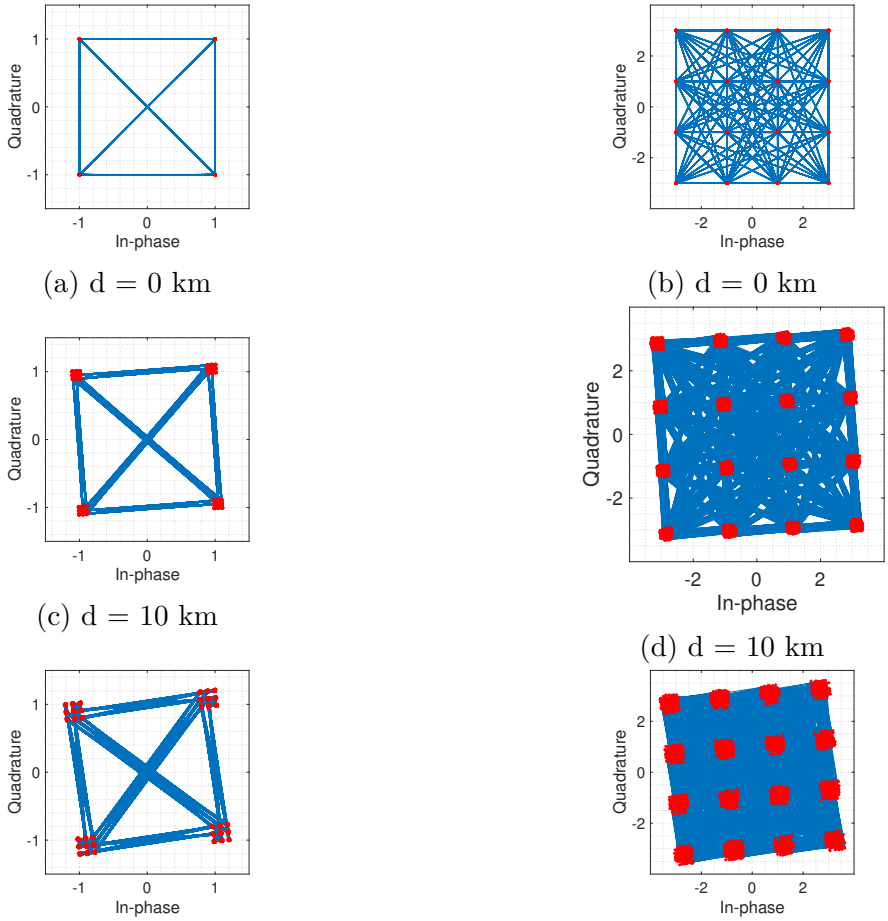

(a) d = 0 km (b) d = 0 km

(c) d = 10 km (d) d = 10 km

(e) d = 20 km (f) d = 20 km

Figure 3.5 – Effect of CD on QPSK (left) and 16-QAM (right) constellation diagrams using SRRC pulse-shaping filter (with $\beta = 75\%$).

In Table 3.1, we report the values of the linear properties of several well-known commercially available fibers, namely standard single mode fiber which is the major deployed fiber, large effective area fiber, teralight, truewave, and the pure silica core fiber. The CD and attenuation values are given at the reference wavelength of 1550 nm.

Dispersion can be compensated in the optical domain either using dispersion compensating fibers (DCFs), fiber Bragg gratings (FBG) [72], etc. The dispersion compensating fiber has the opposite sign of β_2 compared to the single-mode fiber. To prevent additional nonlinearities or losses induced by optical CD compensation modules, coherent transmission system digital signal processings (DSPs) include CD compensation blocks

Fiber type	ITU standard	CD (ps/nm.km)	PMD (ps/$\sqrt{\text{km}}$)	loss (dB/km)	Effective area (μm^2)
SSMF	G.652	16-17	<0.08	0.19	80
LEAF	G.655	4.2	<0.04	0.21	72
Teralight	G.655	8	<0.04	0.21	62
Truewave	G.655	6	<0.04	0.21	55
PSCF	G.654	20	<0.04	0.16	80-115

Table 3.1 – Typical values of CD, PMD, loss and effective area for different fiber types

which consist of digital filters in the receiver. In fact, one of the issues with the use of DCFs is that they are relatively lossy and nonlinear (compared to transmission fibers). Furthermore, one of the features of coherent detection is that it maps the electric field to the electrical domain without loss of information on the phase as for direct-detection. Hence, dispersion compensation can be done in the electrical domain which in turns means that the existing loss and nonlinearity of DCFs can be alleviated. Later on, we present chromatic dispersion compensation via appropriate and optimized digital filters.

3.1.2.3 Polarization Mode Dispersion

Polarization-mode dispersion (PMD) is a stochastic effect that limits optical transmission systems. PMD is caused by fiber birefringence, which leads to the presence of a polarization dependent propagation constants.

The birefringence comes from the imperfections in the core geometry along the fiber occurred during the manufacturing process and external mechanical or thermal applied constraints. The core asymmetry means that the refractive index is not the same in two polarization states resulting in a slow and fast axis. Consequently, the two orthogonal polarizations propagate at different group velocities, resulting in pulse broadening.

As depicted in Fig. 3.6, for a uniform birefringence along a short fiber, the projections of the field onto the two axes of the polarization basis propagate through the fiber at different velocities due to the difference in the refractive indices.

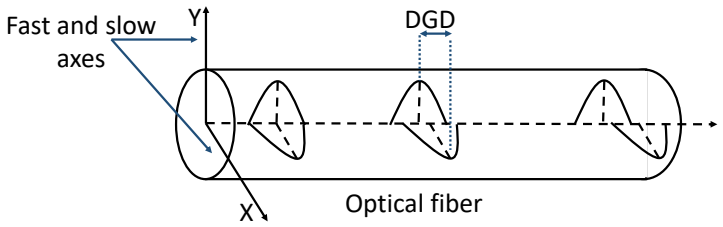

Figure 3.6 – DGD effect of SMF fiber.

Birefringence introduces a delay $\Delta\beta_1$ between the two modes referred to as differential group delay (DGD), which can be calculated by

$$\Delta\beta_1 = \left|\beta_{1,X} - \beta_{1,Y}\right| = \frac{\omega}{c}|n_X - n_Y|\,, \tag{3.8}$$

where n_X and n_Y are the effective refractive indices for the two orthogonal polarizations. The DGD broadens the transmitted signal and introduces PMD effects causing inter-symbol interference modeled as

$$\text{PMD} = \frac{\mathbb{E}(\Delta\beta_1)}{\sqrt{L}}, \tag{3.9}$$

where L is the distance of the transmission and $\mathbb{E}(\,\cdot\,)$ denotes the statistic average.

Poole [73], and Foschini et al. [74], showed that the DGD $\Delta\beta_1$ is a random process following a Maxwell distribution. In fact, for long fibers, birefringence is no longer constant. Axes and birefringence values fluctuate along the fiber length. A link can be modelled as a concatenation of uniform birefringent sections with rotations of the axes between sections.

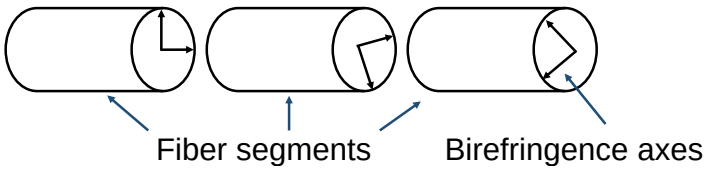

Figure 3.7 – Long fiber modeled as a concatenation of birefringent segments.

The PMD parameter for a high quality fiber has a typical values of order of 0.05 ps/$\sqrt{\text{km}}$ and of 2 ps/$\sqrt{\text{km}}$. for a poor quality old fiber.

The statistical nature of PMD makes compensation very challenging in the optical domain, whereas, in the DSP building blocks, PMD can be compensated for with a 2×2 multiple-input multiple-output (MIMO) adaptive equalizer.

3.1.2.4 Polarization Dependent Loss

As the optical signal passes through the fiber link, it suffers optical power loss along different polarization axes due to polarization dependence in the optical component such as couplers, isolators and EDFAs. This loss is known as polarization-dependent loss and can lower the signal-to-noise ratio and reduce the orthogonality between polarizations, deteriorating the signal quality and inducing penalty [75, 76].

PDL is accumulated over signal propagation through optical component and is expressed

in decibels by the ratio between the highest and lowest gains of the system i.e.

$$\mathrm{PDL} = 10\log_{10}\left(\frac{1+\vartheta}{1-\vartheta}\right), \tag{3.10}$$

where $(1+\vartheta)$ and $(1-\vartheta)$ represent the highest and lowest power gain of a generic optical element, and ϑ is the attenuation.

3.1.2.5 Fiber Nonlinearity

The coefficient γ given in Eq.3.1 causes nonlinear signal distortion due to the optical Kerr effect [77]. Since the refractive index of optical fibers changes according to the intensity of light, the overall performance of the fiber-optic system will be deteriorated by this effect. Hence, the power launched at the transmitted side is crucial to know whether the dispersion or the nonlinearity will arise. In the absence of CD and for loss-less fiber (i.e. $\beta_2 = 0$ and $\alpha = 0$), Eq. 3.1 is simplified to

$$\frac{\partial\vec{\mathbf{E}}(z,t)}{\partial z} = j\ \gamma\ \left|\vec{\mathbf{E}}(z,t)\right|^2 \vec{\mathbf{E}}(z,t). \tag{3.11}$$

The solution of this equation is

$$\vec{\mathbf{E}}(L,t) = \vec{\mathbf{E}}(0,t)e^{\left(j\ \gamma\ \left\|\vec{\mathbf{E}}(0,t)\right\|^2\ L_{\text{eff}}\right)}, \tag{3.12}$$

where L is the length of the fiber and $L_{\text{eff}} = \frac{1-e^{(\alpha L)}}{\alpha}$, is the length where fiber nonlinearities were effective. As illustrated in the equation above, the signal amplitude of one waveform modulated on a signal wavelength remains unchanged in the time domain while a nonlinear phase shift $\phi_{NL} = \gamma\ \left\|\vec{\mathbf{E}}(0,t)\right\|^2 L_{\text{eff}}$ is introduced. The chirp increases in magnitude with the transmission distance. Thus, new frequency components are continuously generated as the pulse propagates down the fiber. This effect is called self-phase modulation (SPM).

Furthermore, in wavelength-division multiplexing systems, the nonlinear phase shift of a pulse depends on the light intensity of co-propagating pulses. Thus, a propagating optical signal not only modifies its own phase but also the phase of other neighboring co-propagating signals. This phenomenon is called cross phase modulation (XPM). XPM causes spectral broadening, timing jitter and amplitude distortion in time domain.

four wave mixing (FWM) is another phenomenon where three co-propagating subwaves with three frequencies ω_1, ω_2, ω_3 generate a fourth wave with frequency ω_4. Generally,

FWM is less critical using SMF in transmission link as the dispersion of the fiber is predominant.

Finally, SPM, XPM and FWM are grouped among deterministic signal-signal interactions. They can result in additive Gaussian noise, phase variation and phase and polarization rotations [78, 79].

Table 3.2 – Classification of nonlinearities in optical fibers. Intra-channel and inter-channel stand for nonlinearities occurring within or between WDM channels, respectively. SPM: self-phase modulation; (I)XPM: (intra-channel) cross-phase modulation; (I)FWM: (intra-channel) four-wave mixing; MI: modulation instability; NL: nonlinear.

	Intra-channel	Inter-channel
Signal-Signal	SPM: -Pulse SPM -IXPM -IFWM -Scattering effects	WDM nonlinearities: -XPM -FWM -Scattering effects
Signal-Noise	NL phase noise: -SPM induced Parametric amplification: -MI	NL phase noise: -XPM-induced

Other effects known as signal-noise and noise-noise interactions are derived from co-action between the ASE and Kerr nonlinearities [80] (see Table 3.2). These interactions are stochastic and result in nonlinear phase noise which deteriorates the system performance [81]. It is essential to understand the origin of non-linearities that can be observed on received signals from experimental systems whereas throughout this thesis, we consider only the linear impairments generated by transmission along the optical fiber.

3.2 Impairments Mitigation

In the framework of a coherent receiver, the goal of digital signal processing is to compensate for the propagation linear impairments as well as the circuit imperfections. The different algorithms introduced in the literature to make the transmission robust to distortions and disturbances of the optical channel could be handled in two different ways; either a joint processing dealing with all the impairments or by splitting the processing

into several steps and each step will only focus on one impairment. Both digital receiver architectures found in the literature are considered and detailed in the next sections.

3.2.1 One Impairment Per Stage

Once the receiver matched filtering is applied, signal processing steps dedicated to eliminate each channel or system imperfection are discussed in separate sections. The order of the steps in Fig. 3.8 is proposed in this section but this sequencing is not compulsory.

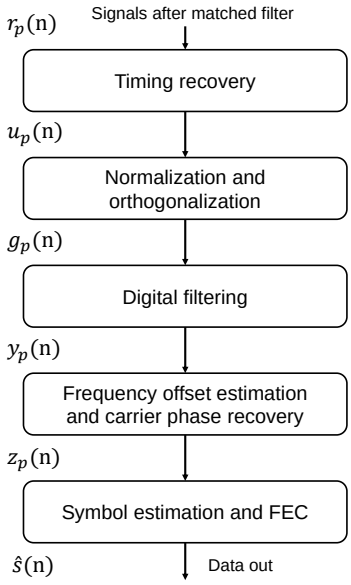

Figure 3.8 – Receiver DSP blocks.

3.2.1.1 Timing Recovery

In a digital communication system, the received signal must be sampled periodically at the symbol rate and more precisely at the time instant $t_m = mT + \tau T$, where T is the symbol interval, $m \in \mathbb{N}$ and τT is a time delay that is due to a time shift between transmitter and receiver clocks, τ is the fractional delay and its range is between $[-0.5, 0.5]$.

In fact, in real communication systems, there always exists a small difference between the frequencies of the two separate and free running clocks of the transmitter and the receiver. The mechanism of controlling the sampling process is called timing recovery or symbol synchronization. If the time delay is well compensated, the choice of sampling instant within the symbol interval is called the timing phase.

Note that different solutions have been proposed for timing recovery. At first, a distinction has to be made between analog techniques based on phase locked loops with different phase comparators [82] and digital algorithms working on sampled data.

In this manuscript, the consideration is on various algorithms that can be performed on the received signal to handle the symbol synchronization process. Generally, digital timing recovery comprises two basic steps: timing error detection and timing error correction. Timing error detection could be dealt either with data-aided or non-data-aided algorithms. Data-aided approaches rely on the transmission of additional symbol clock information at the expense of bandwidth allocation dedicated for useful data information. On the other hand, non data-aided techniques do not require prior knowledge about the timing and demonstrate blind synchronization effectiveness. In this thesis, only non-data aided approaches are considered. Regarding timing error correction, interpolation filters are adopted for this purpose. In the following, we treat feed-forward and feedback methods for timing recovery techniques.

Feed-Forward Approaches

As depicted in Fig. 3.9, two main steps are required in the feed-forward structure; the estimation of the timing error which serves to calculate the input signal phase shift associated with a time delay followed by the timing corrector that yields the interpolation of the signal according to the estimated timing phase shift.

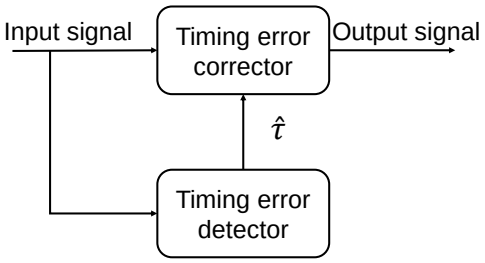

Figure 3.9 – Feed-forward timing recovery scheme.

Time phase estimation is derived by exploiting the phase information of the second-order cyclic statistic which is relevant for linear modulated signals with arbitrary constellation shape [83]. The algorithm presented in [83] is developed for estimating both frequency offset and symbol timing recovery. From [83], Oerder and Meyr derive in [84] a new estimation approach dedicated only to the fractional delay called square timing recovery.

Indeed, the block diagram of square timing timing error detector (TED) is depicted in Fig. 3.10.

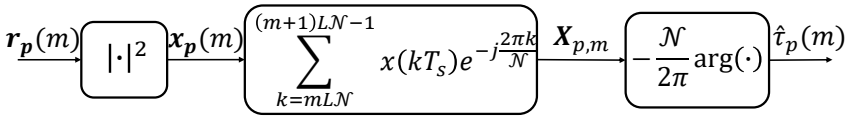

Figure 3.10 – Block diagram of the square timing recovery algorithm.

Where $\hat{\tau}_p$ is the estimated timing error on the p polarization, $\mathcal{N}$ is the oversampling rate with respect to the Nyquist frequency, L is the number of symbols used for the estimation of $\hat{\tau}_p$, T_s is the sampling time and $\mathbf{r_p}(m)$ takes the values $\mathbf{r_p}(m) = r_p(kT_s)$ where $mL\mathcal{N} \leq k \leq (m+1)L\mathcal{N} - 1$ constituting the observation interval of the signal on the p polarization. Thus, each observation is composed of $L\mathcal{N}$ samples.

The squared elements of the observation interval contains a spectral component at $\frac{1}{\mathcal{N}T_s}$, which can be used in the estimation of the timing error

$$\mathbf{x_p}(m) = x_p(kT_s) \quad \text{with} \quad mL\mathcal{N} \leq k \leq (m+1)L\mathcal{N} - 1, \tag{3.13}$$

where $x_p(kT_s) = \left|r_p(kT_s)\right|^2$. The spectral component is extracted by computing the complex Fourier coefficients

$$\mathbf{X}_{p,m} = \sum_{k=mL\mathcal{N}}^{(m+1)L\mathcal{N}-1} x_p(kT_s)e^{-j\frac{2\pi k}{\mathcal{N}}}. \tag{3.14}$$

Then, the argument of Fourier transform gives the timing error estimate within a factor of $-\frac{\mathcal{N}}{2\pi}$ as

$$\hat{\tau}_p = -\frac{\mathcal{N}}{2\pi}\arg \mathbf{X}_{p,m}. \tag{3.15}$$

It can be shown that the square timing recovery algorithm demonstrates its effectiveness for phase-shift keying (PSK) and QPSK modulation formats where the signal samples which alternate between positive and negative values with approximately the same amplitude. In this case, the squared 4-QAM signal produces a binary phase-shift keying. The QPSK has no discrete spectral components, after being squared, it has two strong spectral components, which can be used for synchronization. Nevertheless, the square timing recovery is less effective for higher order modulation formats. Moreover, the algorithm assumes a constant timing phase for all the input observation samples in the block which means it is less effective when there is a variable timing phase between the clocks. In fact, to track fluctuations of the synchronization, feed-forward involves dividing the received

signal into observation intervals that are short enough to make the approximation that the timing shift is constant.

The square timing recovery algorithm was implemented and tested numerically. QPSK modulation formats of 10^4 symbols were generated, up-sampled by a factor $\mathcal{N} = 8$ and corrupted by added AWGN with an SNR of 20 dB. Next, a variable fractional delay was introduced. In this case, the timing offset drifts over time.

The resulting feed-forward estimator of the fractional delay after applying the square timing recovery at the output of the blocks is shown in Fig. 3.11.

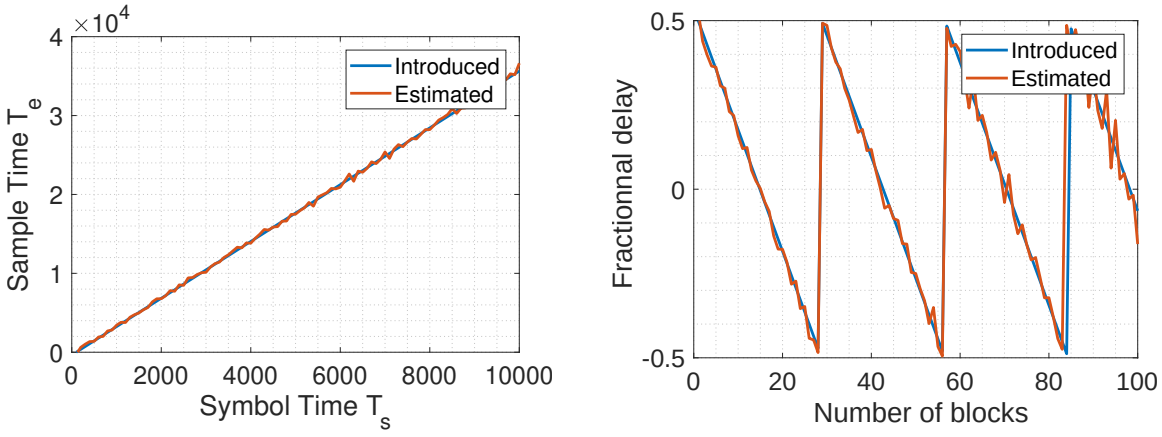

Figure 3.11 – (a) Timing shift evolution, (b) fractional delay evolution.

As demonstrated in Fig. 3.11(a), the timing shift is very large. As the oversampling factor is 8, $T = 8\,T_s$, and the timing shift is 3.6% of the symbol duration. The square timing recovery algorithm estimation shows a successful track of the timing shift. Such an estimate is converted to a sawtooth function, so that the compensation of the timing offset would be possible using fractional interpolation. The role of the sawtooth function is to unwrap the data into a defined interval. The subsequent result is depicted in Fig. 3.11(b).

As depicted in Fig. 3.12(a), the QPSK constellation suffers from inter-symbols interference if timing error is not compensated. Once this fractional delay is correctly and iteratively estimated and compensated using interpolation filters, the resulting QPSK constellation is inter-symbols interference free as depicted in Fig. 3.12(b).

From a complexity point of views, the algorithm does no require performed hardware

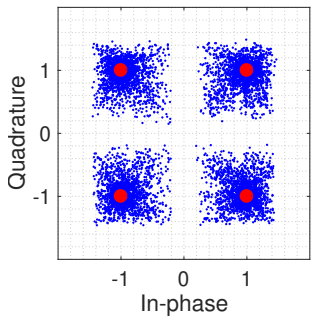

(a) QPSK corrupted with timing offset

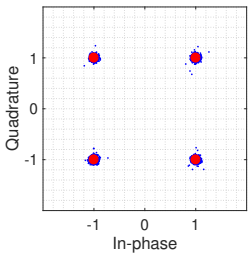

(b) Compensated timing offset

Figure 3.12 – QPSK constellation (a) with variable fractional timing offset, (b) with compensated fractional timing offset.

resources for an oversampling value of $\mathcal{N} = 4$. In fact, in this case, Eq. 3.15 becomes

$$\frac{\hat{\tau}_p}{\mathcal{N}} = -\frac{1}{2\pi} \arg\left(\sum_{k=0}^{L-1} \cdot \sum_{n=0}^{3} x_p(kT_s) j^n \right) \tag{3.16}$$

As expressed by Eq. 3.16, there is no need to perform Fourier transformation and exponential multiplication are reduced to simple addition and subtraction operations (see Fig. 3.13).

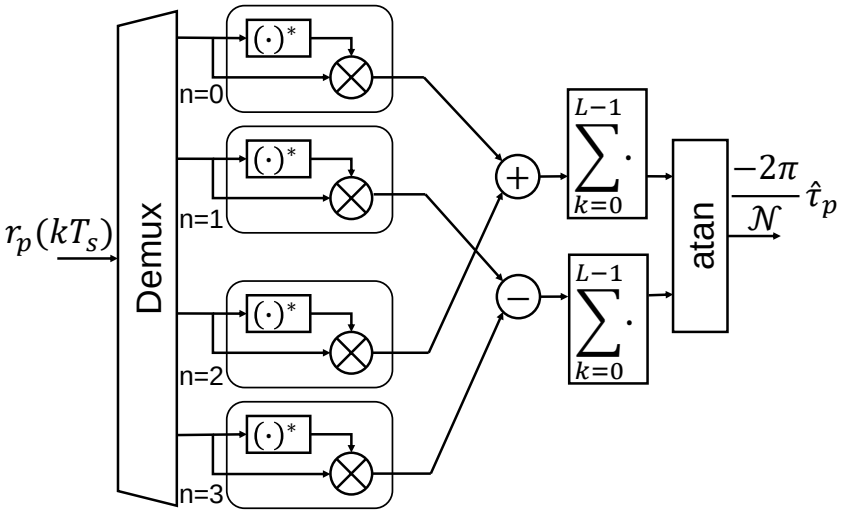

Figure 3.13 – Implementation of the square timing recovery algorithm for an oversampling of 4

Finally, it is important to mention that the square timing recovery algorithm requires at least four samples per symbol for proper operation. Generally, such method is relatively

faster than feedback algorithm in performing timing estimation. In what follows, we introduce some of the typical feedback schemes.

Feedback Approaches

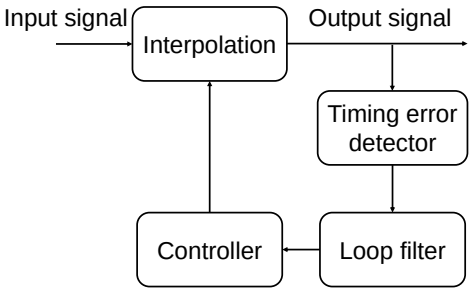

Figure 3.14 – Feedback timing recovery scheme.

The architecture of a feedback timing recovery scheme is depicted in Fig. 3.14. Several algorithms are popular to perform timing synchronization in a feedback structure [85, 86] among which we will introduce the early-late timing recovery and Gardner algorithm [87]. In a feedback timing recovery scheme, the input signal is interpolated through the factor of interpolation provided by the controller output. The latter uses the estimated timing phase generated by the loop filter to determine the interpolation factor. The loop filter updates the current estimated timing phase of the symbol based on the calculated timing error and the previously estimated timing phase. The timing error generates an error signal that is proportional to the difference between the actual and the estimated timing offset. The structure of the loop filter varies depending on the need of simplicity, speed and performance.

Next, we will detail the two basic steps of a feedback method which are the timing error detector and the interpolation.

1. Timing Error Detector

In this section, two main timing error detectors namely the early-late algorithm and the Gardner approach are introduced. The important performance evaluation parameter of these timing error detectors is the self-noise. The self-noise of the timing error detector is defined as a nonzero value obtained when there is no data transition, even at the optimum sampling instant. Early-late method has more self-noise when compared to the Gardner scheme. Also, the S-curves of these tools are outlined to gain an insight on their behaviors.

Early-Late Algorithm

The early-late method [88] relies on the property that the absolute value of the signal amplitude is at its highest at the optimal sample point when averaged over a number of symbols (see Fig. 3.15).

Assuming a timing shift of the received signal by $\tau(m)$, the early-late algorithm requires samples of the signal at three different points: $r_p(mT + \tau(m) - \delta T)$, $r_p(mT + \tau(m))$ and $r_p(mT + \tau(m) + \delta T)$. The values $r_p(mT + \tau(m) - \delta T)$ and $r_p(mT + \tau(m) + \delta T)$ can be interpolated from the nearby sample $r_p(mT + \tau(m))$.

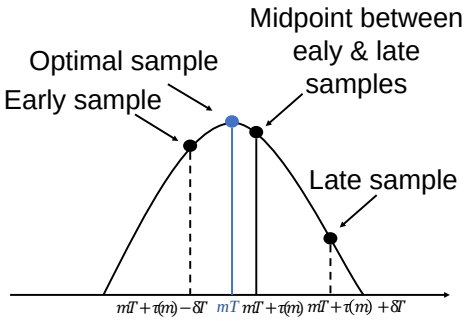

Figure 3.15 – Feedback timing recovery scheme.

Based on the required three samples, the timing error is calculated by tacking the difference between the absolute values of the early and late samples. The resulted output is fed to a loop filter to smooth the noise corrupting the signal samples. This loop filter plays the role of a low-pass filter and is characterized by its relatively narrow bandwidth compared to the symbol rate $1/T$.

The value of the bandwidth is set with respect to the variation of the timing drift. For instance, a narrow-band loop is preferred when the channel propagation delay is constant and the timing offset does not drift with time. Thus, a narrow bandwidth provides more averaging over the additive noise and better estimation of the sampling samples. On the other hand, if the channel propagation delay is varying and/or the timing offset is also drifting with time, the loop bandwidth must be increased at the expense of a reduced noise rejection but faster tracking of time offset variations.

If the sampled sampling is distinct of the optimal value, then the error signal at the output of the low-pass filter is non-zero and the provided estimate is either retarded or advanced depending on the sign of the error.

The early-late algorithm discussed above approximates the maximum likelihood timing recovery estimator as given by Eq. 3.17

$$\hat{\tau}_p(m+1) = \hat{\tau}_p(m) + \mu e_p(m), \tag{3.17}$$

where $e_p(m)$ is the early-late timing error at the m^{th} instant, given for non-data aided decision directed approach by

$$e_p(m) = r_p(mT + \tau(m)) \left(r_p(mT + \tau(m) + \delta T) - r_p(mT + \tau(m) - \delta T) \right). \tag{3.18}$$

Because a sample rate of a 2 samples/symbol is commonly used, $\delta = 0.5$ is a popular choice. μ is the step size, ant its value is related to the loop bandwidth B_L as

$$B_L T = \frac{\mu A}{2(2 - \mu A)},$$

where A is the slope of the S-curve when the timing error is equal to zero. Note that the S-curve of the early-late algorithm is obtained by computing the average of the timing error for a constant timing offset τ in Eq. 3.18 through N symbols as

$$\tilde{e}_p(m) = \frac{1}{N} \sum_{i=0}^{N-1} e_p(m - i).$$

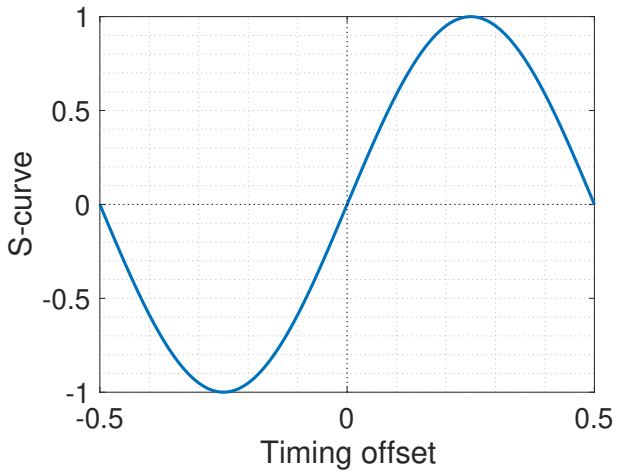

Figure 3.16 – S-curve for the non-data aided early-late timing error detector.

Fig. 3.16 outlines the S-curve of non-data aided early and late timing error detector.

This S-curve has been calculated for QPSK constellation diagram using a square-root raised-cosine pulse shape with a roll-off of 0.5 and an oversampling ratio of 2.

The timing recovery estimator expressed in Eq. 3.17 is calculated while introducing a fixed timing offset of -0.4. The curve of the offset estimation along with the subsequent in-phase component of the QPSK constellation diagram are depicted in Fig. 3.17. As outlined in Fig. 3.17(a), the in-phase component of the QPSK is widely dispersed as the algorithm has not reached yet its steady-state target, but as the method approaches its convergent point, the estimate of the in-phase components converges well.

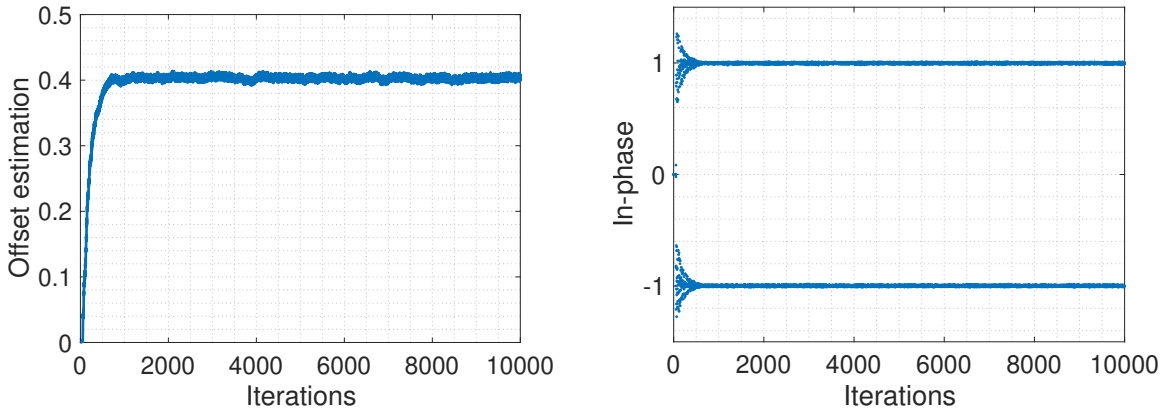

(a) (b)

Figure 3.17 – Estimated timing offset $\hat{\tau}$ and subsequent effect on the constellation diagram's in-phase component using early-late timing error detector for QPSK constellation.

Gardner Algorithm

The Gardner algorithm [89] aims to find the zero crossing in the eye diagram of the in-phase (or quadrature) component of the received signal. It operates at 2 samples per symbol and performs on BPSK or QPSK constellation signals. The Gardner timing error signal is given by

$$e_p(m) = r_p\left((m-1/2)T + \tau(m)\right)\Big(r_p((m-1)T + \tau(m)) - r_p(mT + \tau(m))\Big)\,. \tag{3.19}$$

The timing error detector $e_p(m)$ aims to adjust the estimated timing offset by the loop filter and the controller. Its value is negative when sampling occurs too early, but when sampling is too late, its value is positive and it is null at the optimal position.

The advantage of the Gardner algorithm is that it is rotationally invariant. This means that for a fixed $\hat{\tau}$, $e_p(m)$ is independent of any carrier phase rotation. Hence, the Gardner timing error detector is suited for achieving timing synchronization before carrier phase synchronization in systems using QPSK or BPSK modulation formats.

On the other hand, as the optimal sample is at half a symbol of the zero-crossing position, the two points on each side of the middle point need to have approximately the same amplitude. However, for M-QAM ($M \geq 16$) signals, it is no longer the case which makes the Gardner algorithm less suitable for these kinds of modulation formats.

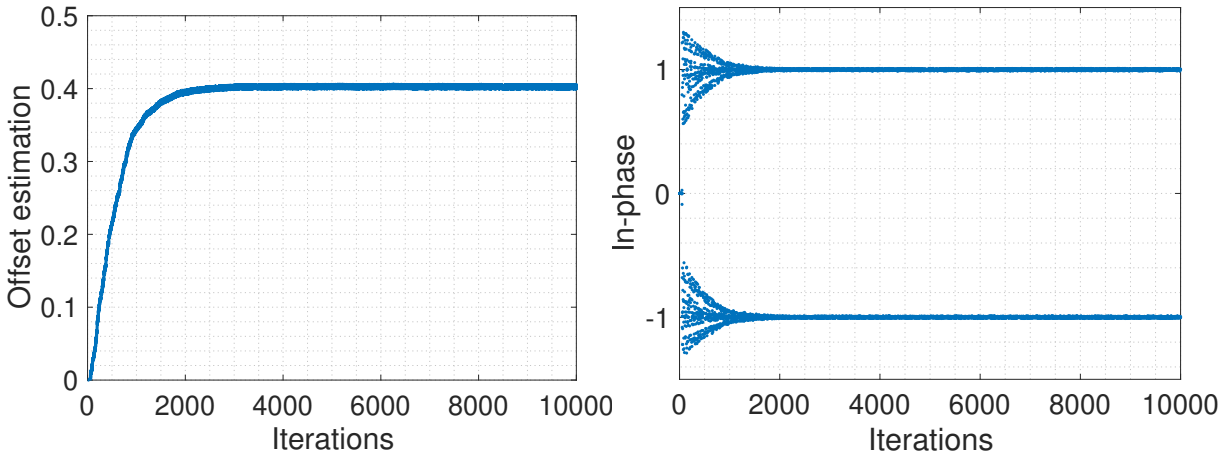

(a) (b)

Figure 3.18 – Estimated timing offset $\hat{\tau}$ and subsequent effect on the constellation diagram's in-phase component using Gardner timing error detector for QPSK constellation.

Fig. 3.18 presents the trajectory of the estimated offset value using the Gardner approach as well as the in-phase component of the QPSK constellation. Either with the early-late or Gardner detector, the timing error detector estimates the correct value of the constant introduced timing offset.

Fig. 3.19 outlines a plot of the Gardner detector S-curve. Similarly to that of the early-late detector, the Gardner's S-curve has a sinusoidal shape, is odd and nearly linear about $\tau = 0$.

2. Interpolation

The role of the interpolation is to provide the correct sampling instances if the sampling is not synchronized with the data symbols. The information of the estimated timing samples is driven by the TED and the loop filter introduced in the previous section.

Indeed, the received samples $r_{p_s}(k\,T_s)$ can reconstruct the complete analog signal $r_p(t)$.

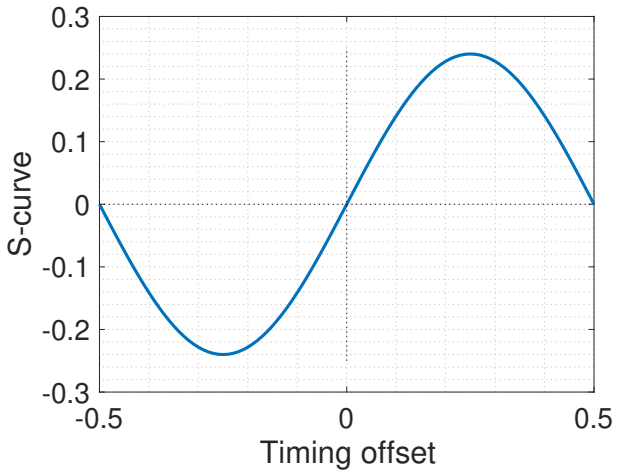

Figure 3.19 – S-curve for the Gardner timing error detector.

Of course, the sampling period T_s is supposed to verify the Nyquist criterion so that the sampling rate $F_s > 2\,B$ where B is the highest frequency present in $r_p(t)$. Thanks to the Nyquist sampling theorem, the signal $r_p(t)$ can be reconstructed exactly at any time τ as

$$r_p(\tau) = \sum_{k=-\infty}^{\infty} r_{p_s}(k\,T_s)\ \mathrm{sinc}(\tau - kT_s). \tag{3.20}$$

For exact value of $r_p(\tau)$, the optimum interpolation filter sinc, which is a low-pass filter, is employed with a sum taken over all time. However, for practical reason, the sum must be taken over a finite time window and the ideal infinite impulse response (IIR) filter sinc implies unacceptable computational burden.

As a consequence, finite impluse response (FIR) filters that approximate the ideal interpolation filter are selected in digital communication application. Interpolation methods in the literature are various and the choice of the interpolation approach depends on the number of data points needed or the required targets such as accuracy, cost and smoothness of the resulting interpolant function.

A typical class of FIR interpolation filters consists in piecewise polynomial filters adopted in this thesis and discussed below. Note that to implement the interpolation filter using polynomial approximation method, we adopt the Farrow structure or the Lagrange method as they are hardware efficient, popular and commonly implemented.

Lagrange Interpolation

Lagrange interpolation constructs a polynomial $f(x)$ to estimate a function that includes all given $N+1$ known samples in the following way. Given a set of $N+1$ known samples $f(x_k)$, $k = 0, 1, 2, \cdots, N$, the problem is to find the unique polynomial $f(x)$ with order N which interpolates the samples. The solution can be expressed as a linear combination of elementary N^{th} order polynomials as

$$f(x) = \sum_{k=0}^{N} l_k(x) f(x_k),$$

where the functions $l_k(x)$ are defined as

$$l_k(x) = \frac{(x - x_0) \cdots (x - x_{k-1})(x - x_{k+1}) \cdots (x - x_N)}{(x_k - x_0) \cdots (x_k - x_{k-1})(x_k - x_{k+1}) \cdots (x_k - x_N)}$$

l_k is a polynomial having zeros at all the samples except for the k^{th} where it takes the value 1.

Lagrange Interpolation theory leads to FIR filters which approximate fractional delays. More explicitly, given a desired fractional delay of Δ, the Lagrange fraction-delay impulse response can be written in closed form as

$$l_\Delta(n) = \prod_{\substack{k=0 \\ k \neq n}} \frac{\Delta - k}{n - k}, \quad n = 0, 1, 2, \cdots, N.$$

For $N = 1$, Lagrange interpolation is reduced to linear interpolation. For higher order N, the filter approximately produces a time delay of the form $(D_{int} + \Delta)T_s$, where $D_{int} = \lfloor \frac{N}{2} \rfloor$ is an integer, Δ is a fractional number (usually $0 \leq \Delta \leq 1$), and T_s is the sampling interval.

In order to demonstrate how an increase in the filter order contributes to the phase delay and the magnitude characteristics, Lagrange fractional-delay filters of the orders $N = 1, 3, 5, \text{and} 7$ are generated with the fixed value of fractional delay of $\Delta = 0.4$.

Fig. 3.20 depicts the Lagrange fractional-delay filter frequency responses. Fig. 3.20(a) shows that the magnitude characteristic maintains its flat frequency behaviour for higher values of the filter order N. It is to be expected that an increase in the filter order should increase the overall delay D of the fractional delay filter. For the N^{th} order FIR filter, we obtain $D = (D_{int} + \Delta)$, and consequently for $N = 1, 3, 5, 7$, and $\Delta = 0.4$, $D = 0.4, 1.4, 2.4$ and 3.4 as Fig. 3.20(b) illustrates.

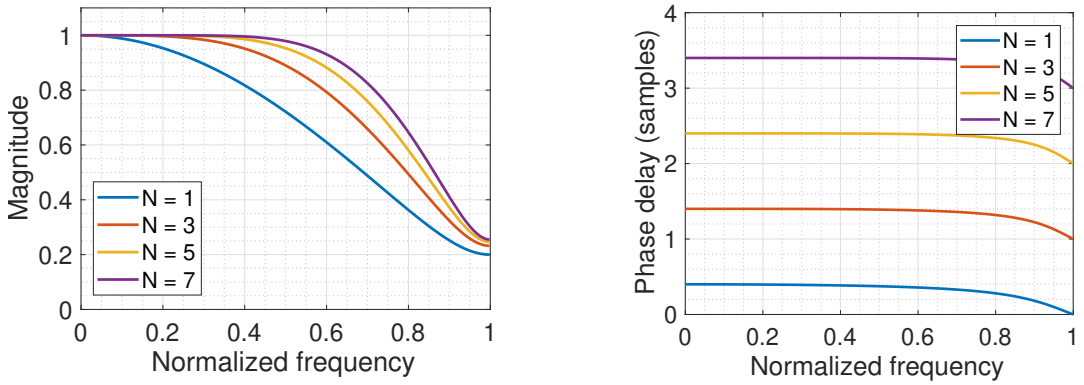

(a) (b)

Figure 3.20 – Lagrange fractional-delay filter frequency response.

Farrow Structure

Farrow structure offers a parametrization of a filter by a single variable Δ. It is suggested that every coefficient of a FIR filter could be expressed as an N^{th}-order polynomial in the variable delay parameter Δ. Fig. 3.21 shows the general Farrow structure.

The main advantage of the Farrow structure is that all the sub-filter coefficients are fixed, the only changeable parameter is the fractional delay Δ, which leads to a less computation intensive implementation. The whole filter structure could be pipelined to lower the intensity calculation during a single clock cycle, therefore allowing the increase of the maximal clock frequency.

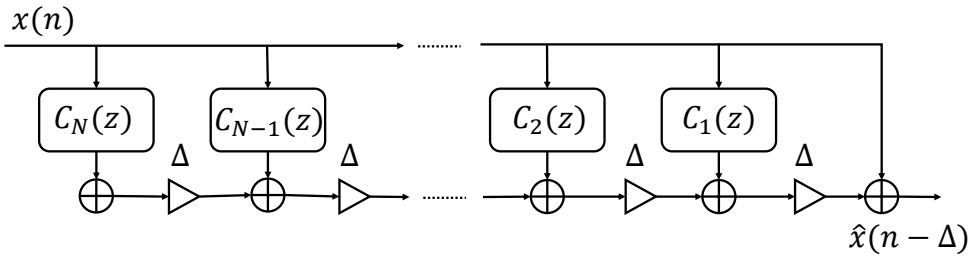

Figure 3.21 – Farrow structure for implementing parameterized filters with multiplications of an adjustable fractional delay Δ and $C_0(z) = 1$.

3.2.1.2 Orthogonalization Algorithms

As discussed in section 3.1.1, IQ imbalance comes from a mismatching between the in-phase and quadrature branches of the optical signals, which results in a loss of orthogonality between the signals components. Such mismatch (in phase and/or gain) can be modeled either in symmetrical or asymmetrical systems [90]. In the symmetrical model, the imbalance is equally introduced on both the I and Q channels, whereas it only appears within the Q channel in the asymmetrical representation. In this thesis, the symmetrical model is adopted. In this case, considering single polarization systems and taking into account the origin of the IQ imbalance (at the transmitter $v = \text{Tx}$, and/or at the receiver $v = \text{Rx}$), we denote by ε_v and φ_v the amount of amplitude and phase error respectively. Hence, in the branch I, the amplitude and the phase mismatch are characterized by $1 + \varepsilon_v$ and φ_v, respectively. In the branch Q, the amplitude and the phase mismatches are given by $1 - \varepsilon_v$ and $-\varphi_v$, respectively.

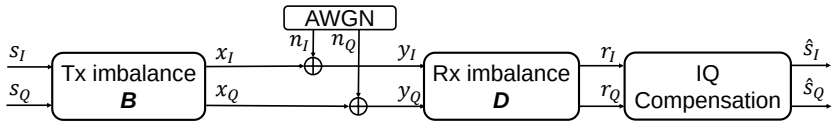

Figure 3.22 – Block diagram of the communication system with Tx and Rx IQ imbalances and Rx compensation.

By noting $s(n) = s_I(n) + js_Q(n)$ the complex envelope of a modulated and unimpaired (source) signal and $x(n) = x_I(n) + jx_Q(n)$ the transmitted signal, the relation between $s(n)$ and $x(n)$, based on Fig. 3.22 is given by

$$\begin{pmatrix} x_I(n) \\ x_Q(n) \end{pmatrix} = \mathbf{B} \cdot \begin{pmatrix} s_I(n) \\ s_Q(n) \end{pmatrix}, \tag{3.21}$$

where

$$\mathbf{B} = \begin{pmatrix} (1+\varepsilon_{\text{Tx}})\cos(\varphi_{\text{Tx}}) & (1-\varepsilon_{\text{Tx}})\sin(\varphi_{\text{Tx}}) \\ (1+\varepsilon_{\text{Tx}})\sin(\varphi_{\text{Tx}}) & (1-\varepsilon_{\text{Tx}})\cos(\varphi_{\text{Tx}}) \end{pmatrix}, \tag{3.22}$$

and $\mathbf{B}$ is defined as the Tx imbalance matrix. Similarly, the IQ imbalanced signal at the receiver part is expressed by

$$\begin{pmatrix} r_I(n) \\ r_Q(n) \end{pmatrix} = \mathbf{D} \cdot \begin{pmatrix} y_I(n) \\ y_Q(n) \end{pmatrix}, \tag{3.23}$$

where $r(n) = r_I(n) + jr_Q(n)$ is the signal that needs to be compensated, and $\mathbf{D}$ is the Rx imbalance matrix given by

$$\mathbf{D} = \begin{pmatrix} (1+\varepsilon_{\mathrm{Rx}})\cos(\varphi_{\mathrm{Rx}}) & (1+\varepsilon_{\mathrm{Rx}})\sin(\varphi_{Rx}) \\ (1-\varepsilon_{Rx})\sin(\varphi_{\mathrm{Rx}}) & (1-\varepsilon_{\mathrm{Rx}})\cos(\varphi_{\mathrm{Rx}}) \end{pmatrix}. \tag{3.24}$$

Note that the IQ imbalance at Tx cannot be completely compensated with an ideal compensator placed at the receiver due to the effect of additive noise. In fact, the optimal IQ imbalance compensation is given by

$$\begin{aligned} \begin{pmatrix} \hat{s}_I(n) \\ \hat{s}_Q(n) \end{pmatrix} &= (\mathbf{DB})^{-1}\mathbf{DB}\begin{pmatrix} s_I(n) \\ s_Q(n) \end{pmatrix} + (\mathbf{DB})^{-1}\mathbf{D}\begin{pmatrix} n_I(n) \\ n_Q(n) \end{pmatrix} \\ \begin{pmatrix} \hat{s}_I(n) \\ \hat{s}_Q(n) \end{pmatrix} &= \begin{pmatrix} s_I(n) \\ s_Q(n) \end{pmatrix} + \mathbf{B}^{-1}\begin{pmatrix} n_I(n) \\ n_Q(n) \end{pmatrix}. \end{aligned} \tag{3.25}$$

We note that throughout this thesis, optimal IQ imbalance compensation implies optimality under the zero forcing criterion to find back the initial values regardless the impact on the additive noise and with perfect knowledge of the distorsion model. Fig. 3.23 depicts the BER curves of QPSK signal without IQ imbalance, with optimal IQ imbalance compensation and with uncompensated IQ imbalance distortions ($\varepsilon_{\mathrm{Tx}} = 0.1$, $\varphi_{\mathrm{Tx}} = 5°$, $\varepsilon_{\mathrm{Rx}} = 0.05$ and $\varphi_{\mathrm{Rx}} = 10°$). As can be seen, the system performance is degraded and the information sent is not retrieved when IQ imbalance is not compensated. Added to this, even if the IQ imbalance is mitigated with the ideal approach, the BER curve will not be equal the theoretical one. Hence, a penalty is considered for high signal-to-noise ratios (E_s/N_0).

Regarding the points of the constellation of the QPSK signal, their shapes are rather elliptical than circular one. In fact, as outlined in Fig. 3.23(a), there is no longer any deviation between the channels I and Q, but the Tx IQ imbalance cannot be completely mitigated by the ideal matrix at the receiver part.

On the other hand, in the absence of prior information about gain and phase mismatches, the compensation techniques could be applied to estimate the IQ imbalance parameters either with pilot signals or in a blind manner. The pilot method consists of adding known data to be transmitted through the optical channel to be able to estimate and subsequently increase the system performance [91, 92]. However, such an approach requires redundant pilot information, decreasing the spectral efficiency, and could be limited by possible

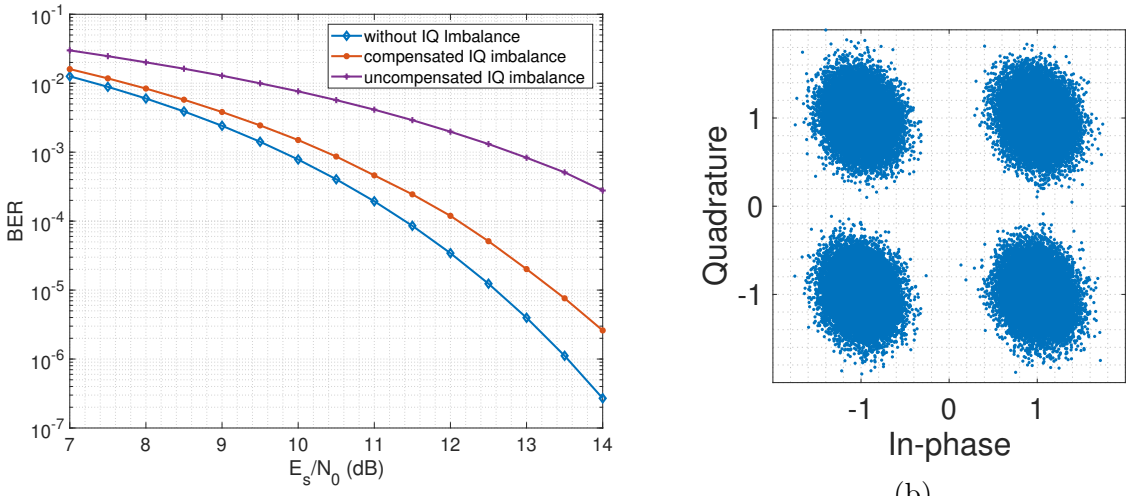

(a) (b)

Figure 3.23 – (a) BER curves (b) QPSK constellation with ideal compensation and $E_s/N_0 = 14$ dB.

corruption of the pilot with the various system and channel imperfections.

Regarding blind schemes, no prior information is needed to estimate the IQ imbalance parameters. Various algorithms have been proposed to blindly compensate for the IQ imbalance, including the Gram-Schmidt orthogonalization procedure (GSOP) [1], ellipse correction (EC) [2], adaptive filtering algorithms [3, 4] and blind source separation (BSS) techniques [93]. The aforementioned algorithms mainly focus on the compensation of IQ imbalance either at Tx or Rx side and currently only few algorithms can estimate both Tx and Rx IQ imbalances without training data. In the following, some of the aforementioned blind techniques are detailed.

Gram-Schmidt Orthogonalization Procedure

The GSOP aims to transform non orthogonal components of the received signal ($r_I(n)$ and $r_Q(n)$) to a new pair of orthogonal signals denoted by $I(n)$ and $Q(n)$ as

$$\begin{aligned} I(n) &= \frac{r_I(n)}{\sqrt{P_I}} \\ Q(n) &= \frac{1}{\sqrt{P_Q}} \cdot \left(r_Q(n) - \rho \frac{r_I(n)}{P_I} \right) \end{aligned} \tag{3.26}$$

where $\rho = \mathbb{E}\Big[r_I(n) \cdot r_Q(n)\Big]$ is the correlation coefficient, $P_I = \mathbb{E}\Big[r_I^2(n)\Big]$, $P_Q = \mathbb{E}\Big[r_Q^2(n)\Big]$.

The GSOP is insensitive to phase rotation. However, it is only applicable to the compensation of Rx-IQ imbalances and is inefficient in compensating Tx-IQ imbalances [94]. Moreover, it introduces phase ambiguities, which require a subsequent phase rotation step.

Fig. 3.24, presents the application of GSOP on QPSK modulation formats corrupted by Rx-IQ imbalance ($\varepsilon_{\text{Rx}} = 0.1$ and $\varphi_{\text{Rx}} = 10°$) and additive white Gaussian noise ($E_s/N_0 = 20$ dB). The GSOP corrects the Rx-IQ mismatch and ensures orthogonality between I and Q components as well as the normalization of the amplitudes.

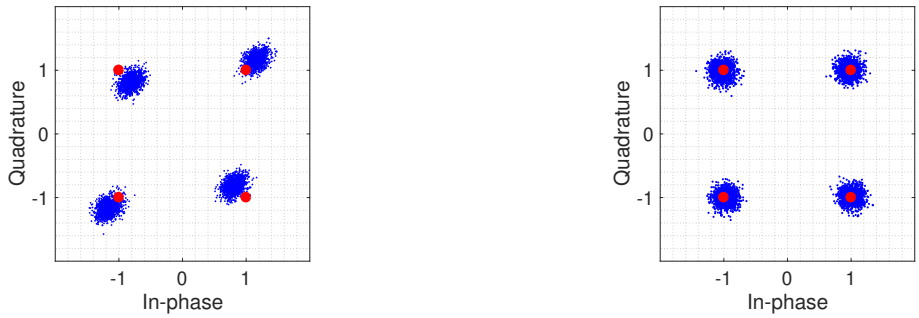

(a) (b)

Figure 3.24 – Illustration of the GSOP for QPSK constellation (a) with Rx-IQ imbalance distortion (b) with compensated Rx-IQ imbalance distortion with the GSOP approach.

BASS Algorithm

Another IQ imbalance algorithm can also be performed based on blind and adaptive source separation has been proposed by Valkama [5]. The algorithm supposes a conjugate signal model meaning that the observed signal $r(n)$ is a linear combination of the desired signal $s(n)$ and its complex conjugate $s^*(n)$ and under this assumption, blind signal estimation would be possible via second-order statistics.

Practically, whitening (decorrelation for complete elimination of $s^*(n)$) problem is solved by using the principle of the natural gradient that leads to an adaptive rule converging to the first-order approximation of the inverse square root of the input covariance matrix. The adaptive rule is given by

$$\mathbf{W}(n+1) = \mathbf{W}(n) - \mu \left[\mathbf{g}(n)\mathbf{g}(n)^H - \mathbf{I}\right], \tag{3.27}$$

where μ is the learning parameter or adaptation step size, $\mathbf{I}$ is the 2×2 identity matrix,

the whitening term $\mathbf{W}(n)$ is a 2×2 matrix, $\mathbf{g}(n) = \mathbf{W}(n)\mathbf{r}(n)$ is a 2×1 vector and $\mathbf{r}(n)$ is the corrupted signal by IQ imbalance and takes the form $\mathbf{r}(n) = [r(n), r^*(n)]^T$.

Fig. 3.25(a) depicts the corrupted signals with both Tx and Rx-IQ imbalances with parameters $\varepsilon_{\text{Tx}} = 0.1$, $\varphi_{\text{Tx}} = 5°$, $\varepsilon_{\text{Rx}} = 0.05$ and $\varphi_{\text{Rx}} = 10°$ for an SNR of $E_s/N_0 = 20$ dB.

Fig. 3.25(b) demonstrates the capability of BASS algorithm to reconstruct the orthogonality between I and Q components of the QPSK signal.

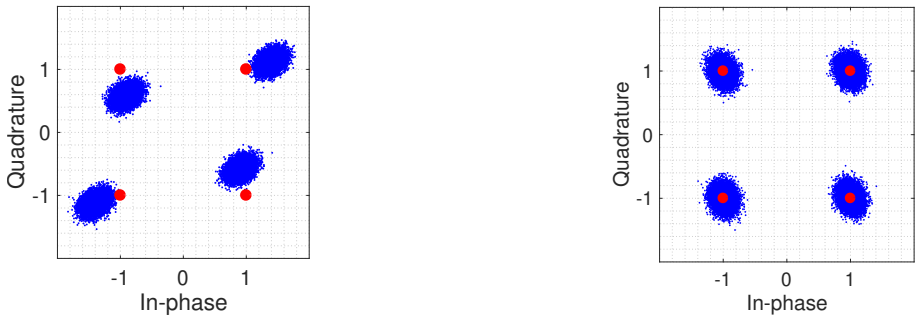

(a) (b)

Figure 3.25 – Illustration of the BASS for QPSK constellation (a) with Tx and Rx-IQ imbalance distortion (b) with compensated IQ imbalance distortion with the BASS approach.

Comparison between GSOP and BASS

Table 3.3 presents a comparison of existing IQ imbalance compensation methods in terms of their implementation, ability to compensate Tx/Rx IQ imbalance, complexity and possibility of joint compensation of other impairments.

Algorithm	Polarization	IQ imbalance position	Complexity of update rule (real multiplications)	Joint/Independant compensation
GSOP	Single	Rx	6 N+4	Independant
BASS	Single	Tx/Rx	22 N	Independant

N-Total number of samples used for IQ imbalance compensation.

Table 3.3 – Comparison between GSOP and BASS

Both GSOP and BASS algorithms are applied separately on two independent polarizations and are dedicaded only for IQ imbalance compensation (these techniques do not handle the resulted phase ambiguities). Nevertheless, the advantage of BASS over GSOP comes in its ability to compensate both Tx and Rx IQ imbalances whereas GSOP deals only with Rx IQ imbalance and requires less real multiplication resources.

3.2.1.3 Chromatic Dispersion Compensation

Chromatic dispersion can be compensated in either optical or electrical domain. Regarding the optical domain compensation, it is done using special fibers known as dispersion compensating fiber (DCF) [95] or adding optical equalizing filters such as interferometric filters [96, 97] or fiber Bragg gratings [98]. Unfortunately, using such optical compensation techniques result in high loss requiring the insertion of additional optical amplifiers which increase the noise level and deteriorate the system performance, in addition to the pricey cost of the optical compensator [99].

Electronic digital signal processing techniques allow for transmission over standard fiber without optical dispersion compensation. Electronic dispersion compensation relies on the use of filtering methods with all the consequent advantages of the ease of deployment and reconfiguration as well as the reproducibility of the system [100, 101]. Indeed, EDC can be handled with different techniques; using linear FIR filters [101, 102] at the transmitter side (known also by pre-compensator) or at the receiver side (post compensator) or using nonlinear filters based on look-up tables at the transmitter [100]. Actually, in real-time systems, linear and nonlinear filters have already been implemented in a single-mode fiber [103, 104].

In the following, EDC is considered using FIR filters at the receiver side either in the time domain or the frequency domain. Thus, a linear filter whose transfer function is the inverse of the transfer function of CD is used to mitigate CD distortion and to get the desired signal.

Time Domain CD Compensation

CD compensation in the time domain involves the use of popular digital filters such as the least mean square (LMS) coefficient adaptation method [105, 106] as well as the fiber dispersion finite impulse response filter [107, 108]. The idea behind this filter is to calculate the inverse Fourier transform of the transfer function of the CD.

Indeed, chromatic dispersion can be modeled as an all-pass filter

$$H_{cd}(\omega, z) = e^{-j\omega^2 \frac{\beta_2}{2} z}. \tag{3.28}$$

with z is the length of the fiber. Thus, the frequency response of the chromatic dispersion compensation filter can be expressed as the inverse of the frequency response of the fiber

channel by

$$H_{icd}(\omega, z) = e^{j\omega^2 \frac{\beta_2}{2} z}. \tag{3.29}$$

Consequently, the filter coefficients, obtained by performing the inverse Fourier transform, can be written as

$$h_{icd}(t, z) = \sqrt{\frac{j}{2\pi\beta_2 z}} e^{-j\frac{t^2}{2\beta_2 z}}. \tag{3.30}$$

In order to avoid inter-symbol interference, the time domain window of the FD-FIR filter should be truncated by using the Nyquist frequency [108] or obtained through resolving optimization problem to get a more precise bound [109]. In other words, an upper bound of the number of taps should be determined. By denoting f_p the double-sided bandwidth of the pulse shape, the maximum frequency of the chirp f_m should be at least equal to the maximum frequency of the pulse chirp ($f_p/2$), without forgetting the Nyquist sampling criterion which assumes that $f_s \geq 2f_p$. Thus, this inequality could be derived

$$\frac{f_p}{2} \leq f_m \leq \frac{f_s}{2}, \tag{3.31}$$

The expression of the maximum frequency of the chirp f_m is derived from the phase component of impulse response of the inverse of the CD. Hence, the maximum frequency of the chirp is expressed by

$$f_m = \frac{1}{2\pi} \frac{\partial}{\partial t} \left(\frac{t^2}{2z\beta_2} \right) \Big|_{t=t_m} = \frac{t_m}{2z\pi\beta_2}, \tag{3.32}$$

where t_m is the time at the end of the truncated impulse response. From Eq. 3.32 and Eq. 3.31,

$$\pi\beta_2 z f_s f_p \leq \frac{t_m}{\Delta t} \leq \pi\beta_2 z f_s^2, \tag{3.33}$$

where $\Delta t = \frac{1}{f_s}$.

Assuming that t_m could be bounded as $n_1\Delta t \leq t_m \leq (n_1 + 1)\Delta t$, $n_1 \in \mathbb{N}$. By denoting N the total number of taps, N will be equal to $N = 2n_1 + 1$. According to the above equation, n_1 verifies the inequality

$$\lceil \pi\beta_2 z f_s f_p \rceil \leq n_1 \leq \lfloor \pi\beta_2 z f_s^2 \rfloor, \tag{3.34}$$

and N verifies

$$2\lceil \pi\beta_2 z f_s f_p \rceil + 1 \leq N \leq 2\lfloor \pi\beta_2 z f_s^2 \rfloor + 1, \tag{3.35}$$

where $\lceil x \rceil$ is the nearest integer greater than or equal to x and $\lfloor x \rfloor$ is the integer part of x.

As the minimum sampling frequency allowed is $f_s = f_p$, the lower value of number of taps permissible to fulfill CD compensation without inter-symbol interference is

$$N = 2 \times \lfloor \pi \beta_2 z f_p^2 \rfloor + 1. \tag{3.36}$$

Hence, the possible number of taps is pulse shape bandwidth dependent. Truncating the impulse response to less than the limit given by Eq. 3.36 affects the signal bandwidth and leads to distortion and inter-symbol interference. On the other hand, going further the upper limit causes aliasing as the Nyquist-sampling theorem is not validated anymore.

Moreover, additional optimization techniques have been proposed to minimize the number of taps while compensating in the time domain. For instance, as presented earlier (Eq. 3.30), the FD-FIR compensation filter is obtained by performing direct sampling and windowing of the ideal CD compensation impulse response. In fact, CD compensation via this FIR filter attempts to mitigate CD even in the frequency band without signal content as the transmitted signal is band limited due to pulse shaping. The point is that, in this case, the compensation is performed in the total frequency band whereas it does not utilize the effect of pulse shaping filters in limiting the bandwidth of signals which enhances the need of larger number of taps while compensating. Thus, it does not necessarily improve the CD compensation performance when the number of filter taps is relatively increased. Also, it offers sub-optimal performance, especially for modulation formats with higher spectral efficiency.

Therefore, a different filter design is required to compensate for the same accumulated CD in a smaller frequency band thereby reducing the required number of taps and the implementation cost.

This is possible using optimal FIR filters, implemented in the least square sense [109]. These filters can be designed to compensate CD in either a small frequency band or the whole frequency band. By increasing the number of taps, these filters perform good CD compensation, even with modulation formats having high spectral-efficiency. Furthermore, considering the effects of pulse shaping filters in limiting the effective bandwidth, the implementation cost of the required number of taps is additionally reduced.

The optimization problem can be formulated as

$$\begin{aligned} \mathbf{h} &= \arg\min_{\mathbf{h}} \xi_s, \\ &\text{subject to} \quad \xi_o \leq \xi_{\text{o,max}}. \end{aligned} \tag{3.37}$$

where ξ_s is the normalized average filter response error within the signal band as

$$\begin{aligned} \xi_s &= \frac{\int_{\Omega_s} \left| H(e^{j\omega T}) - H_{\text{CD}}^{-1}(e^{j\omega T}) \right|^2 d(\omega T)}{\int_{\Omega_s} d(\omega T)} \\ &= \frac{1}{\Omega_2 - \Omega_1} \int_{\Omega_1}^{\Omega_2} \left| H(e^{j\omega T}) - H_{\text{CD}}^{-1}(e^{j\omega T}) \right|^2 d(\omega T). \end{aligned} \tag{3.38}$$

where Ω_1 and Ω_2 denote the boundary frequencies of the signal band Ω_s. Also, the normalized average out-of-band gain of the filter is

$$\begin{aligned} \xi_o &= \frac{\int_{\Omega_o} \left| H(e^{j\omega T}) \right|^2 d(\omega T)}{\int_{\Omega_o} d(\omega T)} \\ &= \frac{1}{2\pi + \Omega_1 - \Omega_2} \left[\int_{-\pi}^{\Omega_1} \left| H(e^{j\omega T}) \right|^2 d(\omega T) + \int_{\Omega_2}^{\pi} \left| H(e^{j\omega T}) \right|^2 d(\omega T) \right]. \end{aligned} \tag{3.39}$$

where Ω_o denotes the spectral bands with no signal content. Finally, $\xi_{\text{o,max}}$ is a selected threshold on the out-of-band gain.

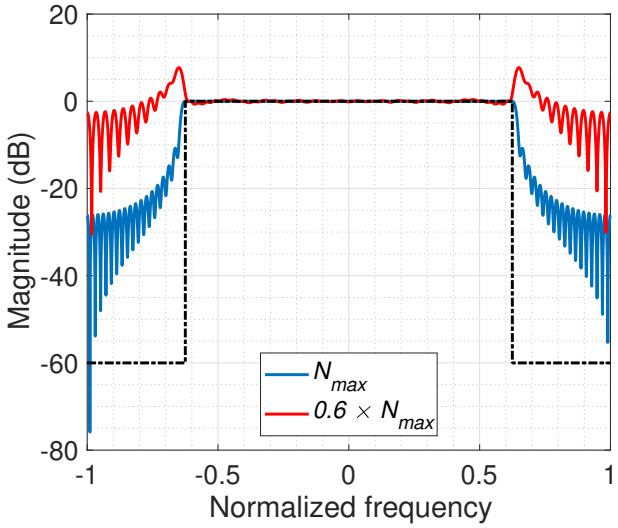

Figure 3.26 – Amplitude response of least-square band-limited filter with N_{max} (blue curve) and $0.6N_{max}$ taps (red curve).

Table 3.4 – Simulation parameters

L (km)	B (Gbaud)	N ($0.6N_{max}$)	D (ps/nm/km)	M	λ (nm)	ρ	$\mathcal{N}$
250	28	61	16	8	1550	0.25	2

Fig. 3.26 depicts the amplitude response of the least square band limited filter with square root raised cosine (SRRC) pulse shaping and parameters given in Table 3.4. The simulation parameters involved in the implementation of such filter are L the length of the fiber, B the baud-rate, N the number of FIR taps, N_{max}, expressed in Eq. 3.36, the maximum number of filter taps so that aliasing does not occur, D the dispersion parameter, $M = \frac{D\lambda^2 L}{4\pi c T^2}$, where c is the speed of light and T is the symbol period, λ is the operating wavelength, ρ is the roll-off factor and $\mathcal{N}$ is the oversampling coefficient.

The filter taps are implemented using floating-point precision. We refer to the in-band frequencies as $\left[-\frac{1+\rho}{2}\pi, \frac{1+\rho}{2}\pi\right]$. The blue curve corresponds to the filter implementation with N_{max} taps and the red curve to that for $0.6 \times N_{max}$ taps. It can be observed that a decrease in the number of filter taps leads to an increase of the out-of-band gain. However, for both N_{max} and $0.6 \times N_{max}$ taps the least square band limited filter can compensate for the accumulated CD.

Other related studies were derived while considering practical finite-precision arithmetic implementation [110].

To sum up, the design of the optimal filters to compensate CD, in the sense of the least square, offers high performances as it can further reduce the implementation cost while mitigating the same amount of CD.

Frequency Domain CD Compensation

Thanks to its considerable computational complexity reduction and its usefulness for long fiber distance [107, 111], great interest has been shown for frequency domain compensation for channel equalization in coherent transmission systems. In fact, since the accumulated CD in long-haul transmission is very large, a large number of taps in time domain equalizer is required. Frequency domain compensation overcomes the above problem as it uses directly Eq. 3.29 which is sampled and multiplied with the FFT of the filter coefficients. This compensation is implemented for real time processing by using the overlap-save or overlap-add zero-padding techniques.

Fig. 3.27 depicts the main steps of performing the frequency domain compensation using overlap-save technique [112, 113].

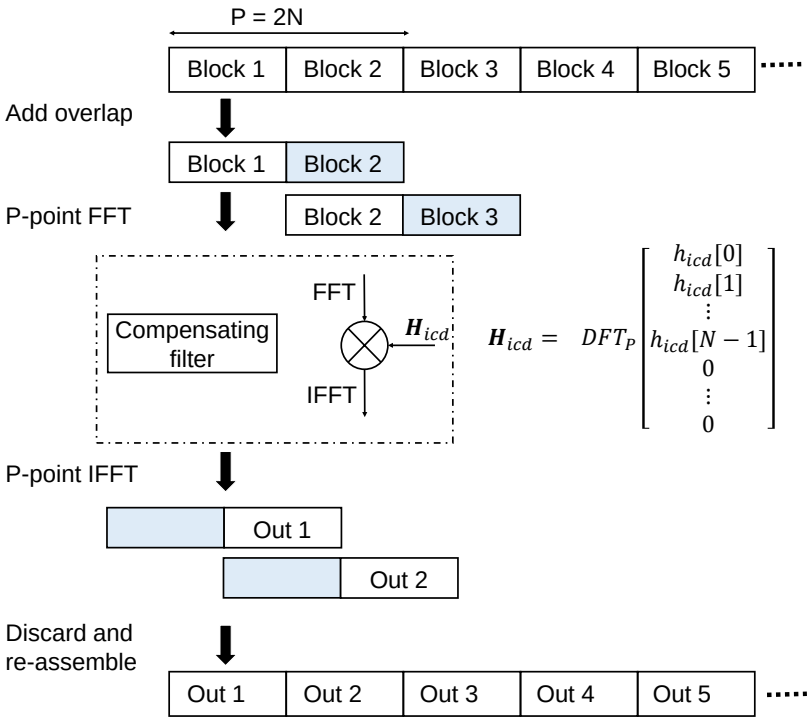

Figure 3.27 – Frequency domain CD compensation using the method overlap-save.

The overlap-save method is based on block processing in the frequency domain, where the received signal is divided into several blocks of size $P = L + N$, each block contains the last N coefficients of the previous block or "overlapped" samples followed by L new samples.

The sequence in each block is transformed into the frequency domain data by the fast Fourier transformation (FFT) operation on P points, and afterwards multiplied term by term by the discrete Fourier transformation on P points of the impulse response of the FIR filter which is calculated once and for all and then stored in memory.

Next, the inverse FFT, IFFT operation is performed to transform the data sequences into the time domain. Each processing block results in N aliasing elements to be eliminated while preserving L terms of linear convolution. Thus, the L last elements of each filtered block are combined together, resulting in the same output obtained by filtering with the FIR filter in the time domain.

Usually, the overlap-save technique is performed with the case $L = N$ (blocks of size

$P = 2N$ and overlap between the blocks of 50%).

Computational Complexity

In this section, the algorithmic complexities of time domain and frequency domain compensations are derived by evaluating the number of required real arithmetic operations (additions and multiplications) per filtered sample.

1. Time Domain Complexity

Assuming time domain implementation of an FIR filter with N complex coefficients, as depicted in Fig. 3.28, N complex multiplications and $N - 1$ complex additions per filtered sample are required. Considering that a complex multiplication corresponds to 4 real multiplications and 2 real additions and that a complex addition corresponds to 2 real additions, then, time domain filtering demands

$$\text{Real multiplications} = 4N$$
$$\text{Real additions} = 4N - 2$$

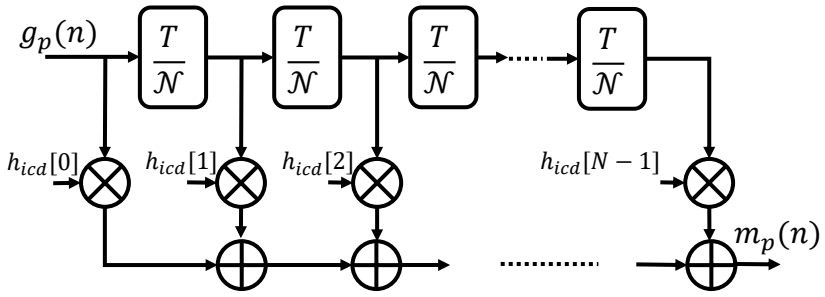

Figure 3.28 – Typical architecture of an FIR filter.

2. Frequency Domain Complexity

In the frequency domain implementation, the algorithmic complexity depends on the FFT or IFFT algorithm chosen for the calculation of discrete Fourier transformations (DFTs) or the inverse discrete Fourier transformations (IDFTs). The split radix algorithm is considered thanks to its low algorithmic complexity as well as its relatively simple structure. In this case, the calculation of the DFT or IDFT using split radix on P points

where P is a power of 2 [113] requires

$$\text{Real multiplications } M_{SR} = P\log_2(P) - 3P + 4,$$
$$\text{Real additions } A_{SR} = 3P\log_2(P) - 3P + 4.$$

In fact, for P samples processing with the overlap save method required

— FFT on P points, requiring M_{SR} real multiplications and A_{SR} real additions.

— P complex multiplications, i.e. $4P$ real multiplications and $2P$ real additions.

— An IFFT on P points, requiring M_{SR} real multiplications and A_{SR} real additions.

In the usual case of an overlap between the blocks of 50% corresponding to the case $P = 2N$, the count of actual operations by filtered sample is given by

$$\text{Real multiplications} = 4\log_2 N + \frac{8}{N},$$
$$\text{Real additions} = 12\log_2 N + 4 + \frac{8}{N}.$$

where N represents the number of taps of the equivalent FIR filter.

By comparing the number of operations as a function of the number of taps N, we deduce that the logarithmic evolution deduced from the number of operations of the frequency domain implementation offers lower complexity in comparison with the direct (temporal) implementation of the FIR filter.

Graphical comparison of the computational complexity of the two implementations is depicted in the Fig. 3.29. It can be seen that the frequency implementation is worthwhile even with FIR filters with small number of taps.

3.2.1.4 Adaptive Filtering

CD compensation requires static equalization, whilst polarization-dependent impairments such as PMD are time-varying phenomena that need adaptive equalization to be mitigated.

Hence, an adaptive equalizer can be used to equalize the unknown and slow variations of the transmission channel. The multiple-input multiple-output equalizer consists of four FIR filters with complex-valued coefficients [114] whose impulse responses are represented by the vectors $\mathbf{c}_{ij}$ of length L with $\{i, j\} \in \{1, 2\}$. Generally, the length of the FIR

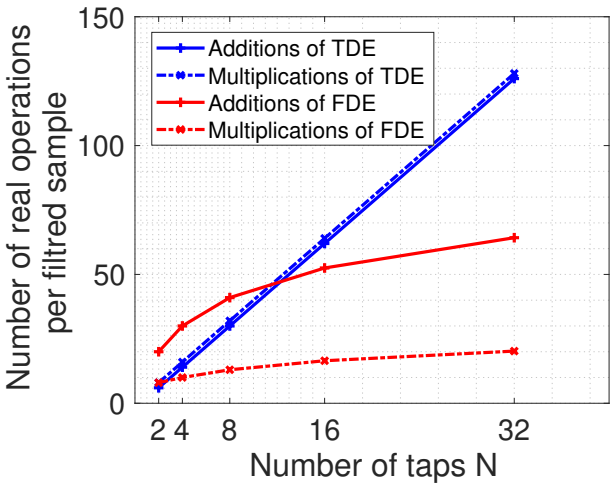

Figure 3.29 – Comparison of the algorithmic complexity between the time and frequency implementations of an FIR filter in terms of the number of real operations per filtered sample.

filters through a butterfly structure is small and can perform PMD and residual CD compensation. A butterfly structure employs four FIR filters $\mathbf{c}_{11}$, $\mathbf{c}_{12}$,$\mathbf{c}_{21}$ and $\mathbf{c}_{22}$ where $\mathbf{c}_{12}$ and $\mathbf{c}_{21}$ compensate for the interference of two orthogonal polarizations with each other.

Fig. 3.30 shows the 4 FIR filters combined with butterfly algorithm implemented for polarization demultiplexing.

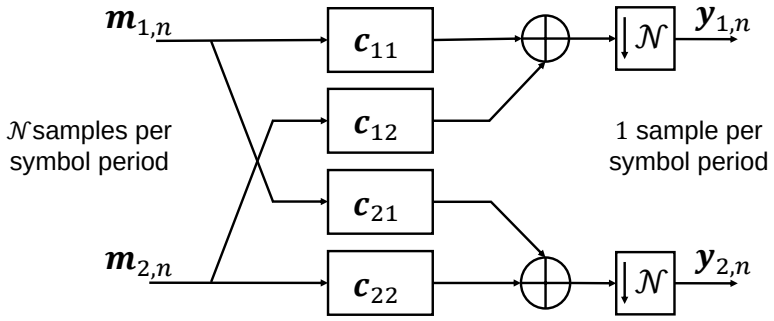

Figure 3.30 – Typical architecture of a 2×2 MIMO fractional equalizer.

At the input of the adaptive fractional equalizer, the signal is up-sampled by a factor of $\mathcal{N}$, meaning that it includes $\mathcal{N}$ samples per symbol, meanwhile, at the output, the signal is decimated or down-sampled to 1 sample per symbol, corresponding to the perfect timing phase of the received symbol ideally free of any interference between symbols due to the other polarization.

Let $\mathbf{m}_{1,n}$ be the discrete-time signals for the X polarization and is the common input

of the impulse response filters $\mathbf{c}_{11}$ and $\mathbf{c}_{21}$ at time n, and $\mathbf{m}_{2,n}$ that of $\mathbf{c}_{12}$ and $\mathbf{c}_{22}$

$$\begin{aligned}\mathbf{m}_{1,n} &= \left[m_{1,\mathcal{N}\,n}, m_{1,\mathcal{N}\,n-1}, \ldots, m_{1,\mathcal{N}\,n-L+1}\right]^T, \\ \mathbf{m}_{2,n} &= \left[m_{2,\mathcal{N}\,n}, m_{2,\mathcal{N}\,n-1}, \ldots, m_{2,\mathcal{N}\,n-L+1}\right]^T\end{aligned}$$

The outputs of the fractional equalizer at time n are then given by

$$\begin{aligned}\mathbf{y}_{1,n} &= \mathbf{c}_{11}^T(n) \cdot \mathbf{m}_{1,n} + \mathbf{c}_{12}^T(n) \cdot \mathbf{m}_{2,n}, \\ \mathbf{y}_{2,n} &= \mathbf{c}_{22}^T(n) \cdot \mathbf{m}_{2,n} + \mathbf{c}_{21}^T(n) \cdot \mathbf{m}_{1,n}.\end{aligned} \tag{3.40}$$

To accomplish the adaptive equalization, the coefficients of the FIR filters are updated recursively by minimizing iteratively a cost function $J\left(\mathbf{c}_{11}, \mathbf{c}_{12}, \mathbf{c}_{21}, \mathbf{c}_{22}\right)$ through an update algorithm such as the stochastic gradient descent. Between two successive iterations, the coefficient $\mathbf{c}_{ij}$ is updated as

$$\mathbf{c}_{ij}(n+1) = \mathbf{c}_{ij}(n) - \frac{\mu}{2}\nabla J\left(\mathbf{c}_{ij}\right)\Big|_{\mathbf{c}_{ij}(n)}, \tag{3.41}$$

where μ is the step size and ∇J is the gradient of the cost function regarding the vector coefficient $\mathbf{c}_{ij}$ at time n.

Blind adaptive equalizers proposed in the literature are distinctive by their cost function used to update the filter taps. For instance, the constant modulus algorithm (CMA) [7] performs blind equalization of transmitted signals with constant modulus amplitude such as phase shift keying modulation formats. However, CMA algorithm seems to be inappropriate for higher-order M-QAM ($M \geq 16$) as the constant radius criterion is not satisfied. This leads to sub-optimal convergence and steady-state performance of the adaptive equalizer [115].

As a consequence, other suggested approaches such as the radius directed equalization (RDE) [116] or the decision-directed least mean square equalizers [117] were proposed for more appropriate higher order QAM modulation equalization. In the following, more details are provided about the aforementioned equalizers.

Constant Modulus Algorithm

The blind adaptive algorithm for PMD mitigation based on the constant modulus criterion [107] looks for the minimization the following cost function in order to update

the filter coefficients

$$J_{CMA}\left(\mathbf{c}_{11},\mathbf{c}_{12},\mathbf{c}_{21},\mathbf{c}_{22}\right)=\mathbb{E}\left[\left(\left|y_{1,n}\right|^2-R\right)^2+\left(\left|y_{2,n}\right|^2-R\right)^2\right],$$

where $R=\frac{\mathbb{E}\left[|d_n|^4\right]}{\mathbb{E}\left[|d_n|^2\right]}$ depends on the modulation formats of the transmitted signal d_n. The update equations of the MIMO filters taps at symbol rate are

$$\begin{aligned}
\mathbf{c}_{11}(n+1)&=\mathbf{c}_{11}(n)-\mu\mathbb{E}\left[e_{1,n}\mathbf{m}_{1,n}^*\right]\\
\mathbf{c}_{12}(n+1)&=\mathbf{c}_{12}(n)-\mu\mathbb{E}\left[e_{1,n}\mathbf{m}_{2,n}^*\right]\\
\mathbf{c}_{21}(n+1)&=\mathbf{c}_{21}(n)-\mu\mathbb{E}\left[e_{2,n}\mathbf{m}_{1,n}^*\right]\\
\mathbf{c}_{22}(n+1)&=\mathbf{c}_{22}(n)-\mu\mathbb{E}\left[e_{2,n}\mathbf{m}_{2,n}^*\right]
\end{aligned}\tag{3.42}$$

The stochastic gradient descent algorithm used to update the filter taps based on the CMA criterion leads to the following error expressions

$$\begin{aligned}
e_{1,n}&=2\left(\left|y_{1,n}\right|^2-R\right)y_{1,n}\\
e_{2,n}&=2\left(\left|y_{2,n}\right|^2-R\right)y_{2,n}
\end{aligned}\tag{3.43}$$

The error function for the CMA is constructed based on the fact that the QPSK symbols have a constant power. This also makes it possible to apply the adaptive equalization before the phase noise and frequency offset are compensated.

The stochastic gradient approximation in order to calculate the terms in $\mathbb{E}\left[e_{p,n}\mathbf{m}_{q,n}^*\right],\{p,q\}\in\{1,2\}$ consists in replacing the gradients by their instantaneous values to get the following equation

$$\begin{aligned}
\mathbf{c}_{11}(n+1)&=\mathbf{c}_{11}(n)-\mu e_{1,n}\mathbf{m}_{1,n}^*\\
\mathbf{c}_{12}(n+1)&=\mathbf{c}_{12}(n)-\mu e_{1,n}\mathbf{m}_{2,n}^*\\
\mathbf{c}_{21}(n+1)&=\mathbf{c}_{21}(n)-\mu e_{2,n}\mathbf{m}_{1,n}^*\\
\mathbf{c}_{22}(n+1)&=\mathbf{c}_{22}(n)-\mu e_{2,n}\mathbf{m}_{2,n}^*
\end{aligned}\tag{3.44}$$

Finally, it is worth mentioning that the CMA is routinely used for pre-convergence [116] of the filter taps to perform a rough polarization demultiplexing, before the equalizer is switched to decision-directed least mean square (DD-LMS) operation as this is found to improve the overall equalization performance [118].

Decision-Directed Least Mean Square Equalization

The mean square error approach is based on the minimization of the cost function

$$J_{MSE}\left(\mathbf{c}_{11},\mathbf{c}_{12},\mathbf{c}_{21},\mathbf{c}_{22}\right)=\mathbb{E}\left[\left|y_{1,n}-\hat{y}_{1,n}\right|^{2}+\left|y_{2,n}-\hat{y}_{2,n}\right|^{2}\right].$$

The error functions $e_{1,n}$ and $e_{2,n}$ are defined by

$$\begin{aligned} e_{1,n} &= y_{1,n}-\hat{y}_{1,n},\\ e_{2,n} &= y_{2,n}-\hat{y}_{2,n}, \end{aligned} \tag{3.45}$$

where $\hat{y}_{1,n}$ and $\hat{y}_{2,n}$ represent the symbol decisions at the reference sample n in X and Y polarizations, respectively. $y_{1,n}$ and $y_{2,n}$ represent the output signals after carrier phase estimation for the X and Y polarizations, respectively. As presented by the equation, the cost function is calculated based on distance minimization to the closest constellation point $\hat{y}_{p,n}$ for the received symbols. The major disadvantage of using the DD-LMS algorithm comes with its impossibility to perform carrier recovery process. As a result, frequency and phase estimation have to be performed before or within the DD-LMS loop in order to be able to make correct decisions and update the coefficients of the equalizer.

Radius Directed Equalization

RDE criterion corresponds to an adaptation of CMA to QAM constellations [116], where the modulus of the points in the constellation is not constant as shown in Fig. 3.31.

In RDE equalization, the cost function can be expressed by

$$J_{RDE}\left(\mathbf{c}_{11},\mathbf{c}_{12},\mathbf{c}_{21},\mathbf{c}_{22}\right)=\mathbb{E}\left[\left(\left|y_{1,n}\right|^{2}-R_{1,n}\right)^{2}+\left(\left|y_{2,n}\right|^{2}-R_{2,n}\right)^{2}\right],$$

where $R_{p,n}$ is given by

$$R_{p,n}=\begin{cases} R_1 & \text{if } \left|y_p(n)\right| \leq \frac{\left(\sqrt{R_1}+\sqrt{R_2}\right)}{2},\\ R_3 & \text{if } \left|y_p(n)\right| \geq \frac{\left(\sqrt{R_2}+\sqrt{R_3}\right)}{2},\\ R_2 & \text{otherwise.} \end{cases} \tag{3.46}$$

As can be seen in Eq. 3.46, each set of symbol is decided according to the closest

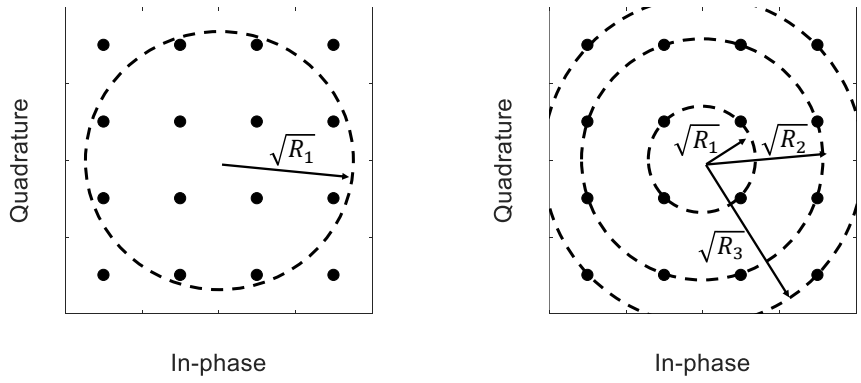

Figure 3.31 – Blind equalizer for 16-QAM constellation (a) CMA algorithm (b) RDE algorithm.

radius. The stochastic gradient algorithm associated with this cost function is similar to that of the CMA criterion where the radius R is to be replaced by the appropriate value of $R_{p,n}$. Practical values of $R_{p,n}$ when using normalized in energy 16-QAM constellation with $E_b = 1$ are $R_1 = 0.2$, $R_2 = 1$ and $R_3 = 1.8$.

Comparison Between the Equalizers

Table 3.5 presents a comparison between the CMA, RDE and DD-LMS equalization approaches.

Table 3.5 – Cost functions, error functions and remarks for adaptive signal processing algorithms

Algorithm	Cost function	Error function	Remarks	
			Advantages	Drawbacks
CMA	$\mathbb{E}\left[\left(\lvert y\rvert^2 - R\right)^2\right]$	$\left(\lvert y\rvert^2 - R\right) y$	-Blind -Insensitive to phase noise -Insensitive to frequency offset	-Slow Convergence but can be used as preconvergence for all formats
RDE	$\mathbb{E}\left[\left(\lvert y\rvert^2 - R_i\right)^2\right]$	$\left(\lvert y\rvert^2 - R_i\right) y$	-Blind -Insensitive to phase noise -Insensitive to frequency offset	-Unstable with low OSNR
DD-LMS	$\mathbb{E}\left[\left(y - \hat{y}^2\right)\right]$	$\left(y - \hat{y}^2\right)$	-Excess MSE is greatly reduced compared to CMA	-Unstable with large phase noise due to decisions

3.2.1.5 Carrier Recovery

Generally, the last stage before symbol estimation and FEC decoding (see Fig. 3.8) is carrier recovery. It is designed to cope with imperfections originating from the transmitter and receiver laser. This stage involves two main sub-units, carrier frequency offset (CFO) estimation and carrier phase recovery (CPR) and requires tailored algorithms. Since most phase recovery methods require a zero frequency offset, the CFO mitigation is often carried out before the phase recovery. The following sections present the details of such systems.

CFO Estimation

As stated earlier, the CFO compensation operates generally after the equalization procedure. Thus the chromatic dispersion and polarization mode dispersion have been efficiently removed. In this case, the signal at the entrance of the CFO block in polarization p is given by

$$y_p(n) = s_p(n)e^{2j\pi\left(\theta_p(n)+n\varphi_1\right)} + b'_p\left(n\right), \tag{3.47}$$

Subsequently, the signal is still corrupted by different effects. The first effect comes with the term $\varphi_1 = \Delta f T$ where Δf is the continuous-time frequency offset between the LO and the transmit laser, expressed in Hz. Δf corresponds to the frequency offset, which is independent of the polarization state of the received multiplexed signals. Second, $\theta_p(n)$ is the phase noise. Third, $b'_p(n)$ corresponds to additive zero mean circularity symmetric complex valued Gaussian noise.

For carrier frequency-offset estimation, various blind approaches in time or frequency domain have been proposed in the literature. Indeed, common time domain approaches based on differential phase have been explored in [119–121]. The block diagram of such frequency estimator is depicted in Fig. 3.32

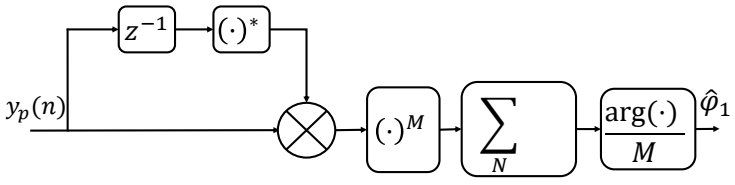

Figure 3.32 – Block diagram of carrier frequency offset estimator for coherent receiver (z^{-1} corresponds to one symbol delay).

First, the received symbol $y_p(n)$ is multiplied with the complex conjugate of the previous

symbol $y_p(n-1)$. This results in a complex number whose phase is equal to the difference in phase of the two symbols. Then, any information that is encoded in the signal phase has to be removed. This is straightforward for phase-shift-keyed signals by taking the M^{th} power of the complex symbol, M being the number of constellation points. Assuming that the CFO is quasi constant within an observation window, N is the number of samples in the observation window sampled at baud-rate, the CFO is estimated via M^{th}-power algorithm [119] as follows

$$\hat{\varphi}_1 = \frac{1}{2\pi M} \arg\Big(\sum_{m=0}^{N-1} \Big[y_p\left(n+1+m\right) y_p^*\left(n+m\right)\Big]^M\Big) \tag{3.48}$$

where $\arg(\,\cdot\,)$ stands for the argument of a complex-valued number. For higher intermediate frequency, a similar method based on recursive estimation is proposed in [122]. Although the complexity of differential phase CFO estimation is relatively low, its accuracy is poor.

On the other hand, spectral methods are also investigated in [123, 124], where the received samples are preprocessed (typically raised to the M^{th} power) and then Fourier transformed, which allows searching for a peak in the spectrum corresponding to the frequency offset. Thanks to the independence between data and noise, the estimation is possible by looking for the maximum of the power spectrum. For complexity reduction, the N-FFT frequencies are considered and the CFO estimates is given by

$$\hat{\varphi}_1 = \frac{1}{N} \arg \max_{k\in\left[-\frac{N}{2}\,\frac{N}{2}-1\right]} \left| \frac{1}{N} \sum_{n=0}^{N-1} y_p\left(n\right)^M e^{-\frac{2j\pi Mkn}{N}} \right|^2 \tag{3.49}$$

Fig. 3.33 represents time domain and frequency CFO estimation techniques. The simulation was conducted on QPSK and 16-QAM signals corrupted with AWGN noise at 20 dB of SNR, and the introduced normalized frequency offset is constant and of value 0.1. As can be seen in Fig. 3.33(a), time domain CFO estimation achieves to get the expected frequency offset but for 16-QAM signal the estimate seems to be inaccurate. To improve the estimation accuracy, iterative methods based on coarse and fine steps were proposed [125, 126]. The coarse step of CFO estimation is done by an FFT of size N and the resulting frequency estimate enables a fine step by initializing a gradient-descent algorithm around the true point or by using a zoom-FFT.

In fact, when estimating the frequency offset based on the coarse approach, the target

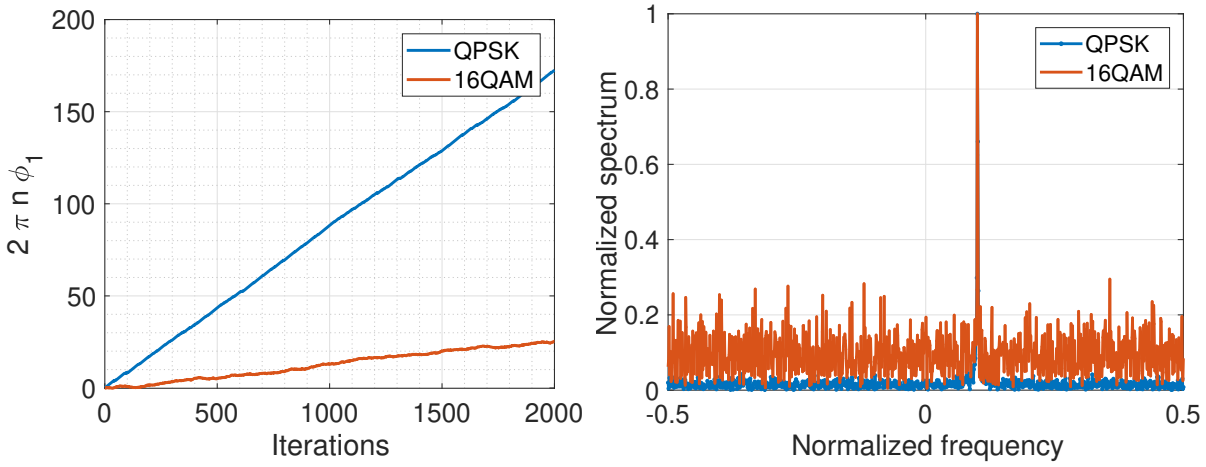

(a) (b)

Figure 3.33 – Carrier frequency offset estimation in (a) time domain, (b) frequency domain (N=1024) for fixed applied normalized CFO of value 0.1.

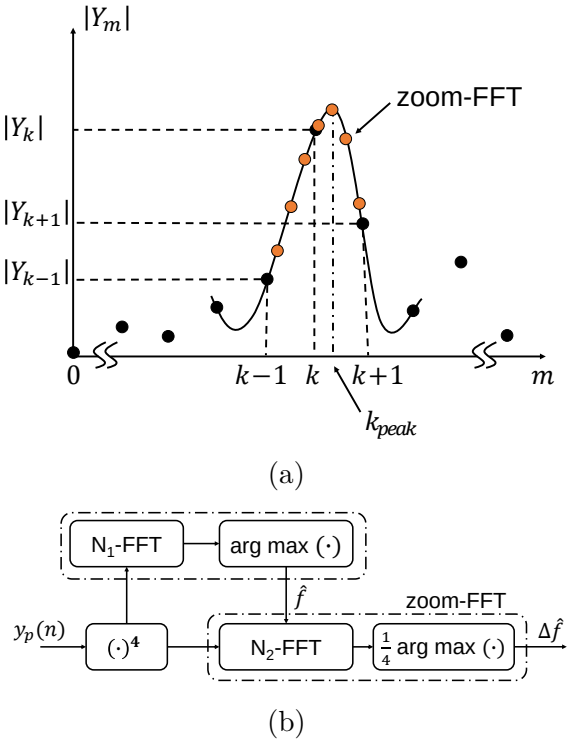

(a)

(b)

Figure 3.34 – (a) N_1-FFT and zoom-FFT magnitude samples of a spectral tone. (b) Schematic diaglram of zoom-FFT.

is to find the spectral peak k_{peak} based on the magnitude of N_1 points FFT of the received

signal y_p (see Fig. 3.34(a)). The problem is that the chosen peak is not necessarily one of the N_1 bins of the discrete Fourier transform. As shown in Fig. 3.34(b), to get a finer estimates, zoom-FFT is operated and another N_2-FFT points are calculated around the coarse frequency offset estimated in the first stage.

As an illustration, Fig. 3.35 outlines the mean squared error (MSE), defined as $\mathbb{E}\left[\|\hat{\varphi}_1 - \varphi_1\|\right]$ of the CFO estimates. Simulations are conducted using 4-, 16-QAM modulation formats. The coarse CFO estimation is operated over N_1-FFT of $N_1 = 1024$ points whereas the fine estimation is over $N_2 = 11$ points. As presented, the CFO estimation based on zoom-FFT outperforms the coarse CFO estimation as it results in a lower MSE values, especially for high E_s/N_0.

It is worth mentioning that the aforementioned algorithms are not efficient for arbitrary QAM formats as there is no trivial operation to remove the data modulation. To circumvent such a problem, M-QAM constellations can be decomposed into rings of phase shape keying. For instance, 16-QAM constellations can be seen consisting of two rings (inner and outer constellation points) of a-QPSK-like and an intermediate ring with eight constellation points and doing so, these CFO estimation algorithms can be applied. Similarly, such approaches can be used for higher order M-QAM signals but more symbols per block are needed in this case.

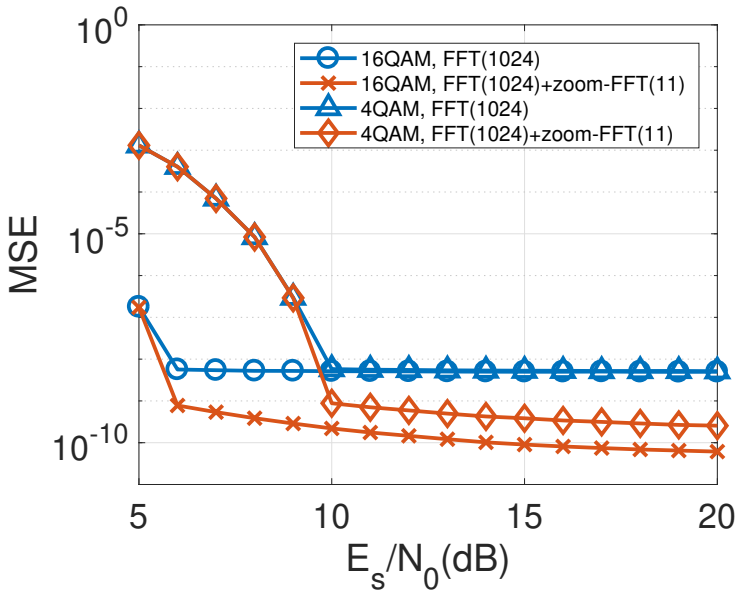

Figure 3.35 – Empirical MSE between introduced and estimated CFO values using FFT and zoom-FFT CFO estimate versus E_s/N_0 for 4-QAM and 16-QAM with $N_1 = 1024$ and $N_2 = 11$.

Table 3.6 – Computational complexity of single stage (N-FFT) and double-stage (FFT+zoom-FFT) CFO estimation approaches

Algorithm	Complex multiplication
N-FFT	$\frac{N}{2}\log_2(N) + L$
FFT+zoom-FFT	$\frac{N_1}{2}\log_2(N_1) + \frac{N_2}{2}\log_2(N_2) + 2L$

The computational complexity of such algorithms in terms of the number of complex multiplications are shown in Table 3.6. N, N_1 and N_2 denote the number of points of the FFT operation and L is the number of symbols in each block.

3.2.1.5.1 Carrier Phase Recovery

As it is depicted in Fig. 3.8, carrier phase recovery is generally carried out after frequency offset compensation and polarization demultiplexing. Off-line DSP algorithms are proposed for carrier phase recovery either in a feedback or a feed-forward scheme. In the following, some of the state-of-the art algorithms are detailed.

1. Feedback Techniques

As depicted in Fig. 3.36, the classical feedback block diagram is generally constituted of three main steps: the first step is the phase detector, the second is a 1$^{\text{st}}$ order loop filter and the third is an integrator (numerical control oscillator).

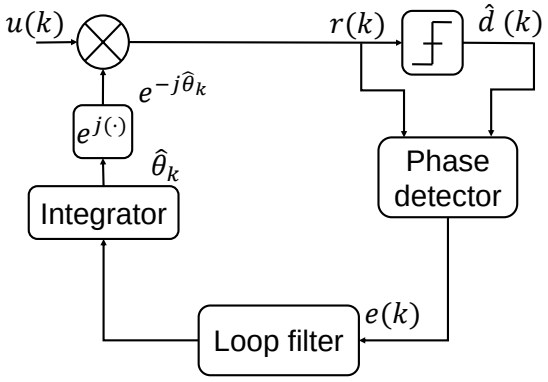

Figure 3.36 – The classical feedback CPR block diagram.

At the output of the integrator, the phase is updated as follow

$$\hat{\theta}_{k+1} = \hat{\theta}_k + \alpha\, e_k + \beta \sum_{j \leq k} e_j \tag{3.50}$$

where e_k is the phase detector result, α is the lead coefficient and β is the lag coefficient of the 1$^{\text{st}}$ order loop filter. It comes from a derivation of the maximum likelihood function with respect to the estimate phase noise and determines the difference between the real value of the phase noise θ_k and its estimated one.

This output is then fed to a 1$^{\text{st}}$ order loop filter which models the gradient algorithm step. This loop filter is controlled by the parameter α which represents the step size of the gradient algorithm. Another integrator filter is also added in order to smooth the output of the phase detector and to allow proper loop operation even for poor signal to noise ratios.

This integrator is controlled by the parameter β. The estimated value of the phase noise is then used to calculate the complex exponential useful to mitigate the phase noise from the received symbol $y(k)$.

After introducing the overall scheme of a feedback block algorithm, the evaluation tools that present the performance of such a mechanism are proposed. Thus, the system function is evaluated by two main steps, the acquisition mode including S-curve characteristics and the tracking mode.

As for the acquisition step, the S-curve metric is used to analyze the overall behavior of the feedback loop. The S-curve is defined as the average of the phase detector output, conditioned on a fixed phase error as follows

$$S(\phi) = \mathbb{E}_{d_k, n_k} \left[e(k) | \phi \right], \tag{3.51}$$

where $\mathbb{E}_{d_k, n_k} [\ \cdot\ ]$ denotes the statistical average over data and noise and $\phi = \theta - \hat{\theta}$.

Fig. 3.37 presents a typical shape of an S-curve evaluated in open loop. Generally, the S-curve has a periodic behavior with a periodicity equals to the symmetry angle of the constellation which is due to the invariance of the constellation to a rotation. For instance, $\frac{k\pi}{2}$ for a M-QAM constellation and $\frac{2\pi}{M}$ for a M-PSK constellation.

In an S-curve, we can distinguish two points at $S(\phi) = 0$, a stable equilibrium point where $\frac{\partial S(\phi)}{\partial \phi} > 0$ and unstable equilibrium points where $\frac{\partial S(\phi)}{\partial \phi} < 0$. A stable equilibrium point represents a global maximum of the likelihood function whereas an unstable equilibrium

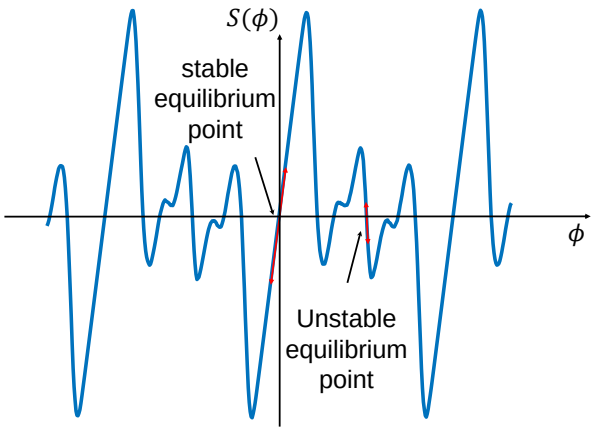

Figure 3.37 – Typical shape of an S-curve for a phase recovery loop.

point corresponds to some false attachment points due to a local maximum of the likelihood function. These attachment points tend to decrease when a small amount of signal-to-noise ratio is added. Also, it is worth mentioning that the S-curve depends on the used phase detector. The expression of the decision-directed phase detector derived from a maximum likelihood approach is given by

$$e_1(k) = \Im\left(\hat{d}^*(k)y(k)e^{-i\theta_k}\right) \quad = \Im\left(\hat{w}^*(k)w(k)\right) \tag{3.52}$$

where $w(k) = y(k)e^{-i\theta_k}$, and $\hat{d}(k) = \hat{w}(k)$ the decision made on $w(k)$, thus

$$e_1(k) = \hat{w}_I\left(k\right) w_Q(k) - \hat{w}_Q(k)w_I(k) \tag{3.53}$$

where $w(k) = w_I(k) + jw_Q(k)$. We note that this phase detector corresponds to the stochastic gradient descent algorithm of the mean square error

$$e_1(k) = \frac{\partial}{\partial\theta}\mathbb{E}\left[\left|w(k) - \hat{w}(k)\right|^2\right] \tag{3.54}$$

Other phase detectors have been proposed using other minimization criteria such as the gradient of the norm 1 minimization i.e. $\|w(k) - \hat{w}(k)\| = |w_I(k) - \hat{w}_I(k)| + \left|w_Q(k) - \hat{w}_Q(k)\right|$ which results in the phase detector

$$e_2(k) = w_I(k)\text{sgn}\left[w_Q(k) - \hat{w}_Q(k)\right] - w_Q(k)\text{sgn}\left[w_I(k) - \hat{w}_I(k)\right] \tag{3.55}$$

Moreover, a more general phase detector equation has been presented by Lectert and

Vandamme [8] given by this equation

$$e(k) = f\left(w_I(k)\right) g\left(w_Q(k)\right) - f\left(w_Q(k)\right) g\left(w_I(k)\right) \tag{3.56}$$

where $f(\,\cdot\,)$ and $g(\,\cdot\,)$ are two odd functions.

Hence, in order to simplify the hardware implementation, we can define the following phase detectors which correspond to sub-optimal solutions associated with the phase detector $e_1(k)$ derived form maximum likelihood criterion

$$\begin{aligned}
e_3(k) &= \operatorname{sgn}\left(w_I(k)\right)\left(w_Q(k) - \hat{w}_Q(k)\right) - \operatorname{sgn}\left(w_Q(k)\right)\left(w_I(k) - \hat{w}_I(k)\right) \\
e_4(k) &= \hat{w}_I(k)\operatorname{sgn}\left(w_Q(k) - \hat{w}_Q(k)\right) - \hat{w}_Q(k)\operatorname{sgn}\left(w_I(k) - \hat{w}_I(k)\right) \\
e_5(k) &= \operatorname{sgn}\left(w_I(k)\right)\operatorname{sgn}\left(w_Q(k) - \hat{w}_Q(k)\right) - \operatorname{sgn}\left(w_Q(k)\right)\operatorname{sgn}\left(w_I(k) - \hat{w}_I(k)\right)
\end{aligned} \tag{3.57}$$

As we can see, the odd functions can take different expressions as $f(x) = x$ or $\hat{x}$ or $\operatorname{sgn}(x)$ and $g(x) = x$ or $x - \hat{x}$ or $\operatorname{sgn}(x - \hat{x})$. The S-curves $S_i(\phi)$ of each phase detectors e_i, $i \in \{1, \cdots, 5\}$ are depicted in Fig. 3.38. Some inner parameters of the S-curve could also be studied such as the choice of the loop filter parameters. If we consider a first order loop, the equivalent noise bandwidth could be approximated by

$$B_L \simeq \frac{\alpha K_e}{4T} \tag{3.58}$$

Hence, it is clear that the choice of α is a compromise between the acquisition time and the precision of the estimation. In fact, if α is small, then B_L is also small resulting in a slow time acquisition and also a slow capacity to track the phase variation but the variance of the estimation error is small. On the other case, if α is high, then the precision of the estimation is poor but the acquisition is rapid and the phase tracking variation is also well performed.

When dealing with a second order loop, the choice of the parameters α and β is important. Previous studies [9] have presented these expressions under the condition $B_L T \ll 1$

$$\begin{aligned}
\alpha &\simeq \frac{4\xi}{\xi + \frac{1}{4}\xi}\frac{B_L T}{K_e} \\
\beta &\simeq \frac{4}{(\xi + \frac{1}{4}\xi)^2}\frac{(B_L T)^2}{K_e}
\end{aligned} \tag{3.59}$$

where ξ is the damping factor that ensures a compromise between the rapidity and the

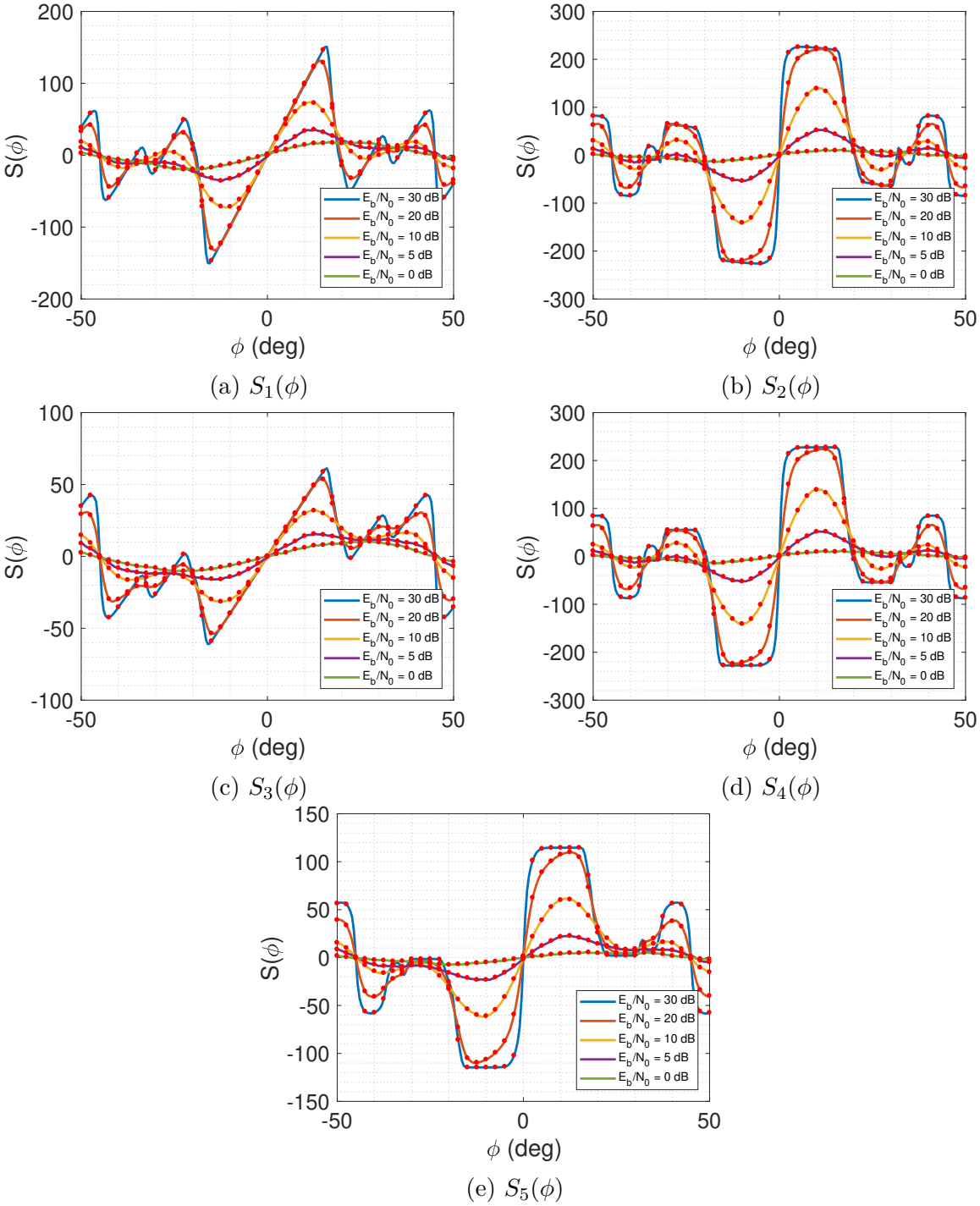

(a) $S_1(\phi)$ (b) $S_2(\phi)$

(c) $S_3(\phi)$ (d) $S_4(\phi)$

(e) $S_5(\phi)$

Figure 3.38 – Plots of the S-curves of the various decision-directed error phase detectors for 16-QAM signals and different SNRs.

precision. Generally, the value of this parameter is $\xi = \frac{1}{\sqrt{2}}$ for best performance, α is the lead coefficient and β is the lag coefficient. Once the damping factor is fixed, the value of B_L is now required to calculate the loop parameters. As mentioned before, the choice of B_L depends on the desired use case such as speed of acquisition, precision of the estimation or variation tracking.

The shape of the S-curve indicates possible problems with the phase detector such as

— **Phase ambiguity**: The periodicity of the S-curve leading to several stable points is the cause of phase ambiguity of $\pi/2$, which could be resolved using prefixes or appropriate frame sequences, or by using differential encoding.

— **Hang up to wrong phase value**: When the phase error is close to an unstable equilibrium point, and the slope of the S-curve in the vicinity of this point is small, the loop takes a long time to get the phase error out of this region. The additive white noise stimulates hang-up problem. In fact, even if the phase detector has a high slope in the vicinity of an unstable equilibrium point (due to the discontinuity at the unstable equilibrium point), the presence of a high value of additive noise can tip the phase error in the opposite direction causing fluctuation around the unstable equilibrium point during a period of time. On the other hand, even if the S-curve is with a saw tooth characteristic i.e. the S-curve presents some discontinuity at the unstable equilibrium point, the hang-up still occurs when noise is present. In fact, the larger the noise is, the smaller the slope at the unstable equilibrium point is and the smaller the restoring force is. Fig. 3.39 depicts the curves of different realizations of the phase error for a first order loop initialized at an unstable equilibrium phase error $\phi_0 = 45°$ for a 4-QAM constellation at 10 dB introduced SNR. Through this plot, it is clear how the hang-up affects the acquisition speed of the loop.

— **Cycle slips due to the change of stable point**: The periodicity trend of the S-curve shape leads to multiple stable equilibrium points spaced by $\pi/2$ for a M-QAM modulation formats and $2\pi/M$ for a M-PSK constellation. In the tracking mode, the phase error has small fluctuations around a stable equilibrium point. The presence of the additive noise can brutally produce a large variation of the phase error which is then attracted to the area of the neighboring equilibrium point. This generates an acquisition period before the loop stabilizes another time. During the acquisition period, a burst of error decisions are produced leading to a significant degradation of the symbol error rate (see Fig. 3.40). Hence, cycle slips phenomena must occur in a very rare manner so that the loop behavior could be qualified as acceptable.

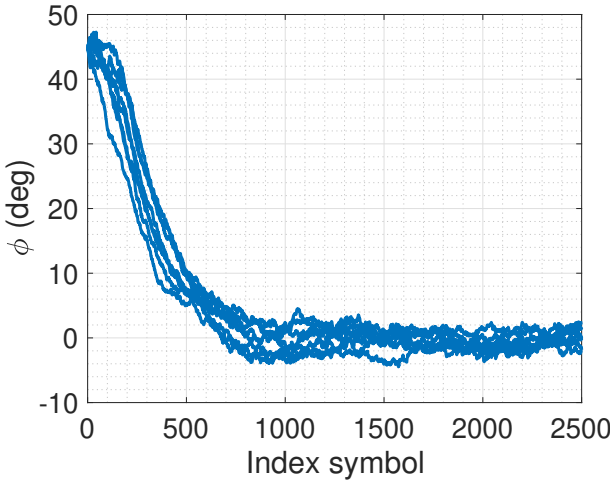

Figure 3.39 – The hang-up phenomenon for a first order loop.

— **Pull-in range:** The pull-in range is the tolerable frequency offset such that the phase is locked. In fact, a small amount of residual uncompensated carrier frequency offset ($|\Delta f| \ll 1/T$) may be present and will be eliminated by the carrier phase recovery block. In this case, the first order loop has a ramp as input $\theta(n) = \Delta f n$. Thus, the system response has a steady state error ϕ_s satisfying $S(\phi_s) = \frac{2\pi\Delta f T}{\alpha}$. Therefore, a maximum value of Δf^{max} could be defined as a threshold beyond which the loop never ends its acquisition time. The value is expressed by $\Delta f^{max} = \frac{\alpha S^{max}}{2\pi T}$, where S^{max} is the maximum amplitude of the S-curve. Also, the lock-in range could be defined by $[-\Delta f^{max}, \Delta f^{max}]$, as the interval in which the acquisition condition of the loop is verified. Generally, the lock-in range is in the order of the equivalent noise bandwidth. In order to suppress this steady state error, a second order loop

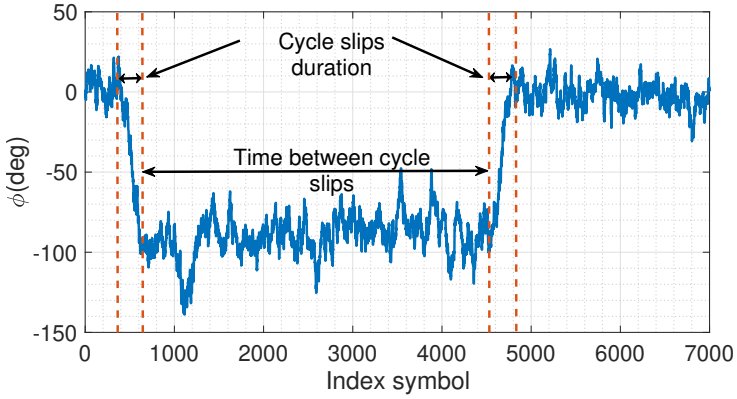

Figure 3.40 – Illustration of the phenomenon of cycle jumps for a first order loop.

is used. However, when $|\Delta f| > \Delta f^{max}$ cycle slips occur and the loop cannot hang a stable point resulting in a long acquisition time for the same loop bandwidth (see Fig. 3.41). The acquisition period increases with the frequency offset $|\Delta f|$. For instance, the acquisition time for a M-PSK constellation in the absence of noise is well approximated by

$$T_{ac} = M^2 \frac{\pi^2(4\xi^2+1)^3}{256\xi^4 B_L}\left(\frac{\Delta f}{B_L}\right)^2 \tag{3.60}$$

where ξ is the damping factor of the second order loop. This expression can be applied as long as $|\Delta f| < \Delta f^p$ (Δf^p is the pull-in frequency). In other cases, the loop slips cycles continuously without ever achieving lock.

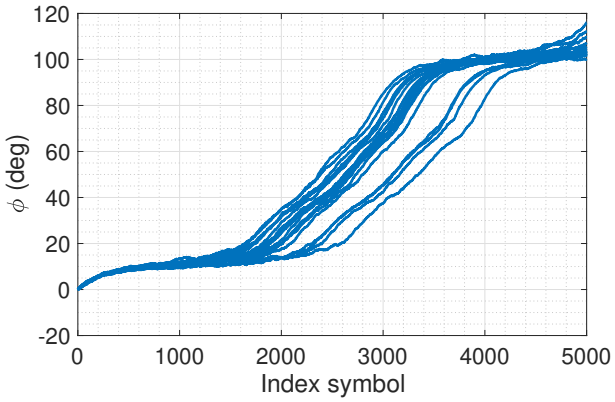

Figure 3.41 – Effect of a frequency offset on the latching time for $|\Delta f| > \Delta f^{max}$ on a 16-QAM and $E_b/N_0 = 10$ dB modulation.

— **Error detector gain**: In addition to the presented characteristics above, we present the error detector gain which is the slope of the S-curve when $\phi = 0$. Thus, $K_e = \lim_{\phi \to 0} \frac{\partial}{\partial \phi} S(\phi)$. Fig. 3.42 shows the gain shape of different phase detectors for a 16-QAM modulation format constellation as a function of the signal-to-noise ratio E_b/N_0.

We can distinguish two different behaviors of the plots. For instance, the plots of K_{e_1} and K_{e_3} have a steady state convergence above $E_b/N_0 = 13$ dB. For E_b/N_0 below 13 dB, these plots have roughly the same shape as the increase of noise smoothing around the origin of the S-curve reduces the value of the gain.

As for K_{e_2}, K_{e_4} and K_{e_5}, these values raise as a function of E_b/N_0 in an exponential manner. The discontinuity points that exist at the origin of their S-curve can explain the shape of these plots. This discontinuity is abrupt with significant value of SNR and is more smoothed (as the slope decreases) with high level of noise.

Finally, the gain of the phase detector is one of the important characteristics of the phase detector as with this parameter we can define the normalized loop bandwidth, which is inversely proportional to the acquisition time $B_L \simeq \frac{\alpha K_e}{4T}$.

Now, we determine the phase detector performance regarding the tracking mode. This can be handled by evaluating the variance of the estimation error in the steady state part and comparing it with the Cramer-Rao bound (CRB), which represents a theoretical lower limit of variance.

An approximate analytical expression relying the variance of the phase detector $\text{var}(\phi)$ to the variance of the phase at the origin $\sigma_e^2(0)$ is given by $\text{var}(\phi) \simeq \frac{2B_L T \mathbb{E}\left[\left|N(k)\right|^2\right]}{{K_e}^2}$, or in an equivalent manner $\text{var}(\phi) \simeq \frac{2B_L T {\sigma_e}^2(0)}{{K_e}^2}$. For the different used phase detectors, we study the evolution of the variance of the normalized error phase by $\frac{2B_L T {\sigma_e}^2(0)}{{K_e}^2}$ for a 16-QAM constellation as a function of E_b/N_0. The CRB is also considered for comparison.

As depicted in Fig. 3.43, for lower SNR values, the phase detector with linear S-curve response (e_1, e_3) demonstrates a phase error variance lower then the phase detector with constant S-curve response (e_2, e_4, e_5). The closest phase detector to the optimal is e_1, reaching the CRB for $E_b/N_0 > 12$ dB but having a higher value at lower SNR range. This is due to the effect of the additive noise, which results in symbol error decisions. Among the constant S-curve response, we remark that the error phase variance of the phase detector e_3 presents the same trend as that of e_1, but it does not reach the CRB as

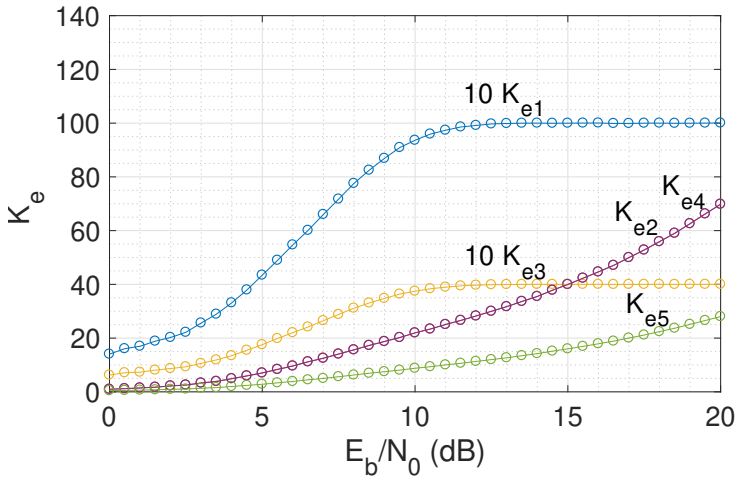

Figure 3.42 – Gain shape of different phase detectors for a 16-QAM modulation format constellation as a function of the signal-to-noise ratios E_b/N_0 and for different phase detectors.

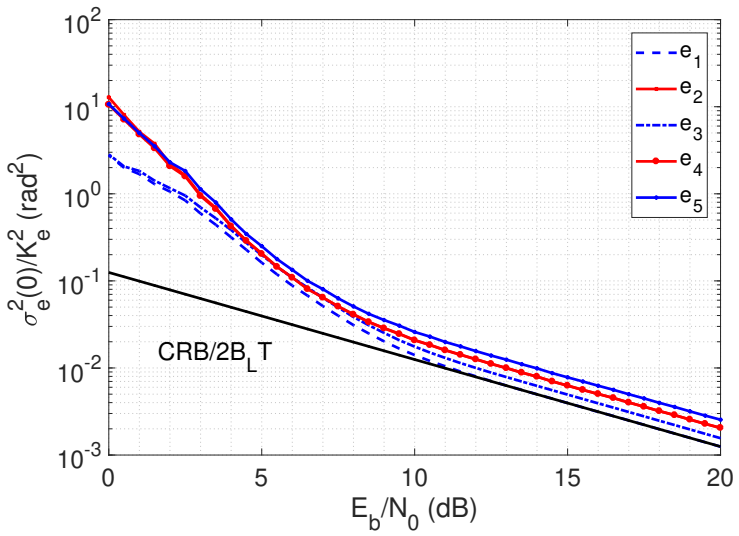

Figure 3.43 – Normalized variance of the phase detector for a 16-QAM constellation as a function of the signal-to-noise ratio E_b/N_0 for different phase detectors.

it uses an approximation of the corrected signal using the operator sgn(.).

In a nutshell, to compare the phase detector performance, two modes are considered. The first mode is the acquisition where the gain, the lock-in range, the linear response and the fault attachment points are evaluated. These properties are demonstrated by the S-curve plot of the phase detector. The second is the tracking mode where the estimation precision is evaluated. This is handled thanks to the plot of the variance of the phase error. As presented above, the phase detectors e_1 and e_3 present the best compromise between the acquisition and the tracking modes as they present a relatively large lock-in range, few fault attachment point, a fixed gain and a low error phase estimation variance.

2. Feed Forward Techniques

After studying feedback loops, this section takes into consideration feed-forward CPR approaches. Blind phase search (BPS), proposed by Timo Pfau [10], is one of the typical methods used for carrier phase recovery. This method is limited to square constellation and it requires B rotation test phases $\theta_k^{(m)} = \frac{m\pi}{2B}$, $m = 0, 1, ..., B-1$, applied to the received signal $y(n)$ and the choice of the best test phase $\theta_k^{(m)}$ is then evaluated thanks the minimum mean square distance error criterion.

In fact, the chosen phase is provided by

$$\hat{\theta}_k = \arg \min_{m \in [0, B-1]} s_{k,m} \tag{3.61}$$

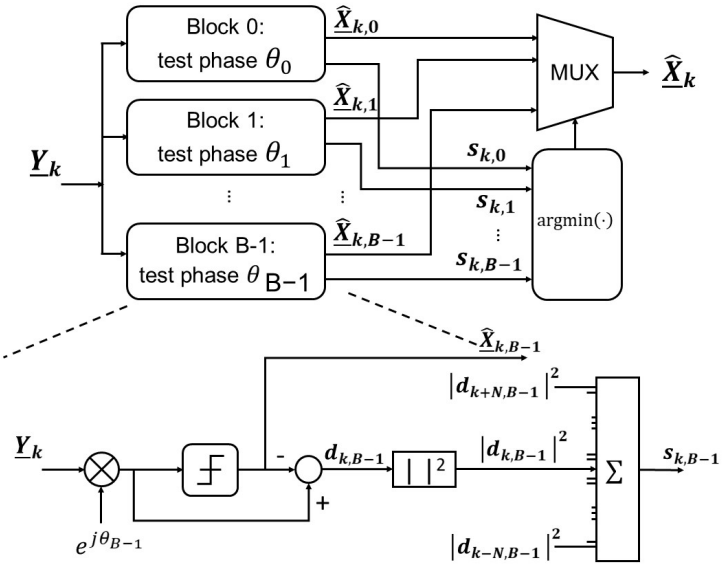

Figure 3.44 – Feed forward carrier recovery using B test phases θ_B.

where $s_{k,m} = \sum_{k=-N}^{N} \left| y(k)e^{-j\theta_k^{(m)}} - \hat{d}(k) \right|^2$ and $W = 2N+1$ is the filter depth. A simplified scheme of the method is depicted in Fig. 3.44.

Due to constellation rotation ambiguities, the generated bits should be differentially encoded/decoded. This results to a differential coding penalty for M-ary square QAM constellation.

Additionally, some unwrapping scheme is also required to perform phase tracking. The goal of phase unwrapping is to overcome the discontinuity in the raw estimated phase noise sequence. This discontinuity comes from the fact of limiting the estimated phase on one of the B test phases, which are in the range of $[0, \pi/2]$.

The unwrapping function ensures a continuity between the actual and the previous phase noise. In other words, if the previous estimated phase noise is $\hat{\theta}_{k-1}^u$, then the next phase noise is the nearest value to $\hat{\theta}_{k-1}^u$ among $\hat{\theta}_k^u = \hat{\theta}_k^r + m\pi/2$, where $m \in -\infty ... + \infty$.

Fig. 3.45 describes the unwrap function steps. The red point $\hat{\theta}_{k-1}^u$ is the unwrapped version of the estimated phase at $k-1$ and serves as reference. The green point $\hat{\theta}_k^r$ is one of the chosen B test phases related to the minimum distance criterion, hence it is in the range of $[0, \pi/2]$. The unwrap function drags the green point to the dark one $\hat{\theta}_k^u$ because the distance d_1 is greater than d_2. The typical expression that is used to calculate the

unwrapped phase is given by

$$\hat{\theta}_k^u = \arg \min_{\hat{\theta}_k + m\pi/2} \left(\left| \hat{\theta}_{k-1}^u - \left(\hat{\theta}_k^r + \frac{m\pi}{2} \right) \right| \right) \tag{3.62}$$

where $m \in -\infty ... + \infty$.

To prevent the differential coding penalty, pilot symbols with classic encoding can be inserted into the data stream. These symbols are known to both transmitter and receiver sides. Then, at the receiver, they are used in order to calculate the carrier phase. With this technique, no differential encoding is required and hardware implementation is possible with any kind of constellation. However, it will add an additional overhead.

The blind phase search approach depends on some crucial quantities such as the number of test phases B and the filter depth $W = 2N+1$. A large number of test phases makes the realization in hardware challenging, whereas a small number results in higher sensitivity penalty. Hence, based on [10], for 4-QAM and 16-QAM formats, B is set to 32. On the other hand, for higher order modulation formats, i.e. $M = 64$ or $M = 256$, B should be equal to $B = 64$.

The filter half depth N depends on the laser line-width times symbol rate product. It is used in order to smooth out the influences of additive white Gaussian noise on error distance by calculating the sum of W consecutive symbols rotated by the same phase angle $\theta^{(m)}$.

In order to analyze the performance of the scheme, we present in Fig. 3.46 the S-curve represented by the error distance as a function of phase compensation error θ_{error} for 4-, 16- and 64-QAM modulation format constellations.

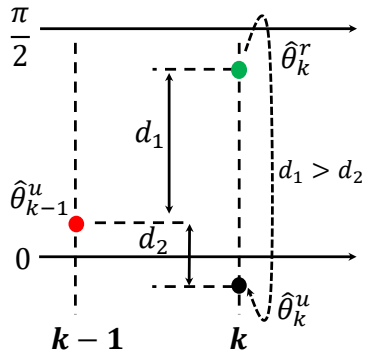

Figure 3.45 – Description of unwrapping function.

As shown in Fig. 3.46, near the zero compensation error angle, the error distance varies practically linearly as function of the phase error. Additionally, the lower the modulation order, the larger the slope of the linear zone response. In other words, the minimum distance notch becomes steeper for higher-order constellations. Therefore, higher angle resolutions are required for phase search, which make the computational complexity prohibitive, otherwise, cycle slips and phase errors occur.

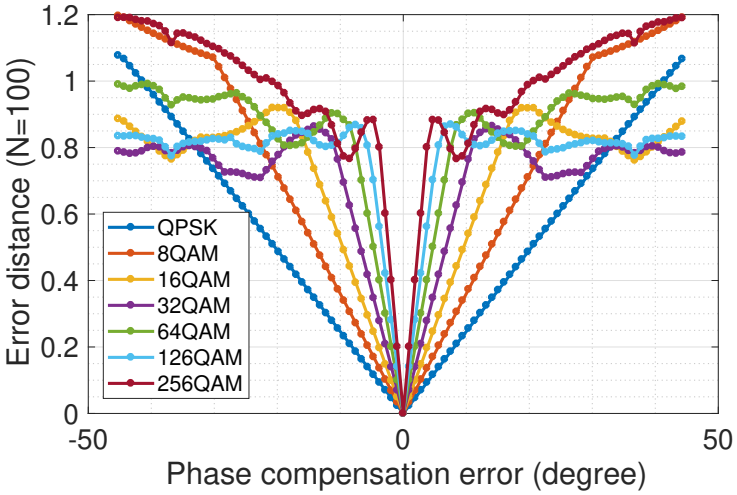

Figure 3.46 – Error distance as function of phase compensation error for different modulation formats.

Other proposed options were established in order to reduce the computational complexity such as the dual-stage or the semi-blind carrier recovery. As for the dual-stage technique, the idea behind this method is to initially calculate a coarse phase estimate using the BPS algorithm and then go to the second stage to get a fine estimate and increase the accuracy.

Several options for a second stage were proposed such as a decision directed feed-forward carrier recovery [127] or a second BPS stage with smaller search interval but higher resolution [128, 129]. Regarding the first stage, it must guarantee an estimated phase to be close or equal the global minimum of error distance.

One similar dual-stage blind approach is the semi-blind carrier recovery. It uses pilot-based carrier recovery in the first stage, and in the second stage, it can use Viterbi and Viterbi (V&V), decision-directed feed-forward options [130, 131]. These techniques do not require differential coding and reduce the overhead compared to pilot-based carrier recovery approach. However, the drawbacks of these techniques are related to the higher required computational complexity and the possibility of some burst errors.

Another promising technique proposed recently by Rozental [132] ensures carrier phase recovery called recursive probability weighted blind phase search (RW-BPS) . The approach uses fewer test phases $B = 6$ and requires a recursive loop to cumulate the best phase for tracking. In Fig. 3.47, the steps of the method are illustrated.

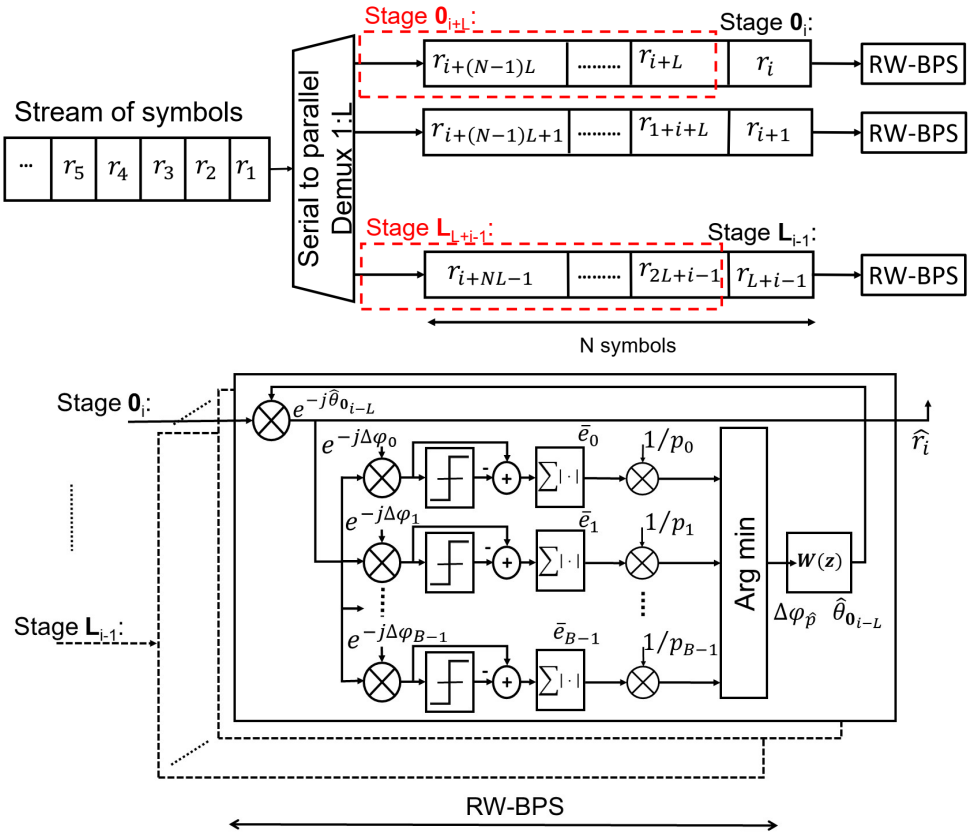

Figure 3.47 – Block diagram of the RW-BPS scheme with interleaving implementation in parallel processing.

First, the incremental test phases are computed according to the sum linewidth of signal and local oscillator lasers Δf, and the symbol period T. Assuming an i.i.d Gaussian random variables $N(0, \sigma^2)$, where $\sigma = \sqrt{2\pi\Delta f T}$, the phases are calculated by $\theta_i = (i + 0.5 - \frac{B}{2})\Delta\Phi$, where $\Delta\Phi = \frac{D}{B}$, where $D = 4\sigma$ represents the non-negligible probability interval which accounts for 99.99% of $\Delta\Phi$ occurrences (see Fig. 3.48).

L parallel processing blocks of length N are fed to B test phases. After phase rotation, the N symbols are put into a decision block and then the absolute distance between the rotated symbol before and after decision is calculated. Then, an average over the N symbols block is performed in order to reduce the impact of the additive noise. The test

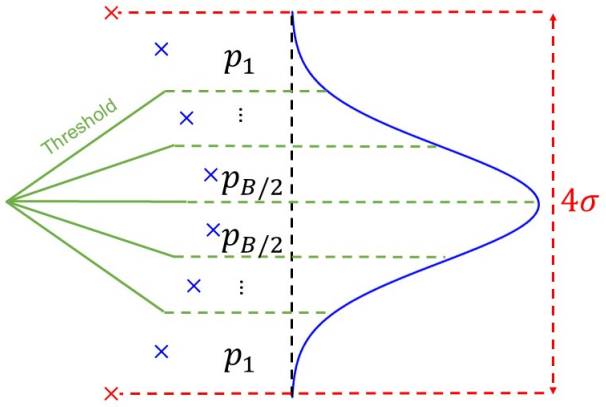

Figure 3.48 – Probabilities of the RW-BPS.

phase that ensures the minimum value of absolute distance is retained and stocked in the buffer to be used after a delay of L blocks. It is worth mentioning that for L processing paths, the phase rotation $\Delta\phi = \frac{D}{B}$, where $D = 4\sigma = 4\sqrt{2\pi\Delta f T L}$.

3.2.1.6 Summary

Thanks to digital coherent systems, the impairments have been transferred from the set-up to the digital domain, which role is to equalize and mitigate those distortions using advanced DSP. In this section, classic DSP algorithms used in coherent systems have been introduced and detailed.

As display of proof, Fig. 3.49 outlines the numerical results of 32 Gbaud signals (QPSK, 16-QAM) after 1000 km transmission with the typical DSP steps. Based on the proposed DSP sub-units, the constellation diagram has been completely retrieved and the imperfections have been undone after all these algorithms. In this demonstration, the signals were processed based on timing squared recovery algorithm for timing recovery, BASS for IQ imbalance compensation, CMA for the equalization. For carrier recovery, the signals were processed by the M^{th} power and FFT technique for frequency offset compensation and the BPS method for carrier phase recovery.

3.2.2 Joint Algorithms Dedicated to Two Impairments

In what follows, some of the state of the art algorithms endowed with the capacity to compensate jointly two different impairments are introduced. In this case, two imperfec-

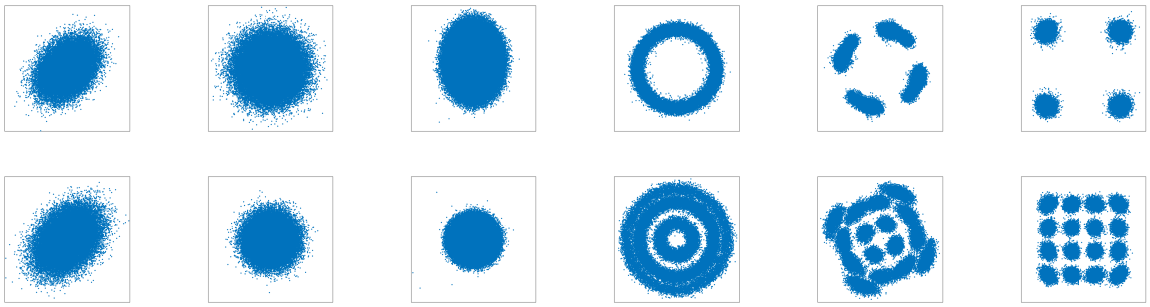

(a) (b) (c) (d) (e) (f)

Figure 3.49 – Constellation of different signals (top 4-QAM, bottom 16-QAM) after 1000 km transmission with DSP(a) after timing synchronization (b) after IQ imbalance compensation (c) after CD compensation (d) after PMD compensation (e) after CFO compensation (f) after CPR.

tions are eliminated in a joint manner with just one algorithm offering possible reduced computational complexity or better system performance. Generally, one algorithm can even compensate for more than two imperfections but in this part the focus will be on algorithms dealing with two impairments.

3.2.2.1 Joint PMD Compensation and Carrier Phase Recovery

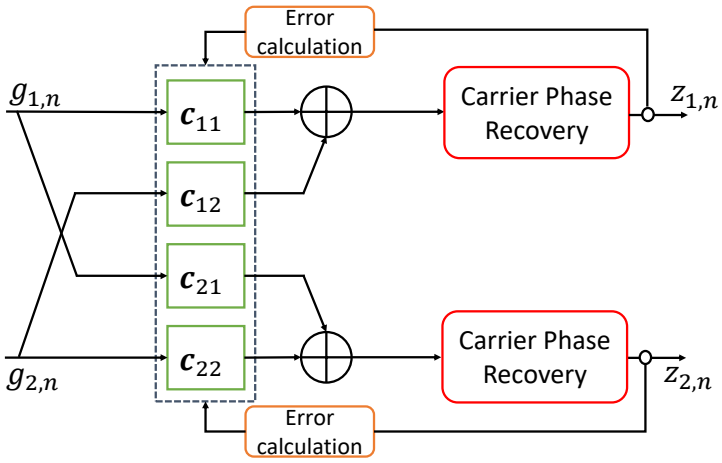

Figure 3.50 – Joint PMD compensation and carrier phase recovery.

In this section, polarization mode dispersion and carrier phase recovery are jointly mitigated using four multi-tap FIR filters connected with carrier phase compensation scheme operated in both polarizations. Such a block diagram is depicted in Fig. 3.50.

The multi-tap finite impulse response filters can be adapted based on different equalizer criteria. Also, carrier phase recovery can be implemented in its feed-forward or feedback schemes. The choice of an algorithm among others depends on the required system performance and hardware implementation. We propose a comparison of DD-LMS and CMA as MIMO equalizers. Also, the Viterbi and Viterbi and decision-directed CPR approaches are selected for comparison. The major strengths and weaknesses of several approaches are summarized in the Table 3.7.

Table 3.7 – Comparison of different equalizer and CPR approaches [133].

Equalizer	CPR	Strengths	Weaknesses	
DD-LMS	Decision-directed	-Small penalty especially for small linewidths -IIR filter can be used for reducing the computational complexity -Phase unwrapping is more robust than for NDA	-Not parallelizable due to CPE feedback	- Equalizer feedback - When used, IIR is susceptible to feedback issues
	V&V (serial/parallel)	-No CPE feedback -IIR filter can still be used in the non-feedforward part of the filter tail -If slow updates are allowed, it is the best option for parallel processing	-Feedforward section needed for parallel implementation	
CMA	Decision-directed	-Smaller penalty than CMA+NDA for large linewidths -IIR filter can be used to reduce the computational complexity -Phase unwrapping is more robust than for NDA	-Not parallelizable due to CPE feedback Higher penalty than DD-LMS+DD	- CMA equalizers can not achieve as low MSE as LMS based, especially for the 16-QAM non constant modulus constellation
	V&V (serial/parallel)	-No CPE feedback -IIR filter can still be used in the non-feedforward part of the filter tail	- Feedforward section needed for parallel implementation	

For illustration purpose, Fig. 3.51 shows the constellation diagram for a 32 Gbaud PM-4-QAM setup. The signals of X and Y polarizations at the input of the algorithm are disturbed with accumulated chromatic dispersion of 850 ps/nm, PMD parameter of 10 ps, polarization rotation of parameters $\alpha = 15°$ and $\theta = 30°$ as well as a laser phase noise of $\Delta fT = 10^{-5}$. Meanwhile, the algorithm outputs are compensated from these distortions.

In this simulation, the DD-LMS criterion was chosen for equalization and the decision-directed CPR approach was selected for carrier recovery. Regarding initial algorithm convergence, two ways could be established. The first option is to use a learning sequence known to the receiver also called data-aided mode. The difficulties in using data-aided mode come in the employing of an appropriate frame synchronization algorithm to temporally align the received signal and the training sequence, while the received signals are usually disturbed by interference between symbols as well as carrier frequency offset and phase noise. This makes the synchronization a hard task. The second option is to initiate the

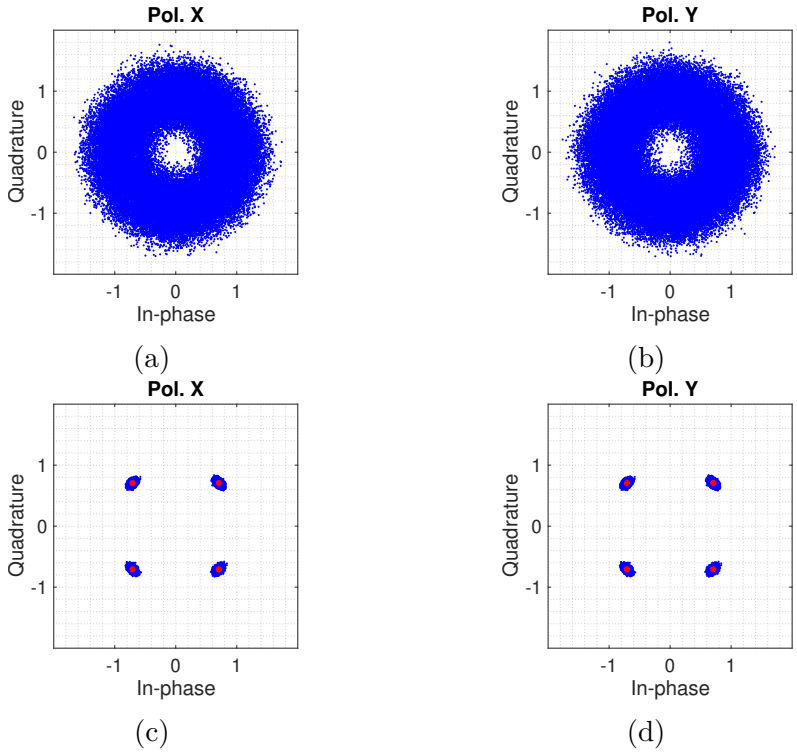

Figure 3.51 – Received constellation diagrams for 4-QAM (a-b) before joint compensation of PMD and carrier phase noise (c-d) after DD-LMS equalizer.

equalizer coefficients update with a blind approach, basically with the CMA algorithm, by decoupling it from carrier phase synchronization. Once the decisions are reliable enough, the receiver then switches to the joint mode.

Additional simulations were conducted for performance comparison between the joint and cascaded algorithms. For instance, the MSE metrics were computed while using MIMO equalizer based on the CMA criterion for polarization demultiplexing and the decision-directed CPR in both joint and cascaded schemes. Also, for further analysis, the joint DD-LMS criterion for polarization demultiplexing and decision-directed CPR algorithm was also implemented.

The simulation parameters are the same as those introduced for constellations visualization in Fig. 3.51. The constant step sizes are adjusted such that we have the same initial convergence. The steady state part is then evaluated for algorithms performance comparison.

As can be seen in Fig. 3.52(a), the CMA criterion is used for polarization demultiplexing and decision-directed CPR for carrier phase recovery. The MSE curves of both joint and

cascaded algorithms present exactly the same performance. In this case, the choice of implementing cascaded scheme or joint approach depends on the presented distortion altering the signals or the required hardware implementation complexity.

When using DD-LMS criterion jointly with the decision-directed CPR, the MSE metric shows a lower steady state level. In fact, it has been studied in digital communication systems that equalizers with decision-directed modes outperform those with algorithms purely relying on convergence toward multiple dense modulus. Thus, in this case, it is better to perform joint DD-LMS and decision-directed CPR for higher signal quality.

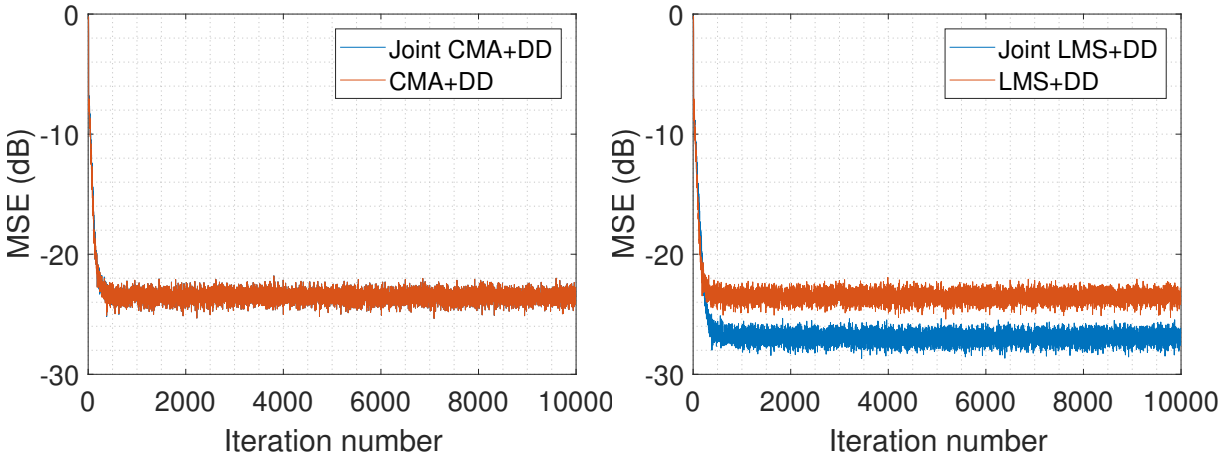

(a) (b)

Figure 3.52 – MSE curves of cascaded and joint algorithms for polarization mode compensation and carrier recovery.

3.2.2.2 Joint PMD and IQ Imbalance Compensation

Some proposed schemes modify the configuration of the conventional adaptive FIR filters in order to perform both IQ imbalance compensation and signal equalization and polarization demultiplexing. Indeed, in [134], the proposed filter modifications perform compensation for receiver-side IQ gain/phase mismatch and IQ delay skew simultaneously, in addition to the tasks of adaptive FIR filters consisting in the polarization demultiplexing and compensation for polarization-mode dispersion.

The proposed scheme in [134] is based on the configuration depicted in Fig. 3.53. As shown, the solution separates the real and imaginary parts of the altered signals before using a MIMO 4×4 real valued adaptive equalizer. In this case, I and Q can now be combined with different gains and delays. Therefore, compensating for IQ gain and

phase imbalance and IQ skew simultaneously, along with polarization demultiplexing and polarization-mode dispersion mitigation is achieved in a back-to-back configuration or in systems with small accumulated dispersion.

However, when accumulated chromatic dispersion is large, this approach fails. In fact, in this situation, a static CD filter is employed before the adaptive equalizer which mixes the real and imaginary part of the signal reducing the capacity of the 4×4 equalizer to compensate the skew. Moreover, this compensation is not applicable to system with Tx-IQ imbalance. Also, the computation complexity of such a scheme is relatively high as it would consume higher logic element for field programmable gate array hardware realization, especially hardware multiplier.

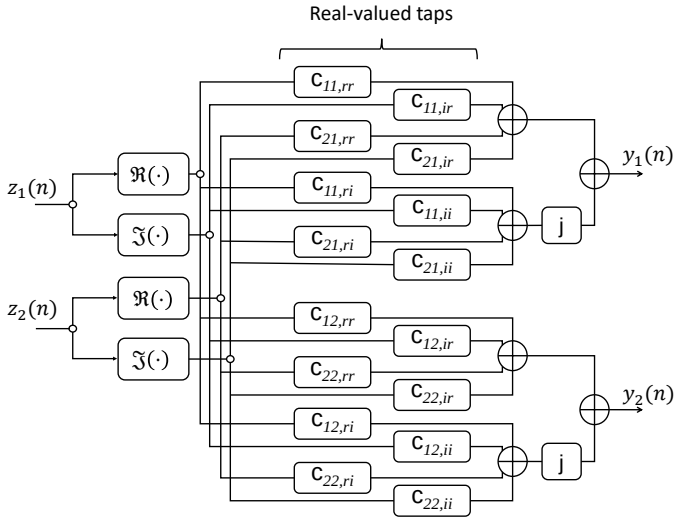

Figure 3.53 – Joint PMD and IQ imbalance compensation with 4×4 FIR filters.

Another alternative scheme called widely linear equalization [3] is utilized for joint PMD and IQ imbalance compensation. This algorithm is derived from the 4×4 MIMO approach as real-valued MIMO filter is equivalent to an augmented complex-valued MIMO filter in which complex valued signals and their complex conjugates are inputs. Thus, augmented complex-valued MIMO filters are known as widely linear filters (see Fig. 3.54).

It is well known that this equalizer is able to compensate for time skew between the IQ components at the receiver side. However, this approach does not take into account the effect of chromatic dispersion compensation prior to the adaptive equalizer, required in long-haul non-dispersion managed systems. Hence, if there is an accumulation of CD through fiber propagation, and if CD compensation is followed by a widely linear MIMO filter, IQ skew can no longer be compensated by using only the widely linear MIMO filter.

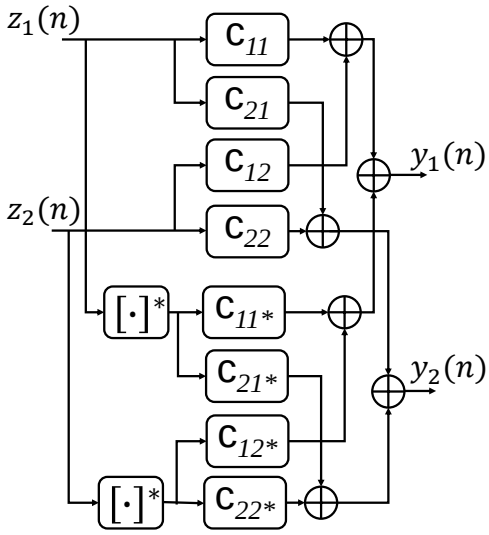

Figure 3.54 – Joint PMD and IQ imbalance compensation with widely linear equalizer.

Also, this algorithm significantly increases the already stressed receiver complexity by at least a factor of two.

3.2.2.3 Joint PMD Compensation and Timing Synchronization

The adaptive digital equalizer cannot operate normally without synchronous sampled data, whereas simple timing error detection algorithm [135] cannot provide precisely the synchronous sampled data based on uncompensated sampled data, because the timing-error detection algorithm is seriously impacted by CD and PMD.

Therefore, some proposed schemes merge the butterfly structured adaptive equalizer in a digital timing recovery loop. It not only effectively solves the aforementioned incompatible problem, but also performs synchronization, equalization and polarization demultiplexing simultaneously without any extra computational cost.

For solving this issue without additional hardware effort, a butterfly-structured adaptive equalizer is added between the interpolator and the timing error detector, as shown in Fig. 3.55.

In this combined structure, the signal can be compensated for residual chromatic dispersion distortion by the equalizer before entering the timing error detector. Thus, the interpolator can complete timing adjustment to output synchronous signals for satisfying the requirement of equalizer.

Therefore, inner modules of the combined structure can operate in a complementar way

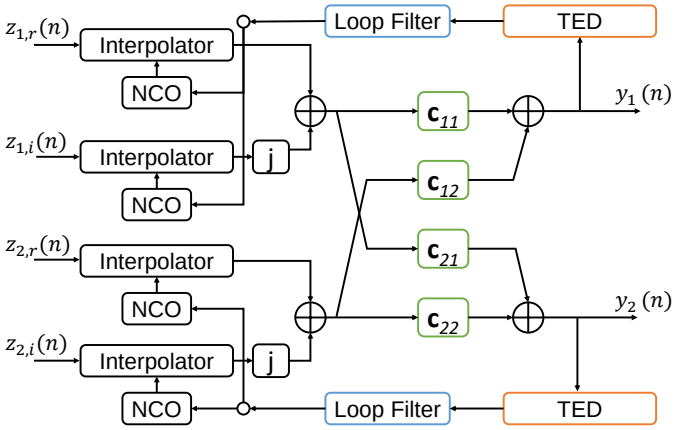

Figure 3.55 – Joint PMD compensation and digital timing recovery.

to complete synchronization, equalization and polarization demultiplexing synchronously.

The problem with this technique is related to its serial timing synchronization structure, which is not valid for the high symbol rate, due to the impact of the current digital hardware devices. Thus, parallel implementation is needed for operation on field programmable gate array (FPGA) platform. Moreover, the presented scheme in [135] are all-digital timing recovery loops with numerically controlled oscillators. Input samples of this kind of loop are provided by an asynchronous clock. So the loop cannot provide the actual DSP chip with a synchronous real clock, which is needed to serve as working clock for subsequent function blocks such as polarization demultiplexing.

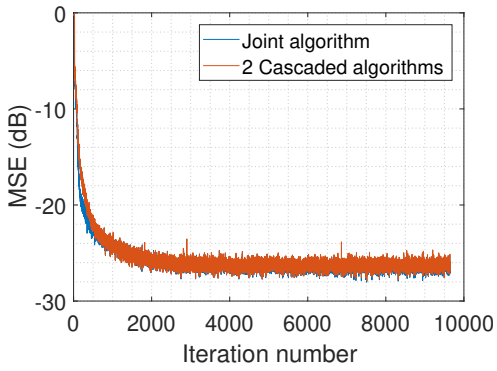

Figure 3.56 – MSE curves of cascaded and joint algorithms for polarization mode commpensation and timing offset recovery.

Through simulations, we will study two different schemes for such polarization demultiplexing and timing recovery. The first scheme is best described as cascaded square timing algorithm for timing synchronization followed by MIMO equalizer based on the CMA

criterion. This has the benefits of sharing the relatively demanding task for each DSP block. The second scheme is illustrated in Fig. 3.55 and uses joint PMD compensation and timing synchronization.

In this simulation, the 16-QAM signals of X and Y polarizations are altered by a fixed E_s/N_0 of 30 dB, residual chromatic dispersion of 850 ps/nm, polarization rotation of parameters $\alpha = 15°$ and $\theta = 30°$ and a constant normalized timing offset of 0.4. The MSE evaluation of the two schemes are plotted. As depicted in Fig. 3.56, the two approaches present the same MSE performance. The choice of a scheme over another one will then depend on the behavior of the algorithm in the presence of other imperfections, the used modulation order and also its complexity.

3.3 Conclusion

In this chapter, we presented the main single mode fiber propagation impairments. We detailed the sources of degradation of the signal quality in the linear transmission regime. The examined impairments have two main categories, the former are generated in the fiber channel, and the latter are hardware related impairments. We refer to the first category as static chromatic dispersion and dynamic polarization effects. On the other hand, the hardware related impairments consist of the carrier frequency offset, the carrier phase noise, sampling frequency offset and IQ imbalances.

Next, typical and conventional algorithms reported in the literature were presented for distortions mitigation. Numerical simulations were conducted to highlight the effectiveness of such algorithms to suppress transmission or hardware related impairments that may alter the optical signal. The introduced digital signal processing algorithms could be employed in joint or independent techniques with the aim of lowering complexity and/or improving performance. For example, joint processing approaches have the advantages of less noise generation, but such methods could degrade the system performance if they are processing some unsolicited impairments or if they are not able to reliably track the dynamic variations of the distortion. Thus, combination between independent algorithms and joint ones is useful to let the algorithm processing the task it is able to perform. In the next chapter, we propose two independent algorithms dedicated to carrier phase recovery and suggest a method for joint polarization demultiplexing and IQ imbalance compensation.

Chapter 4

Proposed DSP Algorithms

In the previous chapters, coherent fiber optical communication system used with advanced digital signal processing techniques have been introduced and discussed enabling the use of multiple dimensions of light waves together with electrical domain compensation of transmission impairments.

In this part, the main challenge is not only to develop digital signal processing techniques that counteract the propagation and the system impairments but also that respond to several requirements such as flexible communication, convergence speed, numerical complexity and other qualitative performance metrics (MSE, BER, EVM, etc.(see section 2.2)).

In fact, optical transponders have been deployed to operate at specified fixed data rates and designed to achieve a target distance given a specific OSNR tolerance at the receiver. In this case, transponders are deployed under the maximum-reach conditions while less demanding network applications are used. This leads to an available system margin that exceeds what is required from the system link budget. Consequently, the solution is to provide a transponder with programmable modulation parameters and DSP that are able to select from among a given set of higher-order modulation formats the suitable one to maintain the adequate channel data rate, spectral efficiency, and/or reach. Link and format specific target will be chosen depending on the application or service that the channel carries over a link. On the other hand, the change in modulation formats will require DSP algorithms that have an extremely fast speed of convergence and that can adaptively tune their parameters while still providing the most accurate results. Also, the DSP algorithms need to handle the complexity and hardware implementation challenges.

The thesis mainly focuses on techniques used for increasing the spectral efficiency namely polarization division multiplexing, and methods to ensure reliable optical communications notably for laser phase noise mitigation within a flexible communication context.

Polarization demultiplexing and IQ imbalance distortions could be handled with a joint algorithm proposed in section 4.1. The principle of the proposed algorithm is reported in addition to numerical simulations which are conducted to present the method's

performance compared to cascaded single impairment algorithms as well as its tolerance against other polarization-related effects such as DGD and PDL. Also, the behavior of such a method is studied in a flexible communication context and in case of dynamic polarization multiplexing.

Laser phase noise mitigation is studied during this thesis in section 4.2, the carrier phase recovery is handled through the proposition of two different algorithms. The first approach presents a feedback CPR with the capability to operate at different signal-to-noise ratios for a 16-QAM modulation format and the second method is a recursive and parallelized modulation format independent tool which offers less computation complexity compared to the conventional decision-directed CPR algorithm. The proposed algorithms are implemented and evaluated under the presence of residual carrier frequency offset. Other numerical simulations were performed either to justify the choice of the system parameters or to highlight the system performance.

4.1 Blind Joint Polarization Demultiplexing and IQ Imbalance Compensation

In this part, both polarization rotation and IQ imbalance distortions are handled in a modulation independent and joint manner. As the Tx-IQ imbalance distortion is more critical than the Rx-IQ imbalance [136], the introduced algorithm is mainly investigated in presence of Tx-IQ imbalance. The study is then extended in the presence of both Tx and Rx-IQ imbalances.

The proposed algorithm is compared to two cascaded mono-impairment algorithms: one for polarization demultiplexing operation and the other for IQ imbalance compensation. The proposed algorithm is also tested in the presence of other polarization-related effects such as polarization dependent loss, differential group delay as well as Rx-IQ imbalance distortion. The robustness of the algorithm in a flexible communication context and dynamic polarization multiplexing is also reported. Finally, the numerical complexity of the algorithm is evaluated.

4.1.1 Principle of the Approach

In this section, models of the transmission impairments are detailed, including those originating from the linear channel as well as IQ imbalance at the transmitter side. In the

following, it is assumed that the signals on each polarization are modeled as complex-valued random signals with zero mean and unit variance.

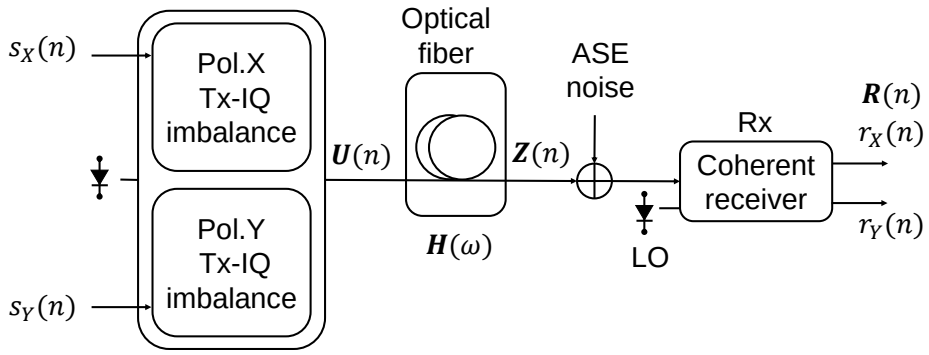

Figure 4.1 – Model of optical transmission.

Fig. 4.1 shows the model of the dual-polarization transmission system with polarization and phase diversity coherent detection. Let $s_p(n)$ be the source signals in both polarizations, i.e. for $p = X$ or $p = Y$. In the presence of IQ phase and amplitude imbalance at the transmitter, the complex representation of a continuous-wave optical signal at angular frequency ω on the p-polarization can be expressed as

$$\begin{aligned} m_{Tx,p}(t) &= k_{1,p}e^{-j\omega t} + k_{2,p}e^{j\omega t}, \\ k_{1,p} &= \cos(\varphi_{p,Tx}) + j\epsilon_{p,Tx}\sin(\varphi_{p,Tx}), \\ k_{2,p} &= \epsilon_{p,Tx}\cos(\varphi_{p,Tx}) + j\sin(\varphi_{p,Tx}). \end{aligned} \tag{4.1}$$

The parameters $\epsilon_{p,Tx}, \varphi_{p,Tx}$ represent the amplitude and phase imbalance induced at the transmitter side for the signal in the p-polarization, respectively. More precisely, the IQ imbalance distortion is configured by 4 parameters $(\epsilon_{X,Tx}, \varphi_{X,Tx})$ and $(\epsilon_{Y,Tx}, \varphi_{Y,Tx})$. Based on (4.1), the signal modulated on each polarization can, in the presence of IQ imbalance, be expressed as [137]

$$u_p(n) = k_{1,p}s_p(n) + k_{2,p}s_p^*(n). \tag{4.2}$$

The distorted signals in X and Y polarizations at the discrete time n can be expressed vectorially by $\mathbf{U}(n) = [u_X(n),\, u_Y(n)]^T$. The signals $\mathbf{U}(n)$ on each polarization are then multiplexed and transmitted over the optical fiber. The optical fiber linear impairments are modeled by

$$\mathbf{H}(\omega) = \mathbf{J}\mathbf{D}(\omega)\mathbf{P}C(z,\omega), \tag{4.3}$$

where $\mathbf{J} = \begin{pmatrix} \cos\alpha & e^{-j\theta}\sin\alpha \\ -e^{j\theta}\sin\alpha & \cos\alpha \end{pmatrix}$ is a Jones matrix representation of the random polarization rotation with random phase shifts between the two axes [138]. α and θ are azimuth and elevation rotation angles, respectively, that can make the signal state of polarization sweep over the entire Poincare sphere.

$\mathbf{D}(\omega) = \begin{pmatrix} e^{j\omega\tau/2} & 0 \\ 0 & e^{-j\omega\tau/2} \end{pmatrix}$ represents the polarization mode dispersion induced differential group delay τ between both polarization waves whose typical values range between 1 and 100 ps [139].

$\mathbf{P} = \begin{pmatrix} \sqrt{1+\gamma} & 0 \\ 0 & \sqrt{1-\gamma} \end{pmatrix}$ represents the polarization dependent loss, responsible for the imbalanced attenuation of orthogonal polarizations. The PDL in its most common definition refers to the difference between the highest and lowest gains of the system expressed in dB.

$C(z,\omega) = e^{-\frac{j\lambda^2 Dz}{4\pi c}\omega^2}$ corresponds to the frequency response of chromatic dispersion where λ is the central wavelength of the transmitted optical wave, D is the fiber chromatic dispersion coefficient, z is the propagation distance and c is the speed of light in vacuum [140].

As mentioned earlier, fiber non-linearities will be neglected and we suppose in this model that chromatic dispersion is perfectly compensated by a digital finite impulse response filter with a fixed number of taps in the DSP unit. The DGD and PDL effects will be omited in this part and their related effects will be studied later. With these assumptions, the optical fiber model will be limited to the polarization rotator operation i.e. $\mathbf{H} = \mathbf{J} = \begin{pmatrix} h_1 & h_2 \\ h_3 & h_4 \end{pmatrix}$.

Next, the expression of the signals $\mathbf{R}(n)$ corrupted by ASE are derived

$$\mathbf{R}(n) = \mathbf{J}\mathbf{U}(n) + \mathbf{N}(n), \tag{4.4}$$

with $\mathbf{N}(n) = [n_X(n), n_Y(n)]^T$, where $n_X(n)$ and $n_Y(n)$ are two independent complex circular white zero-mean Gaussian random variables with variance $N_0/2$ per real dimension. N_0 is the power spectral density (per polarization) of ASE noise introduced by all the optical amplifiers along the link. We can derive from equations (4.2) and (4.4), the expression of the distorted signals related to the source signals in the form

$$\underline{\mathbf{R}}(n) = \mathbf{G}\underline{\mathbf{S}}(n) + \underline{\mathbf{N}}(n). \tag{4.5}$$

If $\mathbf{S}(n) = [s_X(n),\, s_Y(n)]^T$, where s_X and s_Y are the signals in both X and Y polarizations and $[.]^T$ is the transpose of the vector, then $\underline{\mathbf{S}}(n) \stackrel{\text{def}}{=} [s_X(n),\, {s_X}^*(n),\, s_Y(n),\, {s_Y}^*(n)]^T$. In this case, $\underline{\mathbf{R}}(n)$, $\underline{\mathbf{S}}(n)$ and $\underline{\mathbf{N}}(n)$ are 4×1 dimension vectors. In fact, as according to (4.2) the effect of IQ imbalance can be represented as a linear combination of the signal and its conjugate, it is worthy to represent the global model as a 4×1 vector taking into account the signal in both X and Y polarizations (for polarization mixing purpose) and their complex conjugates. Here, the $\mathbf{G}$ matrix includes the effects of both Tx-IQ imbalance and polarization rotation and is expressed by

$$\mathbf{G} = \begin{pmatrix} h_1 k_{1,X} & h_1 k_{2,X} & h_2 k_{1,Y} & h_2 k_{2,Y} \\ h_1 k_{2,X}^* & h_1 k_{1,X}^* & h_2^* k_{2,Y}^* & h_2^* k_{1,Y}^* \\ h_3 k_{1,X} & h_3 k_{2,X} & h_4 k_{1,Y} & h_4 k_{2,Y} \\ h_3^* k_{2,X}^* & h_3^* k_{1,X}^* & h_4 k_{2,Y}^* & h_4 k_{1,Y}^* \end{pmatrix}. \tag{4.6}$$

Note that in the absence of IQ imbalance distorsions ($\epsilon_{p,Tx} = 0$, $\varphi_{p,Tx} = 0$) and when the polarizations are not mixed ($\alpha = 0$, $\theta = 0$), the matrix G becomes diagonal. A mathematical proof of the method to compute the $\mathbf{G}$ matrix elements is proposed in Appendix A.

4.1.2 Proposed Approach

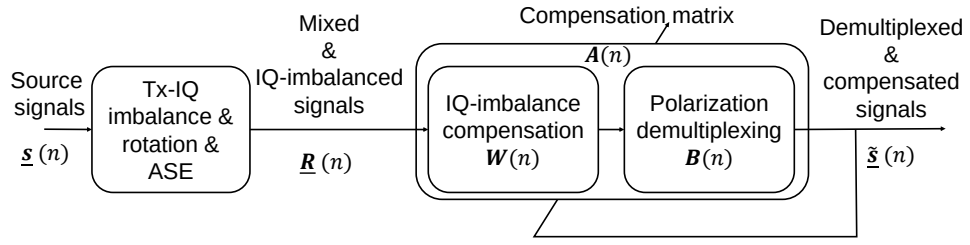

Figure 4.2 – Model of optical transmission system.

Considering equation (4.5), our goal is to find the compensation matrix $\mathbf{A}(n)$ that converges to the inverse of $\mathbf{G}$ in an adaptive manner (see Fig. 4.2). In fact, adaptive algorithms update the estimation of the separating system after receiving each new sample, and produce the output immediately which makes them well-suited to real-time applications and allows to track the solution when the mixture is slowly varying, for instance when the sources are moving.

Hence, the demultiplexed and compensated signals $\underline{\tilde{\mathbf{S}}}(n)$ are given by

$$\underline{\tilde{\mathbf{S}}}(n) = \mathbf{A}(n)\,\mathbf{G}\,\underline{\mathbf{S}}(n) + \mathbf{A}(n)\,\underline{\mathbf{N}}(n) \xrightarrow{n\to\infty} \underline{\mathbf{S}}(n) + \mathbf{A}\,\underline{\mathbf{N}}(n), \tag{4.7}$$

where $\mathbf{A}(n) \xrightarrow{n\to\infty} \mathbf{A}$.

To present the principle of our proposed algorithm, two blind algorithms are considered and modified to respond to our joint and blind requirements. The first is the blind adaptive source separation used for IQ imbalance compensation [5] and the second is the equivariant adaptive separation via independence (EASI) algorithm used for polarization demultiplexing [141].

Blind source separation deals with the recovery of sources based on observing their linear mixture. The term blind is used to highlight that no prior knowledge of the mixing process or the temporal structure of the source signal is needed but only the statistical proprieties are utilized. The idea behind blind signal estimation for IQ imbalance (or the BASS algorithm) is to whiten the received signals so that the complex conjugate component introduced by the IQ imbalance is eliminated. We remind that this algorithm requires circular or proper complex signals and uses second-order statistics for decorrelation. Also, the assumption of statistical independence of the original sources must be verified. Practically, this whitening problem is solved by using the principle of the natural gradient that leads to an adaptive rule converging to the first-order approximation of the inverse square root of the input covariance matrix. The modified adaptive rule according to our study context is given by

$$\mathbf{W}(n+1) = \mathbf{W}(n) - \mu[\underline{\mathbf{S}}_W(n)\underline{\mathbf{S}}_W(n)^H - I_4]\mathbf{W}(n), \tag{4.8}$$

where $\mathbf{W}(n)$ is the whitening 4×4 matrix, μ is the adaptation step size and $\underline{\mathbf{S}}_W(n) = \mathbf{W}(n)\underline{\mathbf{R}}(n)$ are the adjusted signals. In fact the algorithm as presented in paper [5] reports the whitening process in a framework of a single polarization and where the signal is rather expressed in 2 dimensions (representing its in-phase and quadrature components). In our case, we proposed an extension of the work and adapt it for polarization multiplexed systems. Indeed, IQ imbalance compensation operates on the two polarizations at the same time rather than one, so the input signal is expressed as a 4×1 vector as the in-phase and quadrature components of each polarization are used for the whitening process. This is possible since the circular property of the signal constellation is maintained (the statistical expectation $\mathbb{E}(s_p^2) = 0$ holds). In fact, the original I and Q

signals of each polarization are statistically independent (not correlated) which permit them to be recovered blindly using a signal separation algorithm.

At this stage, Tx-IQ imbalance compensation is performed. However, the signals are kept polarization-multiplexed and another blind source separation algorithm needs to be introduced. Hence, we employ the EASI method for demultiplexing the two mixed signals.

The EASI algorithm consists of two stages: the first stage is a whitening stage, which only provides decorrelated signals. The second stage, modeled by an orthogonal matrix, uses high order statistics for completing the separation. The EASI algorithm is related to a serial updating idea, which requires the computation of the so-called natural or relative gradient. Also, it requires some assumptions, namely statistical conditions on the input signals. In fact, this method involves mutually statistically independent zero mean and unit variance target signals, which is the case of our context of work. Finally, the unknown mixing matrix (which, in our case, is the $\mathbf{H}$ matrix) must be full rank.

Considering only polarization rotation, linear instantaneous mixtures $\mathbf{R}(n) = \mathbf{H}\mathbf{S}(n)$, where $\mathbf{S}(n) = [s_X(n)\, s_Y(n)]^T$ denotes the source vector, $\mathbf{R}(n) = [r_X(n)\, r_Y(n)]^T$ is the observation vector, and $\mathbf{H}$ is 2×2 regular mixing matrix. Then the objective of a source separation algorithm is to estimate a separating matrix $\mathbf{B}$ such that the outputs $\tilde{\mathbf{S}} = \mathbf{B}\mathbf{R}$ be the same as source signals.

The EASI algorithm [141] is achieved by minimizing a contrast function $\varphi(\mathbf{B}) = \mathbb{E}[\mathrm{f}(\mathbf{Y})]$ with respect to $\mathbf{B}$. This leads to the following serial updating algorithm

$$\mathbf{B}(n+1) = (\mathbf{I}_2 - \mu\nabla_\varphi(\mathbf{B}(n)))\mathbf{B}(n), \tag{4.9}$$

where $\nabla_\varphi(\mathbf{B}(n)))$ denotes the relative (or natural) gradient

$$\nabla_\varphi(\mathbf{B}(n)) = \nabla\mathbb{E}[\mathrm{f}(\mathbf{Y})] = \mathbb{E}[\mathrm{f}'(\tilde{\mathbf{S}})\tilde{\mathbf{S}}^H]. \tag{4.10}$$

Consequently, the stochastic version of (4.9) becomes

$$\mathbf{B}(n+1) = (\mathbf{I}_2 - \mu\mathrm{g}(\tilde{\mathbf{S}})\tilde{\mathbf{S}}^H)\mathbf{B}(n), \tag{4.11}$$

where $\mathrm{g} = \mathrm{f}'$.

Implementing EASI requires then to chose a component-wise and fixed $\mathrm{g}(\,\cdot\,)$ (e.g. cubic polynomials). Moreover, for avoiding trivial solution $\tilde{\mathbf{S}} = \mathbf{0}$, a normalization term $(\tilde{\mathbf{S}}\tilde{\mathbf{S}}^H - \mathbf{I}_2)$ is added in Eq. 4.11.

Now, when implementing the algorithm on signals distorted by Tx-IQ imbalance $\mathbf{U}(n)$, $\mathbf{R}(n)$ are the received signals, and $\tilde{\mathbf{S}}(n)$ is the EASI algorithm output, then the separating matrix update equation from the normalized EASI algorithm has the form

$$\mathbf{B}(n+1) = \mathbf{B}(n) - \mu\Big[\frac{\tilde{\mathbf{S}}(n)\tilde{\mathbf{S}}(n)^H - I_2}{1+\mu\tilde{\mathbf{S}}(n)^H\tilde{\mathbf{S}}(n)} + \frac{g(\tilde{\mathbf{S}}(n))\tilde{\mathbf{S}}(n)^H - \tilde{\mathbf{S}}(n)g(\tilde{\mathbf{S}}(n))^H}{1+\mu\Big|\tilde{\mathbf{S}}(n)^H g(\tilde{\mathbf{S}}(n))\Big|}\Big]\mathbf{B}(n), \quad (4.12)$$

and $\tilde{\mathbf{S}}(n) = \mathbf{B}(n)\mathbf{R}(n)$, where μ is the adaptation step size, $\mathbf{B}(n)$ is the 2×2 separation matrix and g($\cdot$) is a component-wise nonlinear odd function. In our model, the basic cubic non linearity function is used and it is expressed by $g_i(\tilde{\mathbf{S}}(n)) = \Big|s_p\Big|^2 s_p$ for $p \in \{X, Y\}$.

In this case, signal sources are successfully separated but the IQ imbalance persists. To combine both IQ compensation and demultiplexing procedures, a one stage solution is proposed. In the light of (4.8) and (4.12), the global updating rule is deduced. Instead of just looking to the signals in $\mathbf{R}(n)$, we take into consideration its complex conjugate components and we replace it by $\underline{\mathbf{R}}(n)$. This is possible since the EASI and BASS hypotheses are verified. In fact, the introduced signals are mutually statistically circular with zero mean and unit variance. By construction, the first term $(\underline{\tilde{\mathbf{S}}}(n)\underline{\tilde{\mathbf{S}}}(n)^H - I_4)$ accomplishes blind signal estimation for IQ imbalance compensation and the second term $(g(\underline{\tilde{\mathbf{S}}}(n))\underline{\tilde{\mathbf{S}}}(n)^H - \underline{\tilde{\mathbf{S}}}(n)g(\underline{\tilde{\mathbf{S}}}(n))^H)$ implements the demultiplexing operation. Therefore, the proposed updating equation for both IQ imbalance compensation and polarization demultiplexing is given by

$$\mathbf{A}(n+1) = \mathbf{A}(n) - \mu\Big[\frac{\underline{\tilde{\mathbf{S}}}(n)\underline{\tilde{\mathbf{S}}}(n)^H - I_4}{1+\mu\underline{\tilde{\mathbf{S}}}(n)^H\underline{\tilde{\mathbf{S}}}(n)} + \frac{g(\underline{\tilde{\mathbf{S}}}(n))\underline{\tilde{\mathbf{S}}}(n)^H - \underline{\tilde{\mathbf{S}}}(n)g(\underline{\tilde{\mathbf{S}}}(n))^H}{1+\mu\Big|\underline{\tilde{\mathbf{S}}}(n)^H g(\underline{\tilde{\mathbf{S}}}(n))\Big|}\Big]\mathbf{A}(n). \quad (4.13)$$

Hence, the matrix $\mathbf{A}$ combines the whitening process operated by $\mathbf{W}(n)$ and the demultiplexing task handled by $\mathbf{B}(n)$. Furthermore, it iteratively converges to $\mathbf{G}^{-1}$ ensuring the recovery of the source signals.

Generally, algorithms of dynamic equalization realizing polarization demultiplexing suppose an independent convergence of their two outputs. They employ a cost function that does not discriminate between the two equalized signals. Hence, it is common that this algorithm converges to a setup that produces the same transmitted signal at both equalizer outputs, usually the one that arrived with higher power at the receiver. In such a situation, a singularity problem could appear, i.e. a phenomenon which yields the same equalizer output on both polarizations, preventing successful polarization demultiplexing [140, 142].

Fig. 4.3(a) presents the singularity problem. In this case, the modulus of all coefficients of the mixture matrix $\mathbf{A}(n) \times \mathbf{G}$ converges to the same value leading to the loss of the transmitted signals.

In fact, when the azimuth $\alpha = 45°$, the received signal is given by

$$\begin{pmatrix} r_X \\ r_Y \end{pmatrix} = \mathbf{H} \begin{pmatrix} s_X \\ s_Y \end{pmatrix} = \sqrt{2}/2 \begin{pmatrix} s_X + s_Y e^{-j\theta} \\ s_X e^{j\theta + j\pi} + s_Y \end{pmatrix} \tag{4.14}$$

Because "Joint" is no sensitive to the phase complex field, s_p and $s_p e^{j\theta}$ cannot be distinguished by the algorithm and thus there is no stochastic difference expected between r_X and r_Y. Therefore, if we take the trivial initial tap setting of $\mathbf{A} = I_4$, the two tributaries are equivalent for s_X and s_Y, and "Joint" may converge to a situation where the two outputs meet the same tributary data.

To deal with this issue, some methods using a cross correlation term of the cost function of the equalizer or relying on the selection of a proper initial taps have been proposed [140, 142, 143]. In our joint algorithm, we have dealt with the latter solution.

This procedure determines initial values of tap coefficients so that degeneration of the two tributaries is prevented. In fact, singularity problem depends greatly on the initialization coefficients of the equalizer. Hence, when the coefficients are initialized in a way to converge to a global minimum and that they are far from a local minimum of the cost function, the algorithm will operate correctly and allow straightforward polarization demultiplexing.

Indeed, when considering only the polarization rotation impairments ($k_{1,p} = 1$ and $k_{2,p} = 0$), the channel transfer matrix of the fiber is given by

$$\mathbf{G} = \begin{pmatrix} h_1 & 0 & h_2 & 0 \\ 0 & h_1^* & 0 & h_2^* \\ h_3 & 0 & h_4 & 0 \\ 0 & h_3^* & 0 & h_4^* \end{pmatrix}. \tag{4.15}$$

The optimal equalizer is given by the inverse of the $\mathbf{G}$ matrix as follows

$$\mathbf{G}^{-1} = \begin{pmatrix} \upsilon_1 & 0 & \upsilon_2 & 0 \\ 0 & \upsilon_1^* & 0 & \upsilon_2^* \\ \upsilon_3 & 0 & \upsilon_4 & 0 \\ 0 & \upsilon_3^* & 0 & \upsilon_4^* \end{pmatrix}, \tag{4.16}$$

where υ_1, υ_2, υ_3, υ_4, are expressed from h_1, h_2, h_3, h_4. Further mathematical details of these coefficients are detailed in Appendix A.

This matrix has a particular structure and could be exploited for the initialization of "Joint" coefficients. The following relationships between the components can be used for the initialization of the adaptive matrix $\mathbf{A}(n) = a_{ij}(n)$, $(i,j) = 1 \dots 4$ according to $a_{11} = a_{22}^*$, $a_{13} = a_{24}^*$, $a_{31} = a_{42}^*$, $a_{33} = a_{44}^*$ and the other components are set to zero.

In this case, the singularity problem can be resolved. This additional constraint, which is added in the initial convergence, is released after a certain time. In fact, in a second step, the compensation update for the two polarizations is performed independently. The proposed "Joint" method is as follows

Algorithm 1 "Joint"

1: Set the initial tap values $\mathbf{A}(n)$ by its trivial identity matrix
2: Run iteratively the Eq. 4.13
3: Fix the relation between the matrix $\mathbf{A}(n)$ coefficients based on the expression introduced in Eq. 4.16
4: Repeat previous steps until $\mathbf{A}(n)$ is considered to have reached a convergence
5: Release the constraint and continue "Joint" adaptation according to the Eq.4.13.

The problem is solved as shown in Fig. 4.3(b) , where the diagonal coefficients of the mixture matrix $\mathbf{A}(n) \times \mathbf{G}$ converge towards 1 (orange lines), the anti-diagonal elements converge to 0 (green lines) as well as all the rest of the matrix coefficients (blue lines).

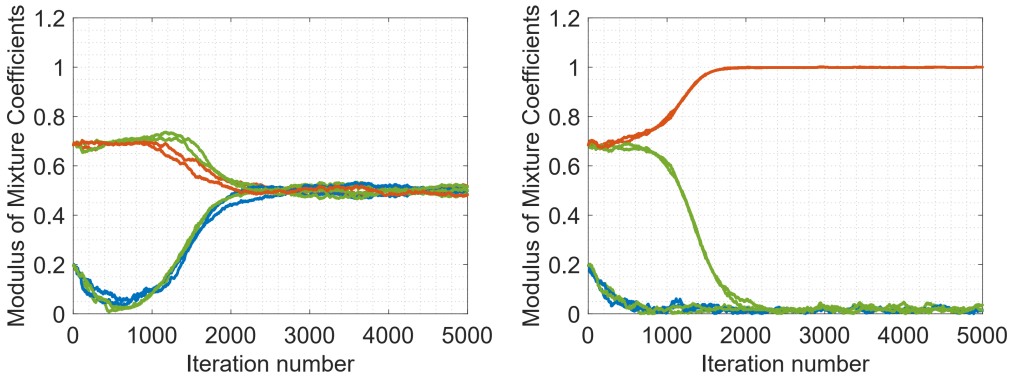

(a) (b)

Figure 4.3 – Modulus of mixture coefficients convergence (a) without proposed initialization procedure (singularity issue), (b) with proposed initialization procedure.

Note that the initialization of the matrix $\mathbf{A}(n)$ is the same for both simulations in Fig. 4.3(a) and Fig. 4.3(b). Hence, the singularity circumvention is performed iteratively

by placing constraints on the matrix $\mathbf{A}(n)$ coefficients as previously detailed.

4.1.3 Numerical Results

In this section, we evaluate the performance of our proposed joint Tx-IQ imbalance compensation and polarization demultiplexing algorithm, hereafter called "joint", compared to the conventional CMA equalizer for polarization demultiplexing cascaded with the blind adaptive source separation algorithm for IQ imbalance compensation (applied twice on each polarization), hereafter labeled "CMA+BASS". The reason to work with the BASS algorithm rather than GSOP is based on earlier results [144], where it has been shown that BASS is less computationally complex and performs better in terms of error vector magnitude and bit error rate than GSOP. Several metrics (MSE, EVM and BER) were calculated to compare the two aforementioned methods (see section 2.2).

4.1.3.1 MSE Performance

Initially, the MSE is calculated. Here, the MSE is obtained by comparing the reference signal, which is obtained by optimal compensation, with the signals compensated by either the "joint" algorithm or by "CMA (with/without) BASS". Optimal compensation is obtained by mitigating the distortions of the received signals by the matrix $\mathbf{G}^{-1}$. Also, we have investigated the performance of "RDE + BASS", so that we can justify the use of the CMA rather than the RDE (see section 2.2) for M-QAM constellation with M greater than 4.

Fig. 4.4 represents the MSE curves of the "joint" algorithm and cascaded "CMA+BASS" employed for 16-QAM modulation in three different use cases: (a) absence of Tx-IQ imbalance, (b) presence of Tx-IQ imbalance without "BASS" algorithm, and (c) presence of Tx-IQ imbalance with "BASS" algorithm. The choice of these three use cases is established to demonstrate the contribution of the "joint" algorithm with respect to the presence or not of the Tx-IQ imbalance distortion. Also, the MSE curve of "RDE + BASS" is illustrated to explain the choice of the application of the CMA algorithm even for higher order modulation formats.

For fair comparison, note that the adaptive equalizers based on the CMA or the RDE criteria are one tap to perform only polarization demultiplexing.

For all numerical simulations, the signal-to-noise ratio is defined as the E_s/N_0. In all use cases, the SNR is fixed in simulations to 15 dB, the chosen operating point for

polarization rotation is set to ($\alpha = 30°, \theta = 50°$), and the Tx-IQ imbalances parameters are ($\epsilon_{p,\mathrm{Tx}} = 0.1, \varphi_{p,\mathrm{Tx}} = 6°$). The MSE calculation is averaged over 500 simulation runs and over the two polarizations. Also, it is worth mentioning that all step sizes are constant and fixed in a way that initial convergence speed is the same for all algorithms.

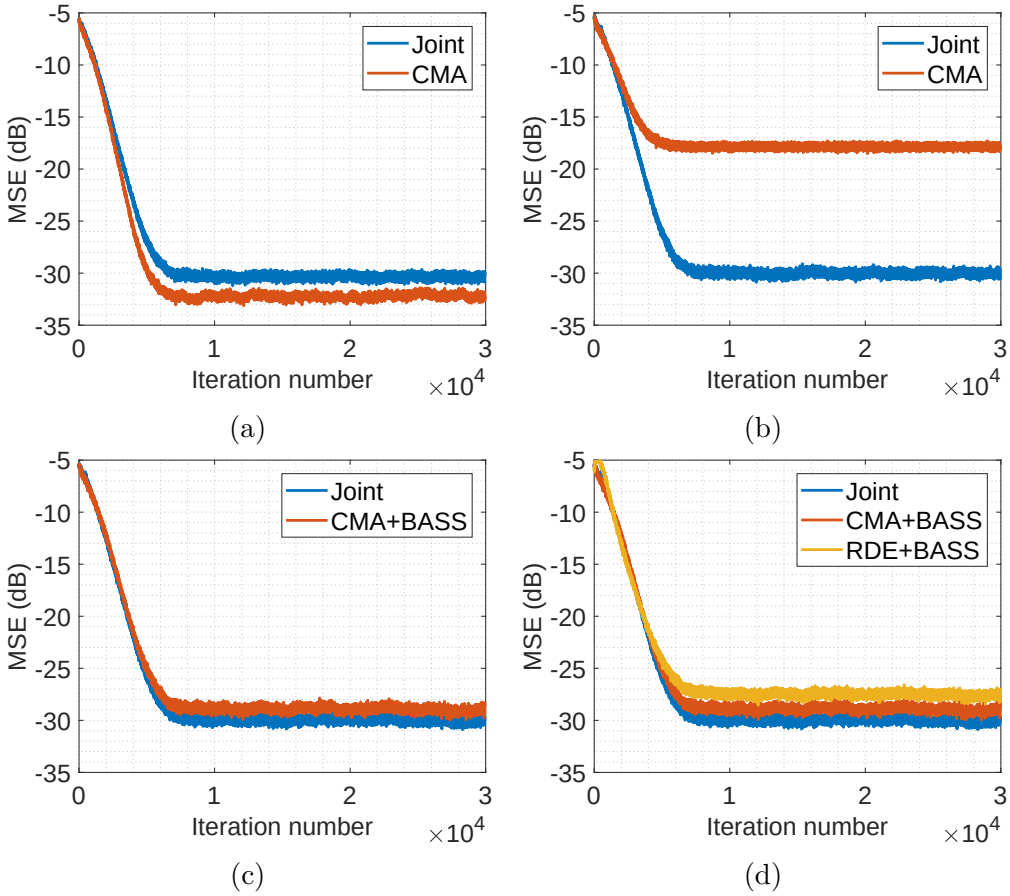

Figure 4.4 – MSE curves over 500 runs ($E_s/N_0 = 15$ dB, $\alpha = 30°, \theta = 50°$) (a) without Tx-IQ imbalance, (b) with Tx-IQ imbalance ($\epsilon_{p,\mathrm{Tx}} = 0.1$, $\varphi_{p,\mathrm{Tx}} = 6°$) and without BASS compensation, (c) with introduced Tx-IQ imbalance ($\epsilon_{p,\mathrm{Tx}} = 0.1$, $\varphi_{p,\mathrm{Tx}} = 6°$) using "CMA+BASS", (d) with introduced Tx-IQ ($\epsilon_{p,\mathrm{Tx}} = 0.1$, $\varphi_{p,\mathrm{Tx}} = 6°$) using "RDE+BASS".

Algorithms are therefore compared only by exploring the steady state convergence. In fact, for a specific application, the choice of one adaptive filter or algorithm over another could be determined by one or more of these factors: rate of convergence, mis-adjustment of the steady state (also called the excess mean square error), computational requirements and numerical robustness. The computational requirements and the numerical robustness are related to a hardware implementation issue. The rate of convergence is defined as the number of iterations required for the algorithm to converge close enough to a stationary

environment. The mis-adjustment of the steady state provides a quantitative measure of the amount by which the final value of the mean square error deviates from the minimum mean square error that is produced by optimal compensation. Regarding numerical simulations, by setting the algorithms to the same rate of convergence, we can compare their performance regarding the steady state mis-adjustment.

Fig. 4.4(a) shows that when there is no Tx-IQ imbalance, the "joint" algorithm has a slightly poorer steady-state performance, i.e. the "joint" algorithm converges to a higher MSE value than CMA. This can be explained by the additional work of IQ imbalance compensation that has been done by the "joint" algorithm.

When adding Tx-IQ imbalance, and without its compensation by the BASS algorithm, Fig. 4.4(b) depicts a huge steady-state performance difference between the two methods. In fact, the "joint" algorithm maintains the same steady-state level as without Tx-IQ imbalance, whereas the CMA algorithm proves to be non-operational for IQ imbalance compensation. But, by appending the BASS algorithm (Fig. 4.4(c)), the two-cascaded algorithms "CMA+BASS" can reach the same level of performance as the "joint" algorithm. Note that in this simulation, the in-phase and quadrature component of the CMA equalized outputs are required to be adjusted with a gain control coefficient. On the other hand, even though the used RDE algorithm quantizes the radius according to the number of possible rings, the system performance does not present any improvement in the MSE sense. In fact, since the signals are deteriorated by the IQ imbalance, the RDE threshold rays will not necessarily place the constellation symbols in their right location. This justifies the reason of working with the conventional CMA rather than the RDE.

To sum up, the "joint" and "CMA+BASS" algorithms were compared in terms of MSE performance. The step sizes of both algorithms were adjusted to have the same rate of convergence while comparing the level of the steady state output. It is shown that when signals are distorted by Tx-IQ imbalance, "joint" slightly outperforms "CMA+BASS".

4.1.3.2 EVM Performance

We evaluate in Fig. 4.5 the average -EVM surfaces (over X and Y polarizations) as a function of Tx-IQ gain imbalance (Fig. 4.5(a)) and Tx-IQ phase imbalance (Fig. 4.5(b)) for 16-QAM modulation in the presence of the same aforementioned polarization rotation parameters ($\alpha = 30°, \theta = 50°$) and 15 dB SNR. The higher -EVM curve is, the better the performance is.

It is worthy to mention that the performance is evaluated in the steady-state regime

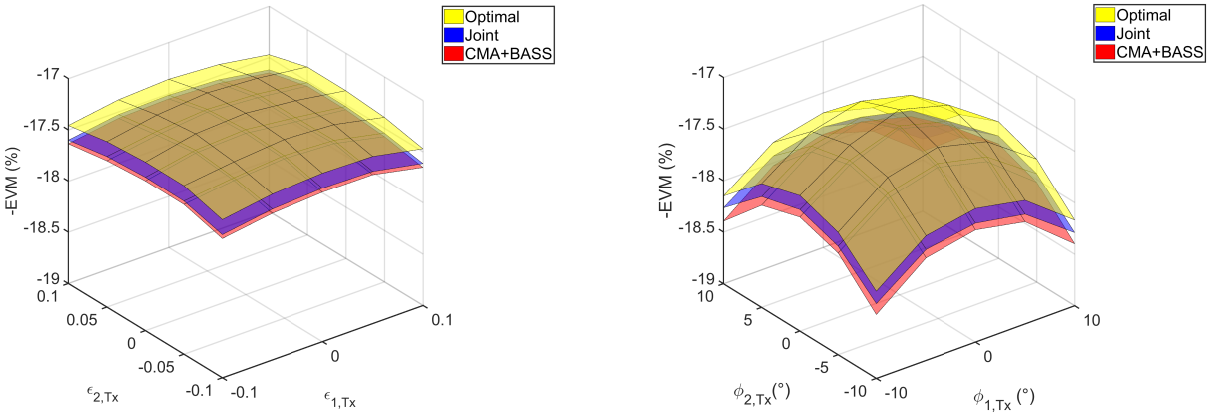

(a) (b)

Figure 4.5 – Average -EVM surfaces as a function of the Tx-IQ imbalance parameters with 16-QAM modulation ($E_s/N_0 = 15$ dB, $\alpha = 30°$, $\theta = 50°$) (a) gain imbalance (b) phase imbalance.

(the asymptotic convergence part in the MSE sense). As can be seen, both "joint" and "CMA+BASS" achievements are degraded in the presence of any of the impairments (either the Tx-IQ gain or the Tx-IQ phase imbalance). Additionally, the phase imbalance is a more limiting effect than the gain imbalance. However, in all cases, the "joint" algorithm maintains better performance compared to "CMA+BASS". Indeed, the "joint" algorithm results in 0.2% better EVM values than "CMA+BASS" over the range of phase imbalances, whereas the results of the two algorithms are globally similar when gain imbalance is introduced.

Fig. 4.6 depicts simulated performance of the presented algorithms in terms of -EVM when varying the polarization rotation parameters (α and θ), in the presence of 0.1 Tx-IQ gain imbalance and 6° Tx-IQ phase imbalance. The results are still averaged over X and Y polarizations and the introduced SNR is 15 dB. We show that the "joint" algorithm outperforms cascaded "CMA+BASS" regardless of the introduced polarization rotation parameters.

In this part, the -EVM performance of "joint" compared to "CMA+BASS" is investigated while tuning the parameters of polarization rotation, Tx-IQ gain imbalance and Tx-IQ phase imbalance. Regardless of the explored values, "joint" maintains better results than "CMA+BASS".

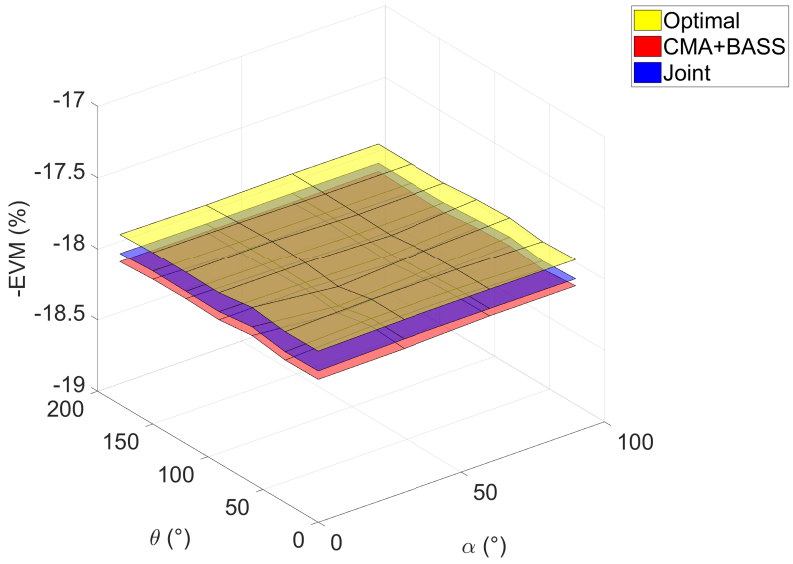

Figure 4.6 – Average -EVM surfaces as a function of the polarization rotation parameters with 16-QAM modulation ($E_s/N_0 = 15$ dB, $\epsilon_{p,\mathrm{Tx}} = 0.1$, $\varphi_{p,\mathrm{Tx}} = 6°$).

4.1.3.3 System Performance with Tx-IQ Imbalance

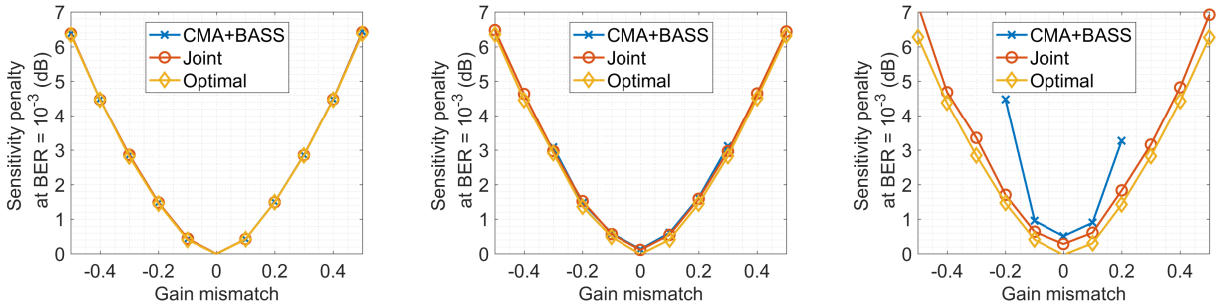

Figure 4.7 – E_b/N_0 penalty at BER of 10^{-3} as a function of the Tx-IQ gain mismatch when no Tx-IQ phase mismatch is included ($\alpha = 30°, \theta = 50°$) (a) 4-QAM, (b) 16-QAM, (c) 64-QAM.

Finally, for the performance evaluation of different orders of modulation formats, BER calculation is done to investigate the penalty for the energy-per-bit-to-noise spectral-power-density ratio at BER of 10^{-3}. The results depicted in Fig. 4.7 concern the X polarization tributary. Nevertheless, similar results are found for the Y polarization

tributary. Fig. 4.7 shows the E_b/N_0 penalty for various values of introduced Tx-IQ gain mismatch when no Tx-IQ phase mismatch is included. Thus, we vary the same gain of $\epsilon_{p,\mathrm{Tx}}$ in both polarizations and assume a phase imbalance $\phi_{p,\mathrm{Tx}} = 0°$. The polarization rotation parameters are set to $\alpha = 30°, \theta = 50°$. As far as the E_b/N_0 penalty is less than 1 dB, tolerances of "CMA+BASS" are roughly within the range of [−0.15, 0.15] dB for 4-QAM and 16-QAM formats and [−0.03, 0.03] dB for 64-QAM format. Nevertheless, with our "joint" algorithm, the tolerances for gain mismatch are maintained within the range of [−0.15, 0.15] dB for 4-, 16-QAM formats and [−0.10, 0.10] dB 64-QAM systems, when the E_b/N_0 penalty is less than 1 dB (see Table 4.1).

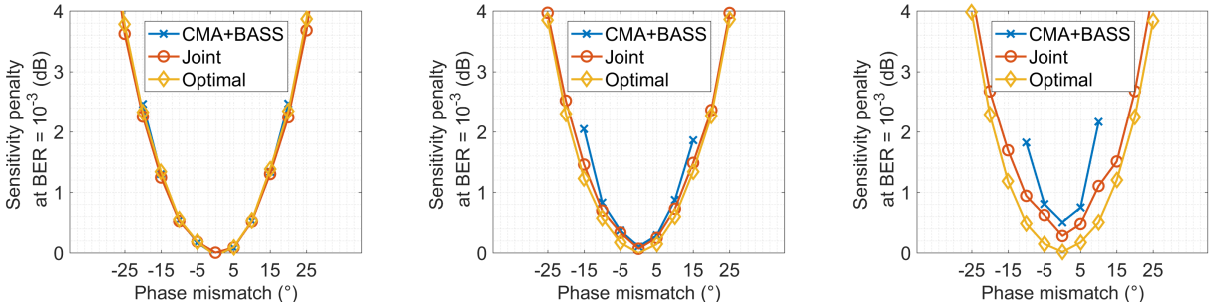

(a) (b) (c)

Figure 4.8 – E_b/N_0 penalty at BER of 10^{-3} as a function of the IQ phase mismatch when no IQ gain mismatch is included ($\alpha = 30°, \theta = 50°$) (a) 4-QAM, (b) 16-QAM, (c) 64-QAM.

Also, The E_b/N_0 penalty as a function of the Tx-IQ phase mismatch is shown in Fig. 4.8 when no Tx-IQ gain imbalance is included.

As far as the E_b/N_0 penalty is less than 1 dB, tolerances of our joint algorithm for the IQ phase mismatch are up to 13°, 12°, 7° for 4-, 16-, 64-QAM formats, respectively. However, with the "CMA+BASS" algorithm tolerances for IQ phase mismatch are up to 13°, 10°, 6° for 4-, 16-, 64-QAM formats, respectively (see Table 4.2).

As can be seen in Fig. 4.7 and Fig. 4.8, the "joint" method presents roughly the same performance as the CMA cascaded with the BASS algorithm in terms of penalty metric at BER of 10^{-3} for 4-QAM and 16-QAM formats. The distortion in EVM of the "CMA+BASS" compared to the "joint" did not have much impact on the algorithm in terms of BER, but it is problematic for higher order modulation formats (64-QAM in this case).

Also, for high introduced values of IQ gain and phase mismatch, the "CMA+BASS" algorithm seems to be not-operational as the received signals are not recovered which

is not the case for the "joint" algorithm that performs roughly like the optimal solution especially with 4-QAM and 16-QAM systems.

In this part, we studied by simulations the performance of our proposed algorithm in terms of MSE, EVM, BER metrics using different order of modulated signals. In terms of MSE, it was shown that the proposed algorithm results in better steady state performance compared to the cascaded CMA and BASS algorithms. As for EVM metric, the two algorithms exhibit roughly the same performance for 16-QAM format. For 64-QAM systems, "joint" offers higher tolerance in both Tx-IQ phase and gain mismatch for E_b/N_0 penalty less than 1 dB. Next, the robustness of the "joint" approach to different polarization related effects, CD as well as Rx-IQ imbalance are explored.

Table 4.1 – Maximum absolute value of gain mismatch for E_b/N_0 penalty less than 1 dB.

Modulation format	4-QAM	16-QAM	64-QAM
"CMA+BASS"	0.15	0.15	0.03
"Joint"	0.15	0.15	0.1
"Optimal"	0.15	0.15	0.15

Table 4.2 – Maximum absolute value of phase mismatch for E_b/N_0 penalty less than 1 dB.

Modulation format	4-QAM	16-QAM	64-QAM
"CMA+BASS"	13	10	6
"Joint"	13	12	17
"Optimal"	13	12.7	13.7

4.1.4 Robustness of the Approach Against PDL, DGD, CD and Rx-IQ Imbalance

In this part, we evaluate the robustness of the proposed method in presence of polarization dependent loss. The performance of the approach in presence of differential group delay as well as chromatic dispersion is also studied. Diverse metrics are presented for qualitative evaluation. In case of system performance degradation, some techniques will be presented to handle the issue.

4.1.4.1 Robustness Against PDL

The proposed "joint" algorithm is tested under the presence of polarization dependent loss. When there is non-zero PDL, numerical simulations prove that the algorithm works well and it could compensate for the PDL between the two polarizations.

Fig. 4.9 depicts the effects of 3 dB added PDL for 4-QAM format, combined with Tx -IQ imbalance with $\epsilon_{p,Tx} = 0.1$ as Tx-IQ gain mismatch and $\delta_{p,Tx} = 6°$ as Tx-IQ phase mismatch. The SNR is fixed in simulation to 30 dB and the chosen operating point for polarization rotation is set to $(\alpha = 30°, \theta = 50°)$.The choice of this level of SNR is to better stress the impact of the PDL without corrupting the constellation symbols with too much noise. The blue dots represent Pol.X signal and the orange dots represent Pol.Y signal.

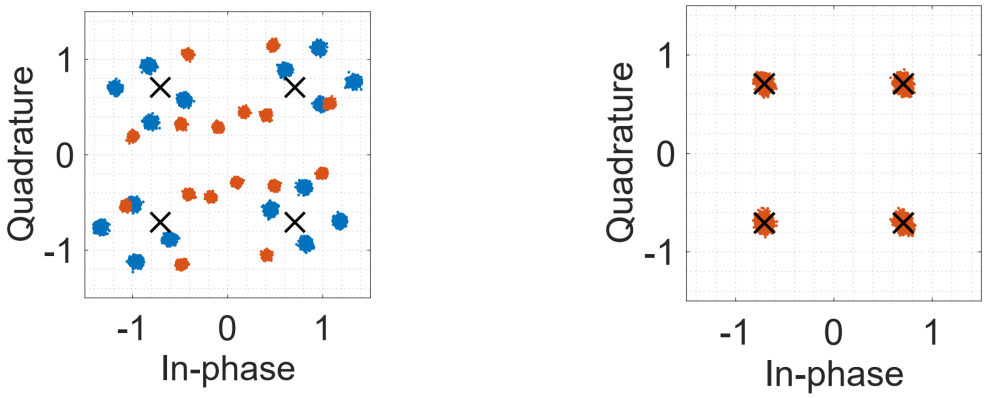

Figure 4.9 – Constellation diagrams ($E_s/N_0 = 15$ dB, $\epsilon_{p,\mathrm{Tx}} = 0.1$, $\varphi_{p,\mathrm{Tx}} = 6°$, $\alpha = 30°$, $\theta = 50°$) (a) multiplexed 4-QAM signals distorted by Tx-IQ imbalance and 3 dB PDL effects (b) compensation of PDL and Tx-IQ imbalance effect via joint algorithm

The "joint" algorithm is able to compensate both PDL and IQ imbalance effects without difficulty. Its structure is inherent in separating the polarizations and in transforming the outputs to centered and unit variance signals. Again, the key is from this term $(\underline{\tilde{\mathbf{S}}}(n)\underline{\tilde{\mathbf{S}}}(n)^H - I_4)$ where the output signals are circular and with unitary variance.

The E_b/N_0 penalty at BER of 10^{-3} is investigated using "joint" and "CMA+BASS" over 4- , 16- and 64-QAM (see Fig. 4.10). Simulations were carried on signals distorted with Tx-IQ imbalance and multiplexed with the rotational matrix with the same aforementioned parameters. The PDL value leading to a 1 dB SNR penalty at BER = 10^{-3} for "joint" and "CMA+BASS" has been listed in Table 4.3. The comparison between our "joint" method

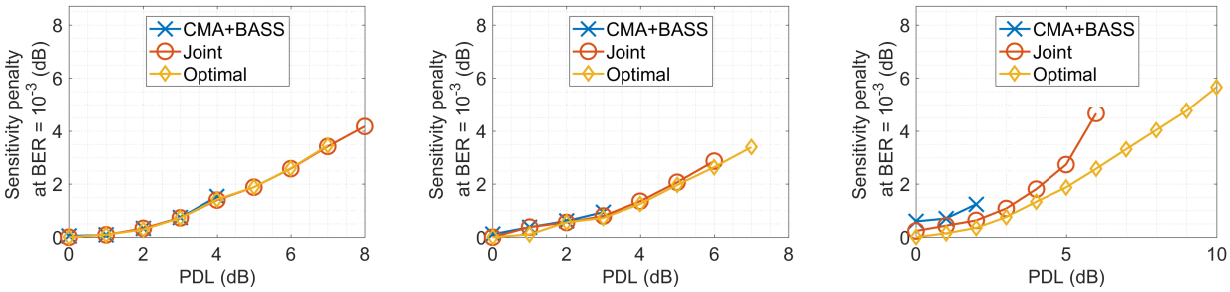

Figure 4.10 – E_b/N_0 penalty at BER of 10^{-3} as a function of the PDL (a) 4-QAM, (b) 16-QAM, (c) 64-QAM.

and "CMA+BASS" is illustrated in Table 4.3.

Table 4.3 – Tolerances in PDL for E_b/N_0 penalty less than 1 dB.

Modulation format	4-QAM	16-QAM	64-QAM
"CMA+BASS"	0.7	1.5	1.5
"Joint"	0.7	1.8	2.8
"Optimal"	1	2.2	3.4

It can be observed that both "joint" and "CMA+BASS" schemes perform similarly in 4- and 16-QAM systems. Nevertheless, our configuration outperforms "CMA+BASS" in 64-QAM as well as at large PDL values.

4.1.4.2 Robustness Against DGD

When there is non-zero differential group delay, the algorithm looses its effectiveness especially when the residual DGD is high. In fact, as the algorithm is a one-tap-compensator, the two signals (i.e. instantaneous mixing of the 2 received signals) must be synchronized to be able to omit the multiplexing effect. Numerical simulations were carried out in presence of a SNR value fixed to 30 dB, polarization rotation of $(\alpha = 30°, \theta = 50°)$ and residual delays, with respect to the symbol duration, varying from -0.5 up to 0.5. In this study, PDL is neglected.

Fig. 4.11 depicts the effect of uncompensated residual delay on the performance of the "joint" algorithm. The SNR quantity highlights the system performance. The higher the SNR value, the better the system performance. Nevertheless, as can be seen in Fig. 4.11, the residual delay has a negative impact on the overall system achievements. Thus, the

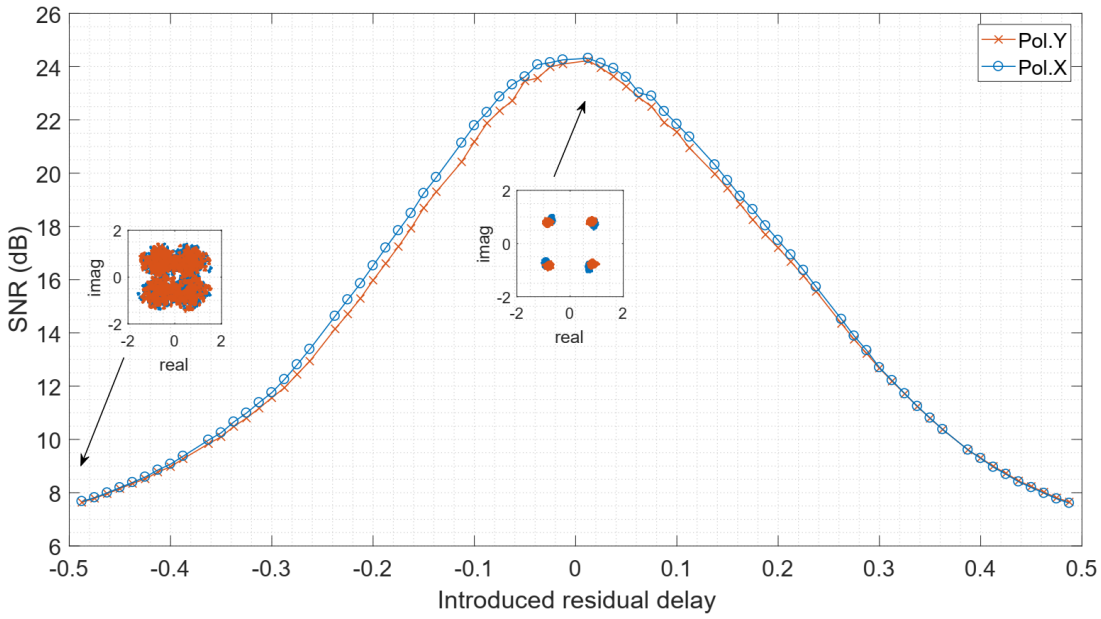

Figure 4.11 – Effect of DGD on the SNR of the compensated signals ($E_s/N_0 = 30$ dB, $\alpha = 30°$, $\theta = 50°$).

"joint" algorithm is not functional in the presence of strong DGD.

This issue is resolved by compensating the DGD before operating the joint algorithm. This could be done by identifying the introduced DGD value through the utilization of the Wiener filter. The idea is to turn off data on one polarization while sending it on the other. Then, at the reception, a Wiener filter is constructed to estimate and to compensate for the DGD issue.

Numerical simulations were accomplished to verify the effectiveness of the solution. For instance, 32 Gbaud PDM-4-QAM signals are generated and altered by the presence of 30 ps of introduced DGD. The polarization rotation parameters are set to $\alpha = 30°$ and $\theta = 50°$, the added $E_s/N_0 = 30$ dB and the Tx-IQ imbalance parameters are of values $\epsilon_{p,Tx} = 0.1$ and $\varphi_{p,Tx} = 6°$ for both polarizations. Note that the oversampling factor is $\mathcal{N} = 8$. In this simulation, 2000 of the transmitted symbols are used to the estimation of the DGD.

Fig. 4.12(a) presents the resulted group delay of the constructed Wiener filter. The estimated group delay of the Wiener filter is consistent with the values introduced in the simulation. Indeed, by averaging the estimated group delay on the frequencies comprising the useful signal (values where the frequencies are less than $1/\mathcal{N}$,), we find a value of 7.65. This value is close to the numerical level of the introduced DGD calculated

by DGD $\times \mathcal{N} \times f_s = 30 \cdot 10^{-12} \times 8 \times 32 \cdot 10^9 = 7.68$. Finally, the signals are properly compensated after cascaded Wiener filter and the "joint" algorithm as seen in Fig. 4.12(b).

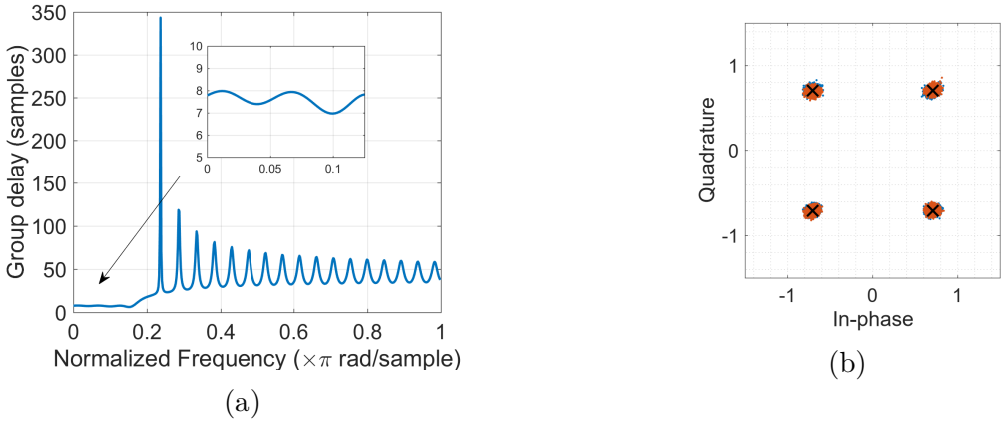

(a) (b)

Figure 4.12 – 32 Gbaud PDM-4-QAM signals (DGD = 30 ps, $E_s/N_0 = 30$ dB, $\alpha = 30°$, $\theta = 50°$, $\epsilon_{p,Tx} = 0.1$ and $\varphi_{p,Tx} = 6°$) (a) group delay of the resulted Wiener filter, (b) signals after cascaded Wiener filter and the joint algorithm.

4.1.4.3 Robustness Against CD

The robustness of our presented "joint" algorithm in the presence of chromatic dispersion is analyzed and discussed in this part. Simulations were conducted under $E_s/N_0 = 20$ dB and a 32 Gbaud PM-16-QAM transmission. Tx-IQ imbalance distortion is introduced which parameters are set to $\epsilon_{p,Tx} = 0.1$ and $\varphi_{p,Tx} = 6°$ and different values of residual CD are applied in the transmission. The diagram of the proposed schemes established to recover the received signals are depicted in Fig. 4.13.

The average MSE over the two output signals $\tilde{s}_1$ and $\tilde{s}_2$ is evaluated in two different cases. The first case, the static CD compensation is omitted so that the tolerance comparison between "joint" and "CMA+BASS" for various values of introduced residual CD could be established. In the second simulation, the signals at the input of "joint" as well as "CMA+BASS" have been already compensated for CD using two static filters with the appropriate number of taps (varying with respect to the introduced CD value). In both cases, the 2×2 MIMO CMA equalizer length is fixed to $L = 3 \cdot \mathcal{N} + 1$ with $\mathcal{N} = 8$.

As can be seen in Fig. 4.14(a), cascaded "CMA+BASS" presents higher performance in terms of -MSE than the "joint" algorithm in presence of low values of residual CD (< 1000 ps/nm). For higher residual CD, both algorithms get roughly the same

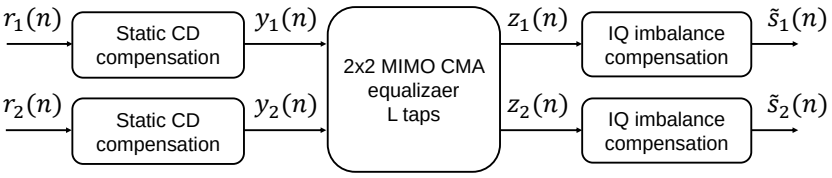

(a)

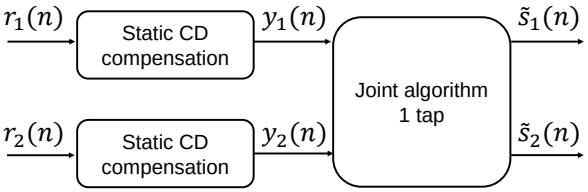

(b)

Figure 4.13 – Diagram of residual CD compensation (a) using L taps of 4 FIR filters (b) using the joint algorithm.

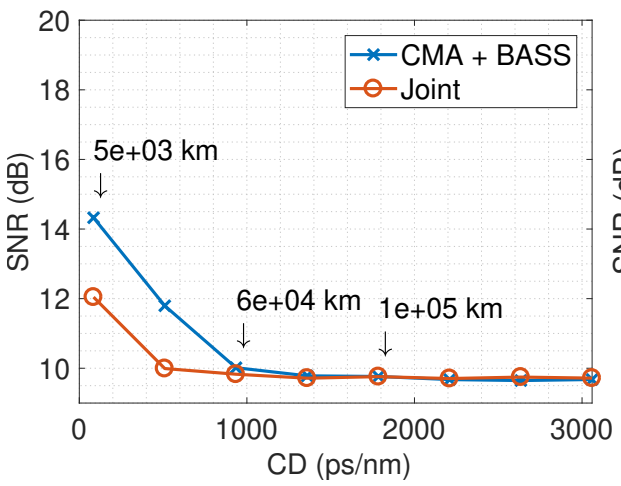

(a)

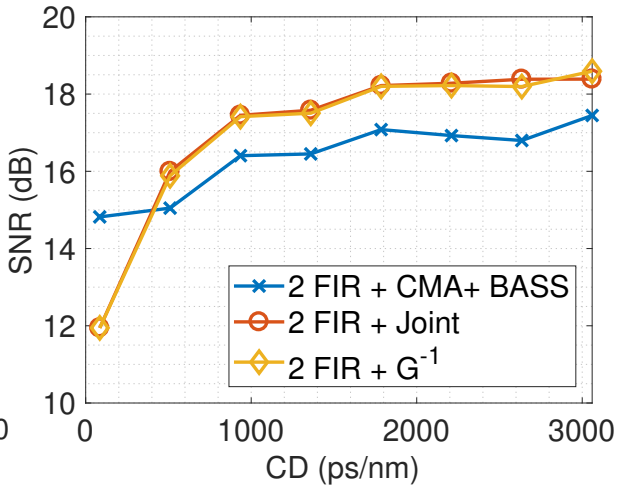

(b)

Figure 4.14 – SNR versus residual CD (a) without static CD compensation (b) with static CD compensation.

performance. The reason is that the number of taps of the CMA is small for this high values of CD so that its observation window can handle only small amounts of CD. Regarding the "joint" algorithm, it would not be possible to compensate CD as it is one-tap approach. When static CD compensation is operated, the joint algorithm demonstrates a remarkably higher performance. In fact, as the most important amount of CD has

already been compensated by the static filter, the number of taps of the algorithm dealing with polarization separation could be small. Even if the equalizer length is small (a 3-symbol period), "CMA+BASS" presents lower performance than "joint". This static performance's gap is originated from the inner noise of the CMA equalizer. The "joint" algorithm operates polarization separation (and IQ imbalance compensation) without high additional penalty. In fact, its SNR output equals that of optimal polarization separation and IQ imbalance compensation operation. Finally, as shown in Fig 4.14(b), the static filter does not achieve an acceptable CD equalization performance for short distance fibers, but it can work well for long fibers.

4.1.4.4 Robustness Against Tx- and Rx-IQ Imbalance

To demonstrate the robustness of our approach regarding Rx-IQ imbalance, intensive computer simulations using dual-polarization 4-, 16-, 64-QAM formats were performed in the presence of Tx- and Rx-IQ imbalance over a wide range of IQ gain and phase mismatch. Consequently, the E_b/N_0 penalty as a function of IQ gain and phase mismatch at BER of 10^{-3} is calculated.

In these simulations, the same values of Tx- and Rx-IQ gain imbalance are applied on both polarizations while the phase mismatch is not included (see Fig. 4.15). Also, the same phase mismatch values on Tx and Rx sides are included while the IQ gain imbalance is null (see Fig. 4.16).

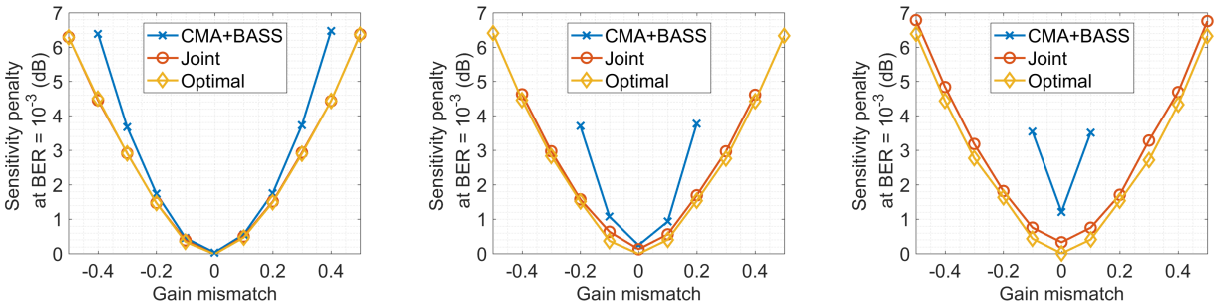

Figure 4.15 – E_b/N_0 penalty at BER of 10^{-3} as a function of the IQ gain mismatch when no IQ phase mismatch is included ($\alpha = 30°, \theta = 50°$) (a) 4-QAM, (b) 16-QAM, (c) 64-QAM.

Our proposed algorithm is functional and accomplishes Tx and Rx-IQ imbalance compensation. In fact, in the presented algorithm, the term $(\underline{\tilde{\mathbf{S}}}(n)\underline{\tilde{\mathbf{S}}}(n)^H - I_4)$ accomplishes blind IQ imbalance compensation regardless the side where the distortion was introduced.

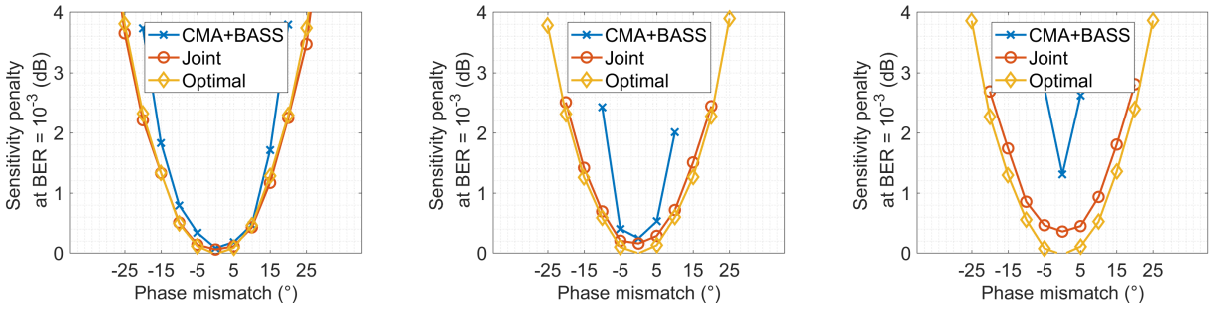

(a) (b) (c)

Figure 4.16 – E_b/N_0 penalty at BER of 10^{-3} as a function of the IQ phase mismatch when no IQ gain mismatch is included ($\alpha = 30°, \theta = 50°$) (a) 4-QAM, (b) 16-QAM, (c) 64-QAM.

This term is derived from stochastic approximation which aims to decorrelate the output signals $\underline{\tilde{\mathbf{S}}}(n)$ by finding the whitening transformation $\mathbf{A}$. Thus, the proposed "joint" algorithm operates efficiently whether IQ imbalance is introduced at Tx side only, Rx side only, or both Tx and Rx sides.

The comparison between our "joint" method and "CMA+BASS" is illustrated in Table 4.4 and Table 4.5.

Table 4.4 – Maximum absolute value of gain mismatch for E_b/N_0 penalty less than 1 dB.

Modulation format	4-QAM	16-QAM	64-QAM
"CMA+BASS"	0.14	0.1	n/a
"Joint"	0.15	0.14	0.12
"Optimal"	0.15	0.15	0.14

Table 4.5 – Maximum absolute value of phase mismatch for E_b/N_0 penalty less than 1 dB.

Modulation format	4-QAM	16-QAM	64-QAM
"CMA+BASS"	11	6.5	n/a
"Joint"	13	12.1	10.4
"Optimal"	13	13.1	13

4.1.4.5 Robustness Against Dynamic Polarization Multiplexing

The performance of our proposed method regarding dynamic polarization multiplexing was evaluated via numerical simulations. To do so, we suppose that our signals are transmitted over different optical links (in this case the number of links is fixed to 3),

and each link has its specific polarization rotation modeling parameters. The purpose of such a model is to simulate a dynamic network reconfiguration, where the transmission impairments may have sudden variations linked to the change in routing. We model the dynamic network reconfiguration by dividing our signals into three equal-duration parts and for each part, the signals are rotated by a polarization rotation matrix generated with parameters randomly chosen from the uniform distributions (see illustration in Fig. 4.17). Indeed, α varies between 0° and 90°, and θ varies between 0° and 180°, and this in a random way. Added Tx-IQ imbalance parameters are set to $(\epsilon_{p,Tx} = 0.1, \phi_{p,Tx} = 6°)$ for both polarizations.

Fig. 4.17 depicts the effect of dynamic polarization multiplexing and Tx-IQ imbalance distortion on 16-QAM signals. It represents the constellations of the entire time window, including three random polarization changes.

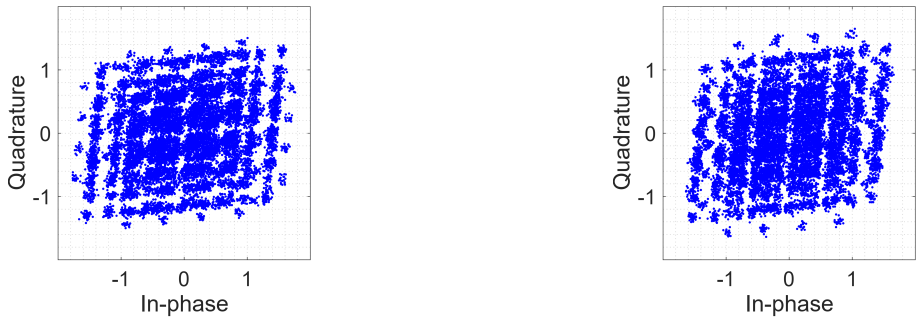

Figure 4.17 – Dynamic multiplexed 16-QAM signals in presence of Tx-IQ imbalance distortions $(E_s/N_0 = 30$ dB$, \epsilon_{p,Tx} = 0.1, \phi_{p,Tx} = 6°)$ (a) Pol. X (b) Pol. Y.

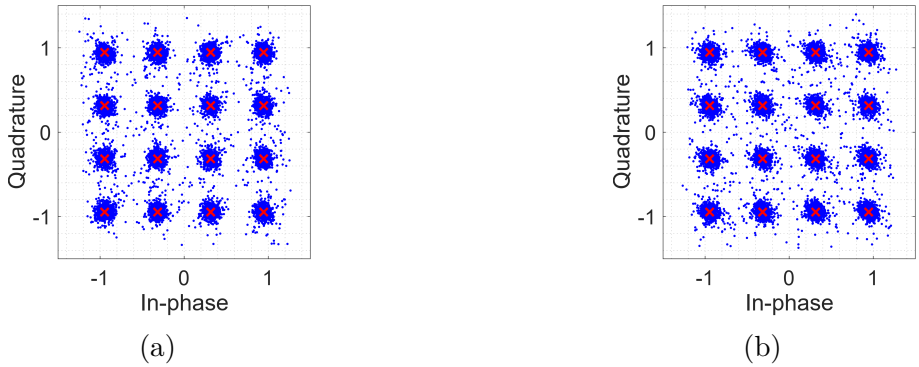

Figure 4.18 – Dynamic polarization demultiplexed and Tx-IQ imbalance compensated 16-QAM signals $(E_s/N_0 = 30$ dB$, \epsilon_{p,Tx} = 0.1, \phi_{p,Tx} = 6°)$ (a) Pol. X (b) Pol. Y.

16-QAM signals are dynamically polarization demultiplexed and Tx-IQ imbalance compensated by the "Joint" algorithm as depicted in Fig. 4.18. As can be seen, 16-QAM separated constellations of the entire time window are obtained regardless of the three random changes. This means that the convergence rate is very rapid and that the algorithm is able to recover data without loosing packets. The compensation of dynamic polarization is done in a fast and flexible way, which makes our algorithm a robust tool for this kind of transmission (see Fig. 4.19 which represents the real part of the 16-QAM constellations presented in Fig. 4.18).

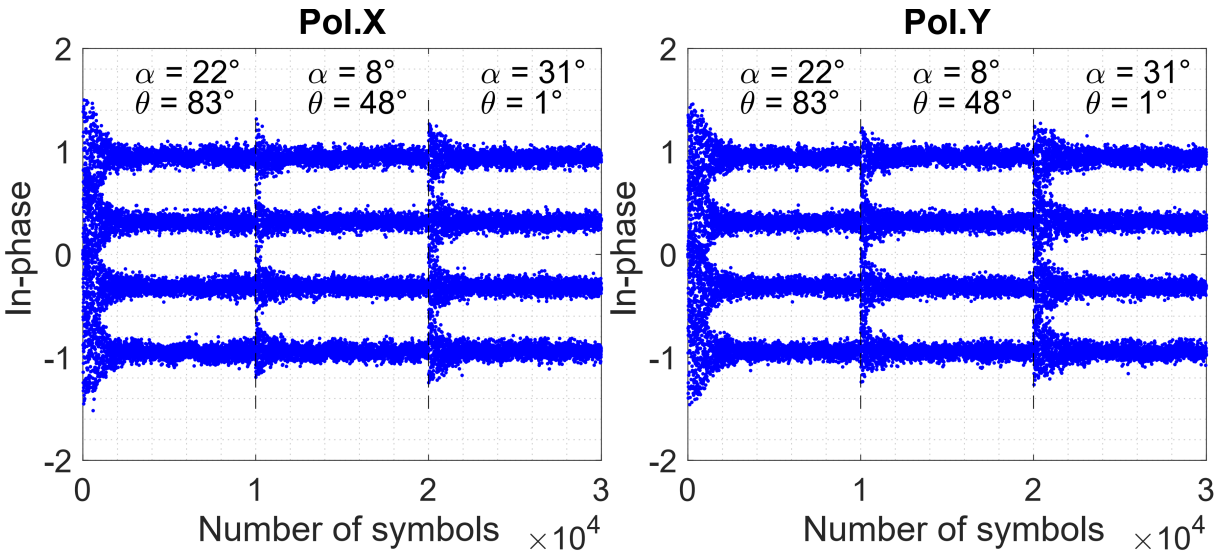

(a) (b)

Figure 4.19 – Real part of dynamic demultiplexed 16-QAM signals via "Joint" in presence of Tx-IQ imbalance distortions ($E_s/N_0 = 30$ dB, $\epsilon_{p,Tx} = 0.1, \phi_{p,Tx} = 6°$).

Nevertheless, with the same generated signals and simulation parameters, the "CMA+BASS" algorithm is inefficient to separate the signals and to recover constellations up to the third link (see Fig. 4.20). This proves that "CMA+BASS" cannot handle the random changes of the polarization rotation and thus, it is not suitable for dynamic polarization multiplexing context.

In this part, we have characterized an important point of the proposed "joint" algorithm which is its ability to actively separate the signals whose polarization rotation parameters may change over time. It demonstrates good efficiency to rapidly retrieve signals from polarization multiplexing and IQ imbalance which is not the case when proceeding with "CMA+BASS". This is another salient element of our proposed algorithm.

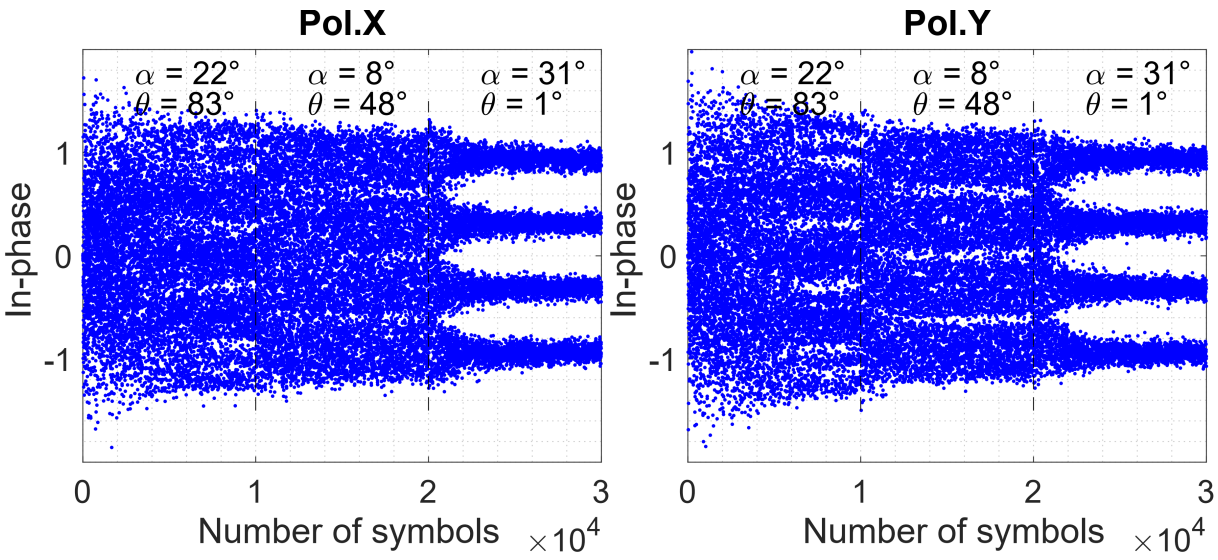

Figure 4.20 – Real part of dynamic demultiplexed 16-QAM signals via "CMA+BASS" in presence of Tx-IQ imbalance distortions ($E_s/N_0 = 30$ dB, $\epsilon_{p,Tx} = 0.1, \phi_{p,Tx} = 6°$).

4.1.5 Behavior in a Flexible Communication Context

After having explored the "joint" algorithm performance under different impairments and introduced SNRs, we will investigate its blind property to handle different modulation formats. To do so, we have transmitted QAM symbols, subdivided equally between three time intervals where the applied modulation format is sequentially 4-, 16- and 64-QAM. The simulation was accomplished under Tx-IQ imbalances ($\epsilon_{p,Tx} = 0.1, \phi_{p,Tx} = 6°$) introduced on both X and Y polarizations, and polarization rotation parameters ($\alpha = 30°, \theta = 50°$). The SNR is set to 23 dB for all the modulation formats. Also, the step-sizes are fixed in order to have the same initial convergence rate.

Fig. 4.21 shows the MSE evolution for "CMA+BASS", "EASI+BASS" and the "joint" algorithms. "EASI+BASS" stands for EASI algorithm cascaded with the BASS.

In Fig. 4.21(a), the radius of the CMA algorithm is kept to the value calculated for QPSK modulation. In this case, the CMA algorithm has no information about the change of the modulation format that is happening thereafter. Indeed, when the modulation format is changed at the transmitter from QPSK to 16-QAM, the CMA algorithm demonstrates a very slow coefficients adaptation compared to the "joint" algorithm. Moreover, the "CMA+BASS" algorithm maintains a slightly higher steady state convergence than the "joint" algorithm. In the contrary, EASI reacts well when the modulation format is changed

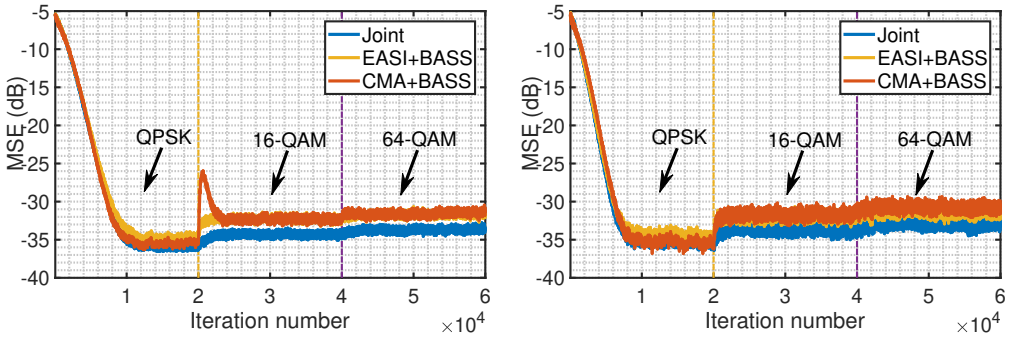

Figure 4.21 – MSE curves in the presence of Tx-IQ imbalance and polarization rotation parameters for different modulation orders ($E_s/N_0 = 23$ dB, $\epsilon_{p,Tx} = 0.1, \phi_{p,Tx} = 6°$, $\alpha = 30°, \theta = 50°$)(a) CMA is unaware of the change of modulation format, (b) CMA is made aware of the change of modulation format.

at the transmitter from QPSK to 16-QAM but it maintains a slightly higher steady state convergence (due to its gradient-noise) than the "joint" algorithm.

Fig. 4.21(b) demonstrates the MSE trends when the CMA algorithm changes its radius according the simulated modulation format. This corresponds to the ideal situation when the CMA is optimally informed about the modulation format that is used at the transmitter. In this case, the "CMA+BASS" converges rapidly but still has a higher steady state performance than the "joint" algorithm. Performance of "EASI+BASS" and "CMA+BASS" are globally equivalent. However, in both cases, the "joint" algorithm reacts well regardless of the introduced modulation formats and maintains better trade-off in terms of speed of convergence and steady state values than "CMA+BASS".

4.1.6 Complexity Comparison

In this section, the required resources of both "CMA+BASS" and the "joint" algorithms are compared in the presence of residual chromatic dispersion. Regarding "CMA+BASS" algorithm, we evaluate its IQ imbalance compensator as well as its taps weight update complexity. As for the "joint" algorithm, it will be cascaded with two complex FIR filters to ensure residual chromatic dispersion compensation. Therefore, we will quantify both algorithms taps weight update computational load. In the above, we consider only the number of real multiplications and additions as they are assumed to dominate the computation cost of the update operations. Indeed, the multiplication operations are considered to be more computationally demanding than the addition.

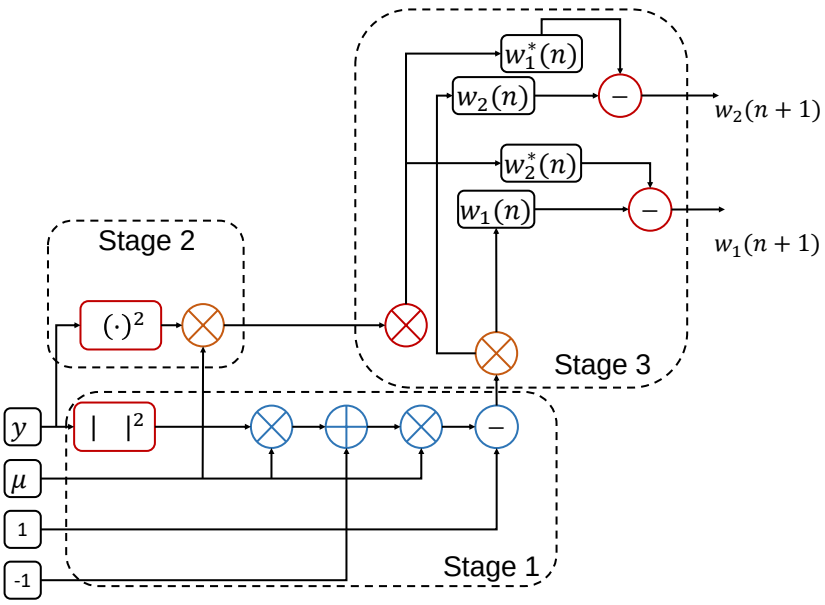

Figure 4.22 – Block diagram of the BASS algorithm.

The required processing complexity for the "BASS" scheme can be derived from Fig. 4.22 and separately calculated for each functional block. Here, we can separate the update rule into 3 parts: calculation of the first term $(1-\mu(|y|^2-1))$ in stage 1, calculation of the second term (μy^2) in stage 2 and the consequent operations in stage 3. In most practical cases, the step size μ is set to be a power of 2, so that a multiplication operation turns to a right shift. However, in our numerical calculation, μ is considered as a real number. The computation complexity is detailed as follows

— To achieve the calculation of the term $(1-\mu(|y|^2-1))$ in the stage 1 for one symbol, it requires 4 real multiplications and 3 real additions, as shown in Fig. 4.22

  — Squaring a complex number requires 2 real multiplications and 1 real addition.

  — Two real multiplications by the step size.

  — Two real subtractions.

— In the stage 2, numerical complexity is evaluated at 6 real multiplications and 2 real additions as depicted in Fig. 4.22

  — One complex multiplication requires 4 real multiplications and 2 real additions.

  — Multiplication of the complex symbol by a real step size coefficient needs 2 real multiplications.

— The already calculated terms out-coming from stage 1 and stage 2 are multiplied with the coefficients of the "BASS" algorithm and summed up to calculate the updated coefficients. After this process, the final update will be made

  — Multiplication of the complex symbol by the real output of stage 1, realized by 2 real multiplications, results to 4 real multiplications for the two coefficients.

  — Complex multiplication between the output of the stage 2 and the "BASS" coefficients requires 8 real multiplications and 4 real additions.

  — Results summation needs 2 complex additions or 4 real additions.

Finally, the overall computational complexity of the BASS per symbol is 22 real multiplications and 13 real additions.

Regarding computational complexity of the EASI, its update matrix rule $\mathbf{B}(n+1) = \mathbf{B}(n) + \mu\mathbf{H}(n)\mathbf{B}(n)$ requires

— Updated matrix $\mathbf{B}(n)$, separating matrix $\mathbf{H}(n)$ as well as a real step size μ product requires $2 \times m^2$ complex multiplications which is translated to $8 \times m^2$ real multiplications and $4 \times m^2$ real additions.

— Updating rule needs additional m^2 complex additions or, in other terms, $2 \times m^2$ real additions.

m denotes the number of sources to be separated. In our case, we deal with four signals. Hence, the final processing complexity for the update rule of the EASI is $8 \times m^2$ real multiplications and $6 \times m^2$ real additions.

Hardware resources allocated for arithmetic operations for the implementation of the CMA algorithm tap weight are also presented. The tap weight update of the CMA requires 4 real multipliers for computing the gradient which is then multiplied by the input vector requiring $4L$ complex multipliers as in the filtering process, where L is the length of the finite impulse response filters used in the CMA algorithm. In total, the complexity of tap weight implementation needs $16L + 4$ real multipliers and $16L$ real additions.

Table 4.6 presents a summary of the arithmetic needs of the "CMA+BASS" and the "joint" algorithms in terms of real multiplications and real additions per symbol.

Fig. 4.23 presents the number of real multiplications of the two presented algorithms per symbol. In our case, $m = 4$. As can be seen in Fig. 4.23, above $L = 13$ taps, our proposed algorithm has less computational needs than the "CMA+BASS". This makes it a good tool for long-haul optical fiber transmission where CD impairment is a critical issue.

Table 4.6 – Computational complexity of the proposed algorithm as compared to "CMA+BASS" algorithm

Algorithm	"CMA+BASS"	"Joint+2 FIR"	"EASI+2 FIR+BASS"
Multiplications	$16L + 26$	$8m^2 + 8L + 2$	$8m^2 + 8L + 24$
Additions	$13 + 16L$	$6m^2 + 8L$	$6m^2 + 8L + 13$
Multiplication practical case	$16L + 26$	$8L + 130$	$8L + 152$

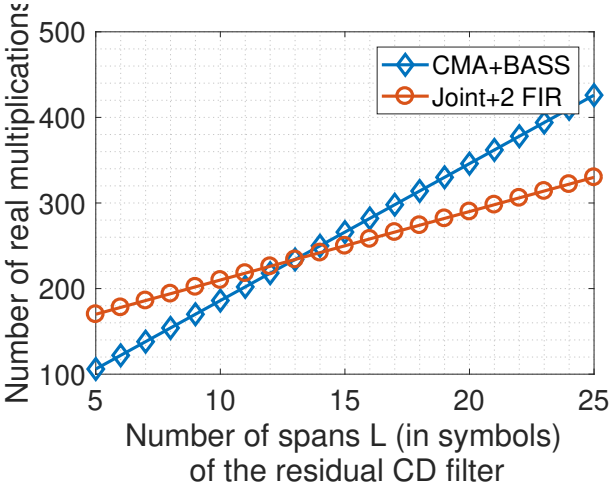

Figure 4.23 – Number of real multiplications per sample versus length of FIR filters.

To sum up, this section discusses the computational needs of both polarization demultiplexing and IQ imbalance compensation algorithms. According to the carried out calculations, the "joint" algorithm brings gain in the number of real multiplications (compared to "CMA+BASS") if the optical transmission conditions require the use of an equalizer for residual chromatic dispersion mitigation with length $L \geq 13$.

4.2 Proposed CPR Techniques

Carrier phase recovery is an essential module to compensate for the random phase shifts induced by both transmitter laser and the local oscillator. In our context of study, some characteristics and criteria are required for a useful CPR algorithm: its tolerance to laser linewidth and residual carrier frequency offset, its low computational complexity, its relevance to any modulation formats and its robustness against large amounts of ASE noise. In this part, two proposed CPR algorithms are introduced and discussed. The

first is a digital phase locked loop approach and the second is a recursive blind phase search based on interleaving parallelization. The two established methods are tested and evaluated with respect to the desired criteria.

4.2.1 Modified Decision Directed 16-QAM CPR

In this section, a new modified decision-directed carrier phase recovery is presented. The proposed algorithm is dedicated to 16-QAM signals and it is evaluated in the presence of a wide input SNR range as well as residual carrier frequency offset.

4.2.1.1 Principle of the Approach

To focus on the inherent properties of the analyzed CPRs, we consider in this study that IQ imbalance, chromatic dispersion, timing error, and polarization impairments are completely compensated before the CPR stage suited to 16-QAM signals. We suppose that the signal available at the input of the CPR unit at time index k is expressed as

$$u(k) = (d(k) + n(k))e^{j(2\pi\varphi_1 k + \theta(k))}, \tag{4.17}$$

where $d(k)$ is the symbol, $n(k)$ is the additive white circular Gaussian noise, φ_1 is the residual CFO between transmitter laser and local oscillator normalized by the sampling frequency, and $\theta(k)$ is the phase noise typically modeled as a Wiener process (see section 3.1.1.5). 16-QAM modulation with symbols belonging to the set of constellation points $A = \{\pm 1 \pm 1i, \pm 3 \pm 3i, \pm 1 \pm 3i, \pm 3 \pm 1i\}$ is used. The ASE noise is specified by the energy per bit to noise spectral density ratio E_b/N_0. The laser phase noise state variance associated to the Wiener process is given by $2\pi\Delta fT$ where Δf is the sum linewidth of the signal and local oscillator lasers and T is the symbol time period.

The proposed modified phase detector method stands for raising the corrected symbol $r(k)$ to the 4^{th} power and adjusting its related decision as will be stated later. Fig. 4.24(a) shows the classical decision-directed feedback block diagram derived from the maximum likelihood criterion. Its phase-error detector equation is defined by $e(k) = \Im(r(k)\hat{d}^*(k))$, where $\Im(.)$ stands for the imaginary part, $r(k) = u(k)e^{-j\hat{\theta}(k)}$ is the symbol corrected by the phase estimation $\hat{\theta}(k)$, $\hat{d}(k)$ is the symbol decision calculated according to $\hat{d}(k) = \arg\min_{\hat{a}\in A}|r(k) - \hat{a}|^2$ with A the constellation points and $(.)^*$ stands for complex conjugate.

Fig. 4.24(b) depicts the 4^{th} power raised 16-QAM constellation. The modified constellation points are divided into 4 subgroups

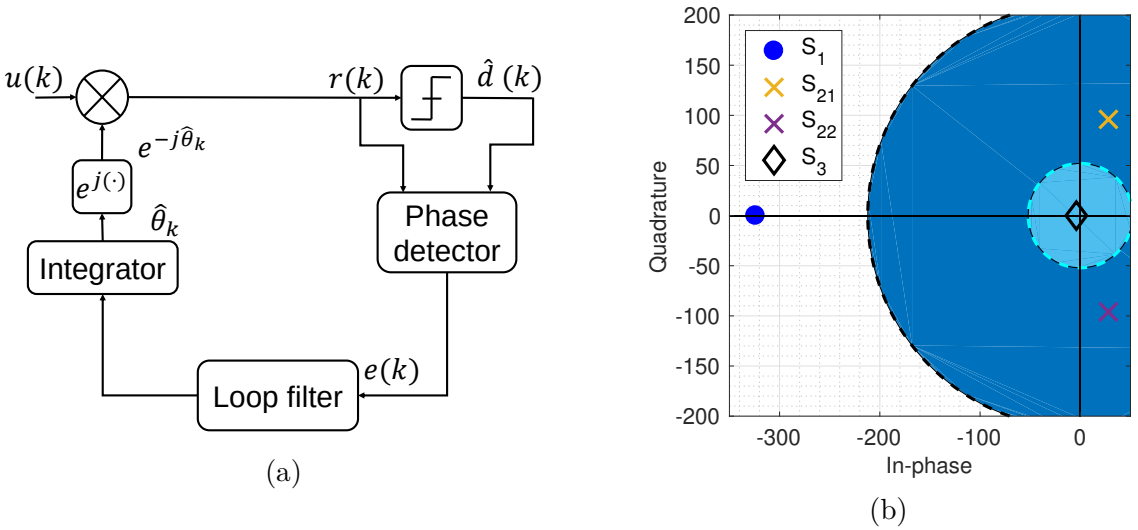

Figure 4.24 – (a) Decision-directed feedback recovery system. (b) 4$^{\text{th}}$ power raised 16-QAM constellation showing the principle of the modified decision.

$S = \{S_1 = -324, S_{21} = 28 + 96i, S_{22} = 28 - 96i, S_3 = -4\}$. Thus, the modules of the 4$^{\text{th}}$ power raised symbols are in the set $B = \{324, 100, 4\}$. By denoting $r'(k) = r(k)^4$, the new decision based on the distance calculation module is

Algorithm 2 "Modified decision scheme"

1: Calculate three distances $\left||r'(k)| - |\hat{b}|\right|^2$ for $\hat{b} \in S$
2: Select $\hat{b} \in S$ that minimizes $\left||r'(k)| - |\hat{b}|\right|^2$
3: If the value of $\hat{b}$ is not equal to 100, $\hat{d}'(k) = \hat{b}$
4: If $\hat{b}$ is equal to 100 then select $\hat{b} \in \{S_{21}, S_{22}\}$ that minimizes $\left|r'(k) - \hat{b}\right|^2$ and $\hat{d}'(k) = \hat{b}$.

Then, the modified phase detector is expressed as $e_m(k) = \Im(r'(k)\hat{d}'^*(k))$. In order to update the estimated phase $\hat{\theta}(k)$, the phase error detector is fed into a feedback loop, a 1$^{\text{st}}$ order loop filter and then a phase integrator as

$$\hat{\theta}(k+1) = \hat{\theta}(k) + \alpha e_m(k) + \beta \sum_{j \leq k} e_m(j), \tag{4.18}$$

where α and β are set according to the compromise between acceptable stability and filter convergence rapidity.

4.2.1.2 Numerical Simulations

As stated earlier, the performance of a phase detector is linked to the so-called S-curve. We recall the definition of the S-curve as being the average output of the phase detector over data and noise. Two properties are important when evaluating the detector, namely its linear response and its gain. A linear response of the S-curve is responsible for increasing the system locking capacity particularly in the presence of small frequency errors while a high S-curve gain ensures a fast phase-lock acquisition.

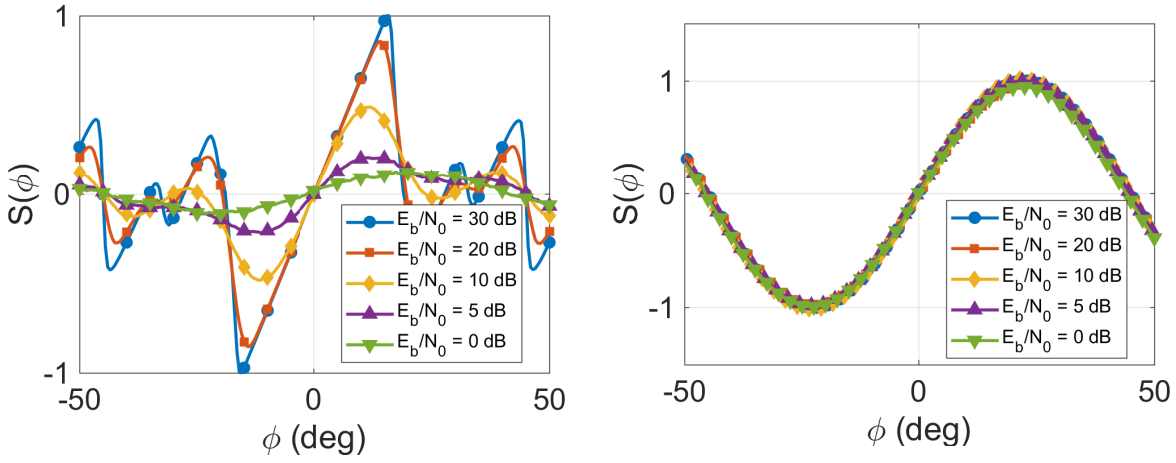

Figure 4.25 – Phase detector S-curve comparison for different values of SNR: (a) classical phase detector S-curve, (b) modified decision phase detector S-curve.

When inspecting Fig. 4.25(b), which plots the S-curve for the proposed model, it is important to realize that the proposed scheme S-curve maintains approximately the same loop filter gain $S'(\phi)_{|\phi=0}$ regardless of the SNR value, which ensures a fast phase acquisition. In contrast, the classical detector in Fig. 4.25(a) presents a gain which is related to the SNR. In such a situation, unsatisfactory results are obtained with a fixed loop-filter gain, especially when operating at low SNRs. Additionally, the modified scheme presents a wider range of quasi-linear response compared to the classical detector. Finally, it exhibits a higher linear response gain that is maintained constant regardless of the SNR value, notably for low E_b/N_0 cases. Hence, all mentioned advantages make the modified phase detector a suitable algorithm for both loop-locking capacity (thanks to the linear phase range) and fast phase acquisition (thanks to the large gain).

4.2.1.3 Robustness Against Residual Frequency Offset

In order to illustrate the performance of our modified algorithm, the receiver sensitivity penalty for the energy-per-bit-to-noise spectral-power-density ratio E_b/N_0 at a BER= 10^{-2} was chosen (the power reference is the phase noise free system without phase estimation). It is worth noting that differential encoding was used in order to resolve the inherent $\pi/2$ ambiguity of the phase error. Simulations were carried out via Monte-Carlo approach and the BER was obtained by processing 2×10^6 samples. Phase noise is modeled as a Wiener process with various state noise variances within the range of $[0,\ 10^{-5}]$. Gaussian noise and normalized CFO in the range of $[0,\ 6 \cdot 10^{-3}]$ were also added for comparison. The loop filter parameters were chosen to be $1/\sqrt{2}$ for the damping factor ξ and $B_L = 10^{-2}$ for the noise equivalent bandwidth.

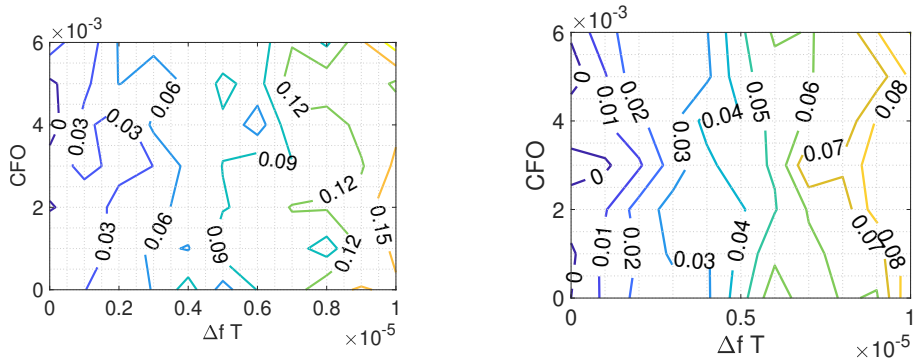

Figure 4.26 – Receiver sensitivity penalty at a BER of 10^{-2}, in dB, for different CFO and combined linewidth time symbol duration products compared to phase noise free system without phase estimation (a) classical phase detector, (b) modified phase detector.

The contour plots in Fig. 4.26 show the receiver sensitivity penalty with respect to the linewidth (linked to the Wiener state noise variance) and the residual normalized CFO. With increasing linewidth, the SNR penalty increases considerably, due to the presence of the noise that can be large enough to abruptly throw the instantaneous phase error outside its attracting region of the stable zero. The modified decision-directed CPR responds robustly against noise since its sensitivity penalty does not exceed 0.08 dB over the investigated linewidth and CFO ranges. On the contrary, the classical decision directed approach reaches higher sensitivity penalty (0.15 dB) over the same range of investigated parameters.

4.2.1.4 Robustness Against Additive White Gaussian Noise

To evaluate the tolerance of the algorithm in the presence of AWGN, numerical simulations were established on 16-QAM signal corrupted by residual normalized CFO of 10^{-3}, and on the condition of a typical laser linewidth times symbol duration product $\Delta fT = 9 \times 10^{-5}$. The added white Gaussian noise specified by E_s/N_0 is incremented in each runs while crossing a range between 14 and 30 dB with a step of 1 dB.

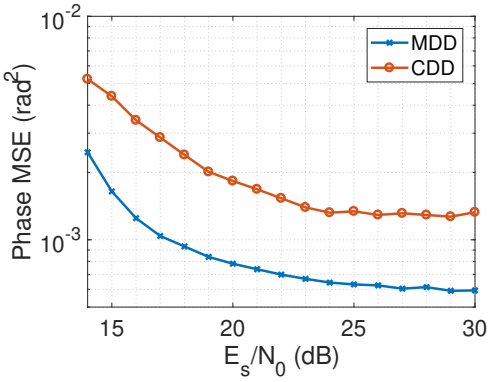

Figure 4.27 – Phase MSE *vs.* E_s/N_0 (CFO =10^{-3}, $\Delta fT = 9 \times 10^{-5}$).

As depicted in Fig. 4.27, when E_s/N_0 is relatively low (around 14 dB), the MDD presents lower MSE values. Afterwards, the algorithms return to the stable state iteratively. Above 18 dB, the MSE curve of the modified phase detector remains constant around 610^{-4}, whilst a higher MSE value for the conventional phase detector is observed.

In this part, we evaluate the performance of the modified phase detector in presence of phase noise, carrier frequency offset and AWGN. The numerical simulation shows that our approach has better tracking accuracy than the conventional phase detector regardless of the amount of the added white Gaussian noise. The simulation parameters have been chosen according to the today's commercial lasers thanks to their cost-efficiency and small foot-print. The linewidth of such lasers is in range of 100 kHz $\leq \Delta f \leq$ 10 MHz. Assuming a symbol rate of 32 Gbaud, the tolerable sum line-width times symbol duration product must be 3.125 $10^{-6} \leq \Delta fT \leq$ 3.125 10^{-4}. The value of the remaining CFO corresponds to 32 MHz which is realistic.

4.2.1.5 Performance in Practical Implementation

To support high sampling rate application, field programmable gate array (FPGA) are required to provide higher throughput. However, modules containing feedback loops

are particularly challenging. In fact, in feedback loops, all the closed loop calculations should be performed in a sample period. Closed loops typically require several pipeline stages when implemented in high throughput applications. Increasing the number of pipelining stages in the loop to achieve higher performance can lead to functionality failure. Indeed, in the hardware-based phase locked loops, the latency or the delay (due to required stages for pipelining) requires a careful study of the CPR performance within the practical implementation constraints.

In this section, the impact of the L symbols delay in the feedback loop is included and investigated in the model. In this case, the received symbol $u(k)$ is buffered for a duration of L symbols until the estimated data value $\hat{d}(k-L)$ becomes available. In a second step, the required phase estimate $\hat{\theta}(k-L)$, which is an old estimate, is applied to the newest observed received symbol $u(k)$ and then a decision is made $\hat{d}(k) = \arg\min_{\hat{a}\in A}\left|u(k)e^{-j\hat{\theta}(k-L)} - \hat{a}\right|^2$. In this case, the symbol decision $\hat{d}(k)$ will be correctly compensated for phase noise provided $\hat{\theta}(k-L)$ is a good phase estimate and the phase has not drifted significantly during L symbols. The problem is that the additive noise disturbances may affect the feedback loop performance significantly as it causes the phase estimate $\hat{\theta}(k)$ to be in error, which in turn causes error burst. The short error burst can become remarkably longer so that it leads to bit errors even after forward error corrector decoding. To successfully overcome this problem, differential encoding is used to avoid any cycle slips occurrence.

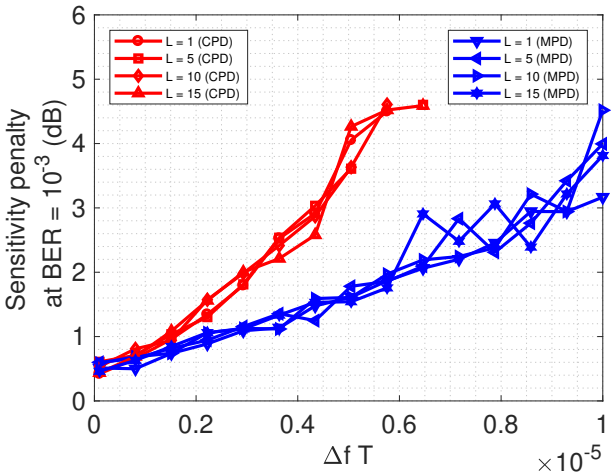

Figure 4.28 – Effect of the delay on the overall performance of the feedback loop using Conventional CPD and Modified MPD Phase Detectors.

To highlight the effectiveness of the proposed algorithm against different introduced delay values, the sensitivity penalty of both decision directed carrier phase recovery and

its modified version against the linewidth times symbol duration product is compared. As shown in Fig. 4.28, our proposed algorithm maintains its robustness over the investigate linewidth range regardless of the introduced delay value while the classical version demonstrates lower tolerable linewidth times symbol duration product especially for sensitivity penalty above 2 dB regardless of the introduced delay value.

4.2.1.6 Complexity Comparison

In this part, the computational complexity of both presented algorithms are detailed and compared. The number of real multipliers, real adders and decisions is determined for each received symbol. Also, each complex multiplier is calculated as 4 real multipliers and 2 real adders. Regarding raising symbol to the 4^{th} power, more sophisticated and hardware efficient technique can be used.

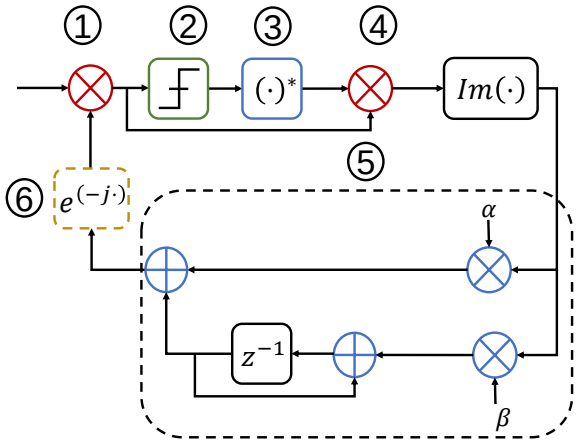

Figure 4.29 – The block diagram of the conventional phase error detector.

The complexity calculation of the conventional phase detector, shown in Fig. 4.29, is as follows

① First, the received symbol is rotated by the earlier estimated phase. This operation requires 1 complex multiplication, or 4 real multiplications and 2 real additions.

② After rotation, the symbol is fed to a decision operation.

③ The complex conjugate is then applied on the decided symbol. This step requires 1 real multiplication in the imaginary part of the complex decided symbol.

④ The complex multiplication is performed between this output and the rotated symbol. This needs 4 real multiplications and 2 real additions.

⑤ The imaginary part is then recovered and this does not require additional computational complexity. To perform second order loop, 2 real multiplications and 2 real additions are required.

⑥ Finally, to calculate the complex exponential of the estimated phase, the CORDIC algorithm [145], detailed hereafter, may be applied.

These required steps make the conventional phase detector comes down with a complexity of 11 real multiplications, 6 real additions and 1 decision.

In the same way, the computational complexity of the modified phase error detector is calculated. As presented in Fig. 4.30, technically, the only difference compared to the classical phase detector is the 4^{th} power operation and a modified version of the decision process.

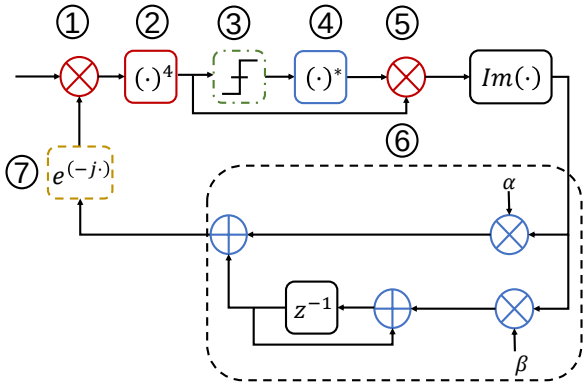

Figure 4.30 – The block diagram of the modified phase detector

Thus, the additional numerical complexity added to the modified phase detector is summed up in the step number ②. Here, a hardware efficient implementation of the 4^{th} power operation is introduced. Raising a complex symbol to the fourth power is calculated according to

$$(a+jb)^4 = (a^2-b^2)^2 - 4a^2b^2 + 4jab(a^2-b^2). \tag{4.19}$$

where a and b denote the real part and imaginary part of the complex value, respectively. The intermediate a^2, b^2 and a^2-b^2 can be reused in 4.19. Also, the operation of multiplying by 4 can be achieved by two shift operations. By using these implementations, the numbers of real multipliers and real adders for each fourth power operation are reduced to 6 and 2, respectively. This corresponds to the amount of hardware complexity to be added if using the proposed modified phase detector.

4.2.2 Parallel R-BPS Algorithm

We have presented earlier a carrier phase recovery approach robust to harsh transmission conditions notably the low SNR values. Besides, the algorithm is suited to hardware implementation in terms of the requested feedback delay. Nevertheless, the modified phase detector is restricted to 16-QAM signals and can not be employed in a flexible communication context as it requires *a priori* knowledge on constellation format. Therefore, a parallel recursive blind phase search (R-BPS) algorithm is introduced in this section. As in BPS (see section 2.), the presented algorithm is an hybrid structure, but it is suitable for higher modulation orders with less hardware complexity.

4.2.2.1 Principle of the Approach

The system of the R-BPS involves a set of B test phases, with values of $\Delta\varphi_p = (p + 0.5 - B/2) \times \Delta$, with $p \in \{0, B-1\}$, $\Delta = 4\sigma/B$, and $\sigma = \sqrt{2\pi\Delta f T}$. Δf is the sum of the linewidths of the transmitter and local oscillator lasers and T is the symbol duration.

Each received symbol r_k is rotated by $\Delta\varphi_p$ test phases to obtain rotated symbols

$$r_{k,p} = r_k e^{-j\Delta\varphi_p}.$$

The rotated symbols are fed into a hard decision circuit to find out the closest constellation point d_k given by

$$d_k = \arg\min_{a_k \in A} \left| (r_{k,p} - a_k)^2 \right|$$

Next, the distance between the rotated symbol and its decision is calculated by

$$e_{k,p} = \left| r_{k,p} - d_k \right|.$$

For white noise rejection, a summation of this distance denoted $\overline{e_p}$ is calculated over a rectangular window of size N

$$\overline{e_p} = \sum_{k=i}^{i+N-1} e_{k,p}.$$

In practice, the optical high-speed transmission rates are larger than the clock speed of any suitable integrated circuit so that the incoming samples from the analog to digital converters must be demultiplexed and processed in parallel streams at lower rates. In this case, the input symbols are interspersed to the L parallel stages. Subsequently, each stage

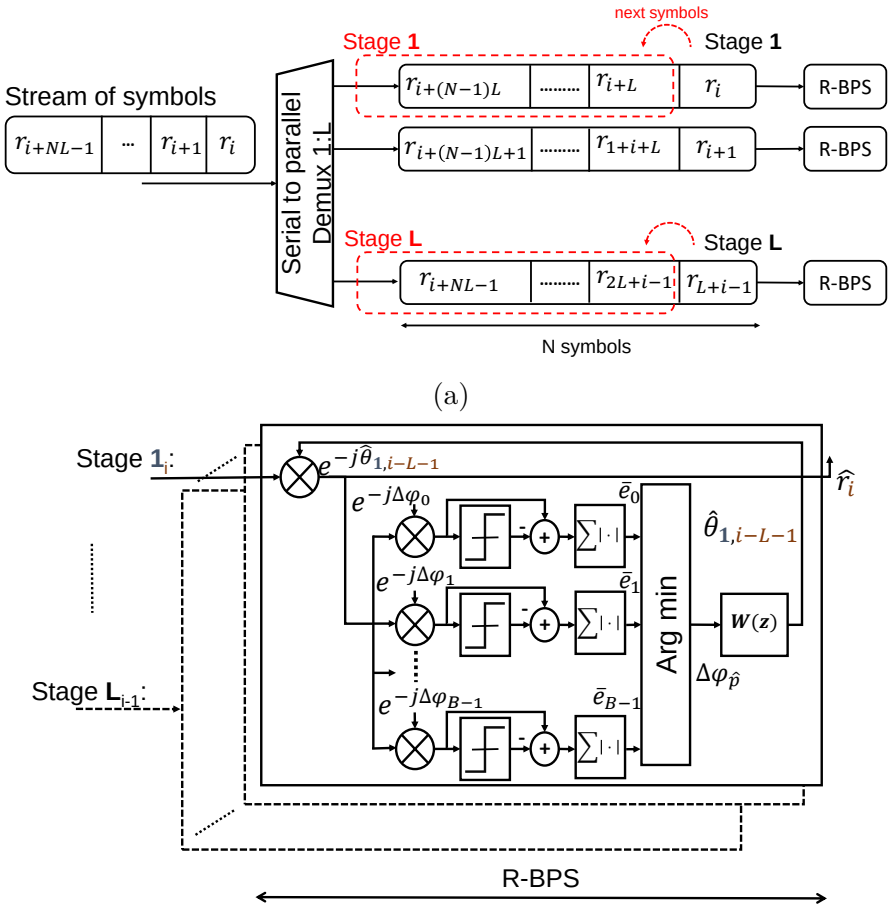

Figure 4.31 – Block diagram of the R-BPS algorithm with interleaving implementation in parallel processing.

of size N does not contain consecutive symbols but symbols equally spaced by $L \times T$, as illustrated in Fig. 4.31(a).

Then, the best phase rotation $\Delta\varphi_{\hat{p}}$ that minimizes this output is chosen. $\hat{p}$ is calculated as

$$\hat{p} = \underset{p\in\{0,B-1\}}{\arg\min}\ \overline{e_p}.$$

This phase is employed in a feed-back loop, with a first-order recursive loop filter to update the estimated phase noise $\hat{\theta}$ according to

$$\hat{\theta}_k = \hat{\theta}_{k-1} + \Delta\varphi_{\hat{p}}.$$

The novelty of the proposed R-BPS with respect to the recursive probability weighted BPS (RW-BPS depicted in Fig. 4.31(b)) lies in the removal of the weighting by probabilities after averaging as it is not obvious to calculate the weighting factors, which, based on our simulations, do not result in significant performance improvement. Also, these probabilities need to be adapted to the phase noise variance and therefore phase noise variance should be blindly estimated to be able to calculate these probabilities which are numerically expensive. In what follows, simulations are carried out with the parallel configuration characterized by two operating parameters which are the number of parallel stages and the window size.

4.2.2.2 Numerical Simulations

Numerical simulations are carried out on a single polarization transmission system. The M-QAM mapped symbols are differentially-encoded to overcome cycle slips. It is important to mention that the number of parallel stages is taken into account when implementing the differential encoding. At the transmitter, differential encoding is performed on each parallel stage independently. Then, laser phase noise is introduced and modeled as a Wiener process with a variance of $\sigma^2 = 2\pi\Delta fT$. At the receiver, ASE noise modeled as additive white Gaussian noise is added to the signal in order to obtain a specified E_s/N_0. To focus on the CPR module performance, other transmission or system impairments are not included in this study. We consider both R-BPS and BPS and the two approaches are compared under the same operating conditions (number of parallel stages L and window size N). We suppose that the initial phase noise is initialized to a random value between $[0,\ 4\sigma]$ rads.

Fig. 4.32 presents the E_b/N_0 penalty in dB (with respect to the theoretical BER versus E_b/N_0 for an AWGN channel in the absence of phase noise), as a function of the linewidth times the symbol duration for 4-, 16- and 64-QAM signals. The simulations are performed for a window size of $N = 9$, $L = 8$ stages, and the BER is calculated over 8×10^5 bits. For BPS, the number of test phases is set to $B = 32$ for both 4- and 16-QAM and $B = 64$ for 64-QAM. As for the proposed R-BPS, the number of test phases resulting in a highly-reduced cost implementation is set to $B = 6$ for 4-, 16- and 64-QAM modulations.

As can be seen in Fig. 4.32, for all used modulation formats, the R-BPS algorithm provides larger linewidth tolerance than the BPS algorithm, especially with 64-QAM (gain in sensitivity of roughly 1 dB for $\Delta fT < 10^{-5}$) and 16-QAM signals (gain in sensitivity of roughly 0.5 dB for $\Delta fT < 10^{-5}$).

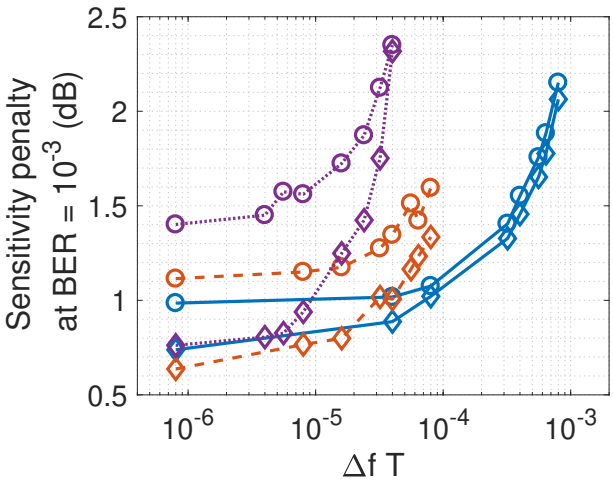

Figure 4.32 – Sensitivity penalty at a BER=10^{-3} of BPS (circle), R-BPS (diamond) for 4-QAM (blue), 16-QAM (orange) and 64-QAM (purple) modulation formats.

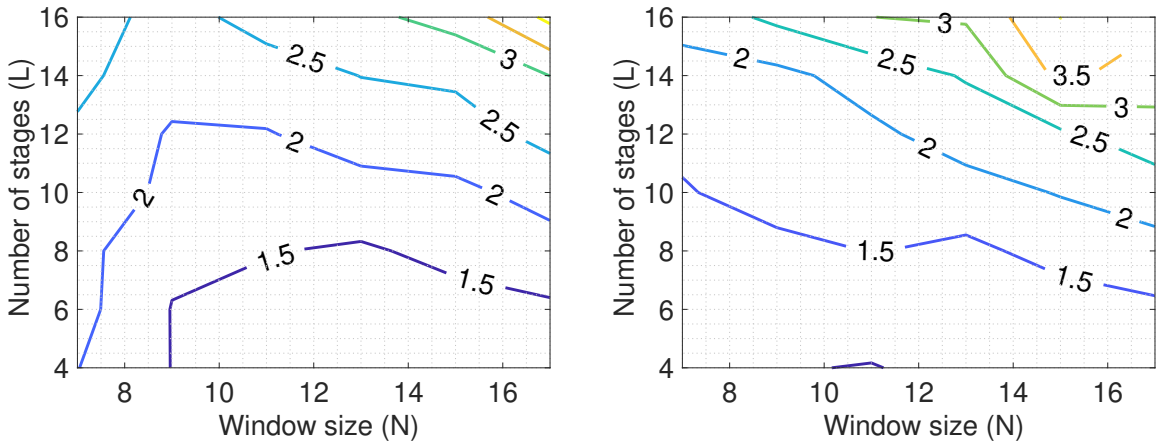

(a) (b)

Figure 4.33 – E_b/N_0 penalty for the BPS algorithm at a BER of 10^{-3} as a function of the algorithm parameters N, L for 16-QAM modulation formats and $\Delta fT = 10^{-5}$ for (a) parallel BPS algorithm, (b) parallel R-BPS algorithm.

Fig. 4.33 presents the E_b/N_0 penalty at a BER of 10^{-3} (with respect to the theoretical BER versus E_s/N_0 for an AWGN channel in the absence of phase noise) as a function of the number of parallel stages L and window size buffer N for both R-BPS and BPS algorithms and 16-QAM modulation for $\Delta fT = 10^{-5}$.

The larger the number of parallel stages L is, the larger the E_b/N_0 penalty is. In fact, in each stage, two consecutive symbols are separated by L streamlined symbols and the associated variance of differential phase noise is thus increased proportionally by the same

factor. The algorithms are not able to track precisely the phase noise evolution, which is translated into a higher required E_b/N_0.

However, the R-BPS algorithm is less sensitive to the window size N, especially for lower values of parallel stages ($L < 10$). In fact, as the symbols of the same stage are rotated by the adequate phase noise correction, the error average is performed basically for additive white noise rejection. Hence, it is clear that the larger the window size is, the less the effect of additive noise is. Moreover, the larger the phase noise is, the smaller the sustainable number of parallel stages is.

On the other hand, BPS is more sensitive to the window size N. As depicted in Fig. 4.33(a), not only are fewer stages needed to minimize the E_b/N_0 penalty, but also a large window size. In fact, with BPS, symbols per stage are not necessarily compensated with the adequate phase noise due to the discretization of test phases introduced by the choice of B, thus the averaging operation incorporates additive noise as well as phase noise bias. Indeed, the estimation of the phase noise is affected by the additive white Gaussian noise. This explains the necessity of a larger window size to get a better estimate of the phase noise, and therefore to reduce the E_b/N_0 requirement.

4.2.2.3 Parallel R-BPS with a Feedback Loop

To cope with the problem of cycle slips related to the parallelization and its subsequent effects on the tacking speed and accuracy, a feedback unit could be introduced to get a better refined carrier phase estimation at the output of the R-BPS approach. In this case, the structure of the proposed carrier recovery algorithm is composed of L parallel stages and a serial digital carrier recovery based on a feedback loop. Consequently, each estimated phase noise at the output of each parallel stage cannot be processed independently because all the parallel stages have to share one loop filter that runs only once per parallel operation period. Fig. 4.34 depicts the configuration of the parallel R-BPS algorithm based on a feedback architecture. Note using this scheme, differential encoding on each stage is not applied as the scheme is immune to cycle slips.

The performance of the R-BPS algorithm with feedback loop is studied through simulation and compared to the R-BPS algorithm without the feedback loop. In this simulation module, the used modulation type is 16-QAM, and the introduced aggregate linewidth of transmitter and local oscillator to emulate phase noise ΔfT is set to 10^{-5}. For this simulation, 8 parallel stages structure is adopted and 9 symbols per stage are used for phase noise tracking. The phase mean square error curve is carried out in Fig. 4.35. The

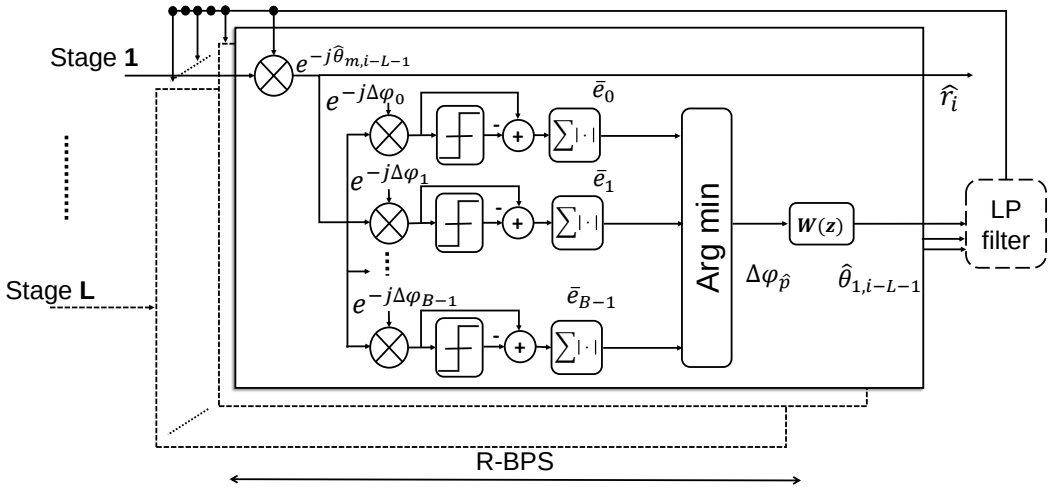

Figure 4.34 – Paralle R-BPS with a feedback loop.

performance loss of the R-BPS increases with low E_s/N_0 values. When the SNR is below 18 dB, the performance loss of R-BPS method is about 1.7 dB compared to the R-BPS with a feedback loop. However, the proposed refined method can perform efficiently with a stable MSE value around 8×10^{-3}. The proposed algorithm effectively improves phase tracking regardless the SNR value.

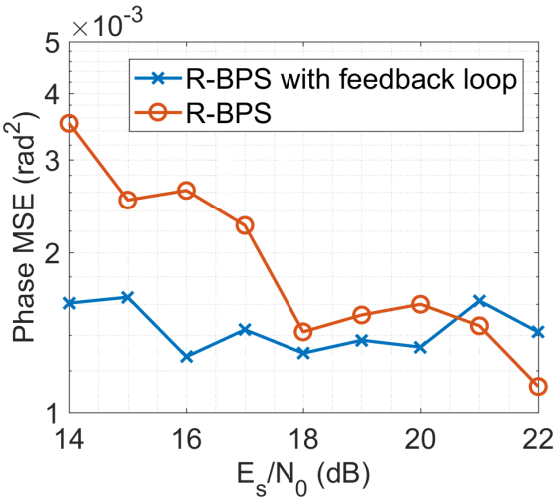

Figure 4.35 – Phase mean square error evolution *vs.* E_s/N_0.

Although the algorithm with the feedback method shows better performance, we will present the rest of the simulation results with the R-BPS approach. The reasons for which we made this choice are essentially related to implementation concerns.

4.2.2.4 Robustness Against Residual CFO

Residual carrier frequency offset can be considered as a phase noise and can be managed with CPR algorithms. The residual CFO is sensitive to phase noise level and can be determinal, as the larger the observation window N used, the larger the drift of the CFO. To study the relevance of our proposed method against the presence of CFO impairments, a fixed parallelized R-BPS with $L = 8$ stages and $N = 9$ as an observation window is proposed. This configuration is tested under different laser linewidth values and residual carrier frequency offsets. 16-QAM modulation format is tested. In this simulation, the receiver sensitivity penalty at a bit error ratio value of BER $= 10^{-3}$ was chosen (the power reference is the phase noise free system without phase estimation and without differential encoding). Fig. 4.36 depicts the E_b/N_0 penalty with respect the theoretical BER curve with differential encoding, at BER $= 10^{-3}$.

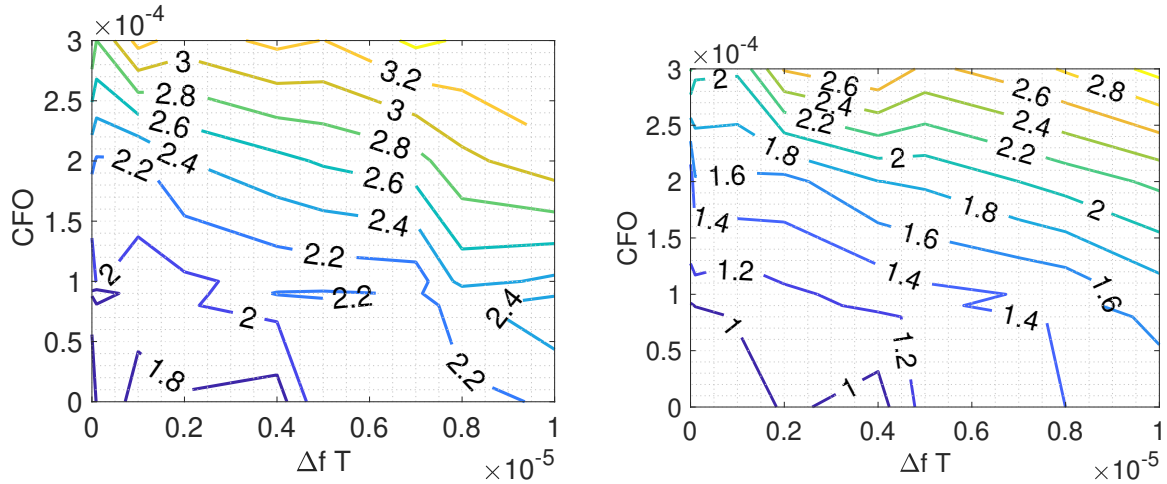

Figure 4.36 – Receiver sensitivity penalty at a BER of 10^{-3}, in dB, for different CFO and combined linewidth time symbol duration products compared to phase noise free system without phase estimation (a) parallel BPS, (b) parallel R-BPS.

As can be seen in Fig. 4.36, for a fixed linewidth, the larger the introduced residual CFO, the larger the sensitivity penalty, since both algorithms need to deal with CFO impairments. Also, for a fixed residual CFO value, the larger ΔfT value is, the larger the sensitivity penalty due to the effect of the phase noise in producing erroneous symbol decision is. The parallel R-BPS presents lower values in terms of receiver sensitivity penalty at a BER of 10^{-3} than the parallel BPS implementation. This means that the

proposed approach responds robustly against phase noise since its sensitivity penalty is often lower than that of the parallel BPS over the investigated linewidth and CFO ranges.

4.2.2.5 Robustness Against Additive White Noise

White noise affects the system performance as low SNRs cause cycle slips to occur. That is why both algorithms make use of an averaging block to filter out the the impact of white Gaussian noise. The idea is to work with an adequate size of window which is not very large which makes the system less efficient in handling fast carrier phase tracking and not too small so that the impact of the additive noise is not reduced.

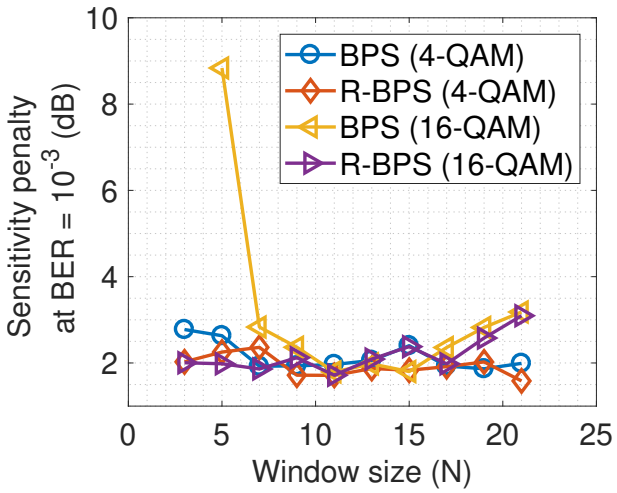

Figure 4.37 – Sensitivity penalty at a BER of 10^{-3} of BPS, R-BPS for 16-QAM modulation format for $\Delta fT = 10^{-5}$ *vs.* the window size (N).

Fig.4.37 depicts the effects of white noise averaging on the overall system performance for 4-QAM and 16-QAM modulation formats for $\Delta fT = 10^{-5}$. The number of test phases are $B = 6$ for the R-BPS and $B = 32$ for the BPS and the parallelization level is set to 8. As presented in Fig. 4.37 the larger the window size is, the lower the E_s/N_0 penalty at BER $= 10^{-3}$ is. For too large window size (N upper than 16), the system performance degrades and looses its effectiveness in phase noise tacking (as the sensitivity penalty increases). In the following simulations, for fair comparison between BPS and R-BPS, both algorithm sets are with $N = 9$ as a window size.

On the other hand, to evaluate the precision of phase tracking, numerical simulations were carried out via 10 Monte Carlo runs, by processing 10^3 generated symbols of $16-$QAM modulation formats for $\Delta fT = 10^{-6}$ and $\Delta fT = 10^{-4}$. For each context, the added SNR

ranges in [14, 22] dB and it is increased by a step value of 1 dB. Also, the same parallel configuration is adopted. In this case, the phase mean square error is evaluated in each case and compared. As depicted in Fig. 4.38, there is no cycle slip occurrences when employing the proposed R-BPS approach. R-BPS maintains lower phase MSE values whatever the introduced additional noise is. Meanwhile, the cycle slips in the BPS are frequent especially for low E_s/N_0 values. Consequently, the R-BPS is robust against cycle slips and this is thanks to the constraints of symbol to symbol phase drifts tracking. As for the BPS, it has a larger window of test phases (between 0 and $\pi/2$) which intensifies the quantization error.

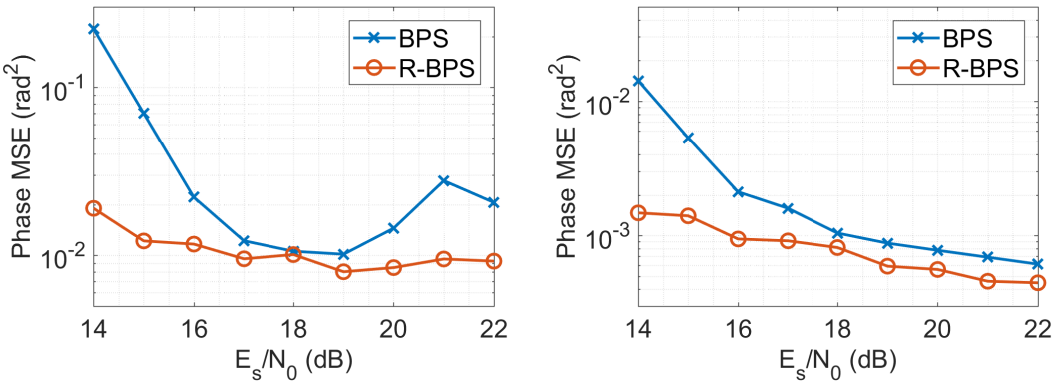

(a) Introduced $\Delta fT = 10^{-4}$ (b) Introduced $\Delta fT = 10^{-6}$

Figure 4.38 – Phase MSE *vs.* E_s/N_0.

4.2.2.6 Required Number of Test Phases

To choose the number of test phases required for phase noise estimation and compensation, simulations were conducted under several range of test phases on 4-QAM and 16-QAM modulation formats for $\Delta fT = 10^{-5}$ and on 16-QAM and 64-QAM modulation formats for $\Delta fT = 10^{-6}$. The number of parallel stages is fixed to 8 and the window size is set to 9. Fig. 4.39 illustrates the tolerable linewidth symbol duration product versus the number of test phases of the BPS and R-BPS schemes for the BER FEC limits of 10^{-3} (with respect to the theoretical BER versus E_s/N_0 for an AWGN channel in the absence of phase noise). For 16-QAM, a gain of 1 dB in sensitivity is observed for the R-BPS compared to BPS, when using test phases larger than 10 in both schemes. For 64-QAM, with 20 test phases, an increase of the phase noise tolerance of 1.5 dB is achieved with the proposed R-BPS. Also, while maintaining the same phase noise tolerance level, the

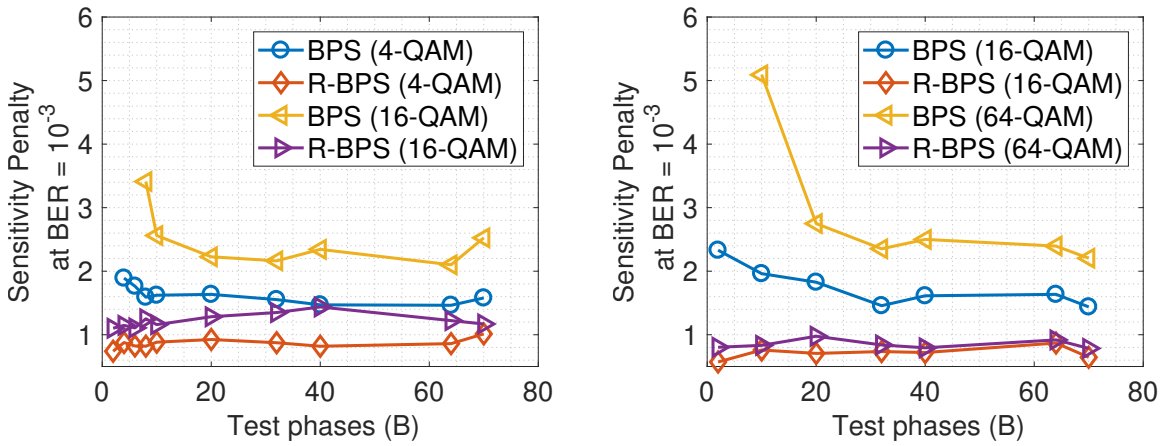

(a) (b)

Figure 4.39 – Sensitivity penalty for different numbers of test phase values (a) for 4-QAM and 16-QAM, (b) 16-QAM and 64-QAM.

R-BPS required less test phase noise ($B = 6$) than the BPS. This will lead to significant consequences on the implementation complexity as the complexity of the filtering window for additive noise mitigation is negligible compared to that of the required computation for each extra test phase.

4.2.2.7 Tolerance to Modulation Order

To evaluate the robustness of the algorithm regarding the change of the modulation order, phase mean square error was evaluated employing 4-, 16- and 64-QAM modulation formats. The linewidth symbol duration product is fixed at 10^{-5} for each modulation scheme. 5 Monte Carlo runs were processed over 5×10^3 generated symbols. The number of test phase is maintained fixed for all the modulation formats and it is $B = 6$ for the R-BPS approach and $B = 32$ for the BPS scheme. The window size parameter is the same for both algorithms and set to $N = 9$. Finally, the parallel processing is performed over $L = 8$ stages.

As shown in Fig. 4.40, R-BPS seems to be robust against the phase noise independently of the introduced modulation format as its MSE curve does not present a fluctuating shape. Meanwhile, the BPS algorithm presents more phase error fluctuations. This demonstrates the superior phase tracking performance of the proposed R-BPS compared to BPS.

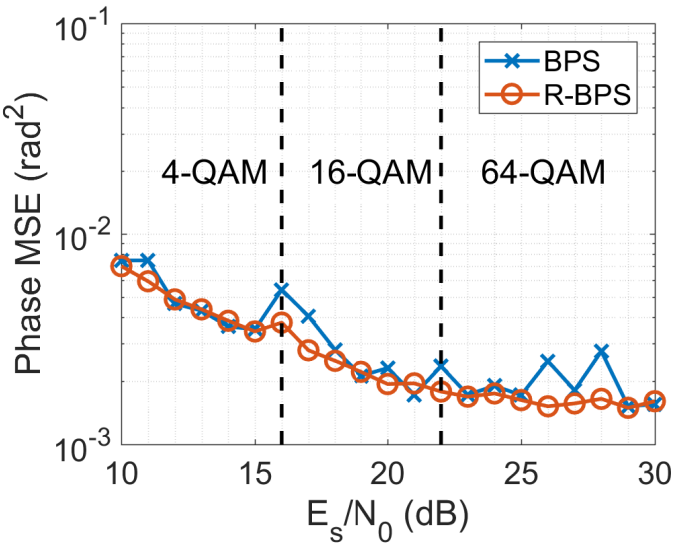

Figure 4.40 – Phase MSE evolution against modulation order change.

4.2.2.8 Complexity Comparison

In this part, the computational complexity of the algorithms are detailed and calculated for each functional block. The complexities are expressed in terms of the number of operations depending on the number of test phases B, the number of parallel stages L and the length of the window size N. The stated numbers of operations assume that a complex multiplication is equivalent to 2 real multiplications and subsequent 4 real adders.

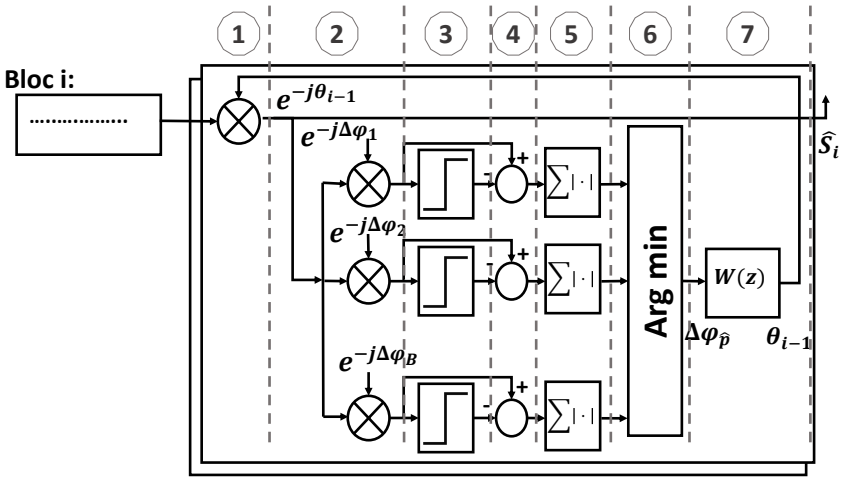

Figure 4.41 – The block diagram of R-BPS algorithm

The process of R-BPS in figure 4.41 is as follows:

① First the received block of N complex symbols are rotated by the last estimated phase via R-BPS algorithm. This operation requires N complex rotations and can be handled via a CORDIC algorithm since the phase value varies over time. Thus, $4N$ real multiplications and $2N$ real additions are processed.

② The output block of symbols is rotated again by B fixed test phases $\Delta\varphi_i$, $i \in 1, .., B$. This procedure demands $N \times B$ complex multiplications, i.e. $4NB$ real multiplications and $2NB$ real additions.

③ After B rotations, the symbols are fed to $N \times B$ decision operations.

④ Once decision is made, the absolute distance for error evaluation is performed. This could be reduced to 1 comparator, 2 real multiplications and 1 real addition per symbol thanks to a DSP trick called magnitude estimator [146]. Hence, the total computational complexity is NB comparators, $2NB$ real multiplications and NB real adders.

⑤ The errors are calculated and averaged. This demands $(N-1) \times B$ real additions.

⑥ The argmin operation needs $B-1$ comparators.

⑦ To accumulate the phase, another real addition operation is needed.

⑧ The output block of symbols is also fed to a decision circuit requiring N decisions.

To sum up, the R-BPS algorithm complexity comes down to $6NB + 4N$ real multiplications, $4NB - B + 2N + 1$ real additions, $NB + N$ decisions, and $NB + B - 1$ comparators.

For the BPS algorithm shown in Fig. 4.42, the process is as follows

① The N corrupted symbols are first rotated by B test phases. This requires $N \times B$ complex multiplications or $4N \times B$ real multiplications and $2N \times B$ real additions.

② Then, a decision circuit is used to calculate the square distance. This also needs $N \times B$ decisions.

③ Similarly, 2 real multipliers and three adders/substractors are needed for the square distance. Thus, $2N \times B$ real multiplications and $3N \times B$ real additions.

④ Also, to find the minimum, the average over N symbols is operated and this requires $(N-1) \times B$ real additions.

⑤ To perform argmin, $B-1$ comparators are needed.

⑥ The unwrapping operation which requires 1 comparator and 2 real additions.

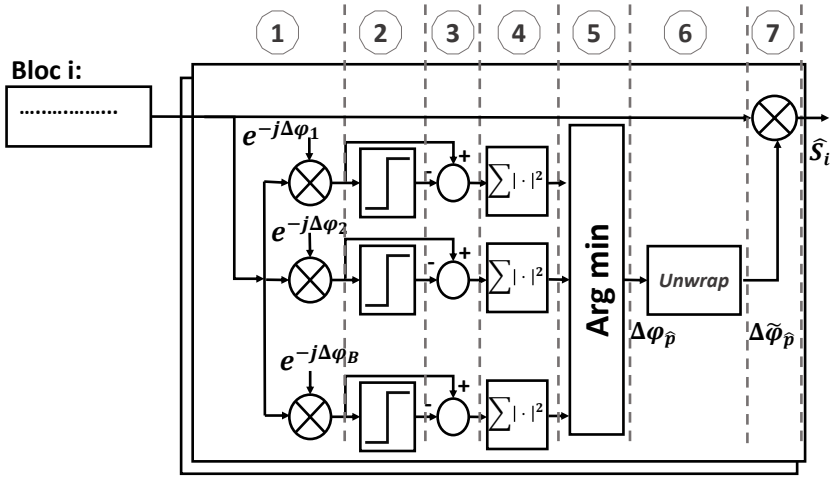

Figure 4.42 – The block diagram of R-BPS algorithm

⑦ Once the phase is estimated, the correction operation is performed and it needs then N complex multiplications or $4N$ real multiplications and $2N$ real additions.

⑧ The output block of symbols is also fed to a decision circuit requiring N decisions.

The total complexity of the BPS algorithm is summed to $6NB+4N$ real multiplications and $6NB - B + 2N + 2$ real additions, B comparators and $NB + N$ decisions.

Hence, the required hardware implementation complexity of both R-BPS and BPS methods is summarized in Table 4.6.

Table 4.7 – Complexity comparison between CPR algorithms

Algorithm	BPS interleaving	R-BPS interleaving
Real multiplier	$(6NB + 4N)L$	$(6NB + 4N)L$
Real adder	$(6NB - B + 2N + 2)L$	$(4NB + 2N - B + 1)L$
Comparators	BL	$(NB + B - 1)L$
Decisions	$(NB + N)L$	$(NB + N)L$

Note that the number of required trial phases B for the R-BPS algorithm is notably less than the one required for the BPS algorithm. Additionally, as presented earlier, R-BPS does not require a large window size N compared to BPS. Consequently, the R-BPS algorithm is clearly less complex than BPS.

4.3 Summary of Contributions

In this chapter, we presented, at first, a new approach for joint polarization demultiplexing and IQ imbalance compensation. This method relies on two blind and modified algorithms in order to perform jointly and adaptively polarization separation and IQ imbalance mitigation. The proposed method helps to compensate for the gain and phase mismatch regardless of the origin of the IQ imbalance distortion (Tx or Rx). Additionally, the introduced method is checked under some polarization related effects such as polarization dependent loss and differential group delay. The "joint" algorithm proves to be effective in the presence of polarization dependent loss, but, it can not handle differential group delay due to its one tap structure. To overcome this issue, a processing technique based on Wiener filtering was proposed. On the other hand, the robustness of "joint" to chromatic dispersion is also studied. it is shown that the approach does not compensate for the CD but once performing an appropriate static equalization, the introduced method works well even with small amounts of residual chromatic dispersion. The salient points of the introduced algorithm are related to its capacity of tracking varying channel. This point is important, as in this case, the "joint" can be adopted in the Rx-DSP chain for flexible communication circumstances. In this context, we have assumed two kinds of variations: polarization mixing and modulation formats change. Regarding the first point, the polarization mixing varies with time leading to inter-polarization interference. Through numerical simulations, we demonstrate that the proposed algorithm is robust to track variation of the state of polarization. As for modulation formats change, "joint" is able to perform its goals rapidly and blindly. Finally, different comparisons have been made with cascaded "CMA+BASS" and often our approach outperforms this conventional scheme in terms of the qualitative performance metrics as well as the computational needs.

Two contributions were introduced for carrier phase recovery. The first approach is a modified decision directed CPR adopted for 16-QAM modulation. The advantages of this contribution mainly lie in its robustness against additive white noise, residual carrier frequency offsets and its effectiveness in practical implementation. Such approach is compared to the conventional decision directed scheme and presents better numerical results. The cost of using modified decision directed algorithm rather than the conventional one is mostly related to complexity as the proposed algorithm presents relatively higher computational load. Another drawback of the approach is that it is only dedicated to 16-QAM modulation formats so that it is not suitable for flexible communications.

This leads us to present another scheme adopted for different order of square modulation types. The proposed approach, called R-BPS, is tested and compared against the conventional BPS with interleaving implementation in parallel processing. The approach demonstrates its robustness against residual carrier frequency offsets, additive white noise. Also, R-BPS proves its efficiency when introducing various modulation formats which makes it a good tool within the flexible communications context. In terms of complexity, the approach is less complex as it requires a smaller number of test phases.

In the next chapter, experimental validations of the presented algorithms are proposed.

Chapter 5

Experimental Validations For Coherent Optical Systems

In the previous chapters, digital signal processing algorithms for optical coherent transmission have been discussed. In the present chapter, we extend our work and report the full experimental demonstration of polarization multiplexed signal generation, fiber-transmission and digital coherent detection. Experimental setups are considered in our investigation to evaluate the performance of the proposed DSP algorithms as well as literature methods designed for fiber optical transmission.

In fact, numerical simulations use suitable design models for capturing and reproducing channel fiber's linearity effects, implementing algorithms for information recovery. Thus, the challenges in numerical simulation are firstly the translation of a detailed signal propagation over optical channel and system models into a form that is suitable for simulation and secondly adapting the right process for compensating those modeled imperfections.

In contrast, the main findings of the experimental data are for verifying that the empirical model matches with that of the channel extracted from the measured data. Moreover, experimental validations demonstrate the effectiveness of the used algorithms through the evaluation of retrieved sent information known by the transmitter.

Throughout this chapter, only the linear propagation impairments will be assumed. These imperfections are mainly chromatic dispersion, clock jitter, in-phase and quadrature imbalance and carrier phase and frequency offset.

Thus, the common configuration of optical coherent receiver associated with DSP algorithms used in these experiments is composed of static equalization block used to compensate for chromatic dispersion, IQ imbalance compensation algorithm for signal whitening, clock recovery block implemented to correct digital sampling error, polarization mode dispersion mitigated by using a butterfly filter composed of four FIR filters and phase and frequency offset recovery block employed to correct phase and frequency difference

between received signal and LO.

The chapter is organized as follows: in section 5.1, we introduce the experimental study to validate state of the art algorithms for single polarization transmission in the context of optical back-to-back (B2B) without chromatic dispersion or PMD emulator as well as in the context of optical transmission system thanks to the real signals provided by FOTON Institute in Lannion.

In section 5.2, the proposed blind joint polarization demultiplexing and IQ imbalance compensation method is tested and verified. In section 5.3, two additional experimental studies are presented to verify the effectiveness of the proposed carrier phase recovery schemes namely the modified decision directed approach and the parallel R-BPS algorithm. Finally, concluding remarks are drawn in section 5.4.

5.1 Experimental Performance of Single Polarization transmission

In this section, we will validate the state of the art algorithms through experimental data. This enables us to investigate the effect that we did not take into account in our previous simulations, such as non-ideal signal generation or the quantization effects. The experimental data have been obtained using the testbed of FOTON institute. In the following sections, we describe the experimental set-up and the DSP structure used to retrieve the transmitted sequence.

5.1.1 Back-to-back Performance

The main objective of the first experiment is to evaluate the back-to-back performance by connecting a transmitter directly to a receiver without a transmission line in between. In this case, we separate the degradations due to different propagation effects (CD, PMD, optical filtering effects etc.) from those related to the impact of the signal-to-noise ratio and Tx/Rx limitations. By degrading only the signal-to-noise ratio, we investigate in a back-to-back configuration with a coherent receiver and off-line digital signal processing, the evolution of the bit error ratio as a function of the OSNR.

5.1.1.1 Experimental Setup

The experimental setup shown in Fig. 5.1 was used to benchmark the state of the art algorithms. In this experiment, we consider only one polarization in order to simplify our setup.

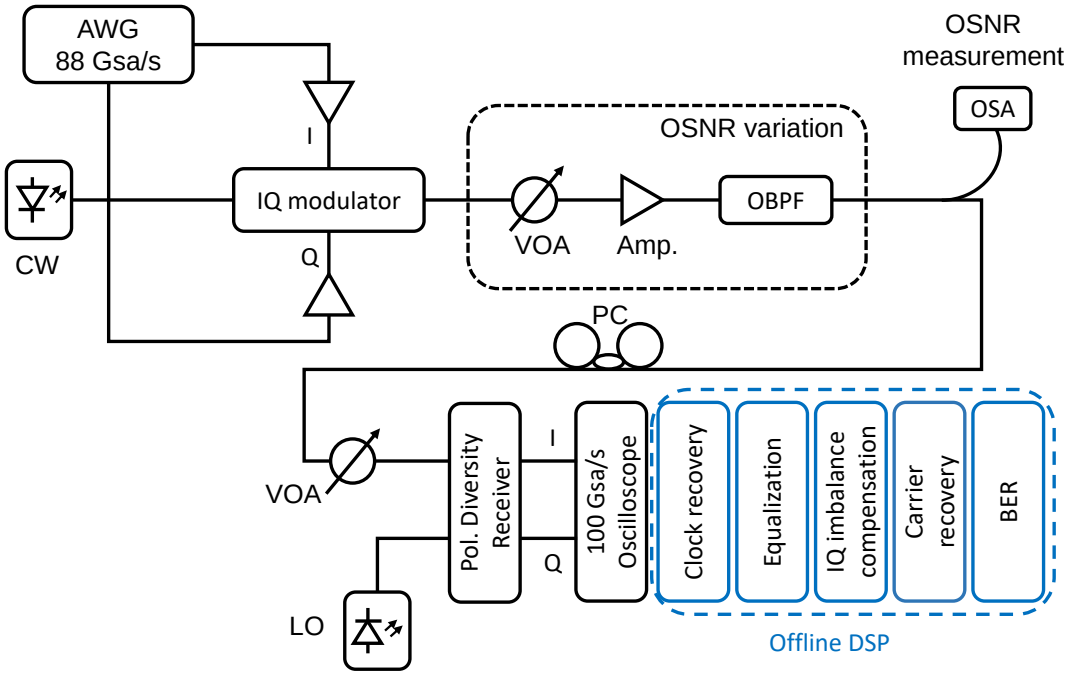

Figure 5.1 – Experimental setup of back-to-back 11 GBd M-QAM transmission ($M \in \{4, 16\}$).

At the transmitter side, a pseudo random binary sequences with length of $2^{11} - 1$ were chosen. This signal is loaded into a high speed arbitrary waveform generator (AWG). The digital signals modulate the optical carrier, originating form a continuous wave (CW) laser, by using an In-phase Quadrature modulator driven by 2 outputs of a 88 Gsa/s AWG generating 11 GBd M-QAM signals ($M \in \{4, 16\}$). An external cavity laser (ECL) with a linewidth of 100 kHz and operating at a wavelength of 1550 nm was used as the transmitter light source. Note that, the IQ modulator operates at the minimum bias point and the electrical signal amplitudes are adjusted so that the modulator is operated in the linear region of its transfer function. The modulated signal at the output of the IQ modulator is attenuated in a variable optical attenuator followed by an optical erbium-doped fiber amplifier in order to adjust the optical signal-to-noise ratio, which is measured in a 0.1 nm noise bandwidth. Another optical band-pass filter is used to reject the out-of-band

amplified spontaneous emission noise. The polarization controller at the receiver input is used to maximize the received signal on one polarization to ensure the state of polarization of the signal matches that of the local oscillator.

At the receiver side, the optical signal is mixed with the local oscillator. The receiver laser has a linewidth of about 100 kHz. The outputs of the 90° optical hybrid are detected by four balanced photo-detectors. The output photo-currents are digitized using a 2-channel real-time digital sampling oscilloscope of 100 Gsa/s sampling rate and 5-bit resolution. Finally, the acquired digital signals are resampled back to the DACs rate (88 Gsa/s), and processed off-line by the digital receiver implementation.

5.1.1.2 Experimental Results

The DSP structure used to retrieve the transmitted sequence and its related parameters is summarized in Table 5.1. To characterize the 16-QAM signal at 44 Gbit/s, the back-to-back BER was measured as function of the OSNR, and the results are presented in Fig. 5.3.

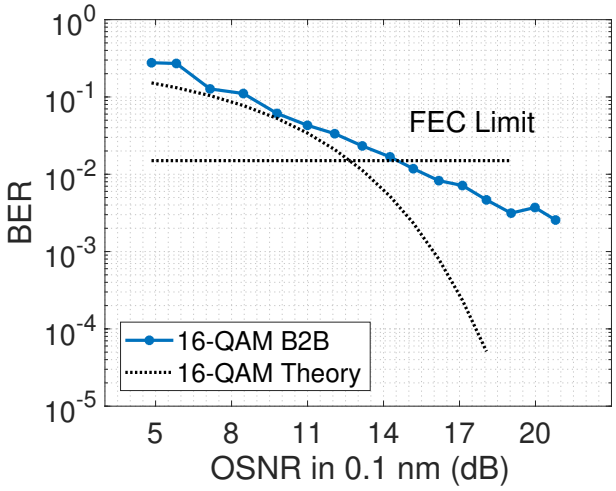

Figure 5.2

Figure 5.3 – Back-to-back BER versus OSNR for 16-QAM signal.

An important parameter for the global reach of an optical transmission system is the OSNR required to achieve a target bit error ratio. For transmission systems using a hard decision error correction code, it is generally considered that a raw bit error ratio of 1.5×10^{-2} at the input of the channel decoder leads to a bit error ratio of less than 10^{-15} after a 20% hard-decision forward error correction.

At BER = 1.5×10^{-2}, the required OSNR values to achieve this BER threshold is 14.5 dB for 16-QAM as shown in Fig. 5.3.

Back-to-back impairments (mainly carrier phase noise, sampling frequency offset and IQ imbalance) create penalty if not compensated for. The sate of the art algorithms can indeed partly compensate them. However, a significant penalty with respect to the performance on Additive White Gaussian Channel is shown and is highlighted by the presence of an error floor.

Table 5.1 – Off-line DSP algorithms blocks for the experimental back-to-back.

Existing impairments	Used algorithms	Related parameters
Sampling frequency offset	Order and Meyer	$L_{block} = 376$ $L_{farrow} = 47$
ISI and timing offset	Joint CMA equalizer and Gardner	$L_{eq} = 201$ $\mu_{eq} = 10^{-3}$ $\gamma_G = -1.5 \times 10^{-3}$
IQ imbalance	Valkama	$\mu_V = 0.1$
Carrier frequency offset	M^{th} power +FFT	$L_{block} = 1024$
Phase noise	decision-directed CPR	$B_T = 10^{-2}$ $\xi = 1/\sqrt{2}$

5.1.2 Transmission system

In this scenario, at the end of the link (consisting in spans of SSMF of length 200 km), the cumulative CD is compensated for using static equalizer at the DSP part. Hence, we can estimate the impact of CD degradation brought about by transmission over optical fiber.

5.1.2.1 Experimental Setup

The experimental setup, shown in Fig. 5.4, is based on an optical 4-QAM transmitter at 11 GBaud corresponding to a bit rate of 22 Gbit/s. The optical signal is launched into a recirculating fiber loop, consisting of two spans of 200 km of standard single mode fiber characterized by a fiber dispersion coefficient whose typical value is 17 ps/nm/km. The fiber loss is compensated for after each loop by using two in-line erbium-doped-fiber-amplifier. At the receiver side, the 4-QAM signal is sent to a 90° hybrid device. An external cavity laser is used for generating the 4-QAM modulated signal. The spectral

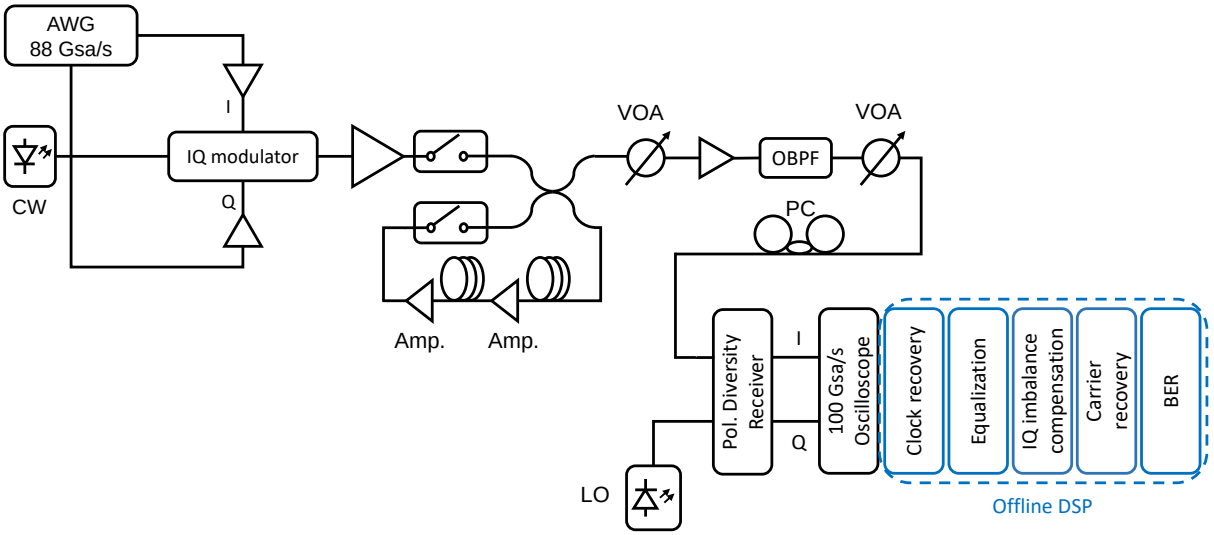

Figure 5.4 – Experimental setup. CW: continuous wave laser; Amp.: optical amplifier; AWG: arbitrary waveform generator; IQ mod.: in-phase/quadrature modulator; VOA: variable optical attenuator; OBPF: optical band-pass filter; PC: polarization controller.

linewidth of the two ECL lasers is 100 kHz. The signals at the outputs of the hybrid devices are detected with two balanced photodiodes to generate the I and Q components for the single polarization. Finally, these two signals are sampled by analog-to-digital converters at 100 Gsa/s. The discrete-time data are stored and processed off-line.

5.1.2.2 Experimental Results

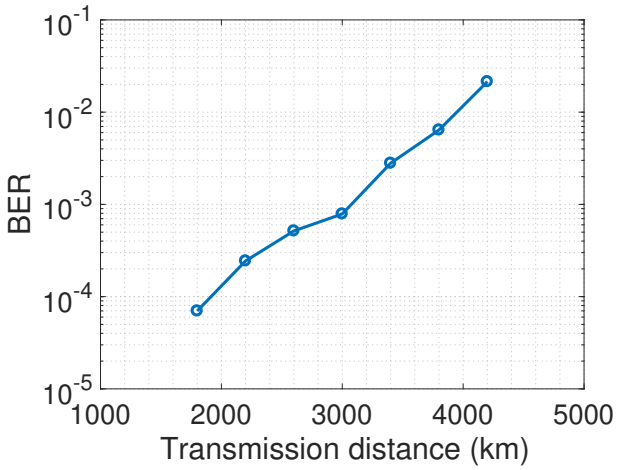

Figure 5.5 – BER vs transmission distance for 35.8 dB received OSNR.

Following the back-to-back performance evaluation, optical transmission experiment over distances of up to 4200 km of uncompensated SSMF were performed. The measured BER values with respect to the transmission distances using ZF-FIR CD compensation method for 4-QAM modulation are plotted in Fig. 5.5. The OSNR value is fixed at 35.8 dB for all the transmission distances. The used algorithms to compensate for the channel propagation impairments and retrieve the information originally sent are listed in Table 5.2.

Table 5.2 – Off-line DSP algorithms blocks for the optical transmission experiment.

Existing impairments	Used algorithms	Related parameters
Sampling frequency offset	Order and Mayer	$L_{block} = 376$ $L_{farrow} = 47$
Chromatic Dispersion	ZF-FIR filter	$L_{eq} = 2 \times \lfloor \pi \beta_2 D f_p^2 \rfloor + 1$
ISI and timing offset	joint CMA equalizer and Gardner	$L_{eq} = 97$ $\mu_{eq} = 10^{-5}$ $\gamma_G = -1.5 \times 10^{-3}$
IQ imbalance	Valkama	$\mu_V = 0.1$
Carrier frequency offset	M^{th} power + FFT	$L_{block} = 1024$
Phase noise	decision-directed CPR	$B_T = 10^{-2}$ $\xi = 1/\sqrt{2}$

As can be seen, the BER grows rapidly. The system exhibits a BER lower than the FEC limit (1.5×10^{-2}) up to 4050 km.

5.2 Experimental Study for the Proposed Joint Algorithm

In this section, we validate our proposed "joint" algorithm along with the proposed experimental setup. Through experimental data using 44 Gbit/s coherent optical system based on polarization multiplexing and 4-QAM modulation over 200 km, we evaluate the overall system performance.

5.2.1 Experimental Setup

The experimental setup shown in Figure 5.6 was used to benchmark the algorithms. At the transmitter side, two pseudo random binary sequences, each of length $2^{11} - 1$ and

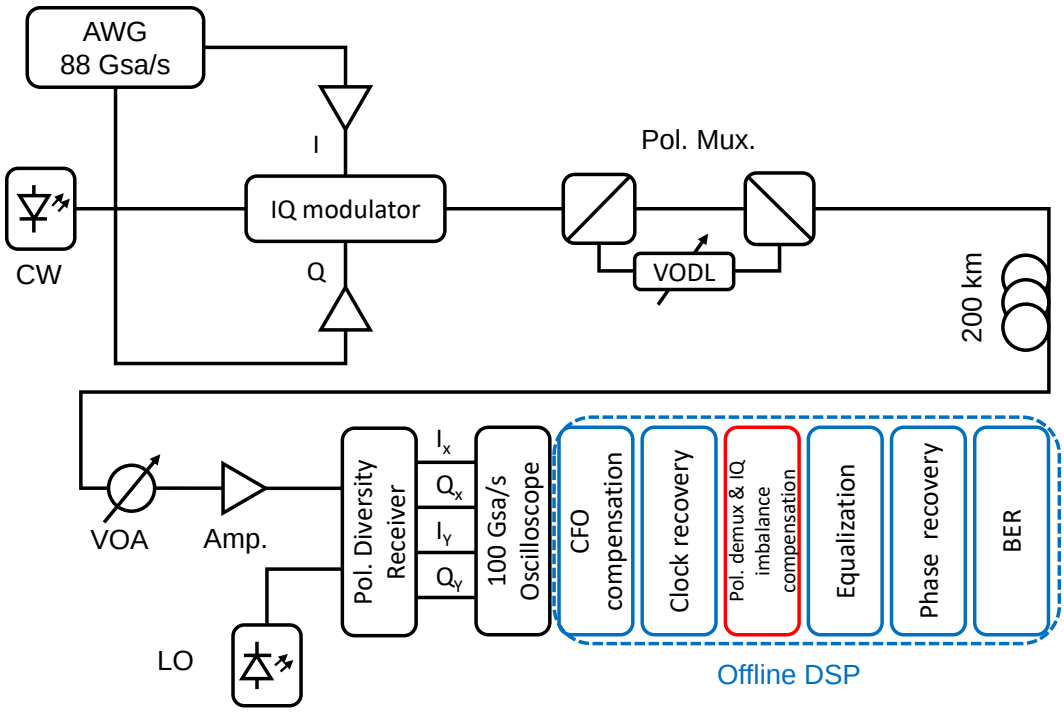

Figure 5.6 – Experimental setup for a 11 GBd PM-M-QAM transmission with 200-km optical fiber ($M \in \{4, 16\}$).

delayed by half a pattern, are generated off-line to generate two QAM signals. These signals are loaded into a high speed arbitrary waveform generator. The digital signals modulate the optical carrier, originating from a continuous wave laser, by using an IQ modulator driven by two outputs of a 88 GSa/s arbitrary waveform generator generating 11 GBd 4-QAM and 16-QAM signals. The laser wavelength is set to 1550 nm. Next, polarization multiplexing is emulated from a single laser source by the polarization beam splitter and polarization beam combiner. The multiplexed signal is then transmitted over a 200-km long standard-single-mode optical fiber and passed to a variable optical attenuator followed by an EDFA to adjust the optical signal-to-noise ratio, which is measured in a 0.1 nm noise bandwidth. The signal, mixed with ASE noise for various OSNR values, is fed to a polarization diversity coherent receiver to produce two base-band electrical signals. Next, the electrical signals were sampled at 100-GHz and stored for off-line processing.

5.2.2 Experimental Results

The off-line DSP algorithms employed in this experiment are outlined in Table 5.3.

Table 5.3 – Off-line DSP algorithms blocks using the "joint" algorithm.

Existing impairments	Used algorithms	Related parameters
Carrier frequency offset	M^{th} power + FFT	$L_{block} = 1024$
Sampling frequency offset	Order and Mayer	$L_{block} = 376$ $L_{farrow} = 47$
Polarization multiplexing and IQ imbalance	"joint" algorithm	$\mathbf{B} = I_4$ $\mu_J = 1.2 \times 10^{-4}$ $\gamma_G = -1.5 \times 10^{-3}$
ISI and timing offset	2 CMA equalizers	$L_{eq} = 25$ $\mu_{eq} = 1.2 \times 10^{-4}$
Phase noise	decision-directed CPR	$B_T = 10^{-2}$ $\xi = 1/\sqrt{2}$

As the proposed joint algorithm is modulation format independent, two experimental setups were performed using different modulation formats (4-, and 16-QAM) without the necessity to change the algorithm parameters.

In the "aligned SOPs" experiment setup, we manually adjust the two orthogonal states of polarization (for each polar) of the PM signal match with those of the polarization-diversity receiver. In contrast, the "arbitrary SOPs" experiment stands for no adjustments, and in this case, we are facing a polarization demultiplexing problem. Each acquired experimental data consist of 4 signals (representing the I and Q component of each polarization) composed of 10^6 samples, i.e. 6×10^4 symbols which are stored and processed off-line in a computer.

After DSP off line processing, consisting of carrier frequency offset compensation and re-sampling to 6 samples per symbol, the constellations shown in Fig. 5.7 and Fig. 5.10 have been retrieved. As shown in these figures, it is obvious in this experiment to conclude the origin of IQ imbalance. In fact, as the constellations are altered by residual frequency offset and phase noise, it is possible to distinguish between Tx and Rx IQ imbalance from the constellations. Indeed, Tx IQ imbalance will cause the constellation to become a concentric circle whereas the Rx IQ imbalance will cause the constellation to change from a circle to an ellipse. In view of the obvious characteristics of the resulted constellation, it is fair to conclude that the distortion comes from Tx IQ imbalance.

Fig. 5.7 presents the resulted constellations before and after applying our proposed joint algorithm in the two experimental setups. In the aligned SOPs case, we can see in Fig. 5.7(a) that the constellations of the two polarizations before the "joint" are altered by

the Tx-IQ imbalance, inter-symbol interference as well as the carrier phase. However, in the arbitrary SOPs experiments, the constellations are altered not only by Tx-IQ imbalance, ISI and carrier phase but also by polarization rotation as the ring of the 4-QAM constellation is no longer visible, as depicted in Fig. 5.7(c). The resulted outputs of the joint algorithm for both aligned SOPs and arbitrary SOPs experiments are depicted in Fig. 5.7(b) and Fig. 5.7(d), respectively. It can be qualitatively observed that the IQ mismatch has been correctly compensated. In fact, the obtained constellations present a circular shape with normalized energies. However, based on the constellations, we cannot strictly conclude that the two polarizations have been successfully demultiplexed. Moreover, the joint algorithm is not able to compensate for the residual chromatic dispersion and the phase noise that exist in the practical system. This explains why the constellations are deeply altered by inter-symbol interference.

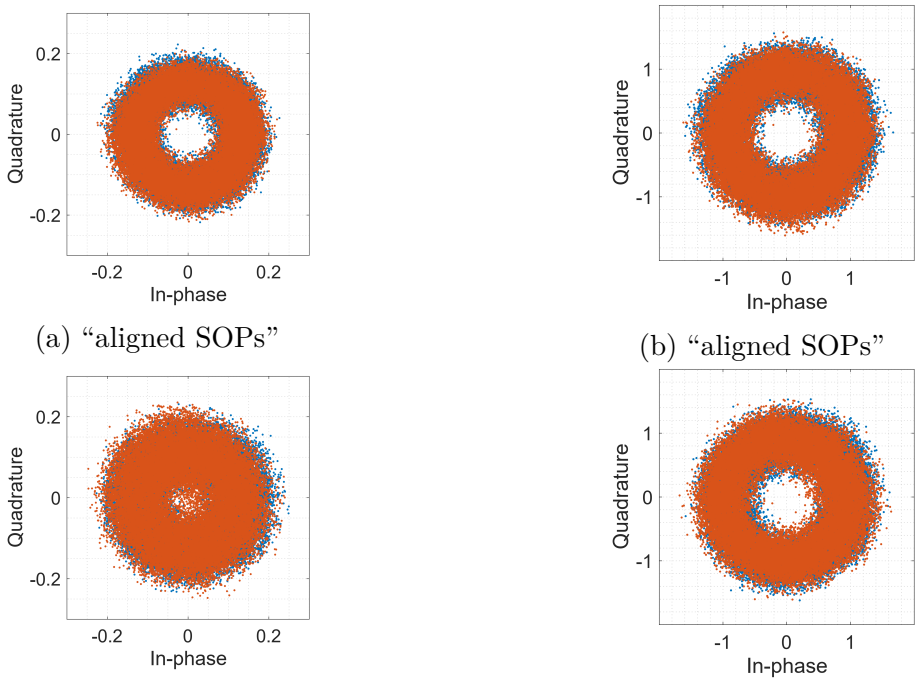

(a) "aligned SOPs" (b) "aligned SOPs"

(c) "arbitrary SOPs" (d) "arbitrary SOPs"

Figure 5.7 – Obtained 11 Gbd PM-4-QAM constellations at a 13.5 dB OSNR before (a-c) and after (b-d) proposed joint algorithm compensation.

To ensure that the demultiplexing process has been accomplished normally, the visualization of the modulus of the compensation matrix coefficients convergence demonstrate whether the received data are correctly retrieved or not. For the "aligned SOPs" experiments, we can see from Fig. 5.8(a) that the modulus of all the diagonal coefficients

represented by the orange lines have converged towards a constant value and that the rest of the coefficients converge towards the values which allow to compensate for the Tx-IQ imbalance. Note that in Fig. 5.8(b), the magnitude of the diagonal elements of the compensation matrix converge to two different constant values. This opens up a path of inquiry into the causes of this convergence. If we assume that nonlinear impairments are omitted, and we look at the general form of the distortion matrix **G** which incorporates the Tx-IQ imbalance and the parameters of the polarization rotation, we see that its diagonal elements are governed by 4 values (see section 4.1.1): h_1 and h_4 linked to the polarization rotation parameters and $k_{1,X}$ and $k_{1,Y}$ those of Tx IQ imbalances in X and Y polarizations. However, normally the magnitude of these 2 values ($k_{1,X}$ and $k_{1,Y}$) are the same since in our experiments only one IQ modulator is considered for the two polarizations. Also, in the absence of the PDL, the magnitude of h_1 and h_4 will be the same (according to the model of the Jones matrix).

Mathematical investigation was conducted to consolidate this interpretation. The inverse of the distortion matrix **G** could be expressed as

$$\mathbf{A} = \begin{pmatrix} \frac{h_4\left|k_{1,X}\right|^2}{k_{1,X}D_1} & -\frac{k_{2,X}h_4{}^*}{D_3} & -\frac{h_2\left|k_{1,X}\right|^2}{k_{1,X}D_1} & \frac{k_{2,X}h_2{}^*}{D_3} \\ -\frac{h_4\left|k_{2,X}\right|^2}{k_{2,X}D_1} & \frac{k_{1,X}h_4{}^*}{D_3} & \frac{h_2\left|k_{2,X}\right|^2}{k_{2,X}D_1} & -\frac{k_{1,X}h_2{}^*}{D_3} \\ -\frac{h_3\left|k_{1,Y}\right|^2}{k_{1,Y}D_2} & \frac{k_{2,Y}h_3{}^*}{D_4} & \frac{h_1\left|k_{1,Y}\right|^2}{k_{1,Y}D_2} & -\frac{k_{2,Y}h_1{}^*}{D_4} \\ \frac{h_3\left|k_{2,Y}\right|^2}{k_{2,Y}D_2} & -\frac{k_{1,Y}h_3{}^*}{D_4} & -\frac{h_1\left|k_{2,Y}\right|^2}{k_{2,Y}D_2} & \frac{k_{1,Y}h_1{}^*}{D_4} \end{pmatrix}. \tag{5.1}$$

where $D_1 = (\left|k_{1,X}\right|^2 - \left|k_{2,X}\right|^2)(h_1h_4 - h_2h_3)$, $D_2 = (\left|k_{1,Y}\right|^2 - \left|k_{2,Y}\right|^2)(h_1h_4 - h_2h_3)$, $D_3 = (\left|k_{1,X}\right|^2 - \left|k_{2,X}\right|^2)(h_1h_4 - h_2h_3)^*$ and $D_4 = (\left|k_{1,Y}\right|^2 - \left|k_{2,Y}\right|^2)(h_1h_4 - h_2h_3)^*$.

When considering the modulus of the compensation matrix, we have $|D_1| = |D_3|$ and $|D_2| = |D_4|$ and

$$|\mathbf{A}| = \begin{pmatrix} \frac{|h_4||k_{1,X}|}{|D_1|} & \frac{|k_{2,X}||h_4|}{|D_1|} & \frac{|h_2||k_{1,X}|}{|D_1|} & \frac{|k_{2,X}||h_2|}{|D_1|} \\ \frac{|h_4||k_{2,X}|}{|D_1|} & \frac{|k_{1,X}||h_4|}{|D_1|} & \frac{|h_2||k_{2,X}|}{|D_1|} & \frac{|k_{1,X}||h_2|}{|D_1|} \\ \frac{|h_3||k_{1,Y}|}{|D_2|} & \frac{|k_{2,Y}||h_3|}{|D_2|} & \frac{|h_1||k_{1,Y}|}{|D_2|} & \frac{|k_{2,Y}||h_1|}{|D_2|} \\ \frac{|h_3||k_{2,Y}|}{|D_2|} & \frac{|k_{1,Y}||h_3|}{|D_2|} & \frac{|h_1||k_{2,Y}|}{|D_2|} & \frac{|k_{1,Y}||h_1|}{|D_2|} \end{pmatrix}. \tag{5.2}$$

In our experiments, a unique IQ modulator is used to modulate the signal components of the two polarizations. In this case, $\left|k_{1,X}\right| = \left|k_{1,Y}\right|$ and $\left|k_{2,X}\right| = \left|k_{2,Y}\right|$ and therefore

$|D_1| = |D_2| = |D_3| = |D_4|$. The modulus of the resulted matrix is then given by

$$|\mathbf{A}| = \frac{1}{|D_1|} \begin{pmatrix} |h_4||k_{1,X}| & |h_4||k_{2,X}| & |h_2||k_{1,X}| & |h_2||k_{2,X}| \\ |h_4||k_{2,X}| & |h_4||k_{1,X}| & |h_2||k_{2,X}| & |h_2||k_{1,X}| \\ |h_3||k_{1,X}| & |h_3||k_{2,X}| & |h_1||k_{1,X}| & |h_1||k_{2,X}| \\ |h_3||k_{2,X}| & |h_3||k_{1,X}| & |h_1||k_{2,X}| & |h_1||k_{1,X}| \end{pmatrix}. \tag{5.3}$$

if we consider only Tx-IQ and polarization rotation and that there is no PDL nor DGD, in this case: $|h_1| = |h_4|$ and $|h_2| = |h_3|$ and we have

$$|\mathbf{A}| = \frac{1}{|D_1|} \begin{pmatrix} |h_1||k_{1,X}| & |h_1||k_{2,X}| & |h_2||k_{1,X}| & |h_2||k_{2,X}| \\ |h_1||k_{2,X}| & |h_1||k_{1,X}| & |h_2||k_{2,X}| & |h_2||k_{1,X}| \\ |h_2||k_{1,X}| & |h_2||k_{2,X}| & |h_1||k_{1,X}| & |h_1||k_{2,X}| \\ |h_2||k_{2,X}| & |h_2||k_{1,X}| & |h_1||k_{2,X}| & |h_1||k_{1,X}| \end{pmatrix}. \tag{5.4}$$

The components of matrix $|\mathbf{A}|$ are presented in 4 different colors indicating the possible levels of convergence of the "joint" algorithm coefficients when the PDL is not considered and only Tx-IQ imbalance is examined and 8 levels otherwise.

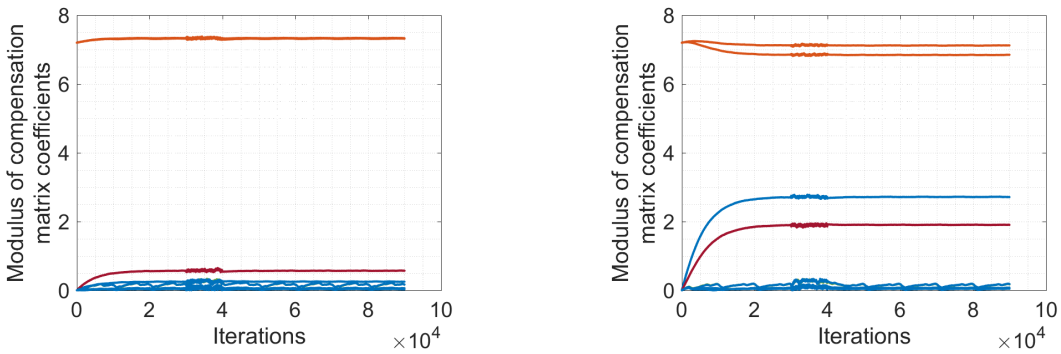

(a) (b)

Figure 5.8 – Modulus of mixture coefficients convergence for PM-4-QAM (a) "aligned SOPs", (b) "arbitrary SOPs".

Therefore, the convergence of the compensation matrix towards two different values in its diagonal concludes the presence of the PDL meaning the attenuation of one polarization with respect to the other.

In this part, we have detailed the mathematical model of the compensation matrix. This allows the investigation of useful information about the presence of polarization

rotation, IQ imbalance as well as the PDL. Through experimental data processing, we were able to indicate the existence of PDL in PM-4-QAM "arbitrary SOPs" system and we tried to compensate for it by applying directly the inverse of the PDL model guaranteeing an equal convergence for the modulus of the coefficients of the diagonal of the compensation matrix. The modulus of matrix compensation coefficients convergence for PM-4-QAM after PDL compensation is depicted in Fig. 5.9.

In Fig. 5.10, the constellations of the 16-QAM modulation formats in both experiments "aligned SOPs" and "arbitrary SOPs" before and after the joint algorithm processing are depicted. In Fig. 5.10(a), we are not able to distinguish the 3 rings of the 16-QAM as the signals are widely corrupted by inter-symbol interference.

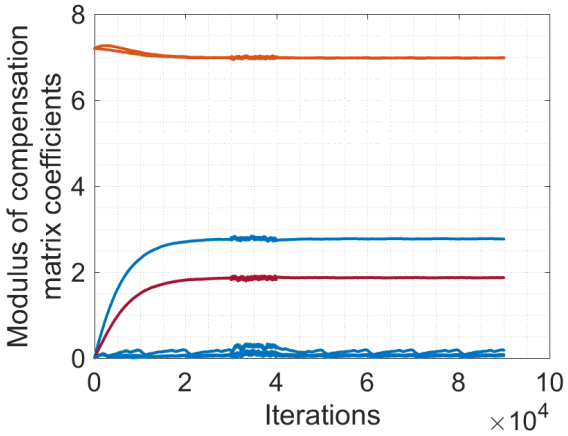

Figure 5.9 – Modulus of mixture coefficients convergence for PM-4-QAM after PDL compensation for the "arbitrary SOPs" experiments.

In this case, both Fig. 5.10(a) and Fig. 5.10(c) have visually the same plots. Nevertheless, signals in Fig. 5.10(a) are issued from manual adjustment of the polarization controller whereas those from Fig. 5.10(c) are rotated by an unknown polarization rotation. In both experiments, the signals have been whitened by the joint algorithm as can be concluded from the overall dynamics of the constellations.

The evolution of the modulus of the compensation coefficients is depicted in Fig. 5.11. For the "aligned SOPs" experiments, the modulus of the diagonal elements converge to a constant value whereas the rest of the matrix elements fluctuate around very small values (see Fig. 5.11(a)). In this case, the compensation matrix has roughly the form of $\alpha \times \mathbf{I}_4$, where $\alpha \in \mathbb{R}_+$. This confirms the fine adjustment of the states of polarization of the signals with the optical hybrid axes in the experiments. On the other hand, Fig. 5.11(b)

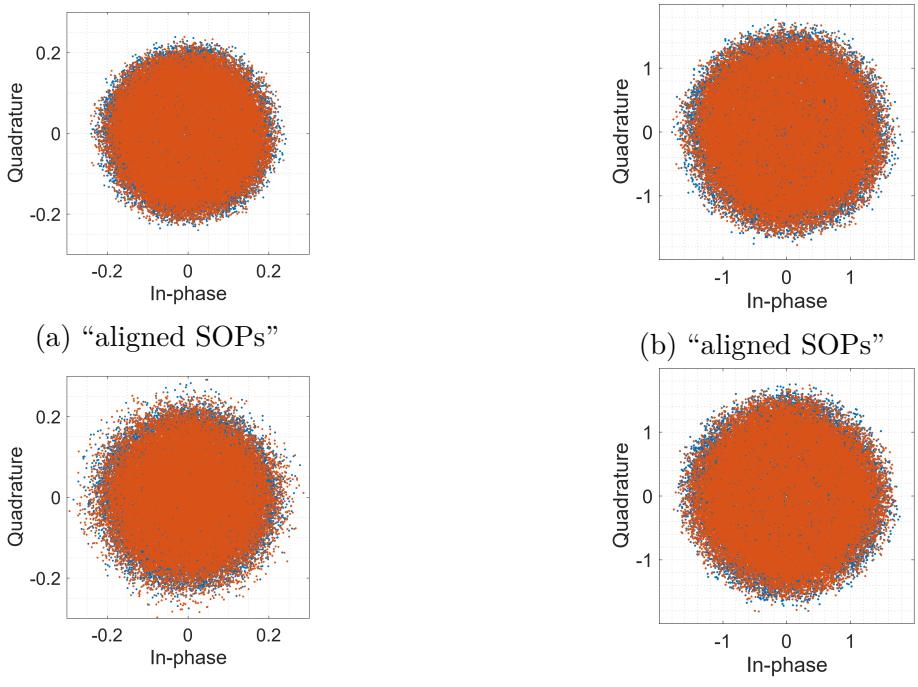

(a) "aligned SOPs" (b) "aligned SOPs"

(c) "arbitrary SOPs" (d) "arbitrary SOPs"

Figure 5.10 – Obtained 11 Gbd PM-16-QAM constellations at a 17.7 dB OSNR before (a-c) and after (b-d) proposed joint algorithm compensation.

shows the appropriate coefficients convergence for joint polarization demultiplexing and IQ imbalance compensation.

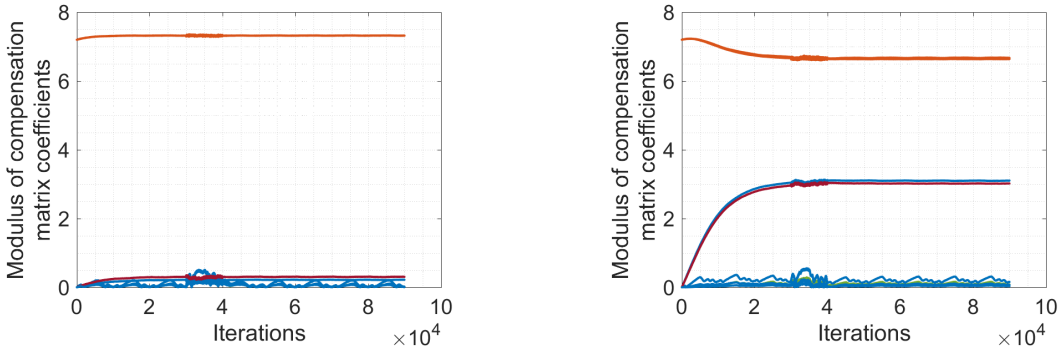

(a) (b)

Figure 5.11 – Modulus of mixture coefficients convergence for PM-16-QAM at a 17.7 dB OSNR (a) "aligned SOPs", (b) "arbitrary SOPs".

After the joint algorithm, each demultiplexed polarization is fed into CMA followed by decision-directed-LMS based equalizer for inter-symbol interference and carrier phase

compensations. The constellation diagrams of the compensated 4-QAM and 16-QAM data are shown in Fig. 5.12 and Fig. 5.13, respectively. For the "aligned SOPs", PM-4-QAM constellations are corrupted by ASE and the two polarizations present roughly the same output performance in terms of SNR and EVM. However, in the "arbitrary SOPs" experiment, it is clear that the constellation of Pol.X presents better performance than that of Pol.Y. This is consistent with the fact that the modulus of the diagonal compensation matrix converge towards two different values as one polarization is attenuated with respect to the other due to PDL. This produces a slight OSNR offset of about 0.8 dB at BER $= 3.8 \times 10^{-3}$ with respect to Pol.X BER curve as can be seen in Fig. 5.14(b).

Fig. 5.13 presents the constellation diagrams of PM-16-QAM. For both "aligned SOPs" and "arbitrary SOPs" experiments, the recovered signals have closely the same achievement with a very slight increase in Pol.Y SNR output compared with Pol.X SNR ouput. This proves the effectiveness of the proposed joint algorithm for polarization demultiplexing and IQ imbalance compensation.

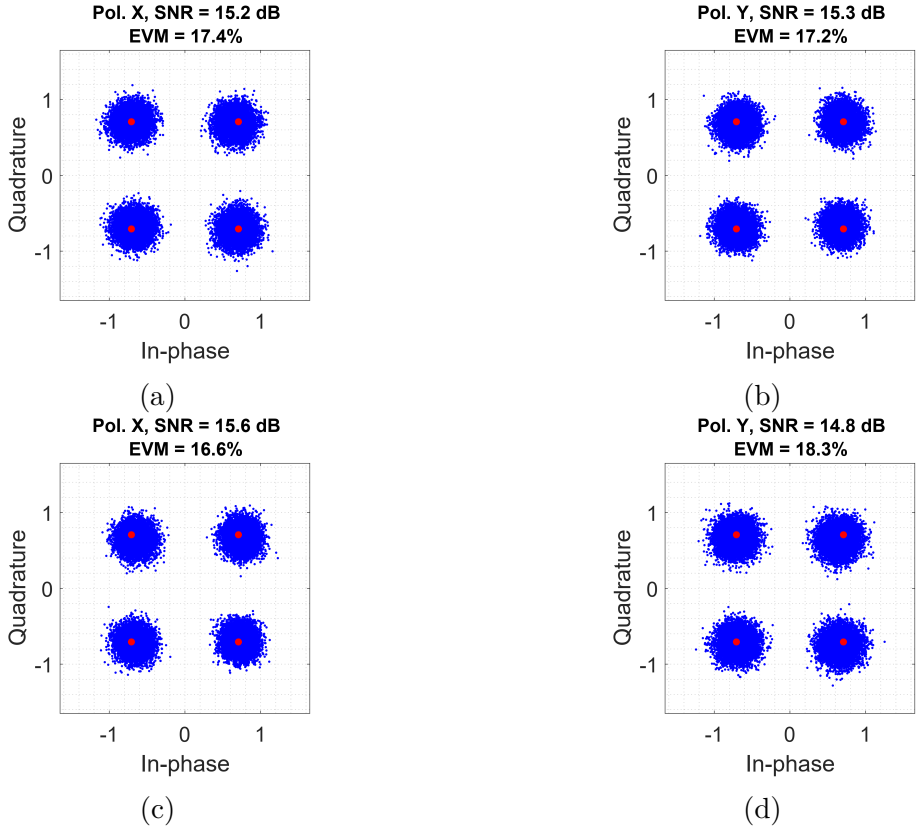

Figure 5.12 – Recovered PM-4-QAM constellations at OSNR = 13.5 dB for the (a-b) "aligned SOPs", (c-d) "arbitrary SOPs" experiments.

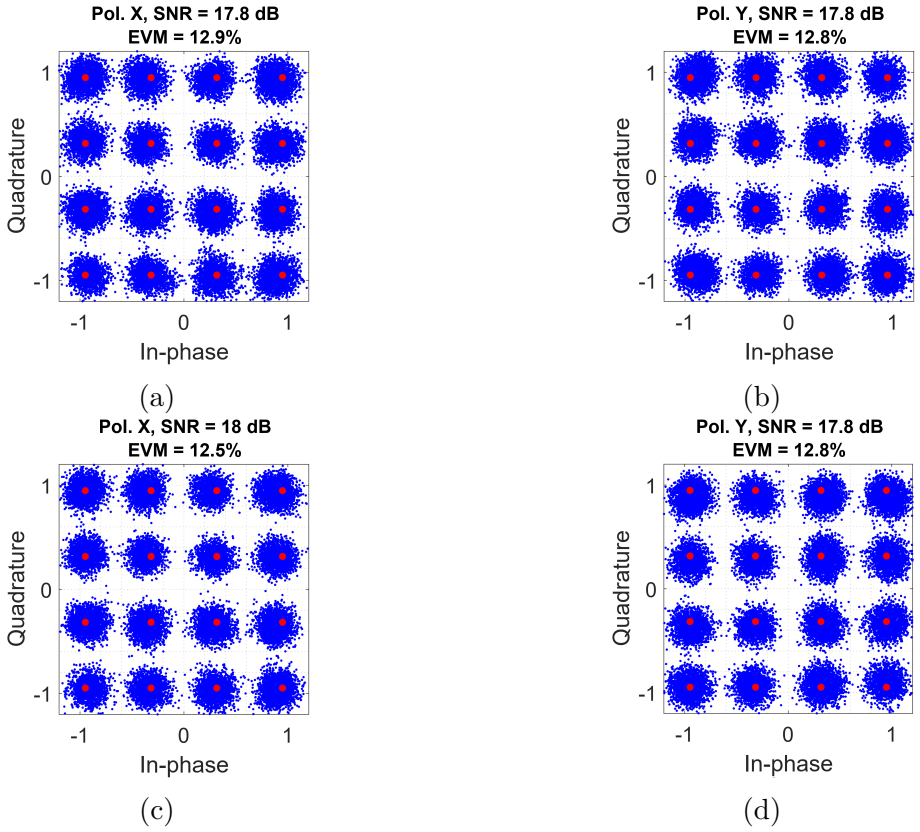

Figure 5.13 – Recovered PM-16-QAM constellations at OSNR = 17.7 dB for (a-b) "aligned SOPs" (c-d) "arbitrary SOPs" experiments.

Fig. 5.14 and Fig. 5.15 represent the BER performance as a function of received optical signal to noise ratio for PM-4-QAM and PM-16-QAM signals, respectively. In Fig. 5.14(b), it is found that the "joint" algorithm succeeded in performing polarization separation and IQ imbalance compensation issued from the experimental transmission. Additionally, experiment results present roughly 2 dB of OSNR penalty at BER = 3.8×10^{-3} compared to the theoretical optimum PM-4-QAM curve. Similarly, Fig. 5.15 depicts the efficiency of the "joint" algorithm for retrieving PM-16-QAM signals.

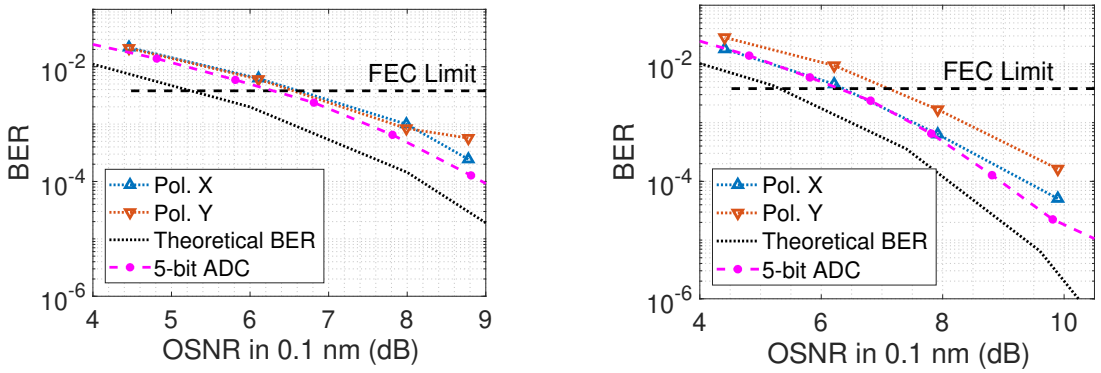

Figure 5.14 – BER as a function of OSNR with compensated IQ imbalance impairments originating from IQ modulator and separated multiplexed 4-QAM signals (a) "aligned SOPs", (b) "arbitrary SOPs".

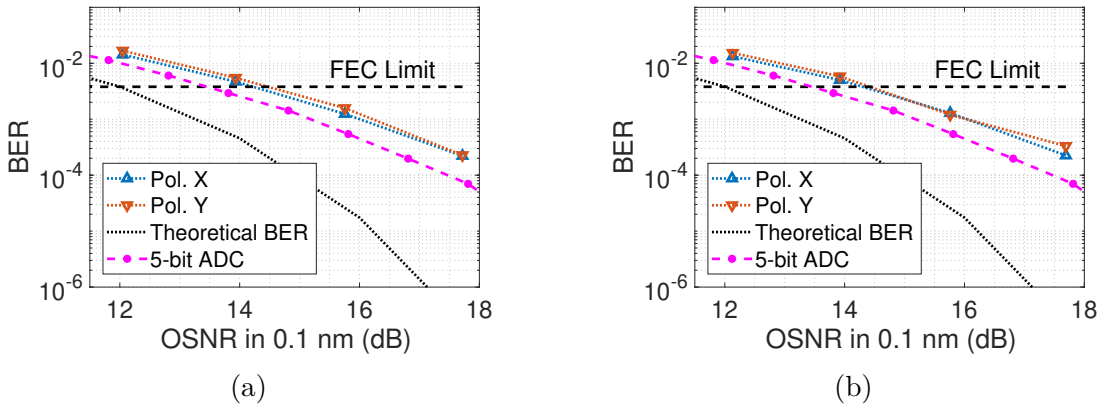

Figure 5.15 – BER as a function of OSNR with compensated IQ imbalance impairments originating from IQ modulator and separated multiplexed 16-QAM signals (a) "aligned SOPs", (b) "arbitrary SOPs".

5.3 Experimental Study for the Proposed CPR Algorithms

5.3.1 modified decision-directed CPR validation

This section provides an experimental validation for two proposed carrier phase recovery algorithms. The same experimental setup is used for both methods and performance evaluations are carried out for the two proposed techniques.

5.3.1.1 Experimental Setup

Fig. 5.16 represents the block diagram of the setup used in the experimental demonstration. Transmission experiments were accomplished using a 11-Gbaud 16-QAM signal with 0.5 roll-off square root raised cosine shaping filter. An arbitrary waveform generator running at 88 GSa/s generates the required analog baseband signal that is subsequently amplified by two radio-frequency amplifiers. Then, the signal is modulated into a 1550-nm optical carrier by an IQ modulator. A combination of a variable optical attenuator, an EDFA, and an optical band-pass filter was used to adjust the received OSNR. An ECL with a spectral linewidth of 100 kHz is used at the receiver to mix the optical signal with the local oscillator. To convert the optical signal onto the electrical domain, a coherent front end was used. The received electrical signal is digitized by a 100-GS/s, 33-GHz bandwidth oscilloscope. The data is processed offline using MATLAB to compensate for the phase noise distortion.

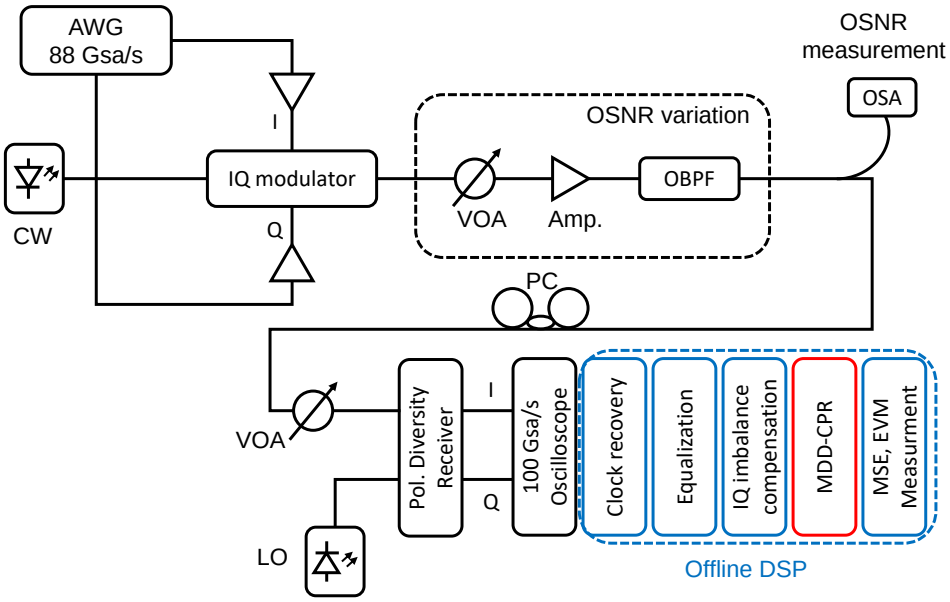

Figure 5.16 – Experimental setup for back-to-back 11 GBd 16-QAM transmission.

5.3.1.2 Experimental Results

In this subsection, we consider the single polarization transmission. The DSP structure used to retrieve the transmitted sequence is outlined in Table 5.4.

Table 5.4 – Off-line DSP algorithms blocks using modified decision-directed CPR.

Existing impairments	Used algorithms	Related parameters
Sampling frequency offset	Order and Mayer	$L_{block} = 376$ $L_{farrow} = 47$
ISI	CMA equalizer	$L_{eq} = 17$ $\mu_{eq} = 1 \times 10^{-2}$
IQ imbalance	Valkama	$\mu_V = 10^{-3}$
Carrier frequency offset	M^{th} power + FFT	$L_{block} = 1024$
Phase noise	modified decision-directed CPR	$B_T = 10^{-3}$ $\xi = 1/\sqrt{2}$ $K_e = 3 \times 10^2$

As we consider only CPR, the comparison between the decision-directed CPR and the modified decision-directed CPR algorithms is performed in terms of the mean square error.

Fig. 5.17 shows the constellation diagrams of the experimental results. As depicted in Fig. 5.17(a), without carrier phase compensation, phase distortion occurs, which limits the system performance. Hence, phase noise canceling had been carried out using our method as well as the decision-directed phase recovery. Fig. 5.17(b) presents the overall performance after the introduction of decision-directed CPR while Fig. 5.17(c) represents the constellation diagram after modified decision-directed CPR algorithm.

Numerical results show that the two aforementioned algorithms have closely the same achievement with a slight increase in the modified decision directed CPR SNR output (25.5 dB in contrast to 24.7 dB using decision-directed CPR) ensuring an SNR gain of 0.8 dB compared with decision-directed CPR.

Fig. 5.18 illustrates the plot of the symbols at the output of the modified decision directed CPR algorithm using the experiments presented in Fig.5.16. The aim of this experimental result is to compare the proposed algorithm with the conventional CPR in the context of dual polarization optical system transmission and its consequent joint equalization and phase noise mitigation. It is observed in Fig. 5.18 that the proposed CPR presents better performance in terms of SNR and EVM than the conventional approach. The good performance of the modified CPR can be confirmed through simple comparison of the resulted constellation shown in Fig. 5.18.

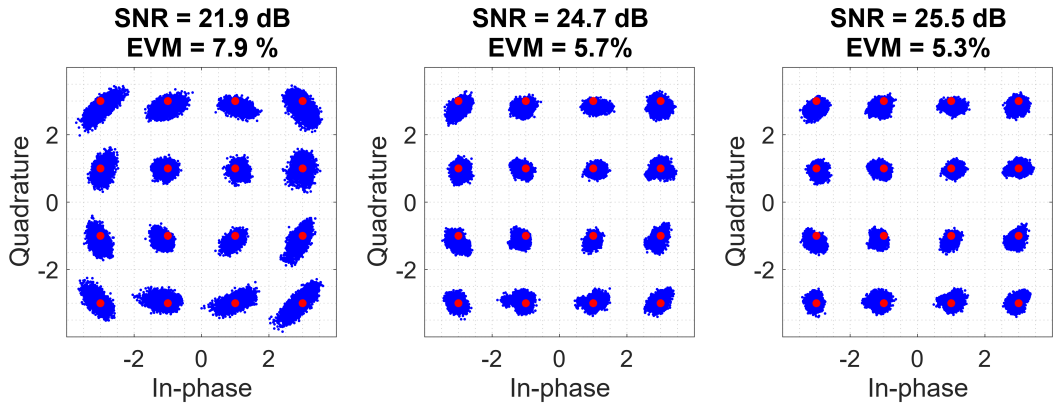

(a) (b) (c)

Figure 5.17 – Constellation diagrams: (a) without CPR, (b) with decision-directed CPR, (c) with modified decision-directed CPR.

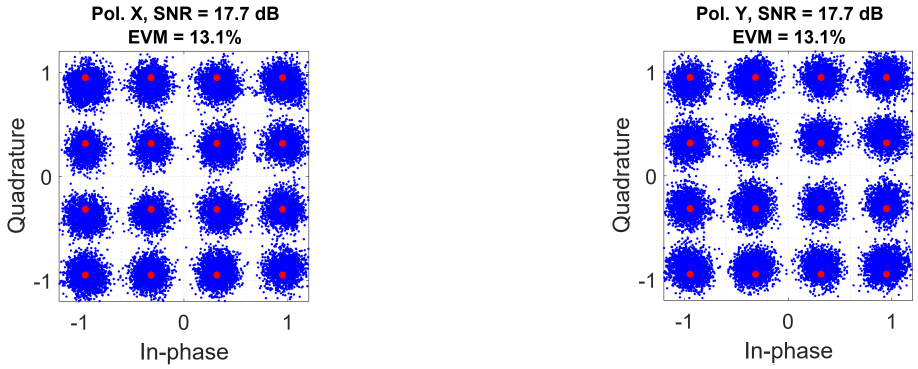

(a) (b)

Figure 5.18 – Recovered PM-16-QAM constellations at OSNR = 17.7 dB for the "arbitrary SOPs" experiments using a decision-directed CPR (a) Pol.X, (b) Pol.Y.

5.3.2 Parallel R-BPS Algorithm

5.3.2.1 Experimental Setup

The experimental setup for the R-BPS algorithm validation is the same as the one presented in Fig. 5.6. At the DSP transmitter part, the mapping process is accomplished using differential encoding per independent stage L. The number of stages used for experimental data acquisition will also be fixed at the level of digital processing at the receiver side to apply parallelism when operating with the R-BPS algorithm.

Table 5.5 – Off-line DSP algorithms blocks using R-BPS.

Existing impairments	Used algorithms	Related parameters
Carrier frequency offset	M^{th} power + FFT	$L_{block} = 1024$
Sampling frequency offset	Order and Meyer	$L_{block} = 606$ $L_{farrow} = 101$
Polarization multiplexing and IQ imbalance	"joint" algorithm	$\mathbf{B} = 7.2 \times I_4$ $\mu_J = 1 \times 10^{-4}$ $\gamma_G = -1.5 \times 10^{-3}$
ISI	2 CMA equalizers	$L_{eq} = 49$ $\mu_{eq} = 5 \times 10^{-5}$
Phase noise	R-BPS	L $N = 9$ $B = 6$

5.3.2.2 Experimental Results

The DSP algorithms used at the receiver part as well as their operating parameters are summarized in Table 5.5. Unless otherwise stated, the size of the observation window of both R-BPS and BPS algorithms is fixed to $N = 9$, the number of test phases is $B = 6$ for the R-BPS and $B = 32$ for the BPS. The number of parallel stages L used in each experiment is indicated case by case.

In our first experiment, the R-BPS and the BPS are processed using one stage ($L = 1$). Fig. 5.19(a) and 5.19(b) show the constellations of Pol.X before and after carrier phase recovery based on the proposed R-BPS algorithm for 6 Gbaud 4-QAM system with 27.8 dB OSNR. The efficiency of the R-BPS can be confirmed through simple comparison between constellations shown in Fig. 5.19.

(a) (b)

Figure 5.19 – (a), (b): constellations for 4-QAM before and after carrier phase recovery using R-BPS at OSNR = 27.8 dB.

It is clear that the received symbols cannot be detected at low BER without carrier recovery. After employing our carrier recovery algorithm, the resulted symbols and the phase estimate are shown in Fig. 5.20(a) and 5.20(b). We study the performance from a system point of view by implementing the EVM and SNR calculation, and the result is shown in Fig. 5.20(a) and in Fig. 5.20(b). As can be seen, the calculated EVM reaches a steady state performance of around 6.4% for Pol.X and 7% for Pol.Y.

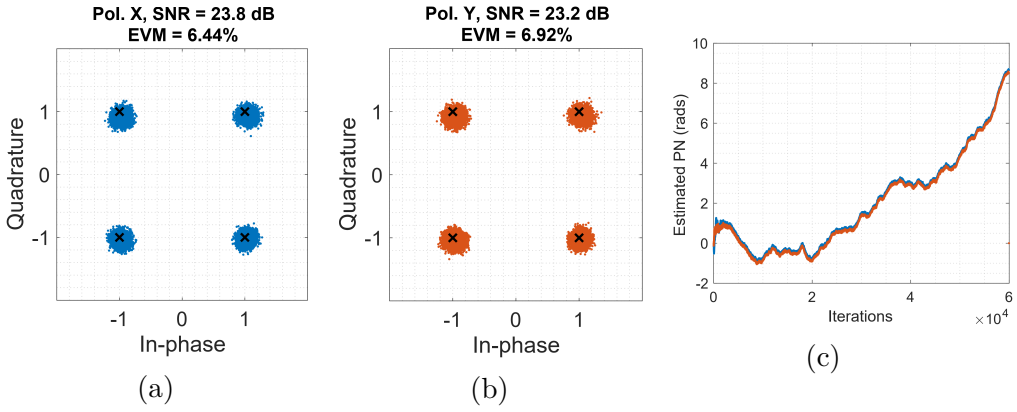

(a) (b) (c)

Figure 5.20 – (a) Recovered PM-4-QAM constellations using R-BPS ($L = 1$) at OSNR = 27.8 dB, Pol. X, (b) Pol. Y (c) Phase noise estimate.

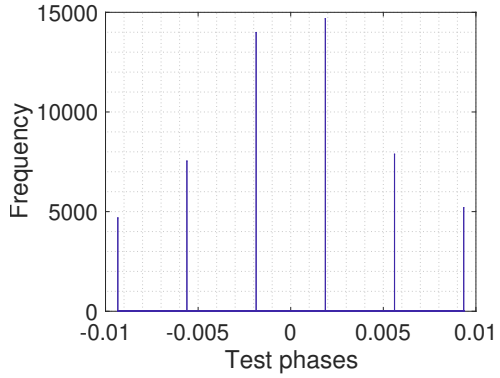

Figure 5.21 – Number of occurrence of each test phase for carrier phase compensation.

Fig. 5.21 shows the histogram of the differential estimated phase noise of signals in Pol.X. Each bin represents one of the 6 test phases used for carrier phase recovery. All the test phases participate in the phase noise compensation with less participation of the extreme values and significant contribution of the centered test phases. Hence, R-BPS seems to perform correctly.

The same results are illustrated when using the BPS approach in Fig. 5.22. Both algorithms perform well in this situation and the EVM in the steady state is of 6.5%.

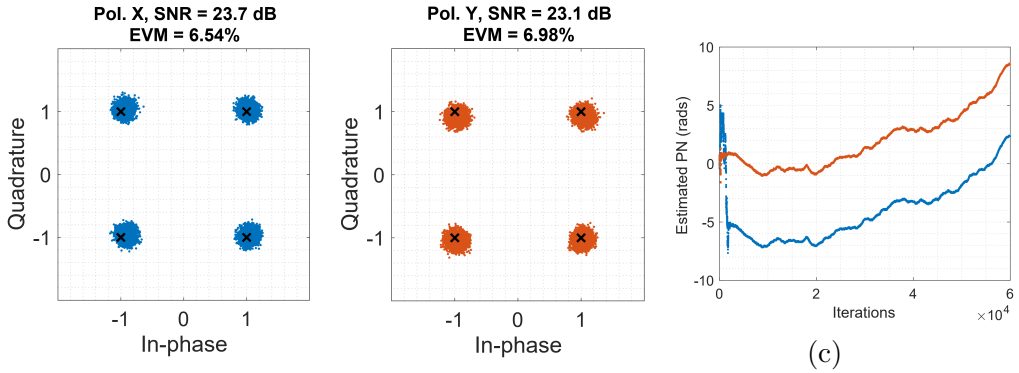

(a) (b) (c)

Figure 5.22 – (a) Recovered PM-4-QAM constellations using BPS ($L = 1$) at OSNR = 27.8 dB, Pol. X, (b) Pol. Y, (c) Phase noise estimate.

Now the experiment is carried out using $L = 4$ stages. In this case, the standard deviation of the phase noise increases by the factor of $\sqrt{L}$.

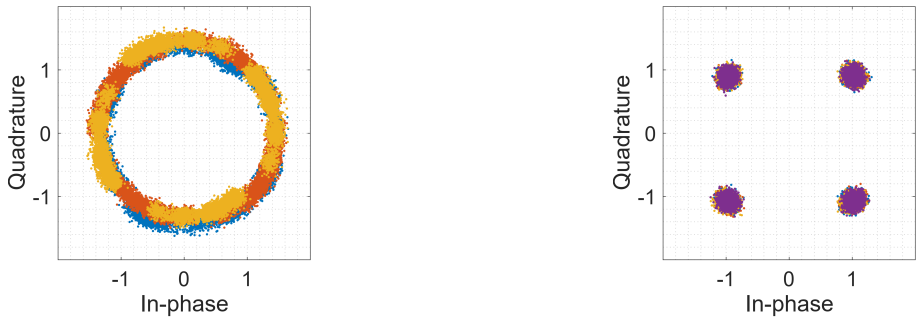

(a) (b)

Figure 5.23 – (a), (b): constellations for 4-QAM before and after carrier phase recovery with a parallel processing of $L = 4$.

The parallel processing with $L = 4$ succeeded to compensate for the carrier phase noise as depicted in Fig. 5.23. As can be seen, the constellation diagram in Pol.X has been degraded dramatically but after phase noise mitigation, 4-QAM constellation has been retrieved.

With 4 stages, the R-BPS approach made it possible to compensate for the phase noise. The constellation diagrams at the output of parallel R-BPS are shown in Fig. 5.24(a) and the subsequent SNR reaches 23.5 dB in Pol.X and 22 dB in Pol.Y.

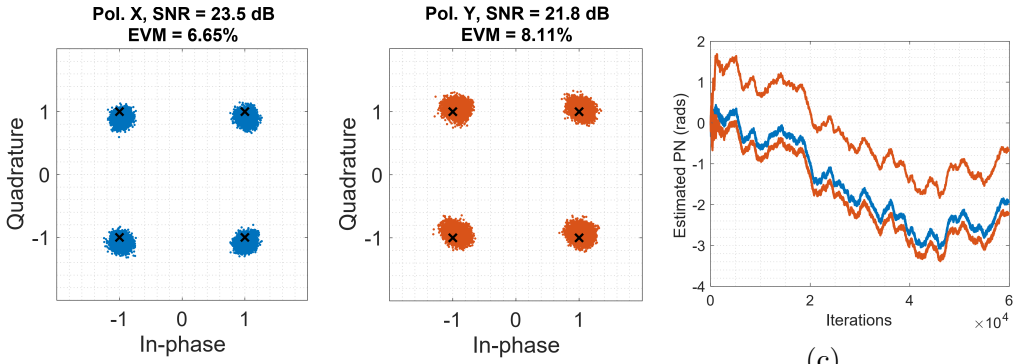

(a) (b) (c)

Figure 5.24 – (a) Recovered PM-4-QAM constellations using parallel R-BPS ($L = 4$) at OSNR = 27.8 dB, Pol. X (b) Pol. Y (c) Phase noise estimate.

On Pol.X, the phase noise compensation provides almost the same phase tracking variations for the 4 stages. Nevertheless, on Pol.Y, stage number 3 (see Fig. 5.25) presents a cycle slip in its phase tracking. Since parallel processing is independent between signal blocks in each stage, the effects of additive noise or a signal phase jump may cause this cycle slip.

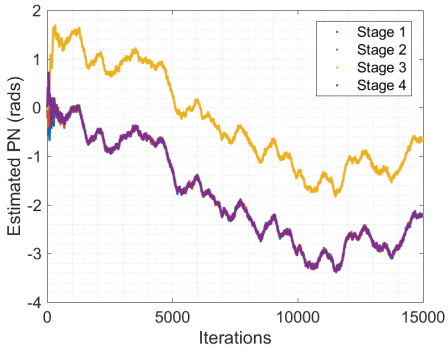

Figure 5.25 – Phase noise estimation.

Roughly the same performance is obtained when the parallel BPS with $L = 4$ stages is used (see Fig. 5.26(a) and Fig. 5.26(c)). The SNR at the output is 23.4 dB in Pol.X and 20.5 dB in Pol.Y. However, there are more cycle slips in the phase noise estimated from signal in Pol.Y. Anyway, both algorithms present the same phase noise trend.

As can be seen, even feed-back loops can present the cycle slip phenomenon. The cycle jump is before hooking phase which is considered as a false hooking point of the S-curve of the decision directed detector.

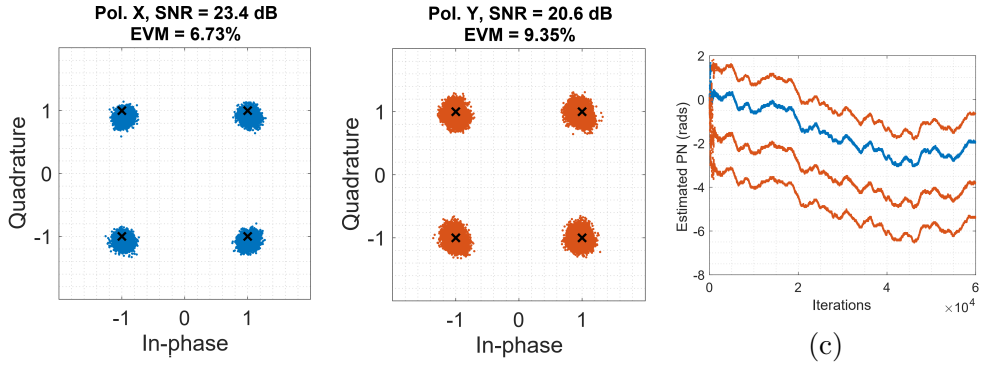

(a) (b) (c)

Figure 5.26 – (a) Recovered PM-4-QAM constellations using parallel BPS ($L = 4$) at OSNR = 27.8 dB, Pol. X, (b) Pol. Y (c) Phase noise estimate.

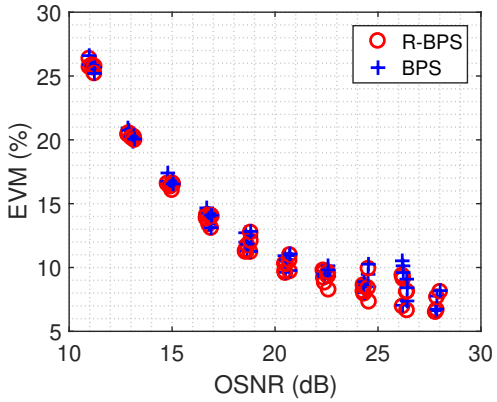

Figure 5.27 – EVM vs OSNR for 4-QAM system with $L \in \{1, 2, 3, 4, 5, 7, 8\}$.

To investigate the performance in a system point of view, we calculate the EVM for different OSNR conditions with different values of parallel stages $L \in \{1, 2, 3, 4, 5, 7, 8\}$, and the results are shown in the Fig.5.27. Both algorithms have roughly the same performance regardless of the used number of stages.

Similarly, we have investigated the R-BPS over experimental 6 Gbaud 16-QAM system. The received symbols cause the degradation of the system performance if the phase noise remains without compensation. In Fig. 5.28(b), the linewidth-induced phase impairment is compensated effectively by using the R-BPS.

Pol.X and Pol.Y signals at the output of the R-BPS algorithm are presented in Fig. 5.28(a). The estimated phase noise for Pol.X and Pol.Y is given in Fig. 5.28(c). Both estimations present the same trends but they are no equal due to cycle slips. On the other hand, roughly, the same values of EVM ouputs are given when using the BPS approach.

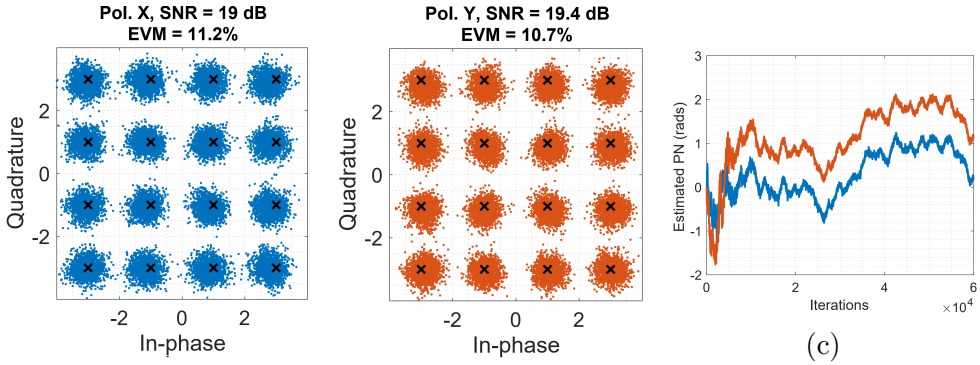

(a) (b) (c)

Figure 5.28 – (a) Recovered PM-16-QAM constellations using R-BPS at OSNR = 25.8 dB, Pol. X, (b) Pol. Y (c) Phase noise estimate.

The estimated phase noise through the BPS algorithm are presented in Fig. 5.29(c).

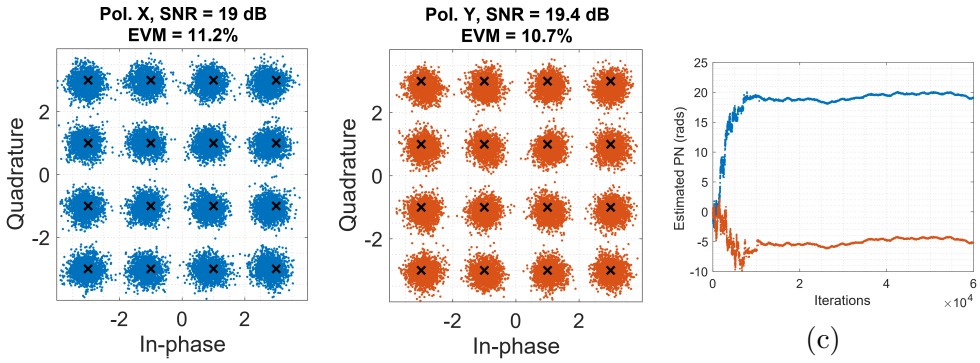

(a) (b) (c)

Figure 5.29 – (a) Recovered PM-16-QAM constellations using BPS at OSNR = 25.8 dB, Pol. X, (b) Pol. Y (c) Phase noise estimate.

Obtained constellation after parallel processing of the BPS and the R-BPS with $L = 4$ stages are shown in Fig. 5.30(a) and Fig. 5.31(a), respectively.

As usual, the parallel BPS presents more cycle slips in its phase noise tracking whereas the R-BPS is more robust to cycle slips.

When varying the number of stages $L \in \{1, 2, 3, 4, 7, 9\}$, the system performance is evaluated through the variation of the EVM value. As can be seen in Fig. 5.32, both algorithms present the same global EVM regardless of the introduced number of stages.

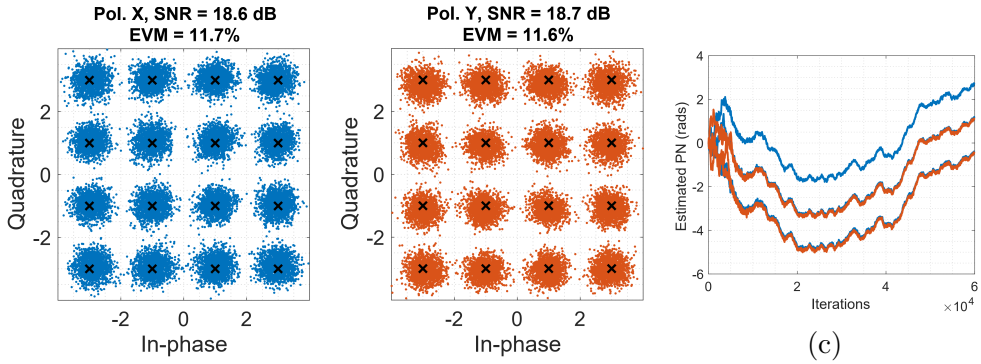

(a) (b) (c)

Figure 5.30 – (a) Recovered PM-16-QAM constellations using parallel R-BPS ($L = 4$) at OSNR = 25.8 dB, Pol. X, (b) Pol. Y (c) Phase noise estimate.

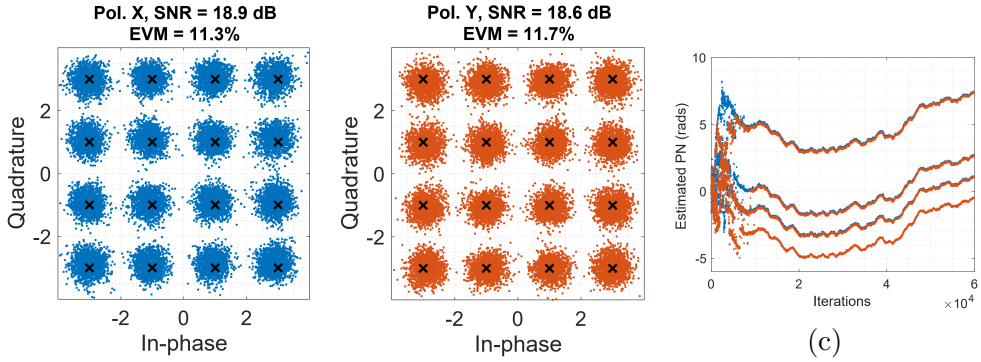

(a) (b) (c)

Figure 5.31 – (a) Recovered PM-16-QAM constellations using parallel BPS ($L = 4$) at OSNR = 27.8 dB, Pol. X, (b) Pol. Y (c) Phase noise estimate.

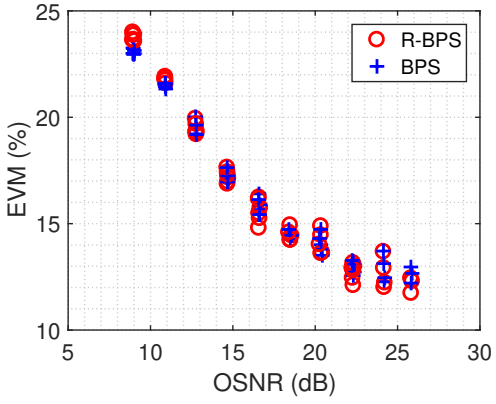

Figure 5.32 – EVM vs OSNR for 16-QAM system with $L \in \{1, 2, 3, 4, 7, 9\}$.

5.4 Summary

In this experimental part, we presented the back-to-back experiments for 4-QAM and 16-QAM signals in order to benchmark and validate the effectiveness of the state of the art algorithms. Ultimate BER metric curves were plotted for this goal. In addition, optical transmission system for up to 4200 km was conducted to transmit 4-QAM constellation signal. The validation of its related receiver algorithms was depicted through the calculation of the BER for all the transmission distances.

Next, we validated the three proposed algorithms through real data acquisitions yield from different experimental setups.

The joint algorithm was experimentally validated for 11 Gbaud 4-QAM and 16-QAM systems. For each modulation scheme, two system configurations ("aligned SOPs" and "arbitrary SOPs") were proposed. We have shown that the joint algorithm allows the separation of polarizations as well as the compensation of IQ imbalance distortion. In addition, an other polarization effect imperfection (PDL) can be investigated by the visualization of the time evolution of the coefficients of the compensation matrix. However the amount of this imperfection cannot be evaluated.

The results of the joint algorithm on 4-QAM and 16-QAM modulation formats regardless of the system configurations ("aligned SOPs" or "arbitrary SOPs") are very close. This confirms that the joint algorithm succeeded in separating the channels suitably.

On the other hand, experimental validation of the modified decision-directed CPR algorithm confirms the effectiveness of the approach for laser phase noise mitigation through experimental data using a 11 Gbaud 16-QAM transmission system. The experimental results obtained using modified decision-directed CPR were compared with those of the decision-directed CPR and it was concluded that our system presents 0.3 dB of gain in SNR at the output. The approach has also been validated with experimental system used for joint algorithm validation in order to test the algorithm jointly with the proposed blind joint polarization multiplexing and IQ imbalance compensation algorithm. The resulted gain in SNR was 0.3 dB in Pol.X and 0.2 dB in Pol.Y compared with decision-directed CPR.

Finally, our R-BPS algorithm has been tested and compared in EVM and SNR metrics under various number of stages L. The proposed algorithm has fewer cycle slips and demonstrates the same overall performance in SNR and EVM compared with the parallel BPS approach.

Conclusion and Perspectives

Conclusion

In this thesis, we are interested in several issues concerning the design of digital signal algorithms for coherent optical detection receivers. In fact, various transmission and optical system impairments are under investigation, such as chromatic dispersion, polarization mode dispersion, phase and frequency transmission offset and IQ imbalance. Hence, basic concept analysis of conventional DSP compensation algorithms are introduced in this thesis including all pass CD compensation, timing squared algorithm, Gardner clock recovery algorithm and BPS carrier recovery algorithm. The main challenge in the implementation of these digital receivers comes from a technological constraints as the implementation of digital signal processing techniques at such rates remains critical despite the continued growth in complementary metal oxide semiconductor technology. As a consequence, it is necessary to adapt the algorithms by reducing their complexity and making them easily transposable on parallel architectures.

The concern to propose digital signal processing techniques for very high bit rate implementations appears in chapters 3 and 4. In chapter 3, we demonstrated the interest of digital equalization of chromatic dispersion in the frequency domain by a detailed assessment of its algorithmic complexity. Thanks to block processing and the use of efficient FFT or IFFT algorithms, signal processing in the frequency domain lends itself well to the constraints of very high speed real-time implementation.

Chapter 4 presents new contributions to the state-of-the-art digital signal processing techniques to compensate for transmission impairments to guarantee an acceptable system performance. Indeed, joint polarization demultiplexing and IQ imbalance compensation DSP algorithm has been proposed to fulfill additional challenges of supporting various services with different users in optical communication networks. The singularity problem, which can occasionally cause demultiplexing to fail and half the information to be lost, is also considered. Several solutions have already been proposed in the literature to counteract this singularity problem. Our selected solution consists in converging the adaptive algorithm in a constrained mode optimized for the compensation of pure PMD.

Moreover, two carrier recovery algorithms have been proposed. Modified Decision directed CPR is a feedback algorithm dealing with 16-QAM modulation and have the capability to handle different introduced SNR. The proposed method presents better performance against residual frequency offset and additive white noise than the conventional DD-CPR. Additionally, the approach shows effective results even when delay in the feedback path exists. On the other hand, parallel R-BPS algorithm is proposed to meet the implementation requirements and has the advantage of being completely transparent to the format of digital data transmission. The algorithm works with small number of test phases and shows high performance against residual carrier frequency offsets and additive white noise. Regarding complexity, the approach is less complex than parallel BPS as it requires few number of test phases. An outlook on possible future research directions are provided in the following section.

Perspectives

Due to the continuously increasing of data rate demand of the optical fiber transmission systems, capacity request of optical communication systems is evolving beyond 40 Gb/s. Today, next generation of optical communication systems require high capacity, better spectrum efficiency and more system flexibilities and data rates of 100 Gb/s, 400 Gb/s and 1 Tbps optical transmission systems are under investigation.

Increasing the data rate could be achieved by different techniques. The first technique deals with the increase of the number of transmitted bits per symbol. By using coherent 16-, 64-QAM, and even more advanced modulation formats, the spectral efficiency can more closely approach the channel capacity predicted from the Shannon's theory. Also, the rapid technological advances in digital sampling speed permits the increase of DP-QPSK signal baud rate from 28 Gbaud to 80 Gbaud. Finally, the use of wavelength division multiplexed systems can scale to higher rates and larger numbers of users.

In the near future, Internet traffic enjoys tremendous growth with dynamic, heterogeneous and unpredictable ways. In these architectures, elastic optical networks are built up with flexible modulation formats, adaptive baud rate and variable transmission distances. In this case, to better support the flexible switch of modulation formats and line rate, the conventional solutions are employing alternative algorithms for different modulation formats, modulation format recognition or modulation format transparent algorithms. Indeed, joint polarization demultiplexing and IQ imbalance compensation responds to this

challenge and is considered one of the pivotal components in elastic optical networks thanks to its capability to operate without dependence on modulation formats. As a consequence, an experimental demonstration of the method behavior where dynamic change of the modulation formats may occur is necessary.

On the other hand, the proposed parallel R-BPS ensures carrier phase recovery regardless the introduced modulation formats. Besides, it performs parallel processing to contemplate a possible hardware implementation, taking into consideration that the FPGA operation has much lower clock frequencies than the signal symbol rate. The two proposed carrier recovery algorithms were successfully validated through experiments. Nevertheless, the experimental validation could be more in-depth by showing the algorithm robustness against higher level of phase noise.

DSP for receiver front-end corrections, CD compensation and sampling frequency offset recovery are essentially modulation format independent while carrier and frequency offset recovery and adaptive signal processing for compensating PMD and other transceiver imperfections are modulation format dependent. It would be ideal for elastic optical networks if a single universal DSP platform could adequately equalize various transmission impairments and recover data for arbitrary modulation formats. We introduce the chain of DSP operations to demodulate the data while responding to the challenge of flexible transmission. While for a particular realization of a digital coherent receiver, the DSP operations may vary, the generic DSP procedures are shown in Fig. 5.33 and their functionalities can be summarized as below.

— Sampling frequency offset compensation: The mismatch of transmitter and receiver sampling frequencies used by the DAC and ADC is blindly compensated using Order and Meyr algorithm.

— CD compensation: The linear impairments of the channel is successfully equalized knowing fiber parameters.

— Polarization demultiplexing and IQ imbalance compensation: Our proposed algorithm tackles signals separation as well as IQ imbalance compensation without the need of the information about the used modulation formats.

— Residual ISI compensation: This could be processed using 2 independents CMA algorithm. The radius of the CMA could be constant and equal to that used for 4-QAM constellation.

— Regarding modulation format recognition stage, machine-learning methods are a prominent research area and could be used for enhancing optical communication

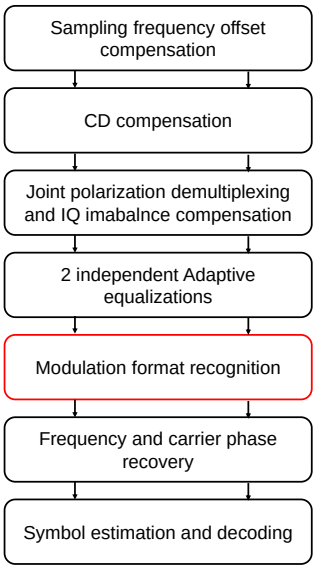

Figure 5.33 – Sequences of DSP operation in a coherent receiver to blindly demodulate the data.

DSP receiver. The potential of the modulation format recognition comes with its rapid capability for tuning and adjusting the parameters of algorithms that follow it. The output of such a scheme is needed for the next DSP stages especially the carrier recovery feed-forward methods. Other methods should be studied in the future in order to find which can converge to the most precise and fastest result.

— Frequency and phase recovery: The frequency mismatch between transmitting laser and LO and the laser phase noise are estimated and compensated.

— Symbols estimation and decoding: Error correction codes are employed and transmitted symbols are estimated.

A crucial next step is to take practical implementation criteria into account, such as the ability to parallelize the computations and the overall power dissipation of the required hardware.

Moving forward to next generation, the recent explosion in the optical fiber enabling the transport of enormous amounts of data over thousands of kilometers is accelerating the tendency of modern data-communications to grow even further. Hence, high performance and low-complexity advanced adaptive digital signal processing techniques have become major focus areas of research. Recently, artificial intelligence (AI) techniques have entered

the field of optics including nanophotonic, quantum mechanics, optical networks and optical communication. Indeed, AI promises effective optimization and performance prediction for systems whose behavior is intrinsically difficult to model and complex. Therefore, AI algorithms may be more efficient and successful tools than traditional signal processing algorithms. In addition, AI for optics hardware has raised considerable interest thanks to its agile computation and low-power consumption.

Indeed, digital signal processing units such as time phase recovery, fiber nonlinearity, carrier phase estimation, equalization, bit error rate prediction etc. have become fundamental and representative features in artificial intelligence using machine learning techniques for optical communication literature. In that case, different machine learning algorithms such as support vector machine, artificial neural network, deep neural networks, Q-Learning, deep reinforcement learning and others have been already used in this context of application.

AI for optical communication is certainly a hot topic and will continue to raise interest for the next few years. This can be through the change of the conventional DSP block structure and replace it with a scheme that could deal with all the steps in a unified and comprehensive way. The goal is to create black-box models such as neural network, gradient boosting or complicated ensembles which are able to mitigate the medium or system impairments. The inner process of these models are harder to understand and it is difficult to inquire how they work exactly and why they produce such good results.

Appendix A

Analytical calculation of matrix G

After IQ imbalance distortion, the signals in both polarizations are given by

$$u_p(n) = k_{1,p}s_p(n) + k_{2,p}s_p^*(n). \tag{A.1}$$

where $k_{1,p}$ and $k_{2,p}$ are function of IQ imbalance parameters $\{\epsilon_p, \varphi_p\}$ as follows:

$$\begin{aligned} k_{1,p} &= \cos(\varphi_p) + j\epsilon_p \sin(\varphi_p), \\ k_{2,p} &= \epsilon_p \cos(\varphi_p) + j \sin(\varphi_p). \end{aligned} \tag{A.2}$$

Hence, the signals are expressed as

$$\begin{aligned} u_p(n) &= \Big(\cos(\varphi_p) + j\epsilon_p \sin(\varphi_p)\Big)\, s_p(n) + \Big(\epsilon_p \cos(\varphi_p) + j \sin(\varphi_p)\Big)\, s_p^*(n) \\ &= \Big(\cos(\varphi_p) + j\epsilon_p \sin(\varphi_p)\Big)\, \Big(s_{I,p}(n) + j s_{Q,p}(n)\Big) \\ &+ \Big(\epsilon_p \cos(\varphi_p) + j \sin(\varphi_p)\Big)\, \Big(s_{I,p}(n) - j s_{Q,p}(n)\Big) \\ &= \Big((1+\epsilon_p)\cos(\varphi_p) s_{I,p}(n) + (1-\epsilon_p)\sin(\varphi_p) s_{Q,p}(n)\Big) + \\ &j\,\Big((1+\epsilon_p)\sin(\varphi_p) s_{I,p}(n) + (1-\epsilon_p)\cos(\varphi_p) s_{Q,p}(n)\Big). \end{aligned} \tag{A.3}$$

Equation of A.3 can be written in another form

$$\begin{pmatrix} u_{I,p}(n) \\ u_{Q,p}(n) \end{pmatrix} = \mathbf{T} \begin{pmatrix} s_{I,p}(n) \\ s_{Q,p}(n) \end{pmatrix} \tag{A.4}$$

where

$$\mathbf{T} = \begin{pmatrix} (1+\epsilon_p)\cos(\varphi_p) & (1-\epsilon_p)\sin(\varphi_p) \\ (1+\epsilon_p)\sin(\varphi_p) & (1-\epsilon_p)\cos(\varphi_p) \end{pmatrix}. \tag{A.5}$$

Hence, the transmitted imbalance can be thoroughly understood via $\mathbf{T}$.

The altered signals with Tx-IQ imbalance are then rotated with the polarization rotation effect as

$$\mathbf{Z}(n) = \begin{pmatrix} z_X(n) \\ z_Y(n) \end{pmatrix} = \mathbf{H} \begin{pmatrix} u_X(n) \\ u_Y(n) \end{pmatrix} \tag{A.6}$$

where

$$\mathbf{H} = \begin{pmatrix} \cos\alpha & e^{-j\theta}\sin\alpha \\ -e^{j\theta}\sin\alpha & \cos\alpha \end{pmatrix} = \begin{pmatrix} h_1 & h_2 \\ h_3 & h_4 \end{pmatrix}. \tag{A.7}$$

Thus,

$$\begin{aligned} z_X(n) &= h_1 u_X(n) + h_2 u_Y(n) \\ &= h_1 \left(k_{1,X} s_X(n) + k_{2,X} s_X^*(n)\right) + h_2 \left(k_{1,Y} s_Y(n) + k_{2,Y} s_Y^*(n)\right) \\ &= \left(h_1 k_{1,X}\right) s_X(n) + \left(h_1 k_{2,X}\right) s_X^*(n) + \left(h_2 k_{1,Y}\right) s_Y(n) + \left(h_2 k_{2,Y}\right) s_Y^*(n). \end{aligned} \tag{A.8}$$

and

$$\begin{aligned} z_Y(n) &= h_3 u_X(n) + h_4 u_Y(n) \\ &= h_3 \left(k_{1,X} s_X(n) + k_{2,X} s_X^*(n)\right) + h_4 \left(k_{1,Y} s_Y(n) + k_{2,Y} s_Y^*(n)\right) \\ &= \left(h_3 k_{1,X}\right) s_X(n) + \left(h_3 k_{2,X}\right) s_X^*(n) + \left(h_4 k_{1,Y}\right) s_Y(n) + \left(h_4 k_{2,Y}\right) s_Y^*(n). \end{aligned} \tag{A.9}$$

A possible expression linking the distorted signals related to the source signals can be given by

$$\underline{\mathbf{Z}}(n) = \begin{pmatrix} z_X(n) \\ z_X^*(n) \\ z_Y(n) \\ z_Y^*(n) \end{pmatrix} = \begin{pmatrix} h_1 k_{1,X} & h_1 k_{2,X} & h_2 k_{1,Y} & h_2 k_{2,Y} \\ h_1^* k_{2,X}^* & h_1^* k_{1,X}^* & h_2^* k_{2,Y}^* & h_2^* k_{1,Y}^* \\ h_3 k_{1,X} & h_3 k_{2,X} & h_4 k_{1,Y} & h_4 k_{2,Y} \\ h_3^* k_{2,X}^* & h_3^* k_{1,X}^* & h_4^* k_{2,Y}^* & h_4^* k_{1,Y}^* \end{pmatrix} \begin{pmatrix} s_X(n) \\ s_X^*(n) \\ s_Y(n) \\ s_Y^*(n) \end{pmatrix} \tag{A.10}$$

where the $\mathbf{G}$ matrix includes the effects of both Tx-IQ imbalance and polarization rotation and taking into account the real coefficients ($h_1^* = h_1$ and $h_4^* = h_4^*$) is expressed by

$$\mathbf{G} = \begin{pmatrix} h_1 k_{1,X} & h_1 k_{2,X} & h_2 k_{1,Y} & h_2 k_{2,Y} \\ h_1 k_{2,X}^* & h_1 k_{1,X}^* & h_2^* k_{2,Y}^* & h_2^* k_{1,Y}^* \\ h_3 k_{1,X} & h_3 k_{2,X} & h_4 k_{1,Y} & h_4 k_{2,Y} \\ h_3^* k_{2,X}^* & h_3^* k_{1,X}^* & h_4 k_{2,Y}^* & h_4 k_{1,Y}^* \end{pmatrix}. \tag{A.11}$$

At this stage, the signals are distorted with Tx-IQ imbalance and polarization rotation. Finally, signals are also corrupted by the additive white Gaussian noise and the final extended expression is given by

$$\underline{\mathbf{R}}(n) = \underline{\mathbf{Z}}(n) + \underline{\mathbf{N}}(n). \tag{A.12}$$

where

$$\underline{\mathbf{R}}(n) = \begin{pmatrix} r_X(n) \\ r_X^*(n) \\ r_Y(n) \\ r_Y^*(n) \end{pmatrix} \quad \text{and} \quad \underline{\mathbf{N}}(n) = \begin{pmatrix} n_X(n) \\ n_X^*(n) \\ n_Y(n) \\ n_Y^*(n) \end{pmatrix} \tag{A.13}$$

with $n_X(n)$ and $n_Y(n)$ two independent complex circular white zero-mean Gaussian random variables with variance $N_0/2$ per real dimension.

Appendix B

CORDIC ALGORITHM

In this part, details about CORDIC algorithm are presented. CORDIC stands for coordinate rotation digital computer and was proposed by Volder in 1959. It is a simple and hardware-efficient method to calculate many functions like trigonometric, hyperbolic, logarithmic, etc. The simplicity of CORDIC is that it can compute any of the above mentioned functions using shifts and additions. Also, this algorithm can be implemented in either rotation or vectoring operating modes. In the rotation mode, the inputs of the algorithm are the coordinate components of a vector and an angle of rotation and the computed outputs are the coordinate components of the original vector after rotation through the given angle. Whereas, in its vectoring mode, the algorithm inputs are the coordinate components of a vector and the calculated outputs are the magnitude and angular argument of the introduced original vector. In either mode, in conventional CORDIC, any given rotation angle is expressed as a linear combination of values of elementary angles but in variable directions. The implementation of such elementary and fixed rotation is performed via iterative sequence of addition or subtraction followed by bit-shift operation. The final output is obtained by appropriate scaling the result obtained after successive iterations. Rotation-mode CORDIC calculates the sine and cosine values of a given angle (in radians) by transforming the coordinates from polar representation to its Cartesian form.

Our goal is to perform iteratively a rotation operation of a vector v_0 with a given angle β as demonstrated in Fig. B.1. If we start with the vector $v_0 = \begin{pmatrix} 1 \\ 0 \end{pmatrix}$ aligned with the x-axis, the first iteration implies a rotation of 45° counterclockwise to get the vector v_1. Successive iterations will rotate the vector in one or the other direction by size decreasing steps, until the desired angle is reached. The successive angles are summarized in Tab. B.1. The vector rotation can be achieved by simply multiplying the vector with a complex number of unit magnitude. The values of the vector v_i at the iteration i is given by $v_i = R_i v_{i-1}$. The rotation matrix R_i is given by

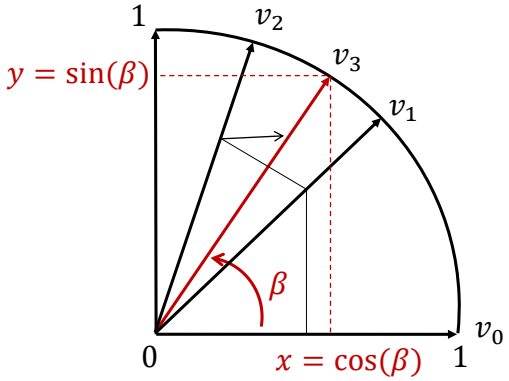

Figure B.1 – Graphical demonstration of CORDIC algorithm.

$$R_i = \begin{pmatrix} \cos(\nu_i) & -\sin(\nu_i) \\ \sin(\nu_i) & \cos(\nu_i) \end{pmatrix}.$$

Taking into account the two following trigonometric identities

$$\cos(\alpha) = \frac{1}{\sqrt{(1+\tan^2(\alpha))}},$$
$$\sin(\alpha) = \frac{\tan(\alpha)}{\sqrt{(1+\tan^2(\alpha))}}.$$

the rotation matrix becomes

$$R_i = \frac{1}{\sqrt{1+\tan^2(\nu_i)}} \begin{pmatrix} 1 & -\tan(\nu_i) \\ \tan(\nu_i) & 1 \end{pmatrix}.$$

Then, the expression of the rotated vector $v_i = R_i v_{i-1}$ becomes

$$v_i = \frac{1}{\sqrt{1+\tan^2(\nu_i)}} \begin{pmatrix} x_{i-1} - y_{i-1}\tan(\nu_i) \\ x_{i-1}\tan(\nu_i) + y_{i-1} \end{pmatrix},$$

where x_{i-1} and y_{i-1} are the components of the v_{i-1}. Note that the desired rotation angle is broken down into a series of small successive shrinking angles. Restricting the angles ν_i so that $\tan(\nu_i)$ takes on the values $\pm 2^{-i}$, the multiplication with the tangent can

be replaced by a division by a power of two, which is efficiently done in digital computer hardware using a bit shift. The expression of the vector then becomes

$$v_i = K_i \begin{pmatrix} x_{i-1} - \sigma_i 2^{-i} y_{i-1} \\ \sigma_i 2^{-i} x_{i-1} + y_{i-1} \end{pmatrix},$$

with $K_i = \frac{1}{\sqrt{1+2^{-2i}}}$, $\sigma_i \in \{-1, 1\}$ used to determinate the direction of the rotation. The direction of rotation of the vector is determined by the value of β_i, where β_i is the difference between the target rotation value and the present angle accumulator value $\beta_i = \beta_{i-1} - \sigma_i \nu_i$, with $\nu_i = \arctan(2^{-i})$ and the initial β value is the angle for which the sine and cosine values are to be calculated.

Table B.1 – Successive Angle Rotation Values.

Iteration (i)	$\alpha(i)$ (in degrees)	$\tan(\alpha(i))$
0	45	1
1	26.5	0.5
2	14.03	0.25
3	7.125	0.125
4	3.576	0.0625
5	1.7899	0.03125
6	0.895	0.01562
7	0.4476	0.00781
8	0.2238	0.00390
9	0.1	0.001953125
10	0.055	0.0009765625

Thus, the new x_i and y_i coordinate values can be given as

$$\begin{aligned} x_i &= x_{i-1} - 2^{-i} y_{i-1} \\ y_i &= y_{i-1} + 2^{-i} x_{i-1}. \end{aligned} \quad \text{if} \quad \beta_i > 0$$

and

$$\begin{aligned} x_i &= x_{i-1} + 2^{-i} y_{i-1} \\ y_i &= y_{i-1} - 2^{-i} x_{i-1}. \end{aligned} \quad \text{if} \quad \beta_i < 0$$

The coefficient k_i can be ignored in the iterative process and applying it afterward by a scaling factor

$$k(n) = \prod_{i=1}^{n-1} k_i$$
$$= \prod_{i=1}^{n-1} \frac{1}{\sqrt{1+2^{-2i}}}.$$

The scaling factor is calculated in advance and stored in a table, or as a single constant for a fixed number of iterations. This correction could also be made in advance, by scaling v_0 and hence saving a multiplication. Additionally it can be noted that $k = \lim_{n\to\infty} k(n) = 0.607$.

Due to the linear rate convergence of the CORDIC, latency of computation is the major issue with its implementation. Indeed, overall latency of computation increases linearly with the product of the word length and the CORDIC iteration period. The speed of CORDIC iterations is therefore constrained by either the precision requirement (iteration count) or the duration of the clock period. In fact, to have n bits precision at the output, $(n+1)$ iterations are required.

The angle recoding (AR) scheme [147] could be applied for reducing the iteration count for CORDIC implementation of constant complex multiplications by encoding the angle of rotation as a linear combination of a set selected elementary angles of micro-rotations. More precisely, in AR methods the constraint is relaxed by adding zero into the linear combination to obtain the desired angle using relatively fewer terms.

An illustration of the performance of the CORDIC algorithm and its optimized version is presented in Tables below

Table B.2 – Iterative process of calculating 20° with CORDIC algorithm with 6 iterations.

Iteration (i)	σ_i	ν_i	β_i (rads)
1	1	0.4636	0.4636
2	-1	0.2450	0.2187
3	1	0.1244	0.3430
4	1	0.0624	0.4054
5	-1	0.0312	0.3742
6	-1	0.0156	0.3586

As can be seen in Tab. B.2, using a CORDIC, with 6 iterations, the cumulative output angle β_i reaches the desired input angle $20° \approx 0.3491$ rad with a precision of 9.5×10^{-3}.

Table B.3 – Iterative process of calculating 20° with AR method with 6 iterations.

Iteration (i)	σ_i	ν_i	β_i (rads)
1	0	-	0
2	1	0.245	0.245
3	1	0.1244	0.3693
4	0	-	0.3693
5	0	-	0.3693
6	-1	0.0156	0.3537

On the contrary, using the angle recoding approach, only 4 iterations are needed to attain a lower precision value of 4.6×10^{-3}.

Appendix C

ADC QUANTIZATION EFFECTS

DSP algorithms process digitized signals coming out from the analog-to-digital conversion. Digitization involves two process: sampling (discrete in time) and quantization (digitization in amplitude). While the sampling process is usually performed by a sample-and-hold circuit, the ADC performs the quantization process. The sample-and-hold and the ADC may be separate modules or may be integrated on the same chip.

The ADC assumes that the input values cover a full-scale range R. After quantization, the sample is represented by B-bits and it is described as a multiple of a basic unit dividing the range of values into $Q = 2^B$ possible quantization levels. If the spacing between these levels is the same throughout the range R, we have a uniform quantized.

C.1 Signal to noise ratio of a uniform quantizer

We consider a signal $x(t)$ that we want to quantify by a uniform quantizer operating on $L = B$ quantization ranges. Assuming a centred signal, the quantization step is given by

$$\Delta = \frac{2x_{sat}}{L} = \frac{x_{sat}}{2^{B-1}}$$

where $x_{sat} \geq 0$ is the saturation threshold of the quantifier.

Assuming that the quantization noise $q(t)$ follows a uniform law on $\left[-\frac{\Delta}{2}, \frac{\Delta}{2}\right]$ and therefore the average power of the quantization noise is obtained according to

$$\sigma_Q^2 = \mathbb{E}(q^2(t)) = \int_{-\frac{\Delta}{2}}^{\frac{\Delta}{2}} q^2 f_Q(q)\ dq = \frac{\Delta^2}{12} = \frac{x_{sat}^2}{3 \times 2^{2B}}$$

The noise band considered at the ADC being of $\beta \times W$ for a band of 100 GHz band, therefore $\beta = \frac{100\ \text{GHz}}{11\ \text{GHz}} \approx 9.1$, and the power spectral density of the noise is therefore

$$N_Q = \frac{\sigma_Q^2}{\beta \times W} = \frac{1}{\beta \times W} \times \frac{x_{sat}^2}{3 \times 2^{2B}}$$

or equivalently

$$N_Q \times W = \frac{x_{sat}^2}{3 \times \beta \times 2^{2B}}$$

C.2 Our experiment

The expressions below are performed only for one of the signal components In-phase or quadrature without loss of generality because

$$\frac{E_s}{N_0} = \frac{P \times T_s}{N_0} = \frac{(P_I + P_Q) \times T_s}{2 \times (N_0/2)} = \frac{2 \times P_I \times T_s}{2 \times (N_0/2)} = \frac{P_I \times T_s}{(N_0/2)} = \frac{E_I}{N_I}$$

where E_I is the average energy of the useful signal on the "In-phase" component and N_I is the Mono-lateral noise spectral density present on the In-phase component. So the signal-to-noise ratio calculated on the complex baseband signal is identical to the signal-to-noise ratio on either In-phase or quadrature components.

The first OSNR value of the BER curve is OSNR = 4 dB and in single polarization OSNR $= \frac{E_s}{N_0} \times \frac{R}{W_{ref}}$, with $W_{ref} \approx 12.5$ GHz and $R = 11$ Gbaud. Thus,

$$\frac{E_s}{N_0} = \text{OSNR} + 0.555 \text{ dB} = 4.555 \text{ dB} = 10\log_{10}(\frac{1}{0.5919})^2 = 10\log_{10}(\frac{\sigma_x^2}{\sigma_{ASE}^2}),$$
$$\sigma_{ASE}^{Nyquist} = 0.5919 \times \sigma_x$$

with σ_x^2 is the variance of the signal and σ_{ASE}^2 is the variance of ASE noise.

As the acquisition is carried out in a 100 GHz band, the signal-to-noise ratio $\frac{E_s}{N_0}$ in oversampling will be lower by a factor β because the power of noise at the input of the ADC is β times greater (for a constant useful signal power), therefore

$$\sigma_{ASE}^{oversamp.} = 0.5919 \times \sigma_x \times \sqrt{\beta}.$$

On one of the channels (In phase or quadrature), the noise follows a normal distribution $U \sim \mathcal{N}(0, \sigma_{ASE}^2)$, and we have $\mathbb{P}(-2\sigma_{ASE}^{oversamp.} \leq U \leq 2\sigma_{ASE}^{oversamp.}) = 95\%$ or $\mathbb{P}(-3\sigma_{ASE}^{oversamp.} \leq U \leq 3\sigma_{ASE}^{oversamp.}) = 99.7\%$.

Experiments have been performed with a full scale adjustment of the dynamics of ADCs to avoid their saturations which imposes the saturation threshold be given by $x_{sat} = x_{max} + n_Q\sigma_{ASE}^{oversamp.}$ with a proportionality factor $n_Q = 2, \text{or } 3$. Therefore,

$$x_{sat} = x_{max} + n_Q \sigma_{ASE}^{oversamp.} = x_{max} + n_Q \times 0.5919 \times \sigma_x \times \sqrt{\beta}.$$

with $x_{max} = \sqrt{(2)}/2$ or a 2-Amplitude Shift Keying alphabet on the In-phase or quadrature component. In this case $\sigma_x^2 = 0.5 \times x_{max}^2 + 0.5 \times (-x_{max})^2 = x_{max}^2$, thus

$$x_{sat} = \sigma_x^2 + n_Q \times 0.5919 \times \sigma_x \times \sqrt{\beta} = (1 + n_Q \times 0.5919 \times \sqrt{\beta}) \times \sigma_x.$$

or

$$\sigma_x^2 = \frac{x_{sat}^2}{(1 + n_Q \times 0.5919 \times \sqrt{\beta})^2}.$$

The signal-to-quantization-noise ratio (SQNR), expressed for a noise band corresponding to the Nyquist band, can therefore be expressed as

$$\text{SQNR} = \frac{E_s}{N_Q} = \frac{\sigma_x^2}{N_Q \times W} = \frac{x_{sat}^2}{(1 + n_Q \times 0.5919 \times \sqrt{\beta})^2} \times \frac{3 \times \beta \times 2^{2B}}{x_{sat}^2},$$

or equivalently

$$\text{SQNR} = \frac{E_s}{N_Q} = \frac{3 \times 2^{2B}}{(1 + n_Q \times 0.5919)^2}.$$

Therefore, the quantization noise generated by the ADC for an ENOB $n_B = 5$ gives a SQNR (in oversampled band) of

$$\text{SQNR}_{\text{min}} = \log_{10}(\frac{3072}{2.184^2}) = \log_{10}(\frac{1}{1.55 \times 10^{-3}}) = 28.09 \text{ dB} \qquad n_Q = 3$$
$$\text{SQNR}_{\text{max}} = \log_{10}(\frac{3072}{2.776^2}) = \log_{10}(\frac{1}{1.02 \times 10^{-3}}) = 29.88 \text{ dB} \qquad n_Q = 2.$$

Therefore,

$$\frac{1}{1.55 \times 10^{-3}} \leq \frac{E_s}{N_Q} \leq \frac{1}{1.02 \times 10^{-3}}.$$

Now, we consider the last OSNR value of the experiment given by OSNR = 13 dB or equivalently $\frac{E_s}{N_0} = 13.55$ dB in the Nyquist band.

So the effective signal to noise ratio (in Nyquist band) is given by

$$\left.\frac{E_s}{N_0}\right|_{\text{effective}} = \log_{10}\left(\frac{E_s}{N_0+N_Q}\right) = \log_{10}\left(\frac{1}{4.415\times10^{-2}+1.55\times10^{-3}}\right) = 13.39 \text{ dB} \quad n_Q = 3$$

$$\left.\frac{E_s}{N_0}\right|_{\text{effective}} = \log_{10}\left(\frac{E_s}{N_0+N_Q}\right) = \log_{10}\left(\frac{1}{4.415\times10^{-2}+1.02\times10^{-3}}\right) = 13.46 \text{ dB} \quad n_Q = 2.$$

That is to say a degradation of $\Delta = 13.55 - \left.\frac{E_s}{N_0}\right|_{\text{effective}} = 0.16$ dB (or 0.09 dB for the case $n_Q = 2$) with respect to the ideal error probability curve (without quantification).

C.3 Matlab simulations of the 5-bit Tx/RX ADC

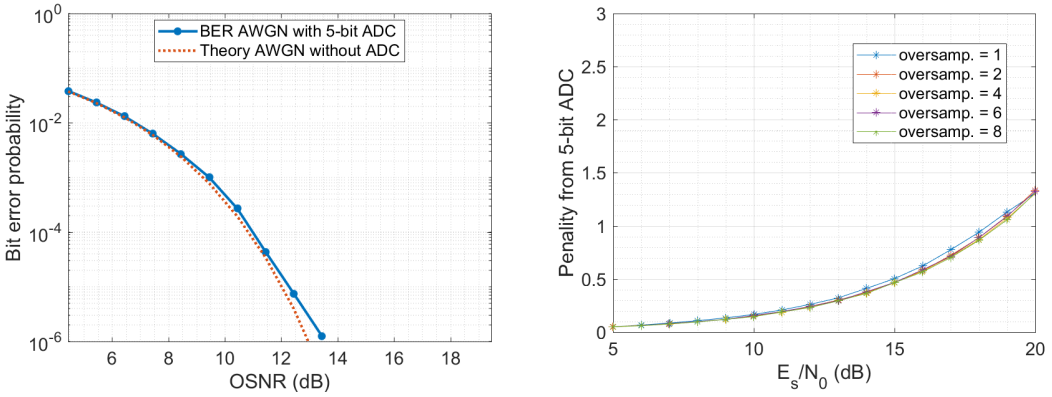

(a) (b)

Figure C.1 – (a) Bit error probability as function of OSNR for 4-QAM signals with a sampling rate of 11 Gbaud and an oversampling factor of 8, (b) Penalty in E_s/N_0 form 5-bit ADC for 4-QAM signals with a sampling rate of 11-Gbaud and an oversampling factor of 8.

Using the exact formula for the probability of bit error as a function of the signal-to-noise ratio per bit ($\frac{E_b}{N_0}$) for a 4-QAM modulation with Gray encoding. The comparison between the theoretical performance obtained in 4-QAM on AWGN channel without 5-bit ADC with BER curves obtained using 4-QAM signals where a 5-bit ADC is used is possible. From Fig. C.1(a) we can conclude that the degradation introduced by the use of the 5-bit ADC is negligible for lower OSNRs (less than 8 dB), and that this degradation is only observed for OSNRs greater than 8 dB.

Fig. C.1(b) depicts the degradation in $\frac{E_s}{N_0}$ between the BERs obtained in the presence of 5-bit ADC and when there is no ADC within the Rx for different oversampling factors. This degradation remains less than 0.5 dB for $\frac{E_s}{N_0}$ less than 13.55 dB.

These results obtained by Monte-Carlo simulations confirm the theoretical calculations carried out previously and the same orders of magnitude of this degradation are found. In fact, the theoretical study assumes a degradation of 0.16 dB (for an OSNR of 13 dB), and the Monte-Carlo simulations presents a degradation of about 0.35 dB (for an $\frac{E_s}{N_0}$ of 13.55 dB or equivalently an OSNR of 13 dB).

References

[1] I. Fatadin, S. J. Savory, and D. Ives, « Compensation of quadrature imbalance in an optical QPSK coherent receiver », *IEEE Photonics Technology Letters*, vol. 20, no. 20, pp. 1733–1735, 2008.

[2] S. H. Chang, H. S. Chung, and K. Kim, « Impact of quadrature imbalance in optical coherent QPSK receiver », *IEEE Photonics Technology Letters*, vol. 21, no. 11, pp. 709–711, 2009.

[3] R. Rios-Müller, J. Renaudier, and G. Charlet, « Blind Receiver Skew Compensation and Estimation for Long-Haul Non-Dispersion Managed Systems Using Adaptive Equalizer », *Journal of Lightwave Technology*, vol. 33, no. 7, pp. 1315–1318, 2015.

[4] C. R. Fludger and T. Kupfer, « Transmitter impairment mitigation and monitoring for high baud-rate, high order modulation systems », in *42nd European Conference on Optical Communication*, VDE, 2016, pp. 1–3.

[5] M. Valkama, M. Renfors, and V. Koivunen, « Blind signal estimation in conjugate signal models with application to I/Q imbalance compensation », *IEEE Signal Processing Letters*, vol. 12, no. 11, pp. 733–736, 2005.

[6] J.-F. Cardoso and B. H. Laheld, « Equivariant adaptive source separation », *IEEE Transactions on signal processing*, vol. 44, no. 12, pp. 3017–3030, 1996.

[7] D. Godard, « Self-recovering equalization and carrier tracking in two-dimensional data communication systems », *IEEE transactions on communications*, vol. 28, no. 11, pp. 1867–1875, 1980.

[8] A Leclert and P Vandamme, « Universal carrier recovery loop for QASK and PSK signal sets », *IEEE Transactions on communications*, vol. 31, no. 1, pp. 130–136, 1983.

[9] D. R. Stephens, *Phase-locked loops for wireless communications: digital, analog and optical implementations*. Springer Science & Business Media, 2007.

[10] T. Pfau, S. Hoffmann, and R. Noe, « Hardware-Efficient Coherent Digital Receiver Concept With Feedforward Carrier Recovery for M-QAM Constellations », *Journal of Lightwave Technology*, vol. 27, no. 8, pp. 989–999, 2009.

[11] *Cisco Annual Internet Report*. [Online]. Available: `https://www.cisco.com/c/en/us/solutions/collateral/executive-perspectives/annual-internet-report/white-paper-c11-741490.html` (visited on 04/20/2020).

[12] K. Nieweglowski, L. Lorenz, K. Bock, M. Catuneanu, and K. Jamshidi, « Electro-optical co-integration of chip-components in optical transceivers for optical inter-chip communication », in *Electronic Components and Technology Conference*, 2020, pp. 139–147.

[13] T. Alexoudi, N. Terzenidis, S. Pitris, M. Moralis-Pegios, P. Maniotis, C. Vagionas, C. Mitsolidou, G. Mourgias-Alexandris, G. T. Kanellos, A. Miliou, K. Vyrsokinos, and N. Pleros, « Optics in Computing: From Photonic Network-on-Chip to Chip-to-Chip Interconnects and Disintegrated Architectures », *Journal of Lightwave Technology*, vol. 37, no. 2, pp. 363–379, 2019.

[14] S. BEA and M. Teich, « Fundamentals of Photonics », *Wiley*, p. 313, 1991.

[15] E. Desurvire, *Erbium-Doped Fiber Amplifiers: Principles and Applications*, ser. Wiley Series in Telecommunicat. Wiley, 2002.

[16] T. H. Maiman, « Stimulated optical radiation in ruby », *Nature*, vol. 187, no. 4736, pp. 493–494, 1960.

[17] F. Kapron, D. B. Keck, and R. D. Maurer, « Radiation losses in glass optical waveguides », *Applied Physics Letters*, vol. 17, no. 10, pp. 423–425, 1970.

[18] K. C. Kao and G. A. Hockham, « Dielectric-fibre surface waveguides for optical frequencies », *Proc. of the Institution of Electrical Engineers*, vol. 113, no. 7, pp. 1151–1158, 1966.

[19] W. J. Tomlinson, « Wavelength multiplexing in multimode optical fibers », *Applied Optics*, vol. 16, no. 8, pp. 2180–2194, 1977.

[20] R. Griffin and A. Carter, « Optical Differential Quadrature Phase-Shift Key for High Capacity Optical Transmission », in *Optical Fiber Communications Conference*, Optical Society of America, 2002, WX6.

[21] *Telia Carrier and Infinera Demonstrate First 600G Transmission in a Production Network*. [Online]. Available: https://investors.infinera.com/new-releases/press-release-details/2018/Telia-Carrier-and-Infinera-Demonstrate-First-600G-Transmission-in-a-Production-Network/.

[22] X. Zhou, J. Yu, Ming-Fang Huang, Yin Shao, Ting Wang, P. Magill, M. Cvijetic, L. Nelson, M. Birk, Guodong Zhang, S. Ten, H. B. Matthew, and S. K. Mishra, « 32Tb/s (320×114Gb/s) PDM-RZ-8QAM transmission over 580km of SMF-28 ultra-low-loss fiber », in *Conference on Optical Fiber Communication*, 2009, pp. 1–3.

[23] A. Sano, H. Masuda, T. Kobayashi, M. Fujiwara, K. Horikoshi, E. Yoshida, Y. Miyamoto, M. Matsui, M. Mizoguchi, H. Yamazaki, Y. Sakamaki, and H. Ishii, « 69.1-Tb/s (432 × 171-Gb/s) C- and extended L-band transmission over 240 km Using PDM-16-QAM modulation and digital coherent detection », in *Conference on Optical Fiber Communication*, 2010, pp. 1–3.

[24] Dayou Qian, Ming-Fang Huang, E. Ip, Yue-Kai Huang, Yin Shao, Junqiang Hu, and Ting Wang, « 101.7-Tb/s (370×294-Gb/s) PDM-128QAM-OFDM transmission over 3×55-km SSMF using pilot-based phase noise mitigation », in *Optical Fiber Communication Conference and Exposition and the National Fiber Optic Engineers Conference*, 2011, pp. 1–3.

[25] A. Sano, T. Kobayashi, S. Yamanaka, A. Matsuura, H. Kawakami, Y. Miyamoto, K. Ishihara, and H. Masuda, « 102.3-Tb/s (224 × 548-Gb/s) C- and extended L-band all-Raman transmission over 240 km using PDM-64QAM single carrier FDM with digital pilot tone », in *Conference on Optical Fiber Communication*, 2012, pp. 1–3.

[26] J. Renaudier, A. C. Meseguer, A. Ghazisaeidi, P. Tran, R. R. Muller, R. Brenot, A. Verdier, F. Blache, K. Mekhazni, B. Duval, H. Debregeas, M. Achouche, A. Boutin, F. Morin, L. Letteron, N. Fontaine, Y. Frignac, and G. Charlet, « First 100-nm Continuous-Band WDM Transmission System with 115Tb/s Transport over 100km Using Novel Ultra-Wideband Semiconductor Optical Amplifiers », in *European Conference on Optical Communication*, 2017, pp. 1–3.

[27] H. Masuda, E. Yamazaki, A. Sano, T. Yoshimatsu, T. Kobayashi, E. Yoshida, Y. Miyamoto, S. Matsuoka, Y. Takatori, M. Mizoguchi, K. Okada, K. Hagimoto, T. Yamada, and S. Kamei, « 13.5-Tb/s (135 × 111-Gb/s/ch) no-guard-interval coherent OFDM transmission over 6,248 km using SNR maximized second-order

DRA in the extended L-band », in *Conference on Optical Fiber Communication*, 2009, pp. 1–3.

[28] M. Salsi, H. Mardoyan, P. Tran, C. Koebele, E. Dutisseuil, G. Charlet, and S. Bigo, « 155×100Gbit/s coherent PDM-QPSK transmission over 7,200km », in *35th European Conference on Optical Communication*, vol. 2009-Supplement, 2009, pp. 1–2.

[29] J. Cai, Y. Cai, C. R. Davidson, A. Lucero, H. Zhang, D. G. Foursa, O. V. Sinkin, W. W. Patterson, A. Pilipetskii, G. Mohs, and N. S. Bergano, « 20 Tbit/s capacity transmission over 6,860 km », in *2011 Optical Fiber Communication Conference and Exposition and the National Fiber Optic Engineers Conference*, 2011, pp. 1–3.

[30] M. Mazurczyk, D. G. Foursa, H. G. Batshon, H. Zhang, C. R. Davidson, J.-X. Cai, A. Pilipetskii, G. Mohs, and N. S. Bergano, « 30 Tb/s Transmission over 6,630 km Using 16QAM Signals at 6.1 bits/s/Hz Spectral Efficiency », in *European Conference and Exhibition on Optical Communication*, Optical Society of America, 2012, Th.3.C.2.

[31] D. G. Foursa *et al.*, « 44.1 Tb/s transmission over 9,100 km using coded modulation based on 16-QAM signals at 4.9 bits/s/Hz spectral efficiency », in *39th European Conference and Exhibition on Optical Communication*, 2013, pp. 1–3.

[32] A. Ghazisaeidi, L. Schmalen, I. F. de Jauregui, P. Tran, C. Simonneau, P. Brindel, and G. Charlet, « 52.9 Tb/s transmission over transoceanic distances using adaptive multi-rate FEC », in *The European Conference on Optical Communication*, 2014, pp. 1–3.

[33] A. Ghazisaeidi, L. Schmalen, P. Tran, C. Simonneau, E. Awwad, B. Uscumlic, P. Brindel, and G. Charlet, « 54.2 Tb/s transoceanic transmission using ultra low loss fiber, multi-rate FEC and digital nonlinear mitigation », in *European Conference on Optical Communication*, 2015, pp. 1–3.

[34] A. Ghazisaeidi, I. Fernandez de Jauregui Ruiz, R. Rios-Müller, L. Schmalen, P. Tran, P. Brindel, A. Carbo Meseguer, Q. Hu, F. Buchali, G. Charlet, and J. Renaudier, « Advanced C+L-Band Transoceanic Transmission Systems Based on Probabilistically Shaped PDM-64QAM », *Journal of Lightwave Technology*, vol. 35, no. 7, pp. 1291–1299, 2017.

[35] J.-X. Cai, H. G. Batshon, M. V. Mazurczyk, O. V. Sinkin, D. Wang, M. Paskov, W. Patterson, C. R. Davidson, P. Corbett, G. Wolter, T. Hammon, M. Bolshtyansky, D. Foursa, and A. Pilipetskii, « 70.4 Tb/s Capacity over 7,600 km in C+L Band Using Coded Modulation with Hybrid Constellation Shaping and Nonlinearity Compensation », in *Optical Fiber Communication Conference Postdeadline Papers*, Optical Society of America, 2017, Th5B.2.

[36] M. Ionescu, D. Lavery, A. Edwards, E. Sillekens, L. Galdino, D. Semrau, R. Killey, W. Pelouch, S. Barnes, and P. Bayvel, « 74.38 Tb/s Transmission Over 6300 km Single Mode Fiber with Hybrid EDFA/Raman Amplifiers », Optical Society of America, 2019, Tu3F.3.

[37] M. Z. Chowdhury, M. T. Hossan, A. Islam, and Y. M. Jang, « A Comparative Survey of Optical Wireless Technologies: Architectures and Applications », *IEEE Access*, vol. 6, pp. 9819–9840, 2018.

[38] *Research and Development of Next Generation Optical Fiber Using Multiple Spatial Channels | NTT Technical Review*. [Online]. Available: `https://www.ntt-review.jp/archive/ntttechnical.php?contents=ntr201706fa5.html`.

[39] R. Gallager, « Low-density parity-check codes », *IRE Transactions on Information Theory*, vol. 8, no. 1, pp. 21–28, 1962.

[40] C. Berrou, A. Glavieux, and P. Thitimajshima, « Near Shannon limit error-correcting coding and decoding: Turbo-codes. 1 », in *IEEE International Conference on Communications*, vol. 2, 1993, pp. 1064–1070.

[41] E. Arikan, « Channel Polarization: A Method for Constructing Capacity-Achieving Codes for Symmetric Binary-Input Memoryless Channels », *IEEE Transactions on Information Theory*, vol. 55, no. 7, pp. 3051–3073, 2009.

[42] F. Buchali, A. Klekamp, L. Schmalen, and T. Drenski, « Implementation of 64QAM at 42.66 GBaud using 1.5 samples per symbol DAC and demonstration of up to 300 km fiber transmission », in *OFC 2014*, 2014, pp. 1–3.

[43] J. G. Proakis and M. Salehi, *Digital communications*. McGraw-hill New York, 2001, vol. 4.

[44] L. Lundberg, P. A. Andrekson, and M. Karlsson, « Power Consumption Analysis of Hybrid EDFA/Raman Amplifiers in Long-Haul Transmission Systems », *Journal of Lightwave Technology*, vol. 35, no. 11, pp. 2132–2142, 2017.

[45] E. Agrell, J. Lassing, E. G. Strom, and T. Ottosson, « Gray Coding for Multilevel Constellations in Gaussian Noise », *IEEE Transactions on Information Theory*, vol. 53, no. 1, pp. 224–235, 2007.

[46] W. Weber, « Differential Encoding for Multiple Amplitude and Phase Shift Keying Systems », *IEEE Transactions on Communications*, vol. 26, no. 3, pp. 385–391, 1978.

[47] M. Ionescu, D. Lavery, A. Edwards, E. Sillekens, L. Galdino, D. Semrau, R. I. Killey, W. Pelouch, S. Barnes, and P. Bayvel, « 74.38 Tb/s Transmission Over 6300 km Single Mode Fiber with Hybrid EDFA/Raman Amplifiers », in *Optical Fiber Communications Conference and Exhibition*, 2019, pp. 1–3.

[48] S. Gringeri, E. B. Basch, and T. J. Xia, « Technical considerations for supporting data rates beyond 100 Gb/s », *IEEE Communications Magazine*, vol. 50, no. 2, s21–s30, 2012.

[49] K. Kasai, J. Hongo, H. Goto, M. Yoshida, and M. Nakazawa, « The use of a Nyquist filter for reducing an optical signal bandwidth in a coherent QAM optical transmission », *IEICE Electronics Express*, vol. 5, no. 1, pp. 6–10, 2008.

[50] C. Laperle and M. O'Sullivan, « Advances in High-Speed DACs, ADCs, and DSP for Optical Coherent Transceivers », *Journal of Lightwave Technology*, vol. 32, no. 4, pp. 629–643, 2014.

[51] R. H. Walden, « Analog-to-digital converter survey and analysis », *IEEE Journal on Selected Areas in Communications*, vol. 17, no. 4, pp. 539–550, 1999.

[52] P. J. Winzer, « High-Spectral-Efficiency Optical Modulation Formats », *Journal of Lightwave Technology*, vol. 30, no. 24, pp. 3824–3835, 2012.

[53] C. Brosseau, *Fundamentals of polarized light*. Wiley, New York, 1998.

[54] K. Hagimoto, S. Nishi, and K. Nakagawa, « An optical bit-rate flexible transmission system with 5-Tb/s-km capacity employing multiple in-line erbium-doped fiber amplifiers », *Journal of Lightwave Technology*, vol. 8, no. 9, pp. 1387–1395, 1990.

[55] D. A. de Arruda Mello, V. N. Rozental, T. C. Lima, F. C. Pereira, A. N. Barreto, M. Camera, and G. Bruno, « Adaptive optical transceivers: Concepts and challenges », *Journal of Communication and Information Systems*, vol. 29, no. 1, 2014.

[56] E. Pottier and J. Saillard, « Fondements mathématiques de la polarimétrie et son application au domaine du radar », in *Annales des télécommunications*, Springer, vol. 47, 1992, pp. 314–336.

[57] M. Seimetz, *High-order modulation for optical fiber transmission*. Springer, 2009, vol. 143.

[58] J. C. Geyer, C. Doerr, M. Aydinlik, N. Nadarajah, A. Caballero, C. Rasmussen, and B. Mikkelsen, « Practical implementation of higher order modulation beyond 16-QAM », in *Optical Fiber Communications Conference and Exhibition*, 2015, pp. 1–3.

[59] P. K. A. Wai and C. R. Menyak, « Polarization mode dispersion, decorrelation, and diffusion in optical fibers with randomly varying birefringence », *Journal of Lightwave Technology*, vol. 14, no. 2, pp. 148–157, 1996.

[60] S. B. Poole, D. N. Payne, and M. E. Fermann, « Fabrication of low-loss optical fibres containing rare-earth ions », *Electronics Letters*, vol. 21, no. 17, pp. 737–738, 1985.

[61] E. Desurvire, J. R. Simpson, and P. Becker, « High-gain erbium-doped traveling-wave fiber amplifier », *Optics letters*, vol. 12, no. 11, pp. 888–890, 1987.

[62] M. Sliskovic, « Sampling frequency offset estimation and correction in OFDM systems », in *8th IEEE International Conference on Electronics, Circuits and Systems*, vol. 1, 2001, pp. 437–440.

[63] Q. Zhang, Y. Yang, C. Guo, X. Zhou, Y. Yao, A. P. T. Lau, and C. Lu, « Algorithms for Blind Separation and Estimation of Transmitter and Receiver IQ Imbalances », *Journal of Lightwave Technology*, vol. 37, no. 10, pp. 2201–2208, 2019.

[64] A. Davis, M. Pettitt, J. King, and S. Wright, « Phase diversity techniques for coherent optical receivers », *Journal of Lightwave Technology*, vol. 5, no. 4, pp. 561–572, 1987.

[65] F. Derr, « Optical QPSK transmission system with novel digital receiver concept », *Electronics Letters*, vol. 27, no. 23, pp. 2177–2179, 1991.

[66] F. Munier, E. Alpman, T. Eriksson, A. Svensson, and H. Zirath, « Estimation of phase noise for QPSK modulation over AWGN channels », in *Proc. from the Seventh Symposium*, Linköping University Electronic Press, 2003.

[67] J. H. Lee and M. H. Sunwoo, « High-speed and low complexity carrier recovery for DP-QPSK transmission », in *IEEE International Symposium of Circuits and Systems*, 2011, pp. 438–441.

[68] R.-J. Essiambre, G. Kramer, P. J. Winzer, G. J. Foschini, and B. Goebel, « Capacity Limits of Optical Fiber Networks », *Journal of Lightwave Technology*, vol. 28, no. 4, pp. 662–701, 2010.

[69] M. Hirano, T. Haruna, Y. Tamura, T. Kawano, S. Ohnuki, Y. Yamamoto, Y. Koyano, and T. Sasaki, « Record low loss, record high FOM optical fiber with manufacturable process », in *Optical Fiber Communication Conference and Exposition and the National Fiber Optic Engineers Conference*, 2013, pp. 1–3.

[70] S. Makovejs, C. C. Roberts, F. Palacios, H. B. Matthews, D. A. Lewis, D. T. Smith, P. G. Diehl, J. J. Johnson, J. D. Patterson, C. R. Towery, and S. Y. Ten, « Record-low (0.1460 dB/km) attenuation ultra-large aeff optical fiber for submarine applications », in *Optical Fiber Communications Conference and Exhibition*, 2015, pp. 1–3.

[71] D. Menashe, A. Shlifer, and U. Ghera, « Optical Amplifiers for Modern Networks », in *2006 International Conference on Transparent Optical Networks*, vol. 1, 2006, pp. 115–118.

[72] K. O. Hill and G. Meltz, « Fiber Bragg grating technology fundamentals and overview », *Journal of Lightwave Technology*, vol. 15, no. 8, pp. 1263–1276, 1997.

[73] C. D. Poole, « Statistical treatment of polarization dispersion in single-mode fiber », *Optics Letters*, vol. 13, no. 8, pp. 687–689, 1988.

[74] G. J. Foschini and C. D. Poole, « Statistical theory of polarization dispersion in single mode fibers », *Journal of Lightwave Technology*, vol. 9, no. 11, pp. 1439–1456, 1991.

[75] E. Lichtman, « Limitations imposed by polarization-dependent gain and loss on all-optical ultralong communication systems », *Journal of Lightwave Technology*, vol. 13, no. 5, pp. 906–913, 1995.

[76] F. Bruyere and O. Audouin, « Penalties in long-haul optical amplifier systems due to polarization dependent loss and gain », *IEEE Photonics Technology Letters*, vol. 6, no. 5, pp. 654–656, 1994.

[77] R. Stolen and A Ashkin, « Optical Kerr effect in glass waveguide », *Applied Physics Letters*, vol. 22, no. 6, pp. 294–296, 1973.

[78] R. Dar, M. Feder, A. Mecozzi, and M. Shtaif, « Properties of nonlinear noise in long, dispersion-uncompensated fiber links », *Optics Express*, vol. 21, no. 22, pp. 25 685–25 699, 2013.

[79] R. Dar, M. Feder, A. Mecozzi, and M. Shtaif, « Inter-Channel Nonlinear Interference Noise in WDM Systems: Modeling and Mitigation », *Journal of Lightwave Technology*, vol. 33, no. 5, pp. 1044–1053, 2015.

[80] P. J. Winzer and R. Essiambre, « Advanced Modulation Formats for High-Capacity Optical Transport Networks », *Journal of Lightwave Technology*, vol. 24, no. 12, pp. 4711–4728, 2006.

[81] R.-J. Essiambre, G. Kramer, P. J. Winzer, G. J. Foschini, and B. Goebel, « Capacity limits of optical fiber networks », *Journal of Lightwave Technology*, vol. 28, no. 4, pp. 662–701, 2010.

[82] I. Kaminow and T. Li, *Optical fiber telecommunications IV-B: systems and impairments*. Elsevier, 2002, vol. 2.

[83] F. Gini and G. B. Giannakis, « Frequency offset and symbol timing recovery in flat-fading channels: a cyclostationary approach », *IEEE Transactions on Communications*, vol. 46, no. 3, pp. 400–411, 1998.

[84] M. Oerder and H. Meyr, « Digital filter and square timing recovery », *IEEE Transactions on Communications*, vol. 36, no. 5, pp. 605–612, May 1988.

[85] D. Godard, « Passband Timing Recovery in an All-Digital Modem Receiver », *IEEE Transactions on Communications*, vol. 26, no. 5, pp. 517–523, 1978.

[86] K. Mueller and M. Muller, « Timing Recovery in Digital Synchronous Data Receivers », *IEEE Transactions on Communications*, vol. 24, no. 5, pp. 516–531, 1976.

[87] F. Gardner, « A BPSK/QPSK Timing-Error Detector for Sampled Receivers », *IEEE Transactions on Communications*, vol. 34, no. 5, pp. 423–429, 1986.

[88] U. Mengali, *Synchronization techniques for digital receivers*. Springer Science & Business Media, 2013.

[89] F. Gardner, « A BPSK/QPSK timing-error detector for sampled receivers », *IEEE Transactions on communications*, vol. 34, no. 5, pp. 423–429, 1986.

[90] Y. Li, *In-Phase and Quadrature Imbalance: Modeling, Estimation, and Compensation*. Springer Science & Business Media, 2013.

[91] W. Chung, « Transmitter IQ mismatch compensation in coherent optical OFDM systems using pilot signals », *Optics express*, vol. 18, no. 20, pp. 21 308–21 314, 2010.

[92] J. Lee, Y. Ha, B.-S. Shin, S. Kim, B.-M. Kim, and W. Chung, « Novel pilot scheme for transmitter IQ mismatch compensation in CO-OFDM system », *IEEE Photonics Technology Letters*, vol. 24, no. 17, pp. 1543–1545, 2012.

[93] G. R. Naik, W. Wang, *et al.*, « Blind source separation », *Berlin: Springer*, vol. 10, pp. 978–3, 2014.

[94] H. S. Chung, S. H. Chang, and K. Kim, « Effect of IQ mismatch compensation in an optical coherent OFDM receiver », *IEEE Photonics Technology Letters*, vol. 22, no. 5, pp. 308–310, 2010.

[95] A. J. Antos and D. K. Smith, « Design and characterization of dispersion compensating fiber based on the LP/sub 01/ mode », *Journal of Lightwave Technology*, vol. 12, no. 10, pp. 1739–1745, 1994.

[96] T. Ozeki, « Optical equalizers », *Optics letters*, vol. 17, no. 5, pp. 375–377, 1992.

[97] A. Gnauck, C. Giles, L. Cimini, J Stone, L. Stulz, S. Korotky, and J. Veselka, « 8-Gb/s-130 km transmission experiment using Er-doped fiber preamplifier and optical dispersion equalization », *IEEE photonics technology letters*, vol. 3, no. 12, pp. 1147–1149, 1991.

[98] F. Ouellette, « Dispersion cancellation using linearly chirped Bragg grating filters in optical waveguides », *Optical Letter*, vol. 12, no. 10, pp. 847–849, 1987.

[99] S. J. Savory, G. Gavioli, R. I. Killey, and P. Bayvel, « Transmission of 42.8Gbit/s Polarization Multiplexed NRZ-QPSK over 6400km of Standard Fiber with no Optical Dispersion Compensation », in *Conference on Optical Fiber Communication and the National Fiber Optic Engineers Conference*, 2007, pp. 1–3.

[100] R. I. Killey, P. M. Watts, V. Mikhailov, M. Glick, and P. Bayvel, « Electronic dispersion compensation by signal predistortion using digital processing and a dual-drive Mach-Zehnder modulator », *IEEE Photonics Technology Letters*, vol. 17, no. 3, pp. 714–716, 2005.

[101] J. McNicol, M O'sullivan, K Roberts, A Comeau, D McGhan, and L Strawczynski, « Electrical domain compensation of optical dispersion [optical fibre communication applications] », in *Optical Fiber Communication Conference*, vol. 4, 2005, p. 3.

[102] M. M. El Said, J. Sitch, and M. I. Elmasry, « An electrically pre-equalized 10-Gb/s duobinary transmission system », *Journal of lightwave technology*, vol. 23, no. 1, p. 388, 2005.

[103] P. M. Watts, R. Waegemans, Y. Benlachtar, V. Mikhailov, P. Bayvel, and R. I. Killey, « 10.7 Gb/s transmission over 1200 km of standard single-mode fiber by electronic predistortion using FPGA-based real-time digital signal processing », *Optics express*, vol. 16, no. 16, pp. 12 171–12 180, 2008.

[104] R. Waegemans, S. Herbst, L. Holbein, P. Watts, P. Bayvel, C. Fürst, and R. I. Killey, « 10.7 Gb/s electronic predistortion transmitter using commercial FPGAs and D/A converters implementing real-time DSP for chromatic dispersion and SPM compensation », *Optics express*, vol. 17, no. 10, pp. 8630–8640, 2009.

[105] H. Bülow, F. Buchali, and A. Klekamp, « Electronic dispersion compensation », *Journal of Lightwave Technology*, vol. 26, no. 1, pp. 158–167, 2008.

[106] A Farbert, « Performance of a 10.7 Gb/s receiver with digital equaliser using maximum likelihood sequence estimation », in *European Conference and Exhibition on Optical Communication*, 2004.

[107] S. J. Savory, « Digital filters for coherent optical receivers », *Optics express*, vol. 16, no. 2, pp. 804–817, 2008.

[108] S. Savory, « Compensation of fibre impairments in digital coherent systems », in *34th European Conference on Optical Communication*, IEEE, 2008, pp. 1–4.

[109] A. Eghbali, H. Johansson, O. Gustafsson, and S. J. Savory, « Optimal least-squares FIR digital filters for compensation of chromatic dispersion in digital coherent optical receivers », *Journal of Lightwave Technology*, vol. 32, no. 8, pp. 1449–1456, 2014.

[110] A. Sheikh, C. Fougstedt, A. G. i. Amat, P. Johannisson, P. Larsson-Edefors, and M. Karlsson, « Dispersion Compensation FIR Filter With Improved Robustness to Coefficient Quantization Errors », *Journal of Lightwave Technology*, vol. 34, no. 22, pp. 5110–5117, 2016.

[111] B Spinnler, « Complexity of algorithms for digital coherent receivers », in *35th European Conference on Optical Communication*, IEEE, 2009, pp. 1–4.

[112] J. G. Proakis, *Digital signal processing: principles, algorithms, and applications*. Pearson Education India, 2007.

[113] Y. Li, H. Minn, and R. Rajatheva, « Synchronization, channel estimation, and equalization in MB-OFDM systems », *IEEE Transactions on Wireless communications*, vol. 7, no. 11, pp. 4341–4352, 2008.

[114] R. Raheli and G. Picchi, « Synchronous and fractionally-spaced blind equalization in dually-polarized digital radio links », in *International Conference on Communications Conference Record*, IEEE, 1991, pp. 156–161.

[115] S. J. Savory, « Digital Coherent Optical Receivers: Algorithms and Subsystems », *IEEE Journal of Selected Topics in Quantum Electronics*, vol. 16, no. 5, pp. 1164–1179, 2010.

[116] I. Fatadin, D. Ives, and S. J. Savory, « Blind Equalization and Carrier Phase Recovery in a 16-QAM Optical Coherent System », *Journal of Lightwave Technology*, vol. 27, no. 15, pp. 3042–3049, 2009.

[117] M. J. Ready and R. P. Gooch, « Blind equalization based on radius directed adaptation », in *International Conference on Acoustics, Speech, and Signal Processing*, IEEE, 1990, pp. 1699–1702.

[118] P. Winzer, A. Gnauck, C. Doerr, M. Magarini, and L. Buhl, « Spectrally efficient long-haul optical networking using 112-Gb/s polarization-multiplexed 16-QAM », *Journal of lightwave technology*, vol. 28, no. 4, pp. 547–556, 2009.

[119] A. Leven, N. Kaneda, U. Koc, and Y. Chen, « Frequency Estimation in Intradyne Reception », *IEEE Photonics Technology Letters*, vol. 19, no. 6, pp. 366–368, 2007.

[120] A. Viterbi, « Nonlinear estimation of PSK-modulated carrier phase with application to burst digital transmission », *IEEE Transactions on Information Theory*, vol. 29, no. 4, pp. 543–551, 1983.

[121] I. Fatadin and S. J. Savory, « Compensation of Frequency Offset for 16-QAM Optical Coherent Systems Using QPSK Partitioning », *IEEE Photonics Technology Letters*, vol. 23, no. 17, pp. 1246–1248, 2011.

[122] S. Hoffmann, S. Bhandare, T. Pfau, O. Adamczyk, C. Wordehoff, R. Peveling, M. Porrmann, and R. Noe, « Frequency and Phase Estimation for Coherent QPSK Transmission With Unlocked DFB Lasers », *IEEE Photonics Technology Letters*, vol. 20, no. 18, pp. 1569–1571, 2008.

[123] M. Morelli and U. Mengali, « Feedforward frequency estimation for PSK: A tutorial review », *European Transactions on Telecommunications*, vol. 9, no. 2, pp. 103–116, 1998.

[124] T. Nakagawa, K. Ishihara, R. Kudo, T. Kobayashi, and Y. Miyamoto, « Frequency-Domain Signal Processing for Chromatic Dispersion Equalization and Carrier Frequency Offset Estimation in Optical Coherent Receivers », in *Advanced Photonics Congress*, 2012, SpTh1B.4.

[125] M. Selmi, Y. Jaouen, and P. Ciblat, « Accurate digital frequency offset estimator for coherent PolMux QAM transmission systems », in *35th European Conference on Optical Communication*, IEEE, 2009, pp. 1–2.

[126] B. Tang, S. Hu, G. Ge, J. Zhang, B. Xu, and K. Qiu, « Low Complexity Carrier Frequency Offset Estimation Scheme Based on Zoom-FFT for M-QAM », in *24th OptoElectronics and Communications Conference and International Conference on Photonics in Switching and Computing*, 2019, pp. 1–3.

[127] X. Zhou, « An Improved Feed-Forward Carrier Recovery Algorithm for Coherent Receivers With M -QAM Modulation Format », *IEEE Photonics Technology Letters*, vol. 22, no. 14, pp. 1051–1053, 2010.

[128] S. M. Bilal and G. Bosco, « Dual stage carrier phase estimation for 16-QAM systems based on a modified QPSK-partitioning algorithm », in *15th International Conference on Transparent Optical Networks*, Cartagena, Spain: IEEE, 2013, pp. 1–4.

[129] J. Li, L. Li, Z. Tao, T. Hoshida, and J. C. Rasmussen, « Laser-Linewidth-Tolerant Feed-Forward Carrier Phase Estimator With Reduced Complexity for QAM », *Journal of Lightwave Technology*, vol. 29, no. 16, pp. 2358–2364, 2011.

[130] M. Magarini, L. Barletta, A. Spalvieri, F. Vacondio, T. Pfau, M. Pepe, M. Bertolini, and G. Gavioli, « Pilot-Symbols-Aided Carrier-Phase Recovery for 100-G PM-QPSK Digital Coherent Receivers », *IEEE Photonics Technology Letters*, vol. 24, no. 9, pp. 739–741, May 2012.

[131] F. Zhang, Y. Li, J. Wu, W. Li, X. Hong, and J. Lin, « Improved Pilot-Aided Optical Carrier Phase Recovery for Coherent M-QAM », *IEEE Photonics Technology Letters*, vol. 24, no. 18, pp. 1577–1580, 2012.

[132] V. N. Rozental, D. Kong, B. Foo, B. Corcoran, and A. Lowery, « Low Complexity Blind Phase Recovery Algorithm with Increased Robustness Against Cycle-Slips », in *European Conference on Optical Communication*, Gothenburg: IEEE, 2017, pp. 1–3.

[133] L. Pessoa, H. Salgado, and I. Darwazeh, « Performance Evaluation of Phase Estimation Algorithms in Equalized Coherent Optical Systems », *IEEE Photonics Technology Letters*, vol. 21, no. 17, pp. 1181–1183, Sep. 2009.

[134] M. S. Faruk and K. Kikuchi, « Compensation for In-Phase/Quadrature Imbalance in Coherent-Receiver Front End for Optical Quadrature Amplitude Modulation », *IEEE Photonics Journal*, vol. 5, no. 2, 2013.

[135] Zhou Xian, Chen Xue, Zhou Weiqing, Fan Yangyang, Zhu Hai, and Li Zhiyu, « Digital timing recovery combined with adaptive equalization for optical coherent receivers », in *Asia Communications and Photonics conference and Exhibition*, 2009, pp. 1–6.

[136] T. Nguyen, P. Scalart, M. Gay, L. Bramerie, O. Sentieys, J. Simon, C. Peucheret, and M. Joindot, « Blind transmitter IQ imbalance compensation in M-QAM optical coherent systems », *IEEE/OSA Journal of Optical Communications and Networking*, vol. 9, no. 9, pp. D42–D50, 2017.

[137] P. Rykaczewski, M. Valkama, and M. Renfors, « On the Connection of I/Q Imbalance and Channel Equalization in Direct-Conversion Transceivers », *IEEE Trans. Veh. Technol.*, vol. 57, no. 3, pp. 1630–1636, 2008.

[138] J. P. Gordon and H. Kogelnik, « PMD fundamentals: Polarization mode dispersion in optical fibers », *Proc. National Academy of Sciences*, vol. 97, no. 9, pp. 4541–4550, 2000.

[139] H. Kogelnik, L. E. Nelson, and R. M. Jopson, « PMD characterization techniques », in *Proc. IEEE Optical Fiber Communication Conference. Technical Digest Post-conference Edition. Trends in Optics and Photonics Vol. 37*, IEEE, vol. 3, 2000, pp. 22–24.

[140] L. Liu *et al.*, « Initial tap setup of constant modulus algorithm for polarization de-multiplexing in optical coherent receivers », in *Proc. Conference on Optical Fiber Communication*, 2009, pp. 1–3.

[141] J.-F. Cardoso and B. Laheld, « Equivariant adaptive source separation », *IEEE Transactions on Signal Processing*, vol. 44, no. 12, pp. 3017–3030, 1996.

[142] C. Xie and S. Chandrasekhar, « Two-stage constant modulus algorithm equalizer for singularity free operation and optical performance monitoring in optical coherent receiver », in *Conference on Optical Fiber Communication, collocated National Fiber Optic Engineers Conference*, 2010, pp. 1–3.

[143] A. Vgenis, C. S. Petrou, C. B. Papadias, I. Roudas, and L. Raptis, « Nonsingular Constant Modulus Equalizer for PDM-QPSK Coherent Optical Receivers », *IEEE Photonics Technology Letters*, vol. 22, no. 1, pp. 45–47, 2010.

[144] T. Nguyen *et al.*, « Joint simple blind IQ imbalance compensation and adaptive equalization for 16-QAM optical communications », in *Proc. IEEE International Conference on Communications*, 2015, pp. 4913–4918.

[145] M. Chinnathambi, N. Bharanidharan, and S. Rajaram, « FPGA implementation of fast and area efficient CORDIC algorithm », in *International Conference on Communication and Network Technologies*, 2014, pp. 228–232.

[146] R. G. Lyons, *Understanding digital signal processing, 3/E*. Pearson Education India, 2004.

[147] Y. H. Hu and S. Naganathan, « Angle recording method for efficient implementation of the CORDIC algorithm », in *IEEE International Symposium on Circuits and Systems,*, 1989, 175–178 vol.1.

DOCTORAT BRETAGNE LOIRE / MATHSTIC

UNIVERSITÉ DE RENNES 1

Titre : Conception d'algorithmes temps réel pour transpondeurs optiques élastiques à très haut débit

Mot clés : Multiplexage en polarisation, Déséquilibre IQ, Bruit de phase de laser, traitement numérique du signal.

Résumé : Cette thèse s'inscrit dans le contexte de la transmission sur fibre optique élastique à très haut débit, se servant du détecteur cohérent et de traitement du signal numérique en chaîne de réception. Trois algorithmes ont été mis en avant. L' algorithme "joint" qui réalise conjointement les opérations de démultiplexage de polarization et de compensation du déséquilibre IQ en plus de deux algorithmes de compensation de bruit de phase de laser "MDD-CPR" et "R-BPS". L'approche "joint" assure l'adaptabilité à une transmission agile. Sa robustesse face à d'autres distorsions (les pertes dépendant de la polarisation, multiplexage dynamique) a été démontrée avec une complexité moindre par rapport à l'approche classique de la littérature "CMA+BASS". La validation expérimentale de "joint" a été assurée sur des données réelles. D'autre part, "MDD-CPR" est une version modifiée de l'algorithme classique de compensation de phase à décision dirigée dont les performances en simulation et avec les signaux réels ont été testées. Des caractéristiques avantageuses de sa courbe en S par rapport à l'approche classique et de sa robustesse face au bruit de phase soulignent son intérêt. "R-BPS" permet de corriger l'effet du bruit de phase de laser avec un nombre minimal de phase de tests réduisant ainsi sa complexité globale. Ses performances avec traitement parallèle pour divers formats de modulation ont mis en évidence sa capacité d'opération meilleure que le "BPS" avec un coût plus faible.

Title: Design of real-time algorithms for very high speed and elastic optical transponders

Keywords: Polarization multiplexing, IQ imbalance, Laser phase noise, digital signal processing.

Abstract: This thesis deals with digital signal processing techniques used in the coherent optical communication systems for high speed and flexible optical transmissions. Three different algorithms have been proposed. The "joint" algorithm performs the polarization demultiplexing and IQ imbalance compensation. Two other carrier phase noise recovery algorithms called " MDD-CPR " and " R-BPS " were introduced. "joint" approach performs well in the flexible context. Its robustness to other distortions (polarization dependent losses, dynamic multiplexing) has been demonstrated with less complexity compared to classic "CMA + BASS" approach and it was validated experimentally on real data. On the other hand, "MDD-CPR" is a modified version of the classic decision-directed algorithm whose performance in simulation and with real signals has been tested. Advantageous characteristics of its S-curve compared to the conventional approach and its robustness against phase noise underline its interest. "R-BPS" allows laser phase noise recovery with a minimum number of test phases. Numerical and experimental parallel processing have demonstrated its ability to operate better than " BPS " with lower overall complexity.